Final Technical Report

ADVANCED INTEGRATION OF MULTI-SCALE MECHANICS AND WELDING PROCESS SIMULATION IN WELD INTEGRITY ASSESSMENT

DOE Award Number: DE-FC36-04GO14040

Project Period: January 2004 - June 2008

by

Authors: Dr. G. Wilkowski (gwilkowski@emc-sq.com, 614-459-3200)
Dr. D. Rudland (drudland@emc-sq.com, 614-459-3200)
Dr. D.J. Shim (dshim@emc-sq.com, 614-459-3200)
Dr. F.W. Brust (bbrust@emc-sq.com, 614-459-3200)

Co-Author: Dr. Sudarsanam Babu (Ohio State University;babu13@osu.edu, 614-247-0001)

Recipient : Engineering Mechanics Corporation of Columbus
3518 Riverside Drive, Suite 202, Columbus, OH 43221

Subrecipients : Massachusetts Institute of Technology
Northwestern University
Oak Ridge National Laboratory

June 2008

ACKNOWLEDGEMENT

This report is based upon work supported by the United States Department of Energy under Award No. DE-FC36-04GO14040.

Additionally, current and former Emc^2 staff members Drs. Y. Chen, W. Cheng, Z. Feng, P. Krishnaswamy, M. Liu, Y. Y. Wang, and T. Zhang and Ms. E. Kurth contributed to this effort and authored numerous technical papers as part of this project.

The following subcontractors who worked on this project also contributed to this report:

- Dr. John Vitek, Oak Ridge National Laboratory (ORNL), TN
- Prof. David Parks, Massachusetts Institute of Technology (MIT), MA
- Dr. Su Hao, Northwestern University (NWU), IL and
- Mr. Tom Groeneveld, Battelle Memorial Institute, OH

We also acknowledge the helpful input and feedback from the following during this program

- US Department of Energy – Dr. Mahesh Jha, Project Monitor, for his insight and timely input during the course of this effort,
- PRCI Staff – Mr. Ken Lorang, and Mr. David Young for their project management assistance and support during this program, and
- PRCI Members – Mr. David Horsley of British Petroleum (formerly of TransCanada Pipelines), and Dr. Joseph Zhou of TCPL, for their technical input and guidance with regard to the impact of this work on the pipeline industry.

DISCLAIMER

This report was prepared by the Engineering Mechanics Corporation of Columbus (Emc^2) and its subcontractors as an account of work sponsored by the U. S. Department of Energy (DOE) and the Pipeline Research Council International (PRCI). Neither DOE, Emc^2, PRCI, members of PRCI, nor any person acting on behalf of these groups:

a. **MAKES ANY WARRANTY OR REPRESENTATION, EXPRESS OR IMPLIED WITH RESPECT TO THE ACCURACY, COMPLETENESS, OR USEFULNESS OF THE INFORMATION CONTAINED IN THIS REPORT, OR THAT THE USE OF ANY INFORMATION, APPARATUS, METHOD, OR PROCESS DISCLOSED IN THIS REPORT MAY NOT INFRINGE PRIVATELY OWNED RIGHTS, OR**

b. **ASSUMES ANY LIABILITY WITH RESPECT TO THE USE OF, OR FOR ANY AND ALL DAMAGES RESULTING FROM THE USE OF, ANY INFORMATION, APPARATUS, METHOD, OR PROCESS DISCLOSED IN THIS REPORT.**

Reference to trade names or specific commercial products, commodities, or services in this report does not represent or constitute an endorsement, recommendation, or favoring by Emc^2, DOE or PRCI or its contractors of the specific commercial product, commodity, or service.

Any findings, opinions, and conclusions or recommendations expressed in this report are those of the authors and do not necessarily reflect the views of either the U.S. Department of Energy or of PRCI.

PROPRIETARY DATA NOTICE

This report does not contain any proprietary data or patentable materials.

TABLE OF CONTENTS

Acknowledgement ii
Disclaimer iii
proprietary data notice iv
Table of Contents v
List of Acronyms vii
List of Figures vii
List of Tables x
Appendices xi
Executive Summary xii
1 Introduction 1
  1.1 Economic Benefit 2
  1.2 Energy Savings 3
2 Background 4
  2.1 Domestic Technology Status and Emerging Technologies 4
  2.2 Program Organization and Structure 4
    2.2.1 Weld Process Model Based Microstructure and Property Determination 5
    2.2.2 Multi-Scale Mechanics 5
    2.2.3 Deterministic Weld Integrity Assessment Procedures 6
    2.2.4 Reliability-Based Structure Integrity Assessment 6
  2.3 Technical Hurdles 6
    2.3.1 Prediction of Weld Microstructure and Mechanical Properties 6
    2.3.2 Measurement of Materials' Resistance to Failure 6
    2.3.3 Crack Driving Force to Failure 7
    2.3.4 Reliability Method 7
  2.4 Project Goal 7
  2.5 Commercialization Path 9
3 Results and Discussion 10
  3.1 Basic Material Properties for Pipeline Weld Materials 10
    3.1.1 Introduction 10
    3.1.2 X70 Steel and Weld Material Properties 10
    3.1.3 X100 Pipe Material, Welding Process, and Weld Properties 13
    3.1.4 Summary of Mechanical Properties 15
  3.2 Weld Process Simulation 16
    3.2.1 Introduction 16
    3.2.2 Weld Process Modeling and Thermal Cycles 19
    3.2.3 Weld Metal Inclusion Model 21
    3.2.4 HAZ Models 23
    3.2.5 Practical Problems: Hot Tap Welds 27
  3.3 Deterministic Procedure Development 29
    3.3.1 Introduction 29
    3.3.2 Driving Force Development 29
    3.3.3 Resistance Measurement 35
    3.3.4 Advanced Modeling of Materials Anisotropy 56
    3.3.5 Stress-Strain Property Predictions 62

        - 3.3.6 Toughness Prediction with Neural Network Model 64
        - 3.3.7 Toughness Prediction with Damage Mechanics Model 66
    - 3.4 Implication of Results for Flaw Assessment Criteria for Girth Welds 71
        - 3.4.1 Stress-Based Design 71
        - 3.4.2 Strain-Based Design Criteria 83
        - 3.4.3 Code Implications 91
        - 3.4.4 Other Flaw Stability Considerations 96
    - 3.5 Probabilistic Procedure Development 100
        - 3.5.1 Introduction 100
        - 3.5.2 Review of Current Reliability-Based Assessments for Girth Weld Defects 100
        - 3.5.3 Updating Reliability Procedures 104
- 4 Accomplishments 106
    - 4.1 Papers 106
    - 4.2 Thesis 108
- 5 Conclusions 109
- 6 Recommendations 111
- 7 References 113

LIST OF ACRONYMS

API - American Petroleum Institute
ASME - American Society of Mechanical Engineers
ASTM - American Society for Testing and Materials
BCC - body centered cubic
BM - base metal
BTU - British Thermal Unit
CMOD - crack mouth opening displacement
CSA - Canadian Standards Association
CT - compact tension
CTOD - crack tip opening displacement
DNV - Det Norske Veritas
DOE - US Department of Energy
DOT - US Department of Transportation
DPZP - dimensionless plastic zone parameter
DWTT - Drop weight tensile tear
ECA - engineering critical assessment
EDM - electro-discharge machining
Emc^2 - Engineering Mechanics Company of Columbus
EP - electric potential
EPFM - elastic-plastic fracture mechanics
EPRG - European Pipeline Research Group
EWI - Edison Welding Institute
FAC - failure assessment curve
FAD - Failure Assessment Diagram
FCAW - flux core arc weld
FCAW-G - flux core arc weld (gas shielded)
FCC - face centered cubic
FE - finite element
FEA - finite element analysis
FFS - fitness for service
FITT - Fracture Initiation Transition Temperature
FORM - First Order reliability method
FPTT - fracture propagation transition temperature
GE - General Electric
GKSS - GKSS Research Centre in Germany
GMAW - gas metal arc weld
GRI - Gas Research Institute (now GTI – Gas Technology Institute)
GTN - Gurson-Tvergaard-Needleman porous plasticity model
HAZ - Heat Affected Zone
HCP - hexagonal close-packed
HIC - hydrogen induced cracking
ID - inner diameter
IMF - Industrial Materials for the Future
IOF - Industry of the Future
LBB - Leak-Before-Break
L-C - longitudinal-circumferential orientation
LEFM - linear elastic fracture mechanics
L-R - longitudinal-radial
LVDT - linear variable differential transformer
MIT - Massachusetts Institute of Technology
MPFEM - multi-physics finite element method
MTS - mechanical testing system
NSC – net-section collapse analysis
NWU - Northwestern University
OD - outside diameter
ODF - orientation distribution function
OIT - Office of Industrial Technologies
ORNL - Oak Ridge National Laboratory
PAGS - prior austenite grain size
PPM - part per million
PRCI - Pipeline Research Council International
PWHT - post weld heat treatment
QA -Quality Assurance
RD - rolling direction
SAW - submerged arc weld
SCC - stress corrosion cracking
SENB - single-edge-notched bend
SENT, SEN(T) - single-edge-notched tension specimen
SINTAP - Structural Integrity Assessment Procedure (European)
SMAW - shielded metal arc weld
SMYS - specified minimum yield stress
SORM - Second Order reliability method
STT - surface tension transfer
TCPL - TransCanada Pipelines Limited
TD - transverse direction
TMCP - thermomechanically controlled-roll processing
TWC - through wall crack
TWI -The Welding Institute
UMAT - user material module for ABAQUS FEA Software tool
UOE - crimp plate to U-shape, press into O shape and welded then Expanded to circle
UTS - Ultimate tensile strength
VHN - Vicker's hardness number
WM - weld metal

LIST OF FIGURES

Figure 2-1 Program Overview and Task Integration 5
Figure 3-1 Stress-strain curves of the X70 pipe material 11
Figure 3-2 Stress-strain curves of the X70 pipe weld material 11
Figure 3-3 Charpy shear area of the X70 girth weld 12
Figure 3-4 CTOD Transition curves and the comparison of test data at 14 F (-10 C) from three different labs of the X70 girth weld 12
Figure 3-5 Stress-strain curves of the X100 pipe material 14
Figure 3-6 Stress-strain curves of the X100 weld material 14
Figure 3-7 Charpy energy and shear area transition of the X100 girth weld 15
Figure 3-8 CTOD transition curves of the X100 girth weld 15
Figure 3-9 Optical microstructure of typical pipeline steels used in the current research: (a) X70 steel with ferrite and pearlite microstructure and (b) X100 steel with ferrite, bainite and martensite microstructure 17
Figure 3-10 Measured hardness-map across a seam-weld made with submerged arc welding process shows the extensive softening in the heat-affected-zone of a typical X100 steel 18
Figure 3-11 Measured hardness-map across a girth weld made with gas metal arc welding process shows only limited amount of softening and also extensive mechanical heterogeneity within the weld metal regions (X100 steel) 18
Figure 3-12 Temperature and fluid flow field at longitudinal cross section at different moments for bead-on-plate case without arc pressure; 1-sec (left) and 4.3 seconds (right) after arc start. Weld movement is from left to right 20
Figure 3-13 Maximum temperature distributions (in degree-K) during deposition of 6-pass pipe girth weld. The ‘far right’ plot shows the maximum temperatures with the ‘grey’ color indicating molten material. 21
Figure3-14 User interface for computational model that predicts inclusion characteristics in weld metal region 22
Figure 3-15 Calculated inclusion composition and 2-D size distributions as a function of two weld metal compositions. The base composition is constant Fe-0.07C-0.8Si-1.7Mn-0.025Ti-0.026Al-0.007N (wt.%) and O_2 content is reduced from (a) 0.084 wt.% (b) 0.04 wt.%. 23
Figure 3-16 Summary of input and comparison of predicted microstructure and hardness by StructureR and Kirkaldy models 25
Figure 3-17 Comparison of measured hardness with predicted hardness for two models: (a) X70 steel and (b) X100 steel 26
Figure 3-18 Schematic of hot-tap weld 27
Figure 3-19 Example hot-tap weld model predictions 28
Figure 3-20 Example results showing the effect of weld metal strength mismatch on crack-driving force [OD and thickness in inches, crack depth (a) and length (2c) in mm] 30
Figure 3-21 Example results showing the effect of weld metal strength mismatch on defect tolerance 30
Figure 3-22 Finite element model and material properties used for the analyses 31
Figure 3-23 Computation of CTOD-driving force from the crack-opening profile 31

Figure 3-24 Effect of HAZ width and softening level on CTOD-driving force 32
Figure 3-25 Effect of HAZ width on the HAZ strain and 2t surface strain concentration 32
Figure 3-26 Effect of HAZ softening on CTOD driving force and 2*t* surface strain concentration for various defect sizes 33
Figure 3-27 Effect of hoop stress on CTOD driving force (no HAZ softening) 34
Figure 3-28 Combined effects of hoop stress and HAZ softening on CTOD-driving force and 2*t* surface strain 34
Figure 3-29 Illustration of differences in constraint between specimen types 36
Figure 3-30 Back-bend specimen 37
Figure 3-31 Photograph of back-bend specimen in fixture with instrumentation 37
Figure 3-32 X70 weld-centerline-cracked back-bend test results 38
Figure 3-33 Displacement at maximum load versus temperature for P109 (X70) weld and HAZ back-bend specimens 39
Figure 3-34 X100 weld-centerline-cracked back-bend test results 40
Figure 3-35 Displacement at maximum load versus temperature for P108 (X100) weld and HAZ back-bend specimens 40
Figure 3-36 A mini-wide-plate specimen 41
Figure 3-37 A mini-wide-plate specimen with the instrumentation 42
Figure 3-38 Strain limits as a function of defect length for X70 and X100 mini-wide-plate specimens with weld defects tested at cold temperature 44
Figure 3-39 Example showing how brittle initiation and ductile initiation were defined for the FITT Master Curve method 47
Figure 3-40 FITT Master Curve example for a material that has a Charpy transition temperature of -10 C 47
Figure 3-41 Brittle fracture surfaces in API girth weld pipe tests in Reference 56 48
Figure 3-42 Charpy and CTOD transition temperature for X100 weld (P108W) 49
Figure 3-43 SENT specimen in test machine and fracture surfaces showing side-grooving, scalloped EDM notch for fatigue precracking fatigue crack (11-12), EDM notch (11-3), darker area is from ductile tearing during the test 50
Figure 3-44 Normalized load versus normalized displacement curves from X100 weld SENT tests (lower-temperature tests offset to visualize easier – all specimens fatigue precracked) 51
Figure 3-45 Experimental and FE analysis comparison of fatigue-precracked versus EDM-notched SENT specimens 54
Figure 3-46 SENT results with fatigue-cracked notch and different machined radii notches 54
Figure 3-47 Effect of notch acuity from CT tests on large variety of nuclear-piping base metals and welds 55
Figure 3-48 Equivalent-strain plastic-zone profile for fatigue-precracked SENT specimen near crack initiation (quarter model with symmetry at crack plane) 55
Figure 3-49 Experimentally measured tension and compression stress-strain relations for the X100 line pipe, from Reference [76] 57
Figure 3-50 Predicted Buckling Strain Using Different Anisotropic Models; (a) Hill Model, (b) nonlinear kinematic and isotropic models 58
Figure 3-51 Experimentally measured texture of X100 line-pipe steel 60
Figure 3-52 Quarter pipe model (due to symmetry) finite element model and residual stresses due to expansion during forming and pipe reeling 61

Figure 3-53 Comparison of line pipe longitudinal test data with the Webster and Bannister correlation equations 63
Figure 3-54 Comparison of the relations between *Y*/*T* ratio and pipe grades from estimation equations and codes 63
Figure 3-55 Predicted Charpy toughness with carbon content using neural network 66
Figure 3-56 FE models of a back-bend and mini-wide-plate specimens 67
Figure 3-57 Normalized load versus load-line displacement of back-bend specimens with cracks in the base metal 68
Figure 3-58 CTOD and load-line displacement at peak loads from experimental tests and FE simulation of back-bend specimens with cracks in X100 base metal 69
Figure 3-59 Normalized load versus load-line displacement of back-bend specimens with cracks in the weld metal 69
Figure 3-60 CTOD and load-line displacement at peak loads from experimental tests and FE simulation of back-bend specimens with cracks in the weld metal 69
Figure 3-61 Load versus applied strain from experimental tests and FE simulation of mini-wide-plate specimens 70
Figure 3-62 Gross strain and CTOD at peak loads from experimental tests and FE simulation of mini-wide-plate specimens 70
Figure 3-63 Illustration of Net-Section-Collapse assumption of flow stress being reached in the entire pipe cross-section 73
Figure 3-64 Comparison of X100 weld mini-wide plate test results to a flat-plate limit-load solution and the Wang-Modified/Miller pipe bending limit-load solution 75
Figure 3-65 Comparison of different limit-load equations 75
Figure 3-66 Comparison of Wang and Miller limit-load solutions using cracked area for x-axis 76
Figure 3-67 Comparisons of unpressurized line-pipe bending tests (no internal pressure) to Wang-modified Miller equation and original NSC equation 79
Figure 3-68 Illustration of invalid limit-load data points from Hopkins and Wilkowski data (Note; virtually all the Glover data were not valid limit-load cases, as well as some of the Worswick tests.) 79
Figure 3-69 Comparison of valid limit-load test data to various limit-load equations 80
Figure 3-70 Comparisons of test data sorted by CTOD value from bend specimens to various limit-load equations 81
Figure 3-71 Determination of crack initiation for an EDM notch in a mini-wide-plate test 85
Figure 3-72 Mini-wide-plate data and FEA analyses results used to illustrate strains at crack initiation for fatigue crack versus sharp-machined notch that has initiation toughness higher than fatigue crack by factor of 1.3 85
Figure 3-73 Mini-wide-plate data used to illustrate change in initiation loads for fatigue crack versus sharp-machined notch that has initiation toughness higher than fatigue crack by factor of 1.3 86
Figure 3-74 Effect of fatigue crack on strain capacity of X70 weld mini-wide-plate tests with a crack length of 5 percent of the pipe circumference or plate width 87
Figure 3-75 Effect of fatigue crack on strain capacity of X100 weld mini-wide-plate tests with a crack length of 5 percent of the pipe circumference or plate width 87
Figure 3-76 Plastic-zone sizes for pressure versus no pressure cases for applied strain to pipe 89

Figure 3-77 FEA analyses showing that the effects of crack-face pressure were not significant for the 36” diameter by 12.7-mm thick X100 pipe with a 3-mm deep and 25-mm long flaw 90
Figure 3-78 Option 1 defect acceptance level at various applied load levels as given in Appendix A of 2007 API (Note P_r = applied stress/flow stress) 93
Figure 3-79 Comparison of API Workmanship flaw sizes (in Section 9 of API 1104 main body) to Option 1 criteria in Appendix A and properly validated limit-load equation from this project (Note; P_r = axial stress/flow stress) 94
Figure 3-80 Comparison of API Workmanship flaw sizes (in Section 9 of API 1104 main body) to Option 1 criteria in Appendix A and properly validated limit-load equation from this project – with axial stress equal to 100% SMYS limit of API 1104 95
Figure 3-81 Dimensionless Plastic-Zone Parameter (DPZP) analysis fit to circumferentially cracked full-scale nuclear pipe test results 96
Figure 3-82 Detailed illustration of energy balance approach for predicting if a pipe will leak or completely break (LBB occurs for medium and low compliance cases in this illustration) 99
Figure 3-83 Comparison of failure strains as a function of CTOD toughness between input data and the fitted equation for elliptical-shaped buried defects (lines: fitted equation; symbols: input data) 103

LIST OF TABLES

Table 3-1 Chemical composition of the line-pipe materials 10
Table 3-2 Summary of Mechanical Properties 16
Table 3-3 Summary of FE matrix considered for weld metal strength mismatch 29
Table 3-4 Test results of X70 girth welds at two critical events 43
Table 3-5 Test results of X100 girth welds at two critical events$^{(a)}$ 44
Table 3-6 Results summary of SENT FEM analyses 53
Table 3-7 Input variables and output of the neural network model for weld toughness 65
Table 3-8 GTN parameters for X100 base and weld metal (mesh size 0.25 mm) 67

APPENDICES

Appendix 1 - Summary progress report on “Weld Metal Toughness Prediction Using Neural Network Methods.”

Appendix 2 - Technical Report to GRI/PRCI titled “Reliability Based Strain Design”

EXECUTIVE SUMMARY

The various efforts in this project spanned a time frame of over four years. This was an extensive undertaking with the opportunity to explore whether specific testing and analysis procedures have value in pragmatic terms for the promotion of high-strength steels in pipeline applications. The potential to save trillions of BTU's in energy usage and billions of dollars in cost on an annual basis based on use of higher strength steel in major oil and gas transmission pipeline construction was a compelling opportunity that was recognized by both the US Department of Energy (DOE) and the Pipeline Research Council International (PRCI). Tellingly, other projects have already begun to pick up on many of the lessons learned in this program.

The use of high-strength steels (X100) as noted above, is expected to result in energy savings across the spectrum, from manufacturing of the pipe itself to transportation to the field and fabrication, including welding of line pipe in the field. Elementary examples of energy savings include more the 25 trillion BTUs saved annually based on lower energy costs to produce the thinner-walled high-strength steel pipe, with the potential for the US part of the Alaskan pipeline alone saving more than 7 trillion BTU in production and much more in transportation and assembling. Annual production, maintenance and installation of just US domestic transmission pipeline is likely to save 5 to 10 times this amount based on current planned and anticipated expansions of oil and gas lines in North America. From an operations and maintenance standpoint, installation of the high-strength steels could save more than $1 billion alone on the Alaska Gas Pipeline from just reduction in weld costs. These uses of high-strength steels and the methodologies used will also eventually spin-off to other industries in such areas as building and construction, military, naval, and aerospace applications.

Among the most important conclusions from these studies were:

- While computational weld models to predict residual stress and distortions are well-established and accurate, related microstructure models need improvement. Based on simulation models, the design of welding processes and filler metals based solely on laboratory testing cannot meet the changing needs of transmission pipeline industries.
- A methodology developed in prior work, the Fracture Initiation Transition Temperature (FITT) Master Curve properly predicts surface-cracked pipe brittle-to-ductile initiation temperature. It has value in developing Codes and Standards to better correlate full-scale behavior from either CTOD or Charpy test results with the proper temperature shifts from the FITT master curve method.
- For stress-based flaw evaluation criteria, the new circumferentially cracked pipe limit-load solution in the 2007 API 1104 Appendix A approach is overly conservative by a factor of $4/\pi$, which has additional implications. The Wang-modified/Miller limit-load equation that was used actually bounds full-scale pipe test data that had CTOD toughness values equal to or greater than 0.10 mm (0.004 inch), hence the EPFM analyses in the 2007 API 1104 Appendix A criteria were not really needed. A more simplified EPFM than the FAD-curve approach in API 1104 Appendix A was suggested. This simpler approach would be parallel to girth weld flaw evaluation procedures in ASME Section XI pipe flaw evaluation procedures that have been in place for decades.

- For strain-based design of girth weld defects, the hoop stress effect is the most significant parameter impacting CTOD-driving force and can increase the crack-driving force by a factor of 2 depending on strain-hardening, pressure level as a % of SMYS, and flaw size.
- From our years of experience in circumferential fracture analyses and experimentation, there has not been sufficient integration of work performed for other industries into analogous problems facing the oil and gas pipeline markets. Some very basic concepts and problems solved previously in these fields could have circumvented inconsistencies seen in the stress-based and strain-based analysis efforts. For example, in nuclear utility piping work, more detailed elastic-plastic fracture analyses were always validated in their ability to predict loads ***and*** displacements (stresses and strains).

Several critical recommendations were made based on the results of the program including:

- It is suggested that both the Kirkaldy (overpredicts the HAZ hardness) and StructureR (underpredicts the hardness) models be used to bound the actual hardness in the HAZ if softening is an issue to be explored. Either model works if HAZ hardening is expected.
- For the FITT master curve approach, additional SENT test data and comparison with bend, Charpy and to existing full-scale data is desirable to give further confidence in the method.
- The limit-load equation, FAD approach, and properly accounting for pipe diameter effects are all aspects that can and should be modified in API 1104 and CSA Z662 to enhance the usability of high-strength steel pipelines.
- There are a number of improvements that could be implemented to the strain-based reliability models, such as including impact of hoop stress, making sure there is consistency in the parameters between stress-based and strain-based analyses, i.e., limits on the flaw length relative the percent of the pipe circumference, and pipe diameter effects.
- The ability to predict weld metal and HAZ Charpy energy (toughness) by neural network analyses showed promise, but much more development is required before the neural network method becomes a practical tool to provide reliability analyses input.
- The Taylor polycrystal plasticity model for anisotropy effect assessment took a large amount of computational time, so that in a realistic sense it is useable on small specimen studies, but currently not practical for large structural analyses.

As can be seen from the summarized conclusions and recommendations, there were a large number of evaluations conducted to promote the use of high-strength steels. Some of the efforts conducted during the program remain as academic approaches with little current pragmatic use (i.e., damage mechanics and polycrystal plasticity for structure applications). Other methodologies show promise of practical application with various levels of importance (i.e., hoop stress effects on the crack-driving force, predicting the fracture initiation transition temperature for surface-cracked pipe for stress-based and strain-based design applications, neural network predictions of weld and HAZ Charpy energy for input to reliability models, prediction of leak-before-break behavior under stress- or strain-based design conditions). Finally, there were aspects that could have immediate impact on Codes and Standards (i.e., change to the "properly validated limit-load" equation in API 1104 and CSA Z662, revisions to FAD-curve approach, and simpler approach than the FAD-curve approach for EPFM analyses). The eventual implementation of these methodologies will result in acceleration of the industry adoption of higher-strength line-pipe steels.

1 INTRODUCTION

The overall objective of this project was to develop weld-process methodologies to encourage the use of high-strength steels in the oil and gas industries to produce energy savings during construction of new pipelines. A key to success is to make reliable welds with flaw tolerances reasonably close to lower grade steels. Hence, the focus of the program was on relative welding aspects of lower grade (X70) and higher grade (X100) steels for oil and gas transmission pipelines. The efforts in the project ranged from exploratory applications of developing technologies to practical applications to improvements of existing codes and standards. Promotion of the use of high-strength steels in this industry will accelerate spillover to other construction industries resulting in additional energy savings. Establishing this effort in understanding multi-scale impacts of welding on industrially important processes is expected to lead to significant energy and cost savings over time.

With the above objective in mind it is worthwhile to review briefly the critical role welding technology plays in fabricated steel structures. Welding is one of the most important and widely used fabrication technologies in modern industry. Over 50% of the United States gross national product is associated with production of welded products. Durable goods manufacturing industries in which welding is a critical enabling-technology account for 90% of total U.S. durable goods production [1]. The Industrial Materials for the Future (IMF) program of DOE OIT identifies welding and joining as an IMF multiple-industry research priority [2]. Although different industries have different specific needs, reliable and economic operations of welded structures are common goals. Welding presents a number of technical challenges to the designer, manufacturer, and end-user of the welded structures. While welds join components of a structure, the complex thermal cycles from welding usually produce a weld joint with microstructures and material properties different from the parent metal. Thermal cycles also result in build-up of residual stresses in the weldment. Furthermore, all welds contain some imperfections. For many DOE OIT Industry of the Future (IOF) sectors, including petroleum, chemical, mining, metal casting, steel, and forest products, the reliable performance of weld joints in service environments is the limiting factor for safe operation and service life of the equipment. For critical structural components, assessment of weld joint reliability is necessary and often mandated by federal regulation. However, accurate performance and reliability assessment of welded structures has been a major technical challenge. According to the Welding Technology Roadmap published by DOE OIT [3], improving weld integrity assessment is among the top R&D challenges for welding, and “linking of integrity assessment to realistic fitness-for-service information” is a *very high priority* R&D need in petroleum/chemical/energy industries.

This project was aimed at determining how fundamental development of advanced methodologies for weld performance and reliability assessment could be used for widespread applications in petroleum, chemical, and other relevant IOF industry sectors. The research focused on; (1) developing welding process modeling techniques capable of predicting weld microstructure and mechanical properties, (2) developing deterministic weld integrity assessment methodologies by incorporating results of welding process modeling, micromechanics, fracture mechanics and damage mechanics analyses, and (3) expanding the deterministic procedure to a reliability-based weld integrity assessment that takes into account natural variation of material properties in welds. This “multi scale” assessment lays the foundation to solve a number of challenging practical industry problems. The advanced assessment methodology can lead to safer and more economical operation of existing infrastructures *and* sound construction and operating practices of new infrastructures in the above-mentioned industries. Better performance over the lifetime of the welded structure will reduce overall energy consumption, while more accurate lifetime prediction will minimize the unexpected premature weld failures that could have significant impacts on safety, health, and the environment.

1.1 Economic Benefit

Successful implementation of this technology will have a major economic impact on multiple sectors of the economy and complete evaluation of these benefits is beyond the scope of the technical effort. However, representative illustrations of anticipated impacts are given below for the petroleum, welding, and energy industry.

Natural gas is one of the fastest growing energy sources in the United States. Nearly all natural gas is transported by a network of 2,000,000 miles of pipeline [4]. The consumption of natural gas is projected to increase to 29-33 tcf/year (trillion cubic feet per year) in 2015 from 22 tcf/year in 1997 under a business-as-usual scenario [5]. The demand for natural gas in electric utilities and non-utility generators could double or triple in next 20 years. This rapidly increasing demand has accelerated the construction of new long-distance transmission pipelines, upgrading/replacing some existing pipelines, and increasing the transmitting capacity of existing pipelines. All these activities require more accurate assessment of integrity of welded pipeline. While easily accessible gas-producing fields are being depleted, gas production is moving into more difficult regions, such as the arctic and deep-water offshore. A significant challenge in developing such fields is building gas transmission pipelines that are reliable and economic to operate.

Welding is extensively used in construction of pipelines, from seam welding of pipe at pipe mills to girth welding of pipes together in the field. Field welding in pipeline construction accounts for 10-15% of project cost. In an early study of the economic and safety consequence of applying FFS defect acceptance criteria versus more traditional workmanship criteria, Coote and Stanistreet demonstrated that FFS-based criteria can reduce weld repair rate from 16.6% rate using workmanship criteria to 8.6% using FFS criteria [6]. Given the total welding cost in the entire project, the reduced repair rate can lead to approximately 2% savings in total cost. Construction of long-distance transmission pipelines is very expensive. Construction cost of the 800-mile trans-Alaska oil pipeline was more than $9 billion. The proposed Alaskan Gas Pipeline could cost more than $20 billion. In a $20 billion project, the cost saving is ***$400 million***. This cost savings in construction does not account for related cost saving. With reduced repair rates, the construction can be completed more quickly. For instance, a six-month reduction in construction time on a $20 billion project can save ***$600 million*** in interest, assuming an annual interest rate of 6%, leading to a total ***$1 billion*** savings potential.

1.2 Energy Savings

The energy savings associated with the advanced welding reliability assessment methodology can be described from several different aspects. One of the major targeted applications of the weld reliability assessment technology is the application of high-strength steels. The use of high-strength steels will result in less tonnage of steels used for the same design load. For instance, in pipeline construction, the highest grade steel used in recent years in U.S. is API 5L X70 in the Alliance Project. In the planned Alaskan and McKenzie Valley natural gas pipelines, X100 is the intended grade if the material satisfies design and construction requirements, including welding. For the same design pressure, the required pipe wall thickness is in inverse relation to the pipe grade. Thus, the use of X100 steel in lieu of X70 steel translates into 30% energy savings in steel making. For each mile of a 52-in diameter main natural gas transmission line, the use of 0.75-inch thick X100 steel over 1-inch thick X70 would save about 300 metric tons of steel, or over 5 billion BTUs (assuming 18 MBTU energy consumption for one ton of steel [7]). If X100 grade steel would be used in the proposed 1,500 miles for the Alaskan Gas Pipeline, the energy savings would be about ***7 trillion BTUs*** in this project alone. The increasing demand on natural gas necessitates the building of several major pipelines in the coming decades. With an average of around 2000 miles of 30-50 inch pipeline under construction on an annual basis in just the US, a conservative estimate of energy savings of 19 TBTU's is achievable. Additionally, transportation costs to site the pipe on location would be considerably lower as the lower weight per segment would permit more segments being shipped. Similarly, the use of high-strength steels for bridge repair or replacement would result in tremendous annual energy savings.

Substantial energy savings would also be realized through less welding. For example, seam welding is usually used to produce pipes from steel plates. For full penetration seam weld, the weld volume is proportional to the wall thickness of the pipe (and the length of the pipe). Electrical energy is used to melt the weld and the surrounding region during welding. A typical seam weld on 20-mm pipe consumes about 6,000 BTU/m of weld length (assuming the submerged arc welding). A 30% reduction of pipe wall through upgrading steel grade from X70 to X100 would mean an energy savings of conservatively 1,800 BTU/m, or about 3 MBTU for each mile of pipeline constructed. Using the same example of 1,500 mile pipeline construction, this would lead to an energy saving of ***4.5 billion BTUs*** for the construction project.

Engineering Mechanics Corporation of Columbus (Emc^2), a company specializing in welded structure reliability assessment, led this research and development effort. Other team members included Oak Ridge National Laboratory (ORNL), Massachusetts Institute of Technology (MIT), The Ohio State University, and Northwestern University. Because of anticipated economic, environmental, and safety benefits from applications of the more accurate weld integrity assessment technology developed in this IMF program, a group of major petrochemical, and energy companies have actively participated in this research program and provided cost-sharing. The industrial participants include the Pipeline Research Council International (PRCI), and its member companies. Emc^2 also participated in the cost-sharing in this program.

2 BACKGROUND

2.1 Domestic Technology Status and Emerging Technologies

For critical welded structures and products in the petroleum, chemical, and energy sectors, welding related defects need to be inspected and evaluated to ensure safe operation of equipment. In most industries, inspection and assessment are mandated by federal regulations. For example, the U.S. Department of Transportation requires that welds of oil and gas pipelines be inspected for defects [8]. The conditions under which girth welds of pipelines must be repaired or replaced are based on API Standard 1104, *Welding of Pipelines and Related Facilities* [9]. In the refining industry, API 579 is widely used to assess a wide range of anomalies and safety-related structure issues [10].

Tolerable defect sizes in welding construction are set traditionally by workmanship-based criteria. These criteria are empirically based and historically proven safe in practice. In the oil and gas industry, construction of the Trans-Alaska pipeline in the 1970's prompted the development of fracture mechanics-based defect tolerance criteria [11] that represented a major advancement over the workmanship-based criteria. Weld integrity assessment based on fracture mechanics principles are referred to as flaw acceptance criteria, fitness-for-service (FFS) assessment, or engineering critical assessment (ECA).

2.2 Program Organization and Structure

The advanced weld structure assessment methodology pursued in this project was based on the so-called "multi-scale mechanics" approach (see Figure 2-1). This multi-scale mechanics approach involves the disciplines of welding, materials science, micromechanics, fracture mechanics, and damage mechanics. The primary motivation for such an approach is that the macro-scale response of a highly heterogeneous weld (weld metal and its heat-affected zone) is intrinsically related to its micro-scale features. It is also recognized that, collectively, the macro-scale response of a weld will have certain scatter or statistical distribution no matter how accurate the deterministic approach might be. Therefore, stochastic treatment is necessary to realistically represent the macro-scale response. Hence the final assessment procedure will illustrate how it can be implemented into a reliability-based framework.

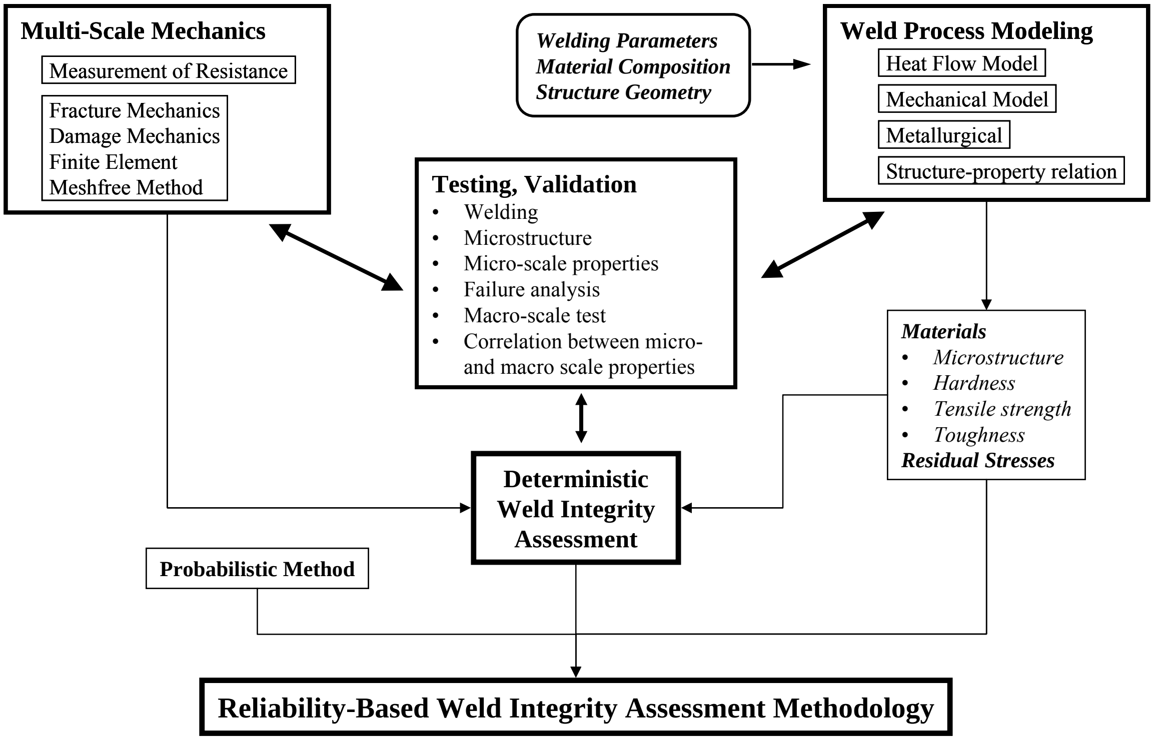

Figure 2-1 Program Overview and Task Integration

2.2.1 Weld Process Model Based Microstructure and Property Determination

Accurate weld structure integrity and performance assessment requires localized properties in the weld region that are difficult to determine experimentally. This project pursued the integrated welding process model to obtain such information. For high-strength (X100) steel acceptance, the most useful aspect of microstructure modeling is the development of a capability to predict if the base metal softens in the HAZ. If a flaw exists in the softened HAZ, then the crack-driving force increases, which makes the flaw tolerance smaller and difficult to meet for X100 steel use. Currently there is a world-wide shortage of alloying elements used for high-strength steels. Hence, having a predictive microstructure model to determine effects of new alloy combinations on HAZ strength has benefits for improved X100 steel weldability at reduced cost.

2.2.2 Multi-Scale Mechanics

Multi-scale mechanics integrates material characterization and measurement techniques employed in solid mechanics, fracture mechanics, micro-mechanics, material science, and welding engineering. The goal of multi-scale mechanics is to predict a material's macro-scale response through fundamental understanding of micro-scale properties. The common thread of this multi-scale mechanics is best understood through damage mechanics, coupled with advanced fracture mechanics. In ductile metals, material rupture is a process that involves void nucleation, growth, and coalescence. One of the most widely used damage mechanics models is the Gurson-Tvergaard-Needleman (GTN) porous plasticity model [12-15]. The GTN model has been successfully used in predicting ductile crack growth in highly ductile stainless steels [16]. Recently, Parks and his colleagues have applied the GTN model to simulate ductile crack growth to a point of complete material separation (rupture) [17].

2.2.3 Deterministic Weld Integrity Assessment Procedures

The current state-of-art procedures in weld integrity assessment are in the form of Failure Assessment Diagram (FAD) first developed and used in Europe. Further refinements to the early FAD approach include more geometric specific stress intensity factor (K_I) and limit-load solutions and more precise treatment of welding residual stress. The most recent advances include incorporation of crack-tip constraint effects and weld strength mismatch. The FAD approach is suitable for applications with nominal stress and strain within the elastic range, i.e., stress-based design. In certain industry sectors, the nominal applied stress and strain can be well into the plastic range. One such example is transmission pipelines that may experience high longitudinal strains imposed by ground movement in areas of discontinuous permafrost, earthquake, slope instability, and pipe laying. Under these conditions, nominal applied strain can be as high as 3%. There are no existing Fitness-For-Service procedures to assess weld defects under high-strain loading for the oil and gas pipeline industry. This program used fundamental understanding of material's deformation process to capture the material's response to both low and high-applied-strain loadings. In the simplest terms, a structure containing weld defects fails when the defect driving force exceeds the materials' resistance.

2.2.4 Reliability-Based Structure Integrity Assessment

The material properties in the weld area have statistical distributions. The traditional approach of running a limited number of mechanical tests cannot capture the entire statistical distribution of the material properties. A reliability-based integrity assessment procedure accounts for the inherent distributions of various input parameters (e.g., loads, flaw sizes, and material properties) and their combined effect on the assessment result. The output of the reliability-based assessment is frequently expressed as failure probability, instead of an absolute outcome of either safe or unsafe.

2.3 Technical Hurdles

The following technical hurdles were addressed in this project.

2.3.1 Prediction of Weld Microstructure and Mechanical Properties

The basic integrated thermal-mechanical-metallurgical modeling framework for weld microstructure, mechanical property, and residual stress has been developed by Emc^2, ORNL, and The Ohio State University. The R&D efforts in this project focused on:

- Improvement of microstructure algorithms of base metal HAZ and weld metal,
- Prediction of toughness of weld region by means of neural network,
- Better prediction of data for phase transformation thermodynamic constants to the base metal composition, and
- Validation experiments to cover range of steels used by the oil/gas industry.

2.3.2 Measurement of Materials' Resistance to Failure

The resistance to failure of structures containing sharp defects (the most injurious weld defect type) is measured by well-established fracture toughness testing, such as *J* or CTOD (crack-tip-opening displacement) toughness testing. In the fossil energy industry, CTOD is the most frequently used test method. However, with the ever-increasing use of high-strength and high-toughness materials, the relevance of this test method is becoming questionable. Moreover, the reported CTOD toughness from such tests depends on specimen size and strength. The other limitation is that the bend test does not represent the same crack-tip constraint state as that of most defects in these structures. Other historically proven tests, including Charpy, K_{Ic}, and J are still very much relevant when proper limitations are observed. In contrast to K_{Ic} and J tests, standard CTOD test has no specimen size validity criteria. For high-toughness materials, CTOD test using standard bend-bar specimens is the most-widely used toughness test method in fossil energy industry, but it can produce underestimates of actual upper-shelf toughness and warmer brittle-to-ductile transition temperatures than occur in actual surface-cracked pipes. One of the tasks in this program was to develop and verify a relevant and reproducible toughness testing method for a low-constraint test specimen. The single-edge-notched tension (SENT) specimen is one that gives good similitude with surface-cracked pipes. Another newer test method is the back-bend test proposed recently by Parks and his co-workers [17].

2.3.3 Crack Driving Force to Failure

The traditional crack-driving force analyses using the CTOD fracture-mechanics parameter was evaluated in the bulk of the work in the project. Literally hundreds (and maybe thousands) of FEA sensitivity analyses were conducted in this project to understand the complicated effects of weld and HAZ-strength-mismatch effects, hoop-stress effects on crack-driving force, explore the use of damage-mechanics approaches, assess large-scale fracture-mechanics tests, examine constraint effects in different specimen types, etc. In addition, advanced analysis methods were examined to assess if neural network analyses can be used to predict the Charpy energy in welds and HAZs. Alternative anisotropy constitutive laws were also examined to assess buckling behavior.

2.3.4 Reliability Method

Significant effort has been devoted in the past to develop efficient reliability methods, as represented by the first-order reliability method (FORM), second-order reliability method (SORM), and others. The primary motivation for these developments is to reduce computational time while retaining accuracy of the reliability method. With ever-increasing computation speed, the need for reducing computational demands has subsided for certain applications. Recent work indicates that standard weld integrity assessment (without accounting for in-service crack growth and inspections) can be accomplished quite quickly using Monte Carlo simulations [18]. The Monte Carlo method has better stability than FORM or SORM, as the computationally faster methods can encounter numerical convergence problems when the underlying limit-state functions are not smooth in first and second derivatives, and is preferred when computational speed is not a factor.

2.4 Project Goal

The principal technology developments included the advanced weld process simulation and multi-scale mechanics approach to weld integrity assessment. This technology is applicable to almost all fusion welds. It will be shown how these technologies can be integrated into a reliability-based integrity assessment procedure that is primarily targeted to energy pipelines. Time and funding limitations did not allow us to address all industry sectors that the fundamental technology was capable of addressing. However, the weld integrity assessment methodology developed is generic and can be applied to any industrial sector.

The objective of the proposed research program was to improve pragmatic structural integrity solutions as well as develop advanced weld integrity assessment procedures for high-strength steel pipeline applications.

2.5 Commercialization Path

PRCI and its member companies provide the primary path for commercialization of these efforts. PRCI includes major energy pipeline companies in the U.S. and a number of companies in Europe, Canada, Mexico, Brazil, Japan, and Saudi Arabia. In addition to PRCI, key members of this project team have long-standing *direct* working relations with major energy companies. PRCI, through its major cash cost match, is taking a long-term stake in the development and commercialization of this technology. It has a proven history of technology deployment. Some of the most widely used pipeline integrity tools, e.g., RSTRENG for corrosion-defect assessment, were developed and commercialized through PRCI. One of the tools recently commercialized by PRCI, the pipeline hot-tap cooling rate model, was enhanced through efforts in this project.

The second stage of commercialization will involve companies in infrastructure construction where welding is a major part of their key technical competence. Commercialization also occurs through the publication of the results in this project at appropriate technical conferences so that industry can implement those technical developments to enhance the use of higher strength steels.

A final commercialization aspect is in the improvements to Codes and Standards for girth weld defect tolerance. The work in this report showed that the analysis procedure implemented into the July 2007 API 1104 Appendix A approach for stress-based girth weld defect tolerance is too conservative. By eliminating that conservatism, it will be easier for industry to implement the usage of X100 steels for pipeline construction. There were also advances for strain-based analysis of pipeline girth weld flaw tolerance, however, the development of those standards are still underway.

3 RESULTS AND DISCUSSION

3.1 Basic Material Properties for Pipeline Weld Materials

3.1.1 Introduction

Two line-pipe materials were made available to this project. The X70 pipe had a diameter of 36 inch (914.4 mm) and a nominal thickness of 0.5 inch (12.7 mm). The X100 pipe had a diameter of 30 inch (762.0 mm) and a nominal wall thickness of 9/16 inch (14.3 mm). Both pipes were manufactured by UOE processes. Girth welds of the X70 pipe were made by the Lincoln Electric Company and shipped to Emc^2 for testing. The girth welds of the X100 pipe were made by RMS Welding Systems under the supervision of TransCanada staff. The X70 and X100 pipes are denoted as P109 and P108, respectively. The basic material properties were developed as part of another effort [19], and are summarized in this section. Additional tensile specimens for each material were tested (at -20 C) as part of this effort to aid in the analyses discussed later in this report. The results from those tests are also summarized in the following sections.

3.1.2 X70 Steel and Weld Material Properties

Both the X70 and X100 line pipes were manufactured circa 2002. The chemical compositions of the steels are given in Table 3-1.

Table 3-1 Chemical composition of the line-pipe materials

	C	Si	Mn	P	S	Nb	V	Ti	Al	Ni	Cu	Cr	Mo	B	N	O	Ceq	Pcm
X70, P109	0.060	0.280	1.500	0.010	0.007	0.037	0.062	0.016	0.044	0.023	0.017	0.033	0.004	0.001			0.33	0.15
X100, P108	0.058	0.223	1.960	0.007	0.002	0.045	0.000	0.014	0.003	0.300	0.210	0.020	0.180	0.000	0.003	0.002	0.46	0.19

The girth welds for the X70 pipe were made at the Lincoln Electric Company using the Autoweld® pipe welding system. The root pass was completed by the STT GMAW process with the Autoweld® 70 STT electrode. The fill and cap passes were completed by a FCAW-G process using the Autoweld® G70M electrode. The preheat temperature was 150 F (65 C) and the maximum interpass temperature was 350 F (175 C).

Tensile tests were conducted on both base and weld materials at room temperature, -10 C, and -40 C in another effort [19]. These specimens were round-bar specimens with a 6.35-mm diameter and a 25-mm gage length. The room temperature specimens were tested by Lincoln, while the low temperature specimens were tested by BMT Fleet Technology. Duplicate specimens were tested in each condition. In addition, Emc^2 tested the weld and base metal at -20 C to provide data for the analyses discussed later in this report. These specimens were round-bar specimens with a 6.35-mm diameter and a 13-mm gage length. Representative specimen data for both the base and weld metal are shown in Figure 3-1 and Figure 3-2. In these figures, the tensile base metal specimens were taken in the longitudinal directions, while the weld specimens were taken in the transverse direction.

The yield strength of duplicate weld metal specimens at room temperature had a variation of approximately 7 ksi (50 MPa). In comparison to the stress-strain curves of the base metal, the weld metal on the average undermatches the base metal by 6-7 ksi (40-50 MPa) from the yield to UTS. The upper-bound weld strength approximately matches the lower-bound base metal strength at room temperature. The lower-bound weld metal strength undermatches the upper-bound base metal strength by 10-15 ksi (70-100 MPa).

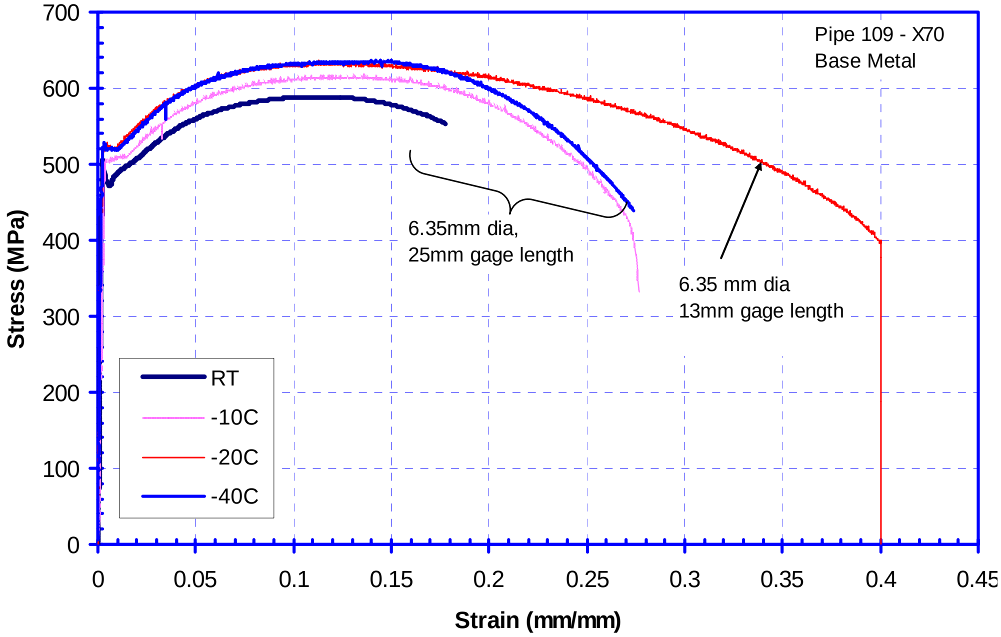

Figure 3-1 Stress-strain curves of the X70 pipe material

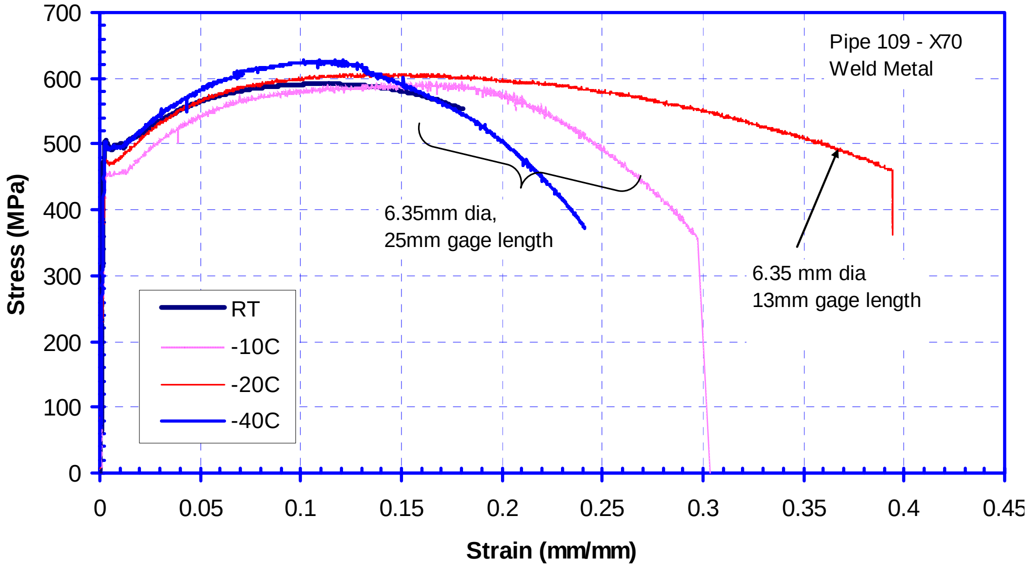

Figure 3-2 Stress-strain curves of the X70 pipe weld material

The Charpy shear area transition curve for the X70 girth weld is given in Figure 3-3. The specimens were taken from 3 and 9 o'clock positions. Specimens from 3 o'clock position have slightly higher Charpy energy than those from 9 o'clock position. The transition temperatures at

85% and 50% shear areas are approximately 32 F (0 C) and -58 F (-50 C), respectively. No base-metal Charpy specimens were tested.

The CTOD transition data for weld and HAZ specimens are given in Figure 3-4. No base metal specimens were tested. The data in Figure 3-4 were from three test labs. The data from Lab 3 are close to those from Lab 1. However, the toughness from Lab 2 is lower than that from other two labs.

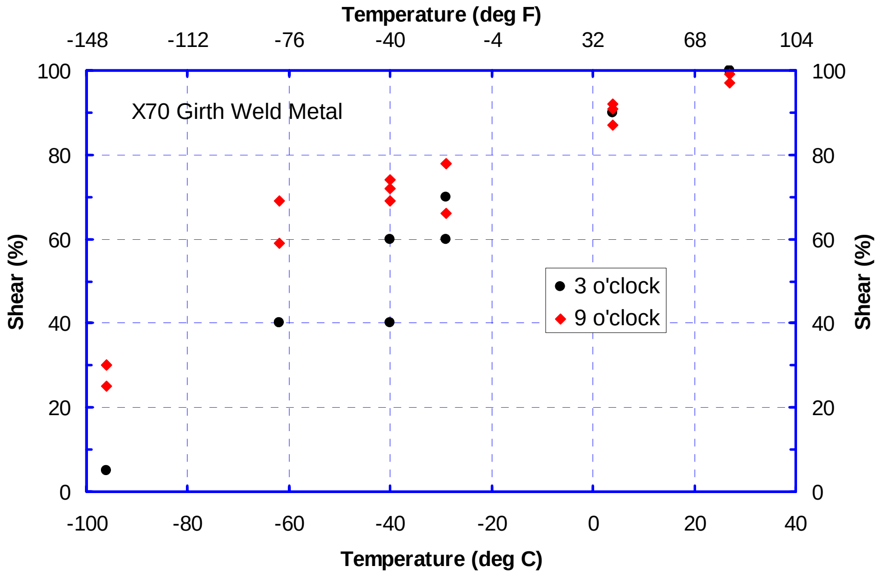

Figure 3-3 Charpy shear area of the X70 girth weld

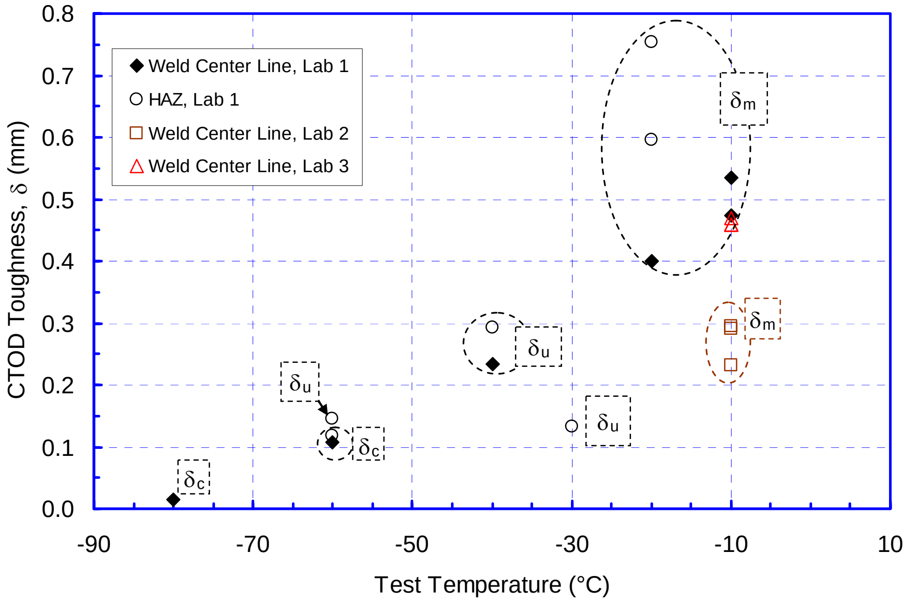

Figure 3-4 CTOD Transition curves and the comparison of test data at 14 F (-10 C) from three different labs of the X70 girth weld

The test data at 14 F (-10 C) were examined in great depth to find the causes of the differences shown in Figure 3-4. The digital records of the fracture surfaces and the load versus CMOD traces were compared. The actual broken pieces of the specimens from Lab 2 and Lab 3 were not available for examination as the tests were done independent of this project. A discussion of the findings for these experiments can be found in Reference 19. In summary, issues with the actual specimen crack depth and calibration problems with the clip-gage most likely caused the differences seen in Figure 3-4.

3.1.3 X100 Pipe Material, Welding Process, and Weld Properties

The X100 girth welds were made by RMS Welding Systems under the supervision of TransCanada staff. The weld bevel for the X100 steel was a K-type. It consists of a single vee for the root pass and J-bevel for the hot, fill, and cap passes. The root bead was made in a vertical downhill position while the pipe sections were held stationary. After the completion of the root pass, the hot, fill, and cap passes were made using a stationary single torch that was positioned at approximately 11 o'clock position while the pipe was being rotated.

Tensile specimens were extracted (6.35-mm diameter and 25-mm gage length) from both the transverse and longitudinal direction for the base metal and the transverse direction only for the weld and tested at room temperature by TCPL. Longitudinal base metal and transverse weld specimens (6.35-mm diameter and 25-mm gage length) were tested at -20 C and -40 C by BMT Fleet Technology. These tests were conducted in another effort [19]. In addition, Emc^2 tested longitudinal base metal and transverse weld specimens (6.35-mm diameter and 13-mm gage length) at -20 C for analysis discussed later in this report. Duplicate specimens were tested in each condition. Representative specimen data for both the base and weld metal are shown in Figure 3-5 and Figure 3-6. The room temperature yield strengths from duplicate specimens have a variation of approximately 3.6 ksi (25 MPa) in the immediate yield region. The weld metal strength overmatches the base metal strength for the entire range of the stress-strain relations, and in the 2 to 6 percent strain range the overmatching of the weld is by 3 percent.

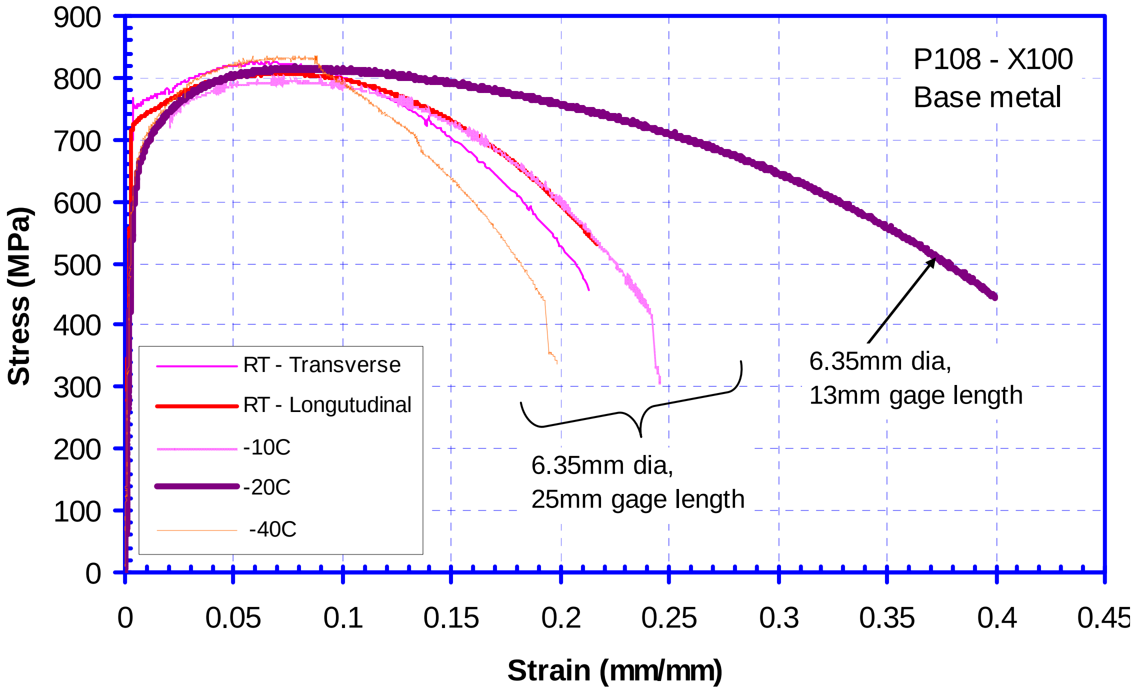

Figure 3-5 Stress-strain curves of the X100 pipe material

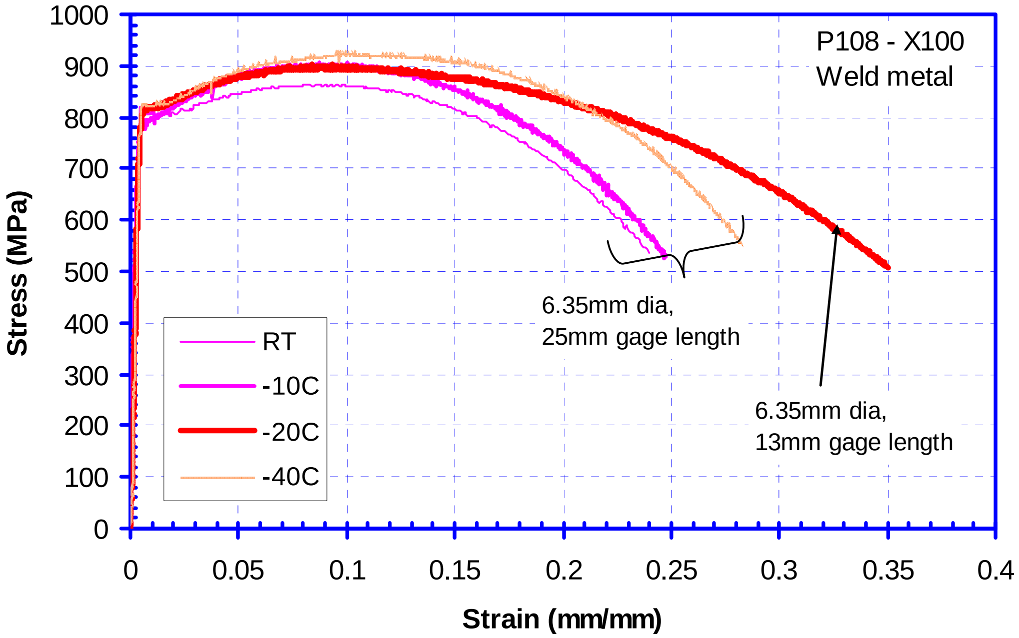

Figure 3-6 Stress-strain curves of the X100 weld material

The Charpy transition data and shear area of the X100 girth weld are given in Figure 3-7. The Charpy specimens had notches in the weld centerline and in the HAZ. The weld metal has lower transition temperature than the HAZ. For the weld metal, the transition temperatures at 85% and 50% shear areas are approximately 14 F (-10 C) and -58 F (-50 C), respectively. For the HAZ, the transition temperatures at 85% and 50% shear areas are approximately 14 F (-10 C) and -40 F

(-40 C). At -40 F (-40 C) the Charpy impact energy of the weld is greater than 150 ft-lb (203J). The HAZ has Charpy energy greater than 80 ft-lb (109J).

The CTOD transition data are given in Figure 3-8. The weld metal has much lower transition temperature than the HAZ [-76 F (-60 C) versus -22 F (-30 C)].

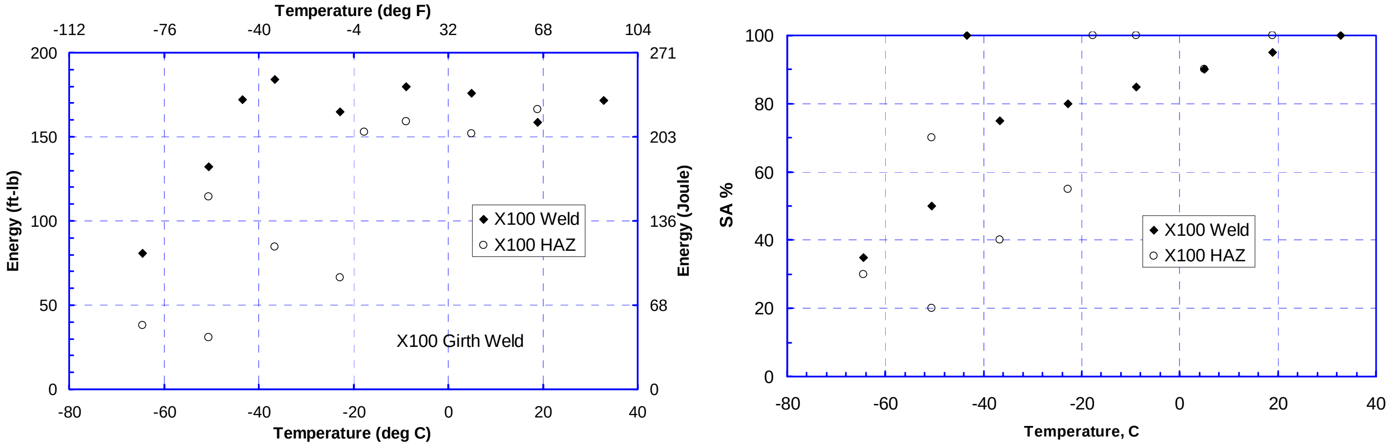

Figure 3-7 Charpy energy and shear area transition of the X100 girth weld

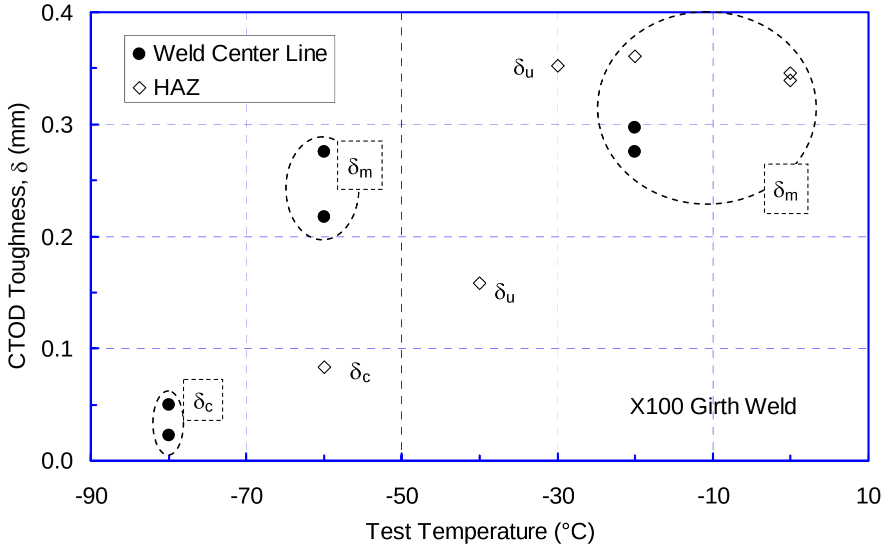

Figure 3-8 CTOD transition curves of the X100 girth weld

3.1.4 Summary of Mechanical Properties

A summary of the mechanical properties for the materials used in this effort is shown in Table 3-2. As shown in this table the room temperature yield strength seems to be slightly higher than the lower temperature yield strengths in most cases. Even though this seems counterintuitive, the difference is due to the Lüder’s band region seen in the room temperature experiments, as is illustrated for the P108 base metal in Figure 3-5. For these specimens, the colder specimens gave a more round-house style stress strain curve, which lowered the yield strength at 0.2% strain. Other than the room temperature experiments, the yield strength and ultimate strength increase with decreasing temperature as expected.

Table 3-2 Summary of Mechanical Properties

	Tensile Data				CTOD	85% shear Charpy energy
	Temperature	Specimen	0.2% yield	UTS	Transition Temp	Transition Temp
Material	C	Orientation	MPa	MPa	C	C
P109 Base	20	Longitudinal	500.00	592.00	N/A	N/A
	-10	Longitudinal	498.45	613.97		
	-20	Longitudinal	524.26	637.51		
	-40	Longitudinal	518.33	635.81		
P109 Weld	20	Transverse	502.00	584.00	-30	0
	-10	Transverse	458.32	589.98		
	-20	Transverse	473.76	618.48		
	-40	Transverse	483.57	626.40		
P108 Base	20	Transverse	764.95	826.11	N/A	N/A
	20	Longitudinal	669.95	789.46		
	-10	Longitudinal	629.90	804.37		
	-20	Longitudinal	648.13	817.44		
	-40	Longitudinal	652.45	840.12		
P108 Weld	20	Transverse	826.61	871.85	-60 - weld -30 - HAZ	-10
	-10	Transverse	774.64	906.74		
	-20	Transverse	813.98	910.24		
	-40	Transverse	832.39	925.31		

3.2 Weld Process Simulation

3.2.1 Introduction

A new generation of pipeline steels has been designed based on micro-alloying additions including vanadium, titanium, niobium and aluminum. In addition, controlled thermo-mechanical processing is used in conjunction with the new micro-alloy elements to design new higher strength steel with desirable transmission pipeline properties. These steels are processed by heating to single-phase (gamma) austenite and then rolled at a different temperature and allowed to transform to wide range of morphologies. For example, the X70 steels constitute ferrite-pearlite [see Figure 3-9a] microstructure and X100 steels constitute ferrite, bainite and martensite microstructure [see Figure 3-9b] even though they have similar steel compositions. This combination of different morphologies is the basis for fine-tuning the pipeline steels for different strength and toughness values.

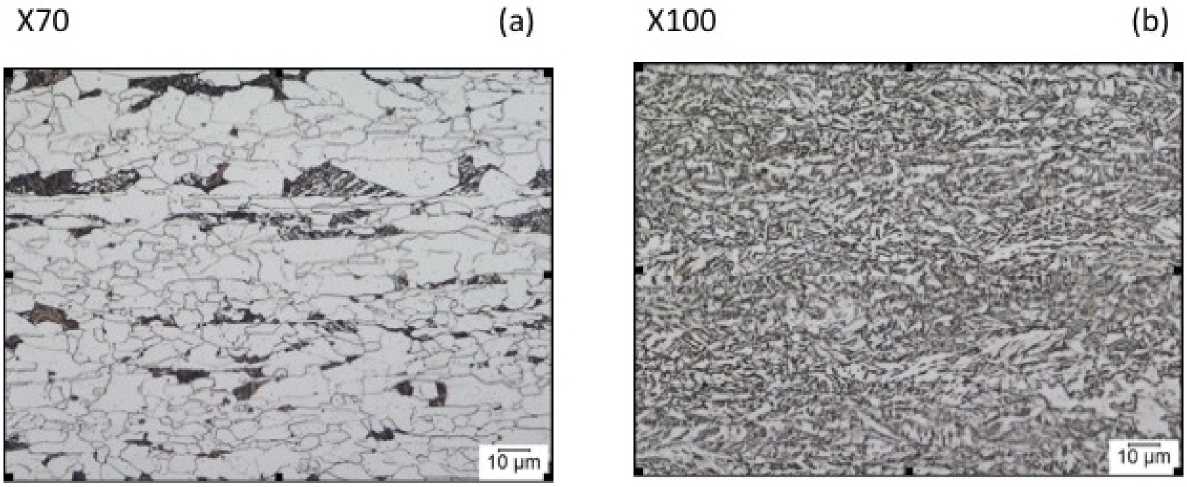

Figure 3-9 Optical microstructure of typical pipeline steels used in the current research: (a) X70 steel with ferrite and pearlite microstructure and (b) X100 steel with ferrite, bainite and martensite microstructure

Due to welding-induced thermo-mechanical cycles, these carefully controlled microstructures are destroyed at locations adjacent to the weld that reach high enough temperatures. As a result, the final mechanical properties in the heat-affected-zone are different from those of the base metal. This is clearly demonstrated in the hardness map (Figure 3-10) obtained from a longitudinal seam-weld made on a typical X100 steel pipeline material. In this case, the heat-affected-zone (HAZ) exhibits softening (as illustrated by the dark blue color in the HAZ in Figure 3-10). The same X100 steel, under girth-weld processing conditions [see Figure 3-11] produced limited softening near the HAZ. In addition, the weld metal microstructure and hardness distributions are also complex due to solidification conditions as well as reheating conditions. Although these apparent differences can be attributed to the differences in the heat-input and filler metal compositions, there is a need to predict these differences for wide range of pipeline steel compositions and process parameter combinations.

If we consider actual field-welding conditions for transmission pipelines, the range of microstructure that can occur in the weld metal (WM) and HAZ regions can be too exhaustive to be described by laboratory experimental research programs. In particular, for the WM region, the inclusion formation [20], solidification to delta-ferrite [21], solid-state transformation of delta ferrite to austenite, and transformation of austenite to different ferrite morphologies occurs [22]. In the HAZ, the solid-state transformations are much more complex due to transformation of ferrite to austenite during the weld heating phase, micro-alloying precipitate growth (e.g., NbC, TiN), precipitate dissolution, reformation of precipitates, and transformation of austenite to different ferrite morphologies during cooling [23]. The above microstructure changes also interact with the evolving weld residual stress and distortion fields caused by weld shrinkage during solidification (See Section 3.2.2). Based on the above, one can conclude that the design of welding processes and filler metals based solely on laboratory testing cannot meet the changing needs of transmission pipeline industries.

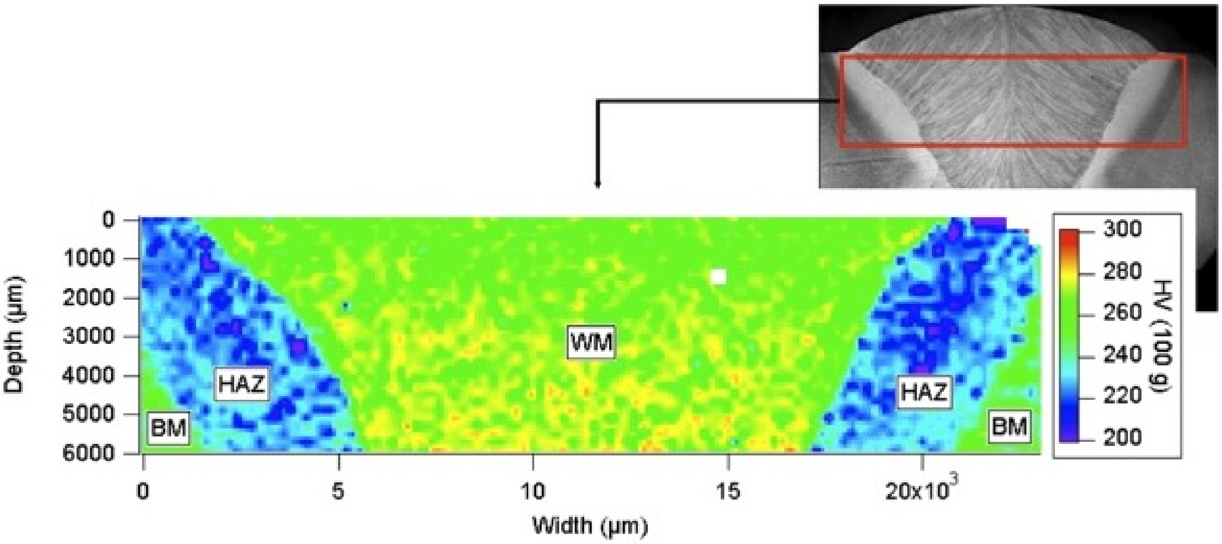

Figure 3-10 Measured hardness-map across a seam-weld made with submerged arc welding process shows the extensive softening in the heat-affected-zone of a typical X100 steel

Therefore, there is a need to develop integrated process-microstructure-performance models capable of predicting microstructure and properties as a function of material and process parameters. These models must be capable of learning from the results obtained from limited laboratory testing, while being powerful enough to predict the integrity and performance under field welding conditions. Realizing this challenge, many organizations have embarked upon predicting microstructure, residual stress, distortion and properties of steel welds by integrated process modeling [24, 25, 26, 27] tools with materials modeling tools.

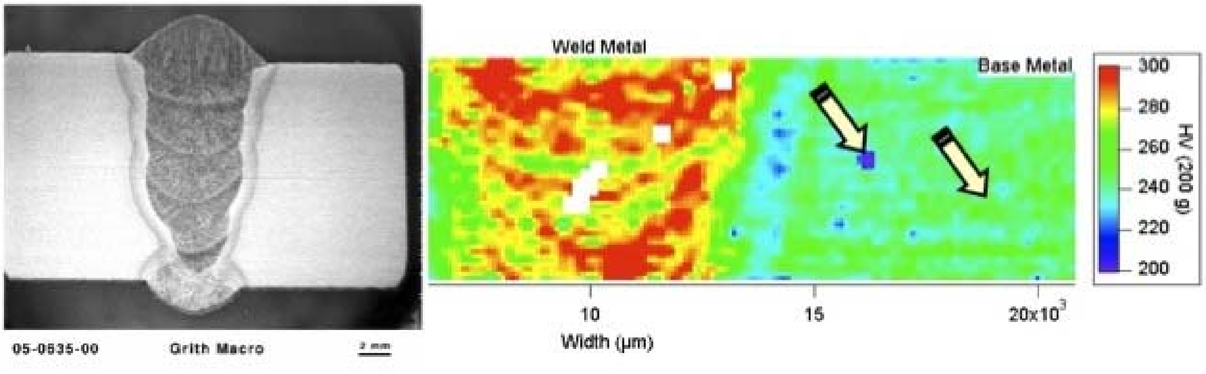

Figure 3-11 Measured hardness-map across a girth weld made with gas metal arc welding process shows only limited amount of softening and also extensive mechanical heterogeneity within the weld metal regions (X100 steel)

The overarching goal of this work is to develop a plug-and-play microstructure model that can predict the microstructure in the HAZ and WM region, for a given thermal cycle, as a function of steel and filler metal composition, respectively. The end-product was to have a tool to provide guidance and how to optimize the steel chemical composition to avoid the deleterious effect of HAZ softening on the crack-driving force for HAZ defects. The first step in the above-integrated model is to predict thermal cycles, as described in the next section.

3.2.2 Weld Process Modeling and Thermal Cycles

Computational weld modeling is challenging because many of the welding processes are highly nonlinear in a mathematical sense. Materials melt and re-solidify, very high transient thermal gradients are experienced, nonlinear temperature-dependent plastic straining and phase transformations occur, among other sources of nonlinearity. Moreover, for weld modeling to have practical advantages in energy production and transportation, computational solution times must be manageable since an optimum weld design of large, complex fabrications requires numerous separate analyses.

Most computational weld models are mathematics and physics based solution processes. There are two main analysis modules; (i) the thermal model, and (ii) the structural model that make up the weld process simulation methodology. Welding simulation normally adopts sequentially coupled thermal structural analysis where the thermal analysis is first performed and then the structural analysis is performed using the temperatures predicted by the thermal solution. For large fabricated structures, the simulations involve hundreds of thousands or millions of degrees of freedom and are computationally intensive [28]. Developing efficient and effective simulation procedures that take into account these contrasting requirements is crucial to practically and successfully applying welding simulations to large problems (see [27] and references cited therein for details of large-scale computational weld modeling). Here the focus is mainly on prediction of temperatures in and near the weld used to predict hardness and microstructures.

3.2.2.1 Thermal Model

Thermal analysis methods can be categorized into three distinct types. These are (in decreasing solution fidelity); (i) full thermal fluids solutions including weld pool dynamics, (ii) numerical thermal solutions which neglect the fluid characteristics of heat transfer within the molten weld pool, and (iii) analytically based solutions. The analytically based solutions use new closed-form solutions for the transient moving weld arc and are attractive for very large distortion control or residual-stress problems because the analytical-solution process [27] is two to three orders of magnitude faster than the conventional numerical thermal solution method type (ii) analysis method, which is at least several orders of magnitude faster than the advanced type (i) analysis method.

Type (i) analysis method is the most accurate method for predicting temperatures in and near welds but it is the most computationally intensive. In recent years, there has been growing recognition that convection in the weld pool can influence the weld pool shape due to enhanced convection heat transfer in the direction of flow [28, 29]. The molten metal fluid flow may affect the profile of the finished weld, it may affect the uniformity of composition in the weld, and it may influence the weld solidification structure by controlling the weld solidification rates. The heat content and impact force of droplets tend to induce a series of physical, chemical, and metallurgical changes in the weld pool. Other complications include weld pool deformation, surface tension and flow within the bead, droplet impact and electromagnetic force, species distribution, material property change effects, and other aspects.

These detailed processes have been included in high fidelity models shown in Figure 3-12 and discussed in References [29]. As seen in Figure 3-12, the fluid flow and direction can significantly affect the temperature versus time histories in the HAZ of welds.

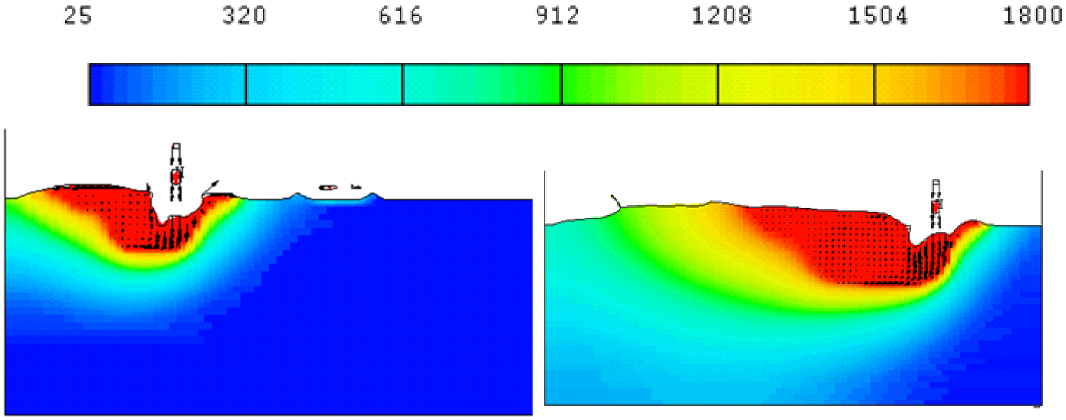

Figure 3-12 Temperature and fluid flow field at longitudinal cross section at different moments for bead-on-plate case without arc pressure; 1-sec (left) and 4.3 seconds (right) after arc start. Weld movement is from left to right

Unfortunately, the solution times required using the advanced weld thermal modeling approach was not practical for use here. As such, thermal calculations were based on method type (ii), numerical thermal solution method. A DFLUX thermal heat flux routine in conjunction with the commercial ABAQUS® finite element code was used. The weld heat flux is based on a modification of Goldak's two and three-dimensional double ellipsoid for moving heat sources [30]. This model has been validated and is thought to be accurate for prediction of microstructure and hardness as long as the weld bead shape is reasonably close to ellipsoidal. However, the advanced approach using fluid flow in the molten weld metal should be used for higher fidelity analyses in future work. One can see from Figure 3-13 temperatures that affect micro-structure and hardness in the HAZ are predicted with this model. It is also seen that different areas of the HAZ will experience different histories of heating and cooling including some points experiencing multiple heating/cooling histories.

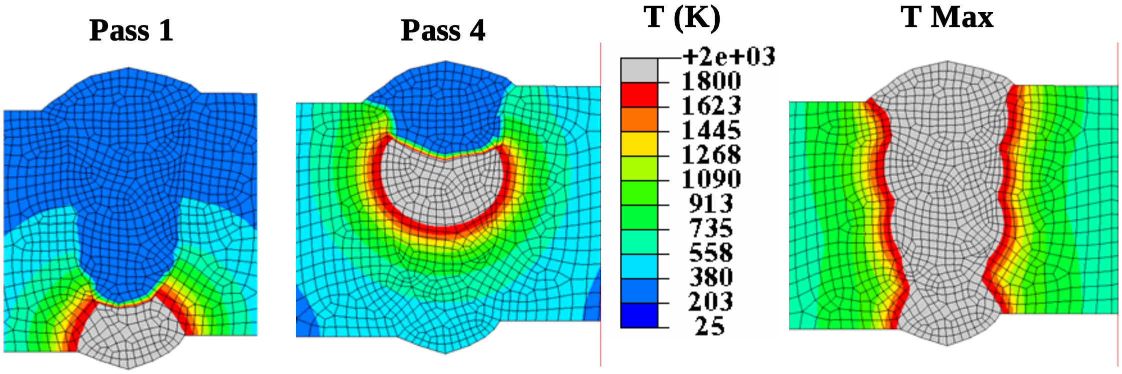

Figure 3-13 Maximum temperature distributions (in degree-K) during deposition of 6-pass pipe girth weld. The 'far right' plot shows the maximum temperatures with the 'grey' color indicating molten material.

3.2.2.2 Structural Solution and Weld Constitutive Model

The structural model portion of a computational weld model is based on ABAQUS commercial finite element code by implementing a special materials module (UMAT), which includes a constitutive law that permits stress relief due to weld melting/re-melting effects, strain-hardening effects, large-deformation mechanisms, rapid weld metal deposition features, as well as phase-transformation plasticity (if needed). Experience clearly suggests that uncoupled thermal/structural solutions for weld problems are accurate in all weld models. Moreover, visco-plastic (or creep) effects are not important since the time spent in the creep regime during welding is negligible. However, creep effects are permitted and are often used to model heat treatments of steels and stress relief due to heat treatment. The constitutive model library within the UMAT permits isotropic, kinematic, and mixed hardening (Lemaitre-Chaboche), along with phase-transformation plasticity.

3.2.3 Weld Metal Inclusion Model

The early work on this program at ORNL led to a robust model for prediction of inclusion formation during weld solidification [20]. The model was based on advanced computational thermodynamics. The model predicted the types of inclusions that formed as a function of composition and temperature. As inclusions precipitated in the molten weld pool during cooling, the model accounted for the change in composition and the effect of this compositional change on the stability of inclusions. In this way, the sequential formation of inclusions was predicted and the model was validated with experimental results. Figure3-14 shows the user interface.

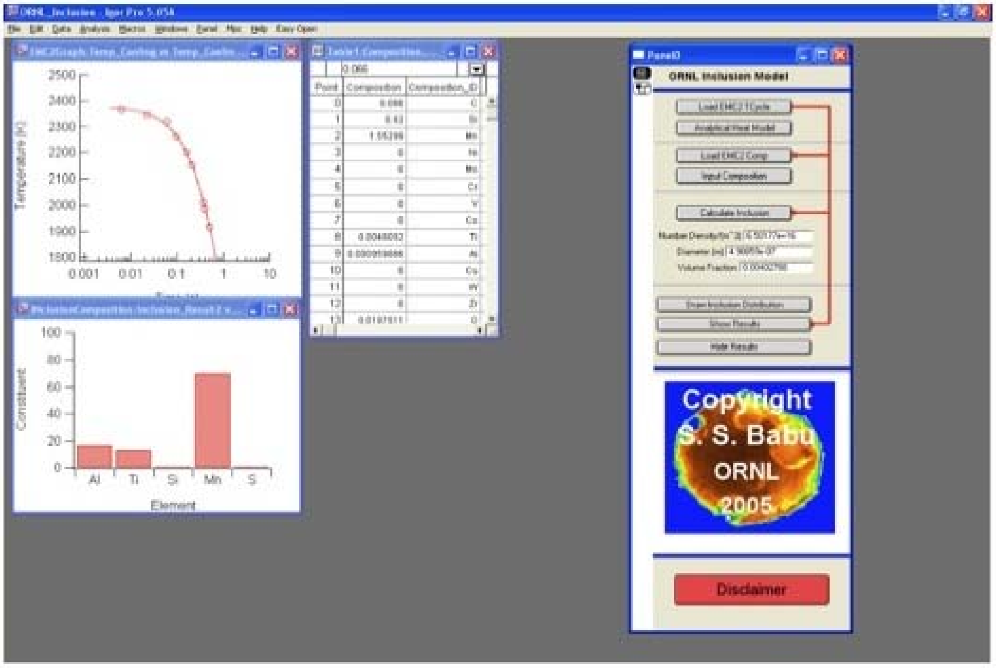

Figure3-14 User interface for computational model that predicts inclusion characteristics in weld metal region

3.2.3.1 Inclusion Model Implementation

This inclusion model was implemented into the IGOR Pro software and a user-friendly interface was created. Furthermore, the interface was integrated with computational thermodynamics software so that the inclusion model could be applied with state-of-the-art thermodynamics calculations.

The thermal history can be input as either a data file with temperature versus time or as an analytical expression for temperature as a function of time. These thermal cycles can be taken from the welding process model described in Section 3.2.2 and illustrated in Figure 3-13 for a girth weld in a pipe. The thermal model will then provide temperature versus time profiles for every location in the weld including different locations in the HAZ. With the thermal profile defined, the chemical composition is entered into the inclusion model. The calculation then determines inclusion characteristics such as inclusion number density, inclusion volume fraction and overall inclusion composition (the actual inclusion population may consist of several oxide inclusion types that form during the overall weld cooling process). The results of a typical calculation with 840 wt. PPM of oxygen and 400 wt. PPM of oxygen are shown in Figure 3-15. *The results show a decrease in inclusion distribution due to the change in oxygen concentration, as well as, the composition of the inclusions*. The low oxygen welds have lower levels of manganese oxide. It is important to note that increased number densities of the inclusions are required to promote the acicular ferrite. Additionally, the inclusions can act as an initiation point for brittle fracture, and lower the material upper-shelf tearing resistance by supplying more sites for void growth and coalescence in the ductile-dimple rupture failure mode. Therefore, the current model can be a tool to optimize inclusion distributions at a minimum level to induce acicular ferrite and not play a deleterious role on the fracture resistance.

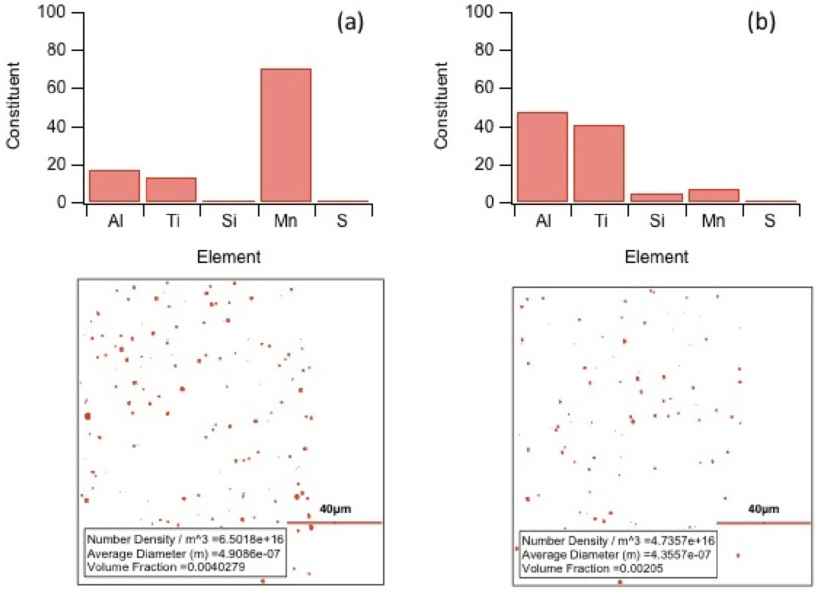

Figure 3-15 Calculated inclusion composition and 2-D size distributions as a function of two weld metal compositions. The base composition is constant Fe-0.07C-0.8Si-1.7Mn-0.025Ti-0.026Al-0.007N (wt.%) and O_2 content is reduced from (a) 0.084 wt.% (b) 0.04 wt.%.

The model has been evaluated with experimental results from submerged arc welds previously [20]. The predictive accuracy has been good. While this inclusion model has not been evaluated with GMAW welds, the model is currently available and can be leveraged by any welding consumable manufacturer to evaluate the role of different alloying elements to filler wire on the inclusion distribution.

3.2.4 HAZ Models

For the HAZ models, there is a need to predict austenite grain growth and the subsequent transformation of the austenite to different ferrite morphologies. A number of studies have been directed towards understanding the kinetics of phase transformation in the HAZ. Kirkaldy [31] showed that phase transformation in steels with relatively low alloy element could be modeled with a rate-based kinetics algorithm. Many other researchers have developed Kirkaldy's model further to allow the prediction for HAZ under continuous cooling conditions [32,33]. These models generally consider sequential formation of different ferrite microstructure during continuous cooling. For example, the austenite transforms first to grain boundary ferrite, which is then followed by Widmanstätten and bainitic ferrite. In rapid cooling conditions, some of the above microstructures can be bypassed with the formation of martensite. Jones and Bhadeshia [34] developed a simultaneous austenite decomposition model that allows for the simultaneous formation of all the ferrite microstructures, which is close to reality. Furthermore, Jones and Bhadeshia considered the inclusion effect in phase-transformation model to allow for the formation of idiomorphic ferrite. However, both models need experimental data to calibrate some of the kinetic parameters.

Ashby and Easterling [35] developed an austenite grain growth model in welds. Many researchers have adopted the approach [36, 37] due to its simplicity. However, the parameters for these models have to be determined by calibration of the models with experimental data from low-alloy steels. As a result, these parameters may not be generally extensible to the current generation of line-pipe steels. Research can be used for only a few chemical compositions. As a result, pipeline research focused on developing better austenite grain growth models that depend on base-metal microstructure and chemical composition. Recently, Moon et al. [38] modified Ashby's equation and related the activation energy to the chemical composition of steel.

In this project, the HAZ model based on Kirkaldy and Venugopalan [39], as applied to welding by Watt et al. [32, 40] and the simultaneous transformation kinetic model of Jones and Bhadeshia [34] (identified as StructureR Model) were adopted and implemented. The predicted microstructures were then used to calculate the final hardness using mixture laws.

3.2.4.1 Implementation

Both the Kirkaldy and StructureR model were implemented in the form of FORTRAN modules. These software modules read the initial composition and thermal cycles and predict; (a) the austenite grain size, (b) microstructures, and (c) hardness. The austenite grain growth model needs further development. Details of these models are published in conference proceedings [26].

The input conditions ranged from X70, X100, and an older line pipe steel (X52) compositions, two different prior austenite grain sizes (30 and 140 μm) and three different cooling rates (10, 30, and 60 C/s). Two different grain sizes were assumed since the original version of these two models does not have a grain growth model and current grain growth models need further work. The chosen cooling rates were those used in Gleeble tests. The StructureR Model is not capable of predicting relative fractions of bainite and martensite. The Kirkaldy model predicts all phases. Hence, for StructureR results, relative distribution of bainite and martensite is assumed to be 50% of the austenite volume fraction that remains after the formation of ferrite and pearlite. In other words, after all ferrite and pearlite are formed, the remaining austenite is assumed to be 50% bainite/50% martensite. The predicted microstructures were converted into Vickers hardness using standard equations.

Figure 3-16 provides a summary of the predictions for all cases examined and are intriguing. The StructureR model predicted that, for a given composition set, moving from slow to high cooling rates, ferrite and pearlite (softer) microstructure will diminish and bainite and martensite (harder) microstructure will increase. In contrast, the Kirkaldy model predictions show an abrupt change. At cooling rates of 10 C/s the microstructure was mostly ferrite, pearlite and (small amounts of) bainite. At 30 C/s and higher, the microstructure was a mixture of pearlite, bainite or martensite with little ferrite. Based on the above, we conclude that these two models are inconsistent in microstructure constituent predictions. However, comparison of predicted hardness from StructureR and the Kirkaldy model showed similar trends, i.e., an increase in cooling rate predicted a hardness increase.

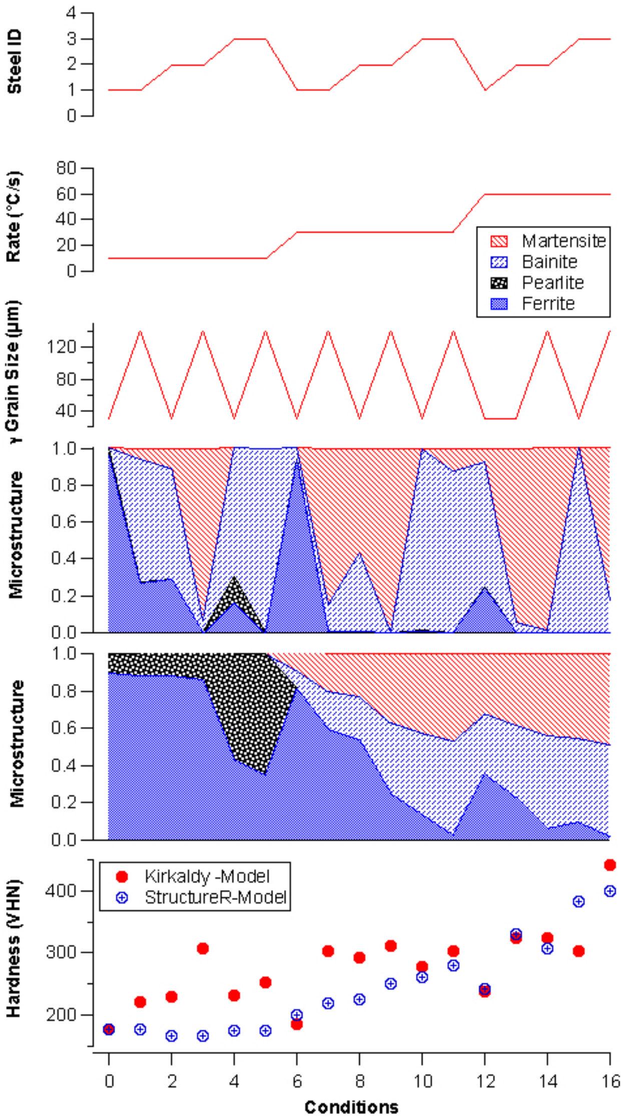

Figure 3-16 Summary of input and comparison of predicted microstructure and hardness by StructureR and Kirkaldy models

3.2.4.2 Typical Calculations

To validate the capabilities of these models to predict the tendency for softening or hardening at the heat-affected-zones of pipeline steel welds, it is useful to consider some fundamental cases. This is discussed by considering X100 steel and assuming a base metal hardness of 200 VHN. The calculations showed that, while cooling at 10 C/s, the HAZ-model predicts (Condition # 3 in Figure 3-16) a hardness of 308 VHN (hardening), where as the Structure-R model predicts 166 VHN (softening). In comparison, while cooling at 60 C/s (Condition # 13 in Figure 3-16), both models predict similar hardening (324 and 330 VHN).

3.2.4.3 Experimental Evaluations

In order to evaluate the predictive accuracies of the StructureR and Kirkaldy models, selected samples from X70 and X100 pipelines were subjected to controlled thermal-cycling experiments in a Gleeble® thermo-mechanical simulator. The samples were heated to different peak temperature (900 C, 1100 C, and 1300 C). With these peak temperatures, the austenite grain sizes are expected to vary from small to large values. After reaching the peak temperature, the samples were cooled at 30 C/s to room temperature. These samples were then sectioned and characterized by optical microscopy and hardness measurements. The results show that experimental hardness values have large scatter, although the average hardness increased with an increase in peak temperature. Optical microscopy also showed that austenite grain size for these peak temperatures may range from 30 to 140-μm with an increase in the peak temperatures from 900 to 1300 C. To compare these measured data with predictions, both the StructureR and Kirkaldy models were used to calculate hardness for X70 and X100 steels with two different austenite grain sizes and a constant cooling rate of 30 C/s. The predicted hardness values for two different extreme grain sizes are compared with experimental measurements[*] (see Figure 3-17).

The plot shows that, for a given cooling rate, the predicted hardness by both StructureR and Kirkaldy models show a similar trend, i.e., an increase in hardness with an increase in the prior austenite grain size (PAGS). However, the StructureR model always underpredicted the hardness and Kirkaldy model overpredicted the hardness. It is interesting to note that these two models bound the experimental hardness measurements.

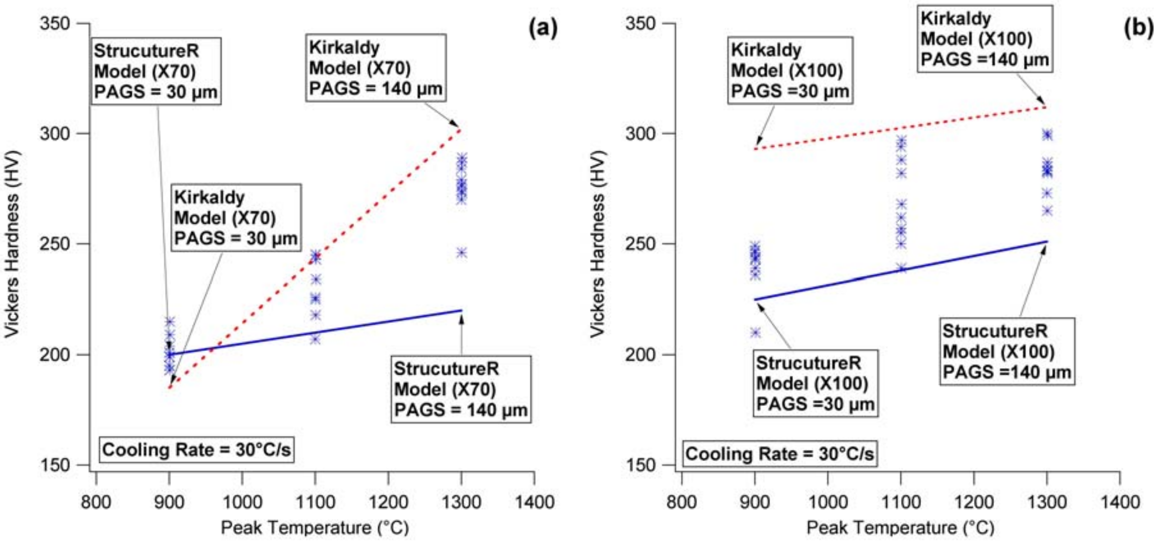

Figure 3-17 Comparison of measured hardness with predicted hardness for two models: (a) X70 steel and (b) X100 steel

---

[*] Original hardness measurements were made using a Rockwell B indenter technique. This measured more of a macro hardness and the results appeared inconsistent. As such, here Vickers hardness measurements of selected samples were made and the results were more consistent with expectations.

3.2.4.4 Significance

Based on the above discussions, we can conclude that the two models can be used to provide upper and lower hardness bounds. The StructureR model will predict relatively large softening in the HAZ, where as the Kirkaldy models may not predict the softening. These inconsistencies between the Kirkaldy and StructureR models are attributed to thermodynamic and kinetic parameters used to describe the transformation kinetics. However, it is recommended at this time that both models be used for evaluating HAZ the upper and lower bound of mechanical performance. In addition, these models must be tested with reference to spatial and stochastic variations of grain size and cooling rate.

3.2.5 Practical Problems: Hot Tap Welds

Advanced computational weld models that are now used to control weld residual stresses and distortions, control microstructure, and predict inclusion population in welds were summarized above. These models are now routinely used to control a variety of weld processes and parameters to achieve service goals of welded components. Here we present an example which illustrates the usefulness of the microstructure and hardness weld models for hot tap welds in transmission pipeline.

3.2.5.1 Hot-Tap Weld Example

Welding onto an in-service pipeline is frequently required to repair damaged areas and for system modifications. There are often significant economic and environmental incentives to perform in-service welding, including the ability to maintain operations during welding and to avoid venting the contents to the atmosphere. Two main issues are of concern regarding hot-tap welds: (i) possible hydrogen-induced cracking (HIC), and (ii) burn through the hot tap. Welds made onto in-service pipelines tend to cool at an accelerated rate. These welds are likely to have high heat-affected zone (HAZ) hardness which increases their susceptibility to hydrogen cracking. Burn through of the weld is caused by high heat input. Figure 3-18 illustrates a typical saddle-type hot-tap connection.

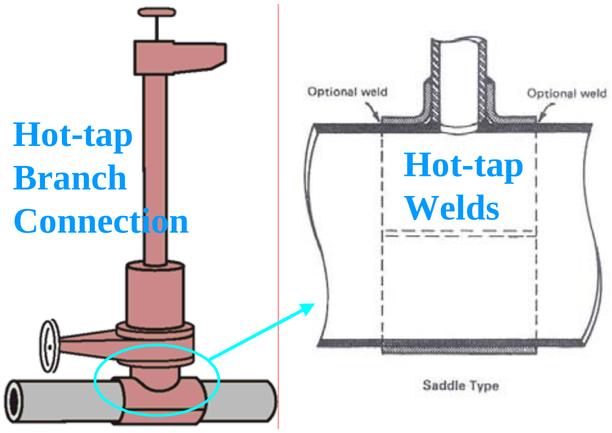

Figure 3-18 Schematic of hot-tap weld

For HIC to occur, three conditions must be present, and elimination of any of these can mitigate it. These conditions are hydrogen, tensile weld residual stresses, and a hardened microstructure (martensite). Here we are concerned with controlling the microstructure although use of low-hydrogen electrodes (or processes) should be specified, and weld methods to reduce tensile weld residual stresses could also be explored as they are used in the nuclear industry. Computational weld models can be used to specify proper heat input to control HAZ microstructure by controlling cooling rate, pre-heat (if used), and weld process. The burn through risk is controlled by controlling the heat input. Figure 3-19 illustrates peak temperatures (for controlling burn through) and hardness (for controlling HIC) in a typical hot tap weld in a pipeline material.

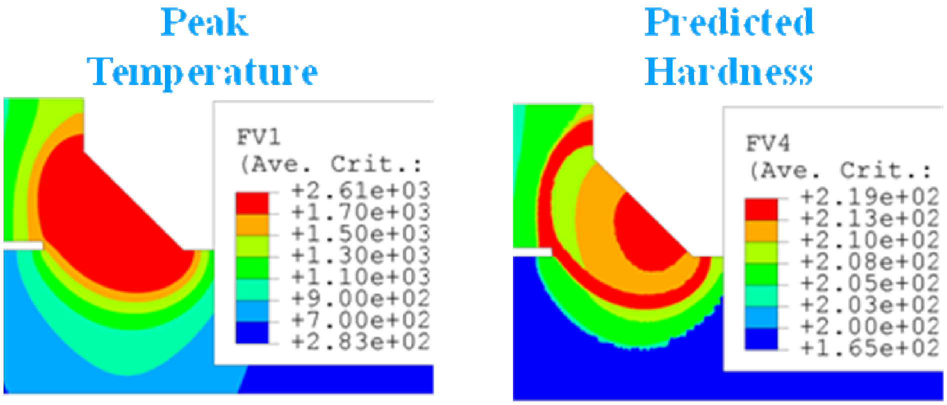

Figure 3-19 Example hot-tap weld model predictions

An additional minor effort was also undertaken to improve the internal heat transfer rate for different fluids flowing in the pipes during the hot-tap welding, as well as debugging some mesh generator problems. The improvements were implemented into the 2008 PRCI/EWI hot-tap code [41].

3.3 Deterministic Procedure Development

3.3.1 Introduction

In order to accurately predict the failure behavior of welds the underlying deterministic models that predict the driving force for flaw initiation and growth and the material's inherent resistance (toughness) to flaw tolerance must be improved. This chapter details; (i) the driving force development, (ii) characterization of the material's resistance, (iii) material anisotropy effects and prediction of the fundamental constitutive models including those that incorporate damage mechanics. These topics are described in the following sections.

3.3.2 Driving Force Development

3.3.2.1 Effect of Weld Metal Strength Mismatch on Crack-Driving Force

In order to investigate the effect of weld metal strength mismatch on the crack-driving force, finite element (FE) analyses were performed for 36-inch diameter pipe with various pipe thicknesses. As shown in Table 3-3, the base metal strength, weld metal mismatch level, weld bevel angle, defect size, and defect location were systematically varied. A total of 768 cases were used in the sensitivity study.

Table 3-3 Summary of FE matrix considered for weld metal strength mismatch

Materials	X60, X70, X80, X100
Pipe Wall Thickness (in)	0.375, 0.5, 0.75
Defect Location	WM center, Fusion line
Defect Depth (mm)	3
Defect Length (mm)	25, 50, 100, 200
Bevel Angle (degree)	16, 60
WM Mismatching Level	25%, 10%, 0%, -10%

From the FE analyses, the effects of weld metal strength mismatch on both the crack-driving force, i.e., crack-tip-opening displacement (CTOD), and the defect tolerance were investigated as demonstrated in Figure 3-20 and Figure 3-21. For these cases the effect of internal pressure was not considered.

3.3.2.2 Effect of HAZ Softening on Crack-Driving Force

Although the phenomenon of HAZ softening has been known for a long time, the impact of the HAZ softening on the integrity of pipeline girth welds is still under investigation. In this work, finite element analyses were conducted to investigate the effects of HAZ softening on crack-driving force and strain concentration in girth welds under longitudinal tensile loading. The material properties of weld metal (WM) and base metal (BM) were obtained from an X100 girth weld. The HAZ was modeled as a functionally graded material based on its measured hardness. The models contained surface-breaking defects located at the fusion boundary simulating lack-of-sidewall fusion defects. Figure 3-22 shows the FE model and the material properties used in the analyses. The effect of internal pressure was not initially considered in these analyses. Uniaxial tensile loading was applied by forcing uniform displacement in the longitudinal direction on all the nodes at the far end of the model.

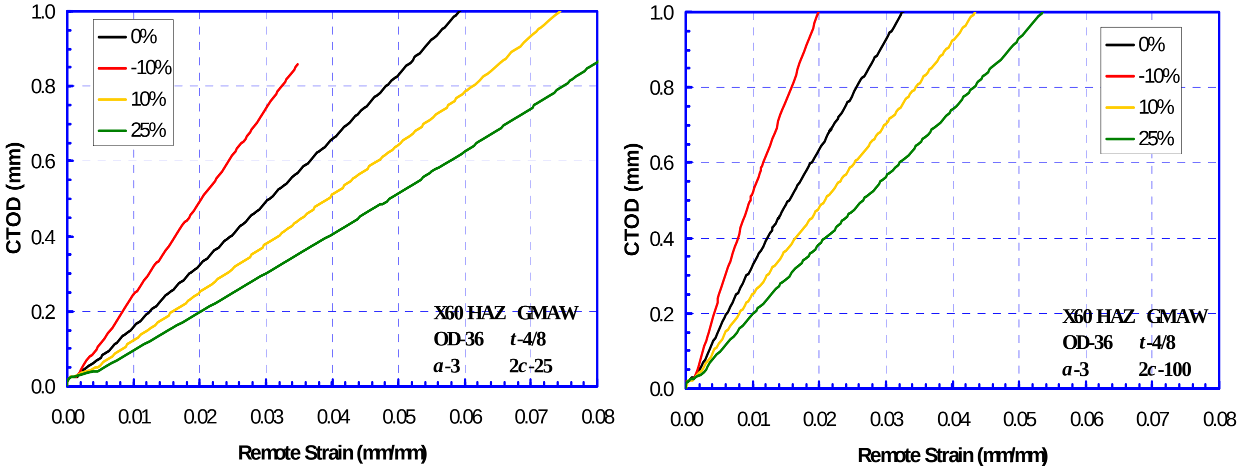

Figure 3-20 Example results showing the effect of weld metal strength mismatch on crack-driving force [OD and thickness in inches, crack depth (a) and length (2c) in mm]

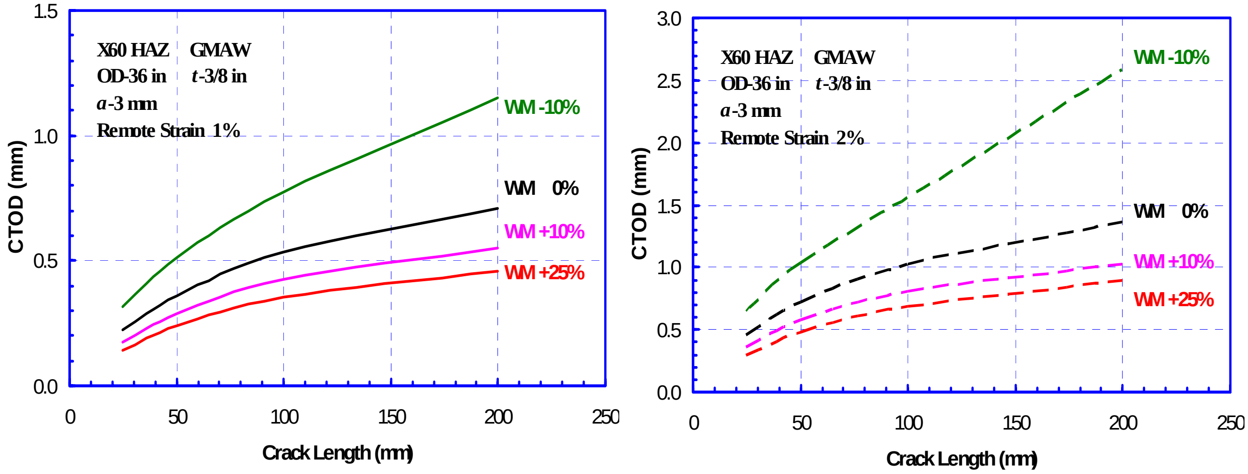

Figure 3-21 Example results showing the effect of weld metal strength mismatch on defect tolerance

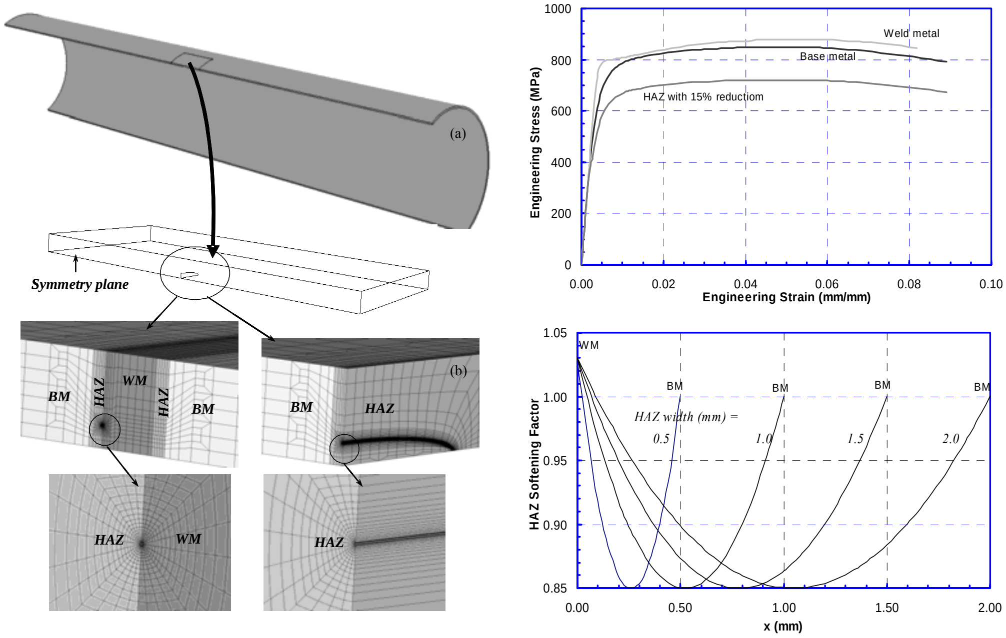

Figure 3-22 Finite element model and material properties used for the analyses

The uniform longitudinal strain at the far end of the model was defined as the remote strain. The CTOD-driving force was calculated at the deepest point of the crack front by the 45°-line intersection method as shown in Figure 3-23. The total CTOD was the sum of the CTOD on the HAZ and the WM side [42].

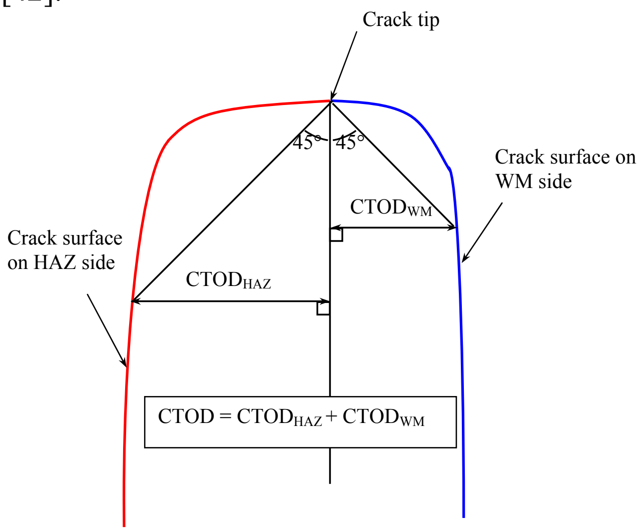

Figure 3-23 Computation of CTOD-driving force from the crack-opening profile

Two strain measures were employed. The calculated strain over a 2*t* wide strip on the OD surface above the deepest point of the crack front was tracked and referred to as "*2t surface strain*". The HAZ strain was the averaged strain over the width of the defect-containing HAZ at a circumferential location remote from the defect (180^0 circumferentially from the center of the defect). The strain concentrations were calculated as the ratios between the above defined strains and the remote strains. The 2*t* surface strain is a measure of strain intensification local to the defect, while the HAZ strain is a measure of remote strain intensification [43].

Figure 3-24 shows an example result which demonstrates the effect of HAZ width and softening level on CTOD driving force. The results show that the CTOD-driving force increases with HAZ softening level and width. At a 2% remote strain, the CTOD-driving force is about 0.57 mm for a 2-mm wide softened HAZ, while the CTOD-driving force is 0.44 mm without HAZ softening (a 30% increase).

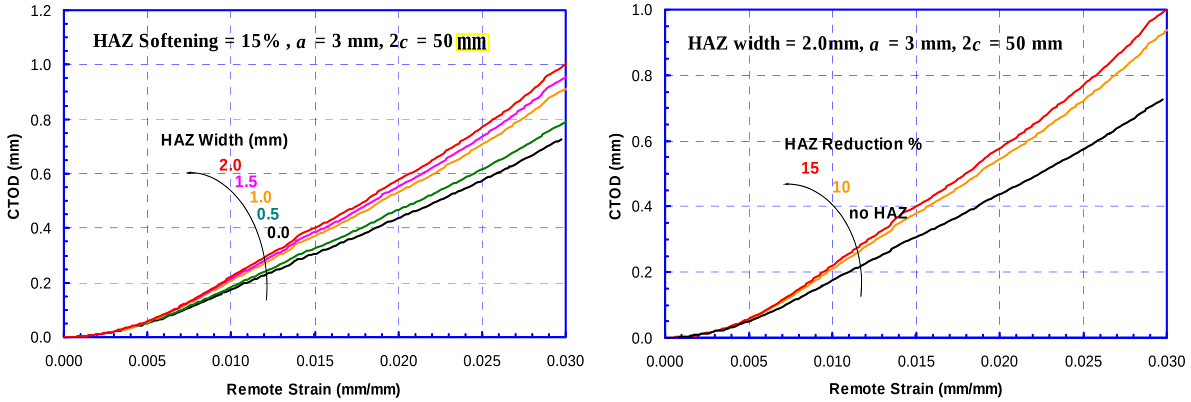

(a) Varying HAZ width (b) Varying HAZ strength

Figure 3-24 Effect of HAZ width and softening level on CTOD-driving force

Figure 3-25 shows an example demonstrating the effect of HAZ width on strain concentration. In Figure 3-25(a), when the remote strain is 2%, the strain concentration in the HAZ is less than 7%, although CTOD could increase by 30% due to HAZ softening. Also, HAZ strain concentration only exists when the HAZ width is beyond a certain value (≥ 1.0 mm here). That is because the overmatched WM restrains deformation and reduces strain in the HAZ. Thus, the effect of HAZ softening is shielded if the HAZ is not wide enough. Figure 3-25(b) shows the variation of 2*t* strain concentration as a function of applied strain at different HAZ widths. As shown, the 2*t* surface strain can provide a good indication of the strain concentration due to the defect.

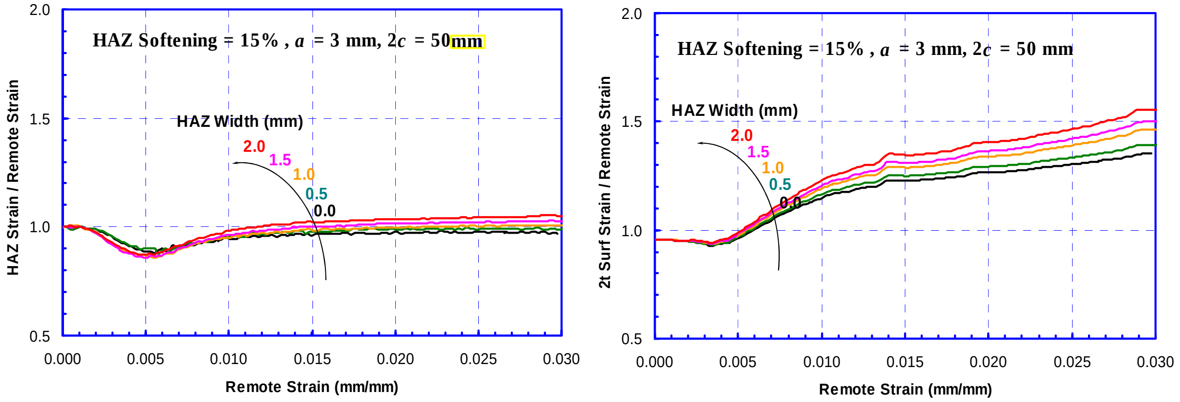

(a) HAZ Strain/Remote Strain (b) 2t Surface Strain/remote Strain

Figure 3-25 Effect of HAZ width on the HAZ strain and 2t surface strain concentration

Figure 3-26 demonstrates the effect of defect size on CTOD and 2*t* surface strain concentration. Figure 3-26(a) shows that defect depth has a larger impact on CTOD than defect length. In Figure 3-26(b), the 2*t* surface-strain concentration shows a strong dependence on defect size. Comparing the results with the no HAZ cases, the effect of HAZ softening is also shown in Figure 3-26. The results show that the relative increase of CTOD due to HAZ softening does not appreciably depend on defect size. For instance, when the remote strain is 1.5%, the CTOD increase due to HAZ softening is 0.06 mm, 0.09 mm, and 0.14 mm for 3 × 25 mm, 3 × 50 mm, and 6 × 25 mm defects, respectively. Those approximately correspond to a 30% increase for all three defects. A similar observation is true for the 2*t* surface-strain concentration shown in Figure 3-26(b).

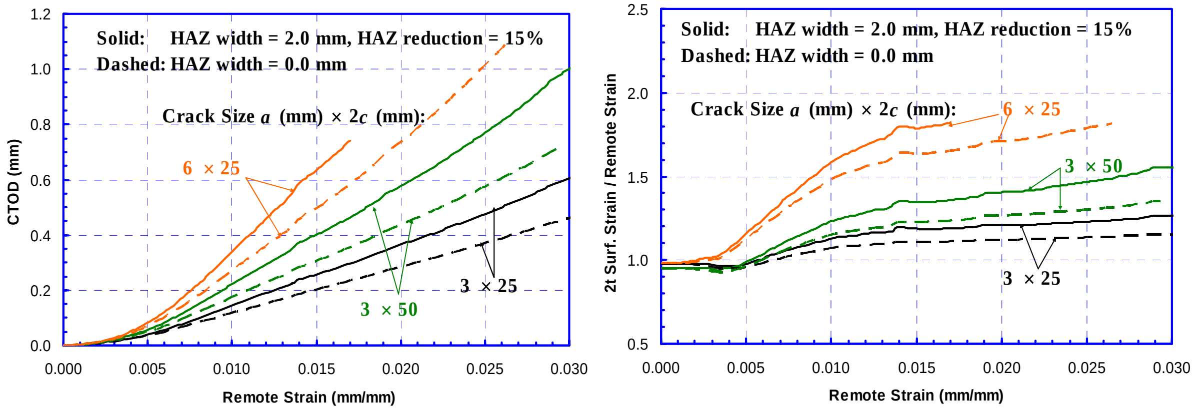

(a) CTOD versus strain (b) 2t surface strain/remote strain

Figure 3-26 Effect of HAZ softening on CTOD driving force and 2*t* surface strain concentration for various defect sizes

3.3.2.3 Effect of Hoop Stress on Crack-Driving Force

In the previous subsections, only longitudinal loading was considered. However, in-service pipelines are subjected to hoop stress from the internal pressure, in addition to possible longitudinal loadings. A biaxial loading condition exists when the longitudinal loading is applied. As will be shown, the hoop stress can greatly alter the materials response to the longitudinal stress/strain. Therefore, the effect of the biaxial loading on girth weld integrity has drawn significant attentions in recent years [44, 45].

In the present work, the effect of hoop stress on the CTOD-driving force was investigated. More detailed information can be found in Reference [46]. Figure 3-27 shows an example of the CTOD-driving force as a function of remote strain for various hoop stress levels with no HAZ softening. It was found that in general, the hoop stress increases the CTOD-driving force. However, instead of a monotonic increase, as the hoop stress increases, the overall CTOD-driving force curves are first increased then decreased. The level of the hoop stress that yields the highest CTOD-driving force curve depends on the material properties and defect geometries. Generally speaking, the higher the strain-hardening capacity and smaller the defect, the higher the hoop stress that yields the maximum-crack driving-force curve. Figure 3-28 demonstrates the combined effects of hoop stress and HAZ softening on CTOD-driving force and 2*t* surface strain. As expected, it shows that both softened HAZ and preexisting hoop stress increase the CTOD-driving force. Compared to the influence of HAZ softening, the hoop stress has a much greater effect on the CTOD-driving force and its effect is very sensitive to defect size. Although the total CTOD-driving force is more affected by defect depth than length, the hoop stress seems to have larger effect on longer defects than deeper defects. Similar effects are shown for the 2*t* surface-strain results. Furthermore, the CTOD-driving force and 2*t* surface strain for various defects showed a linear relationship, which was not sensitive to defect sizes and HAZ softening when high hoop stress exists. However, a weak dependence on defect sizes and HAZ softening can be found when no hoop stress exists. Thus, it was demonstrated that the 2*t* surface strain can be used as a convenient method for measuring the CTOD-driving force in practical experiments, especially for a full-size pipe with internal pressure applied.

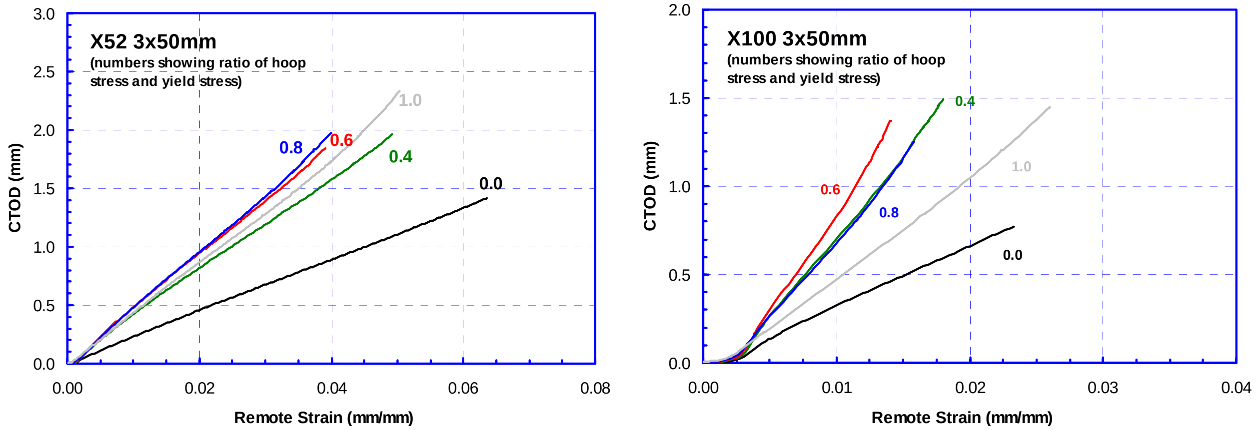

(a) (b)

Figure 3-27 Effect of hoop stress on CTOD driving force (no HAZ softening)

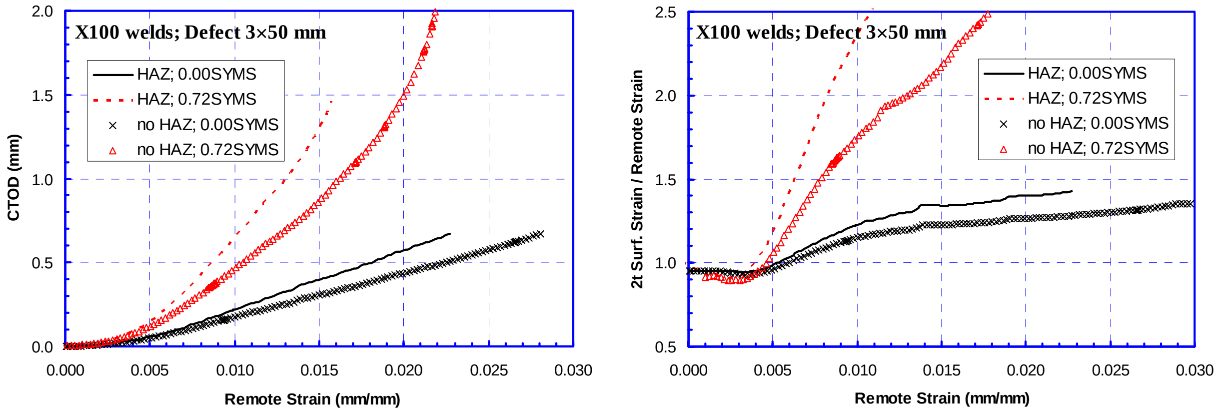

(a) (b)

Figure 3-28 Combined effects of hoop stress and HAZ softening on CTOD-driving force and 2*t* surface strain

3.3.2.4 Meshless FE Modeling

In parallel with the above effort, an additional task undertaken during the project was to investigate the use of meshless FE methods in determining the driving forces for cracks in welds. This effort was initiated briefly at Northwestern University (NWU) under a subcontract and a theoretical framework of a generalized damage mechanics-based constitutive model had been developed already by researchers at NWU. Meshless methods do not use elements and the interpolant functions are made only over 'nodes'. The meshless method continues to be a topic of intense research at present. Two main advantages of meshless methods are that there are no elements and hence 'meshing' the geometry is simple and the method has particular advantages for fluid-structure-interaction problems. The key disadvantage is that the matrices tend to be fully populated rendering the solutions slow compared with finite element methods at present. The meshless model developer here integrates the mechanisms of inclusion, debonding, and hard particle/steel matrix interaction, damage evolution, and coalescence of micro-voids. Dr. Hao at NWU implemented multi-scale damage mechanics models in both finite element and meshless formats [47, 48, 49].

Emc^2 received both 2-D and 3-D "MPFEM" simulation codes for the above damage-mechanics model from NWU. The interface (both input and output) of those codes are such that significant modifications and additions were needed to make the codes a potentially useful tool. Emc^2 spent considerable time to evaluate these codes and how they could be integrated with conventional FE methods. The benefits of using the above simulation codes to the industry in this program were not immediately apparent. Therefore, the effort with NWU was terminated.

3.3.3 Resistance Measurement

Materials loaded in tension, such as girth welds in a pipeline, exhibit higher apparent toughness than the same materials loaded in bending. Specimens in most standardized fracture mechanics tests, such as the crack-tip-opening displacement (CTOD) toughness test, frequently used in the oil and gas industries, are loaded in bending. On the basis of loading mode alone, such bending tests provide conservative values of fracture toughness. On the other hand, the "conservative" value obtained from the bend tests is not representative of the toughness for the geometry and loading mode of interest. The toughness difference due to the loading mode is attributable to the effects of crack-tip constraint, see Figure 3-29 [50]. The integrity of pipeline girth welds can be assessed more accurately by accounting for the constraint effects.

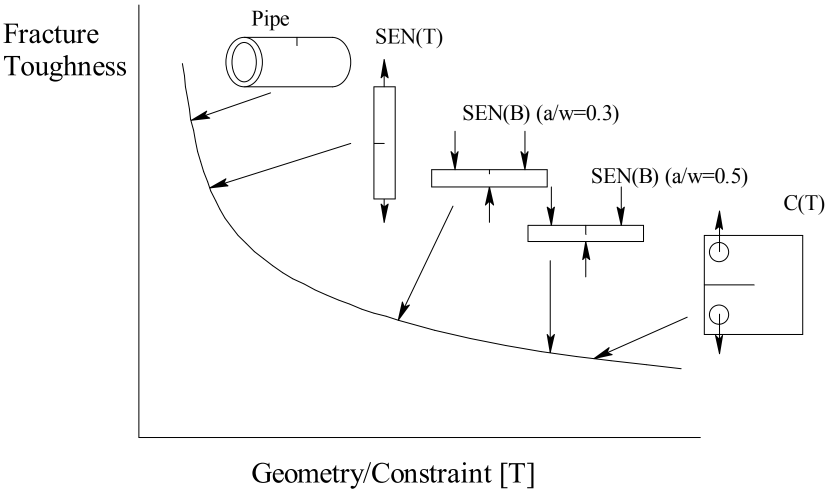

Figure 3-29 Illustration of differences in constraint between specimen types

In this and in other similar efforts [19], attempts were made at testing low-constraint test specimens to characterize the materials resistance to fracture. In References 19 and 51, the back-bend and mini-wide plate experiments are discussed in detail. Summaries of those experiments are given in the next two sections. SENT tests for the same materials were conducted in this project and are given in detail after the back-bend and mini-wide plate summaries.

3.3.3.1 Back-Bend Testing

To help characterize the toughness for low-constraint conditions, a new type of low-constraint test specimen, termed "back-bend" specimen, was used in this project, see Figure 3-30. This test set-up was first introduced by McClintock and Parks at MIT [52, 53]. A bend bar is notched and may be fatigue precracked to create a sharp deep crack. A shim is placed on the opening side of the notch. The specimen is then loaded under four-point bending in reverse bending (hence back-bend) to produce a predominantly tensile loading on the remaining ligament of the specimen. This tensile loading creates a low-constraint condition at the crack tip. The stress state ahead of the crack in the back-bend specimen is similar to a center-cracked panel with through-wall crack loaded in tension.

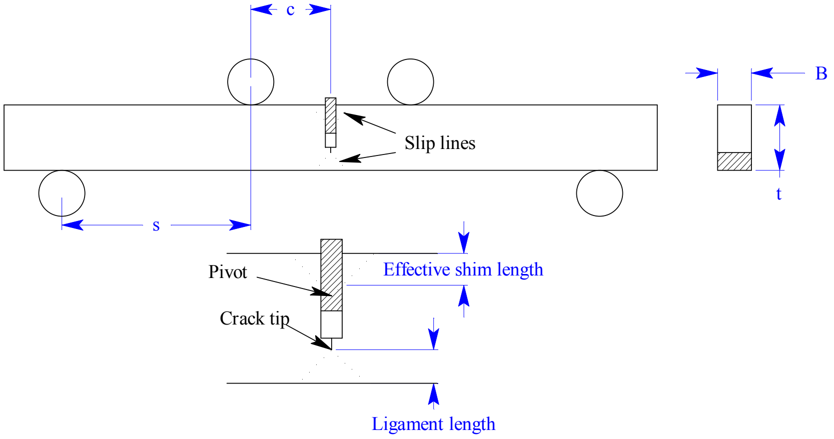

Figure 3-30 Back-bend specimen

In Reference 19, special fixturing and testing apparatus were designed for testing the back-bend specimens at cryogenic temperatures. Figure 3-31 shows a photograph of the test setup without the cooling chamber in place.

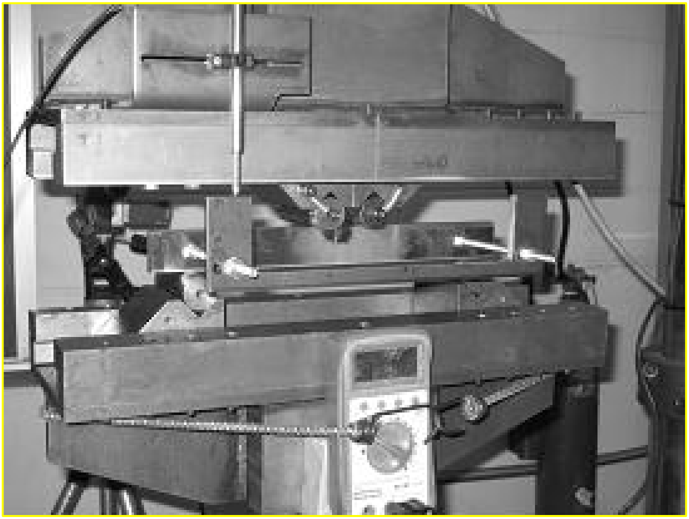

Figure 3-31 Photograph of back-bend specimen in fixture with instrumentation

For this investigation, the toughness of both the weld and heat-affected zone (HAZ) were determined for both the X70 and X100 line-pipe steels. In order to replicate the standard fracture specimen as closely as possible, the cracks were inserted in the specimen at locations similar to typical weld and HAZ fracture specimens. These tests were conducted with sharp-machined (EDM) notches, rather than fatigue cracks. For each of the materials tested, it was attempted to locate the brittle-to-ductile transition temperature for the specimen geometry. Therefore, specimens were tested at a variety of temperatures aimed at locating the brittle-to-ductile crack initiation transition point. The detailed experimental results can be found in Reference 51. An example of the load-displacement traces for the X70 P109 weld specimens is given in Figure 3-32. This figure shows the typical response, which is an increase in load-carrying capacity with a decrease in temperature, and a decrease in displacement as test temperature is decreased below the transition temperature.

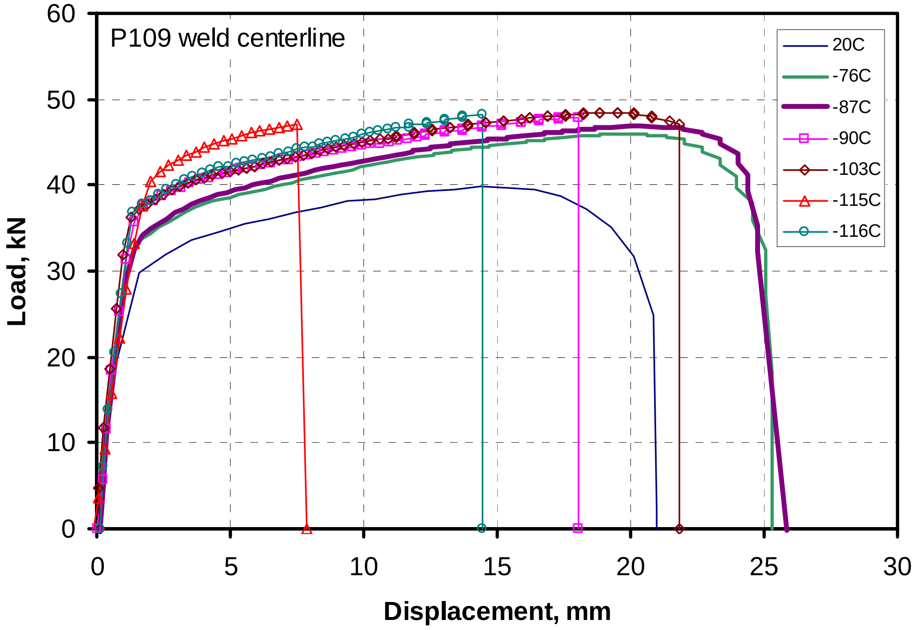

Figure 3-32 X70 weld-centerline-cracked back-bend test results

In order to investigate the brittle-to-ductile fracture initiation transition temperature of these specimens, the displacement at maximum load was extracted from the experimental record and compared to the test temperature. Since crack growth was not measured during these experiments, it was assumed that crack initiation occurs at maximum load. In addition, using slip-line theory, the global displacement of a back-bend specimen has been shown to be related to the crack-tip-opening displacement [54].

The results for the X70 base metal are shown in Figure 3-33. The results indicated that the displacement at maximum load increased as the temperature decreases to a temperature of -80 C. Investigation of the fracture surfaces indicates that ductile crack initiation occurs at these temperatures. This increase in the displacement at maximum load was due to the amount of plasticity that was occurring in the base metal of the specimen relative to the weld. It is hypothesized that the yield strength of the weld is more sensitive to temperature and increases more than the base metal at the same temperature. This effect will force more global deformation in the specimen in order to obtain the same critical strain at the crack tip in the weld/HAZ. As shown in Section 3.1.2, the yield strength and UTS for the weld metal increases as the test temperature decreases.

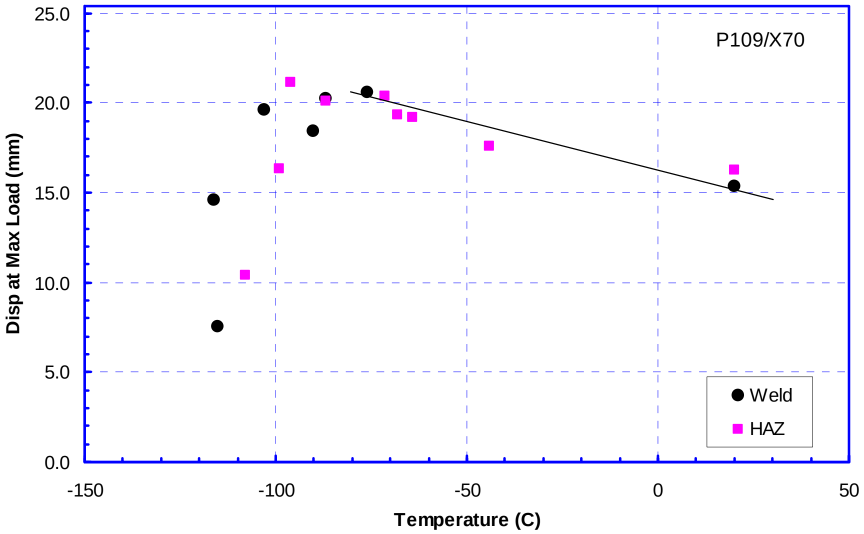

Figure 3-33 Displacement at maximum load versus temperature for P109 (X70) weld and HAZ back-bend specimens

At temperatures below -80 C, the displacement at maximum load decreases rapidly, and the fracture surfaces for these specimens appear brittle in nature. The data were limited, but it appears that the transition temperature between the weld and HAZ was relatively similar. It is possible that the transition temperature for the weld was slightly lower than the HAZ, but there is not sufficient data to substantiate this claim.

The displacement at maximum load as a function of temperature for the X100 weld and HAZ metal specimens was also investigated. The load-displacement data is shown in Figure 3-34. The displacement at maximum load as a function of temperature is shown in Figure 3-35. The trend between displacement and temperature for this material was similar to what was seen for the X70 material. In these tests it can be seen that even at the lowest temperature of approximately -130 C, the specimen load-displacement record still went past maximum load and the transition temperature definition using the displacement at maximum load was not reached. Hence these results showed that the back-bend specimen brittle-to-ductile fracture initiation transition temperature was colder than -130 C (with a sharp EDM notch). It should be noted that the specimen could not be tested at colder temperatures since it became increasingly difficult to reliably control the temperature of the specimens below -130 C.

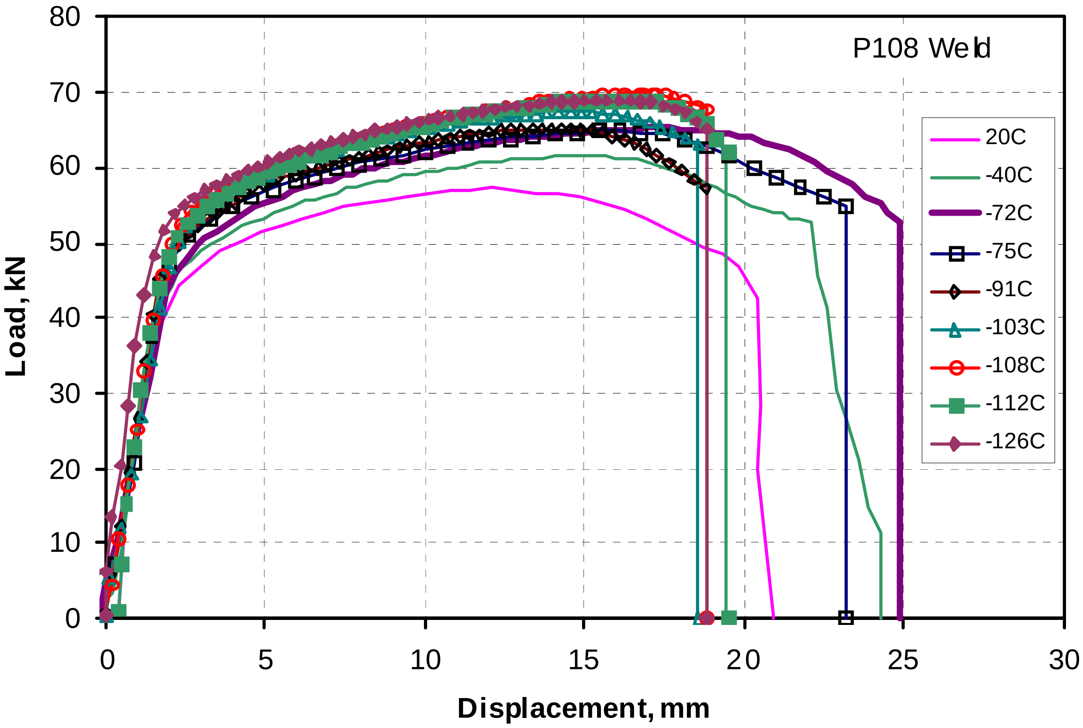

Figure 3-34 X100 weld-centerline-cracked back-bend test results

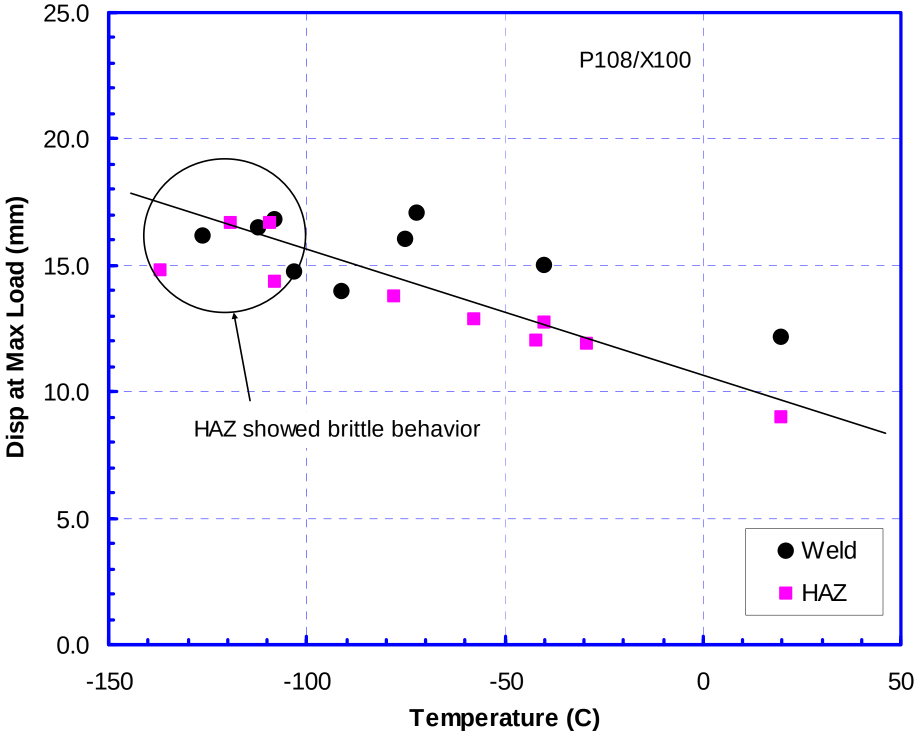

Figure 3-35 Displacement at maximum load versus temperature for P108 (X100) weld and HAZ back-bend specimens

3.3.3.2 Mini-Wide-Plate Testing

A series of "mini-wide" plate specimens were made from the X70 (P109) and X100 (P108) girth welds described in Section 3.1. The nominal gage width of these specimens was about one-half of the "traditional" wide plates, which usually have a nominal gage width of 12 inch (304.8 mm). The current specimens had a gage width of 6 inch (152.4 mm), primarily limited by the load capacity of the test machine; hence the term "mini." A typical mini-wide-plate specimen is shown in Figure 3-36. The test section cut from a pipe retains its original curvature (plus any spring back that might occur). The ends of the test section have wider width than the gage section. The ends were welded to thick steel plates (termed loading plates) at each end.

Figure 3-36 A mini-wide-plate specimen

The specimen geometry was designed in a separate effort [19] and focused on creating a specimen that would be long enough so that a region of uniform far-field strain could be measured. For these experiments both ambient and cold (-20 C) temperature experiments were conducted with the flaws in the center of the weld and HAZ for each material described in Section 3.1. The initial flaws were introduced by EDM using a plunge cut with the tool sharpened to a fine point with a notch-root radius of 0.005 inches (0.127 mm). The mini-wide plate specimens were highly instrumented with a variety of transducers:

- Global load and displacement using the test machine load cell and ram,
- Remote nominal strain above and below the weld on both the ID and OD surfaces using both strain gages and LVDTs,
- Local strain in the weld on both the ID and OD surfaces,
- Crack-mouth-opening displacement using an LVDT,
- Specimen temperature along the gage length, and
- Crack initiation and growth at three locations along the crack front by d-c electric potential.

Figure 3-37 A mini-wide-plate specimen with the instrumentation

A photograph of a room temperature specimen before the experiment is shown in Figure 3-37. All of these tests were conducted at Battelle Memorial Institute (Columbus, OH) in a 3.3 MN (750 kip) servo-hydraulic test machine. Details of the specimen geometry, test arrangement, and detailed test results can be found elsewhere [19].

In order to compare the overall experimental results, critical experimental events need to be defined. The most commonly used “critical” event in mechanical testing is the point of maximum load. Such definition fits well for designs intended to limit stress levels, which cover most engineering designs. Strain-based design, on the other hand, intends to limit strain levels. When post-yield behavior is of concern, such as in the case of strain-based design, small change in load (or stress) can lead to large change in strain when the post-yield stress-strain curve is flat (for low-strain-hardening materials). In view of this variability, a second critical event was defined as 99% of the maximum load (stress). These two critical events allow the comparison of the displacements at these load levels to investigate the flatness of the load-displacement trace near maximum load.

Table 3-4 Test results of X70 girth welds at two critical events

Specimen ID	Flaw Length	Flaw Depth	Flaw Location	Target Test Temp.	Actual Temp. at Max Load	Max Load	Max Nominal Stress		Max Stress / SMYS	Ram Disp at Max Load	99% Max Load	99% Max Nominal Stress		99% Max Stress / SMYS	Ram Disp at 99% Max Load
	mm	mm		C	C	kip	ksi	Mpa		inch	kip	ksi	Mpa		inch
P109-1WCW-01	50	3	Weld	Rm	33	242.7	80.9	557.8	1.16	0.748	240.3	80.1	552.2	1.14	0.655
P109-1WCW-02	50	3	Weld	Rm	33	256.1	85.4	588.6	1.22	1.000	253.5	84.5	582.7	1.21	0.863
P109-1WDW-05	25	3	Weld	Rm	20	257.8	85.9	592.5	1.23	1.420	255.2	85.1	586.6	1.22	1.160
P109-1WDW-06	25	3	Weld	Rm	38	259.7	86.6	596.9	1.24	1.610	257.1	85.7	590.9	1.22	1.210
P109-1WFW-19	25	6	Weld	Rm	20	244.2	81.4	561.2	1.16	0.614	241.7	80.6	555.5	1.15	0.530
P109-1WCH-03	50	3	HAZ	Rm	20	252.8	84.3	581.0	1.20	1.095	250.3	83.4	575.2	1.19	0.935
P109-1WCH-04	50	3	HAZ	Rm	20	250.0	83.3	574.6	1.19	0.970	247.5	82.5	568.8	1.18	0.843
P109-1WDH-07	25	3	HAZ	Rm	20	264.5	88.2	607.9	1.26	1.800	261.9	87.3	601.8	1.25	1.260
P109-1WDH-08	25	3	HAZ	Rm	40	258.7	86.2	594.6	1.23	1.860	256.1	85.4	588.6	1.22	1.320
P109-1WFH-16	25	6	HAZ	Rm	25	252.7	84.2	580.7	1.20	0.936	250.1	83.4	574.9	1.19	0.800
P109-1WCW-09	50	3	Weld	-20	-27	237.2	79.1	545.2	1.13	0.148	N/A	N/A	N/A	N/A	N/A
P109-1WCW-10	50	3	Weld	-20	-21	254.2	84.7	584.2	1.21	0.574	251.7	83.9	578.4	1.20	0.492
P109-1WDW-13	25	3	Weld	-20	-16	267.7	89.2	615.3	1.27	1.112	265.0	88.3	609.1	1.26	0.942
P109-1WEW-18	75	3	Weld	-20	-22	230.4	76.8	529.5	1.10	0.094	228.1	76.0	524.2	1.09	0.083
P109-1WFW-14	25	6	Weld	-20	-18	246.1	82.0	565.7	1.17	0.596	243.7	81.2	560.1	1.16	0.514
P109-1WCH-11	50	3	HAZ	-20	-21	264.6	88.2	608.1	1.26	1.040	262.0	87.3	602.1	1.25	0.924
P109-1WCH-12	50	3	HAZ	-20	-15	260.0	86.7	597.6	1.24	0.942	257.4	85.8	591.7	1.23	0.807
P109-1WEH-17	75	3	HAZ	-20	-18	250.8	83.6	576.4	1.19	0.630	248.3	82.8	570.7	1.18	0.560
P109-1WFH-15	25	6	HAZ	-20	-20	264.8	88.3	608.6	1.26	0.952	262.2	87.4	602.5	1.25	0.822
P109-1WFH-20	25	6	HAZ	-20	-14	269.9	90.0	620.4	1.29	0.874	267.2	89.1	614.2	1.27	0.756

The test results determined at the above “critical” events are given in Table 3-4 and Table 3-5 for the X70 and X100 girth welds, respectively. These tables only list loads, nominal stresses, and ram displacements at the critical events. From these data, the strain limits as a function of defect size were generated in Reference 19, with an example of the weld metal at -20 C shown in Figure 3-38. The results suggest that X70 has a higher strain capacity than the X100, and that this capacity is a function of the defect size. Further discussion can be found in Reference 19 and Section 3.4 of this report.

Table 3-5 Test results of X100 girth welds at two critical events[(a)]

Specimen ID	Flaw Length	Flaw Depth	Flaw Location	Spec Width	Target Test Temp.	Actual Temp. at Max Load	Max Load	Max Nominal Stress		Max Stress / SMYS	Ram Disp at Max Load	99% Max Load	99% Max Nominal Stress		99% Max Stress / SMYS	Ram Disp at 99% Max Load
	mm	mm		inch	C	C	kip	ksi	MPa		inch	kip	ksi	MPa		inch
P108-1WDH-01	25	3	HAZ	6.02	Rm	28	376.1	111.0	765.1	1.11	0.906	372.3	109.9	757.5	1.10	0.674
P108-2WDH-08	25	3	HAZ	6.02	Rm	27	373.8	110.3	760.5	1.10	0.964	370.1	109.2	752.9	1.09	0.716
P108-1WCH-02	50	3	HAZ	6.02	Rm	23	361.6	106.7	735.6	1.07	0.447	358.0	105.6	728.3	1.06	0.372
P108-3WGH-14	38	3	HAZ	6.01	Rm	22	372.0	109.9	758.1	1.10	0.554	368.3	108.8	750.5	1.09	0.434
P108-1WFH-05	25	6	HAZ	5.72	Rm	23	334.8	104.0	716.8	1.04	0.412	331.5	102.9	709.7	1.03	0.342
P108-1WGW-04	38	3	Weld	6.00	Rm	27	373.2	110.5	761.8	1.10	0.782	369.5	109.4	754.1	1.09	0.586
P108-2WCW-09	50	3	Weld	6.00	Rm	22	359.0	106.3	732.8	1.06	0.402	355.4	105.2	725.5	1.05	0.326
P108-3WDW-11	25	3	Weld	6.01	Rm	24	375.3	110.9	764.8	1.11	0.658	371.5	109.8	757.1	1.10	0.530
P108-4WDW-20	25	3	Weld	6.00	Rm	27	373.8	110.7	763.0	1.11	0.970	370.1	109.6	755.4	1.10	0.704
P108-1WDW-03	25	3	Weld	6.01	-20	-13	387.8	114.6	790.3	1.15	1.094	383.9	113.5	782.3	1.13	0.796
P108-3WDW-13	25	3	Weld	5.68	-20	-19	369.7	115.6	797.1	1.16	0.854	366.0	114.5	789.2	1.14	0.684
P108-2WGW-06	38	3	Weld	5.70	-20	-20	367.4	114.5	789.5	1.14	0.774	363.8	113.4	781.6	1.13	0.634
P108-4WGW-18	38	3	Weld	6.00	-20	-17	382.0	113.1	779.7	1.13	0.644	378.2	112.0	771.9	1.12	0.527
P108-2WCW-10	50	3	Weld	6.01	-20	-17	366.2	108.2	746.2	1.08	0.464	362.5	107.1	738.8	1.07	0.397
P108-2WDH-07	25	3	HAZ	6.01	-20	-17	390.3	115.4	795.3	1.15	1.104	386.4	114.2	787.4	1.14	0.802
P108-4WDH-17	25	3	HAZ	5.84	-20	-21	380.9	115.8	798.8	1.16	0.974	377.1	114.7	790.8	1.15	0.752
P108-3WGH-15	38	3	HAZ	5.98	-20	-20	375.2	111.4	768.4	1.11	0.630	371.4	110.3	760.7	1.10	0.526
P108-4WGH-16	38	3	HAZ	5.79	-20	-22	367.6	112.8	777.6	1.13	0.554	363.9	111.6	769.8	1.12	0.464
P108-3WCH-12	50	3	HAZ	6.00	-20	-18	377.7	111.8	771.0	1.12	0.530	373.9	110.7	763.2	1.11	0.451
P108-4WFH-19	25	6	HAZ	5.47	-20	-23	341.8	111.0	765.3	1.11	0.483	338.4	109.9	757.6	1.10	0.396

[(a)] Specimen P109-1WDH-07 failed in the base metal away from the HAZ flaw.

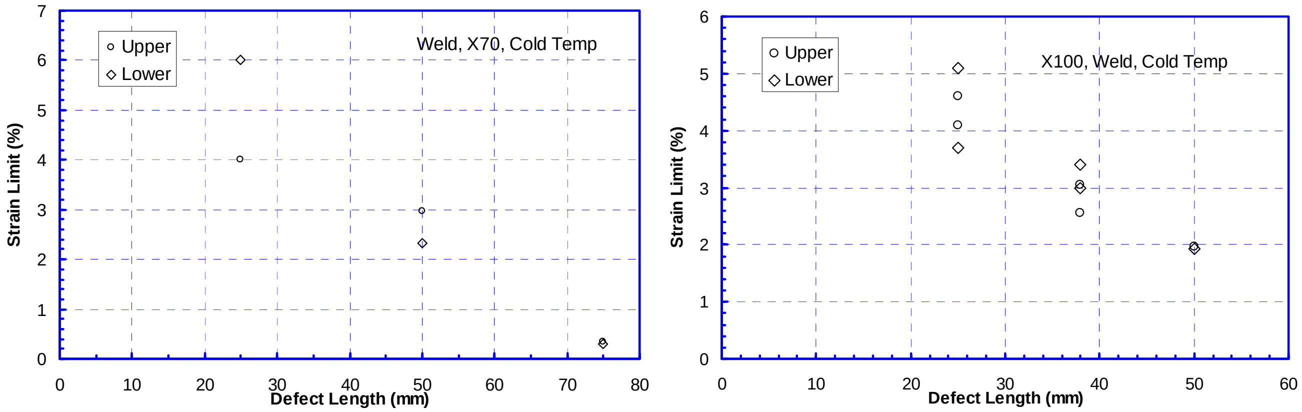

(a) X70 (b) X100

Figure 3-38 Strain limits as a function of defect length for X70 and X100 mini-wide-plate specimens with weld defects tested at cold temperature

3.3.3.3 Constraint Effects on Brittle-to-Ductile Transition Temperature and Upper-Shelf Toughness

The effects of geometry and loading conditions can significantly affect the fracture toughness in the structure. Temperature, thickness, loading rate, specimen/crack geometry and type of loading (tension versus bending) are some of these parameters. The combination of these parameters will determine if the material fractures in a brittle or ductile manner. Thickness, specimen/crack geometry, and tension/bending loading effects are frequently combined and called "constraint conditions". Bending loads give high constraint conditions while tension loads produce lower constraint. Lower constraint produces a lower brittle-to-ductile transition temperature and higher toughness when on the upper-shelf of the material. It is quite possible to have fully ductile behavior with one constraint condition, but brittle behavior at the same temperature and loading rate with another constraint condition.

Standard tests used for quality assurance purposes for welds are the Charpy and CTOD test. Both of these are bend tests that give the highest constraint and hence will tend to predict more brittle behavior and a lower upper-shelf fracture resistance than a surface crack in a pipe which has tension stress in the ligament of the surface crack. It is desirable to be conservative in determining the material toughness, but not overly conservative.

3.3.3.3.1 Constraint Effects on Brittle-to-Ductile Transition Temperature

To assist in understanding the effects of constraint parameters on the brittle-to-ductile transition temperature, a master curve of fracture initiation transition temperatures (FITT) was first proposed by Wilkowski [55]. This relationship was developed from observations of thousands of test specimens and hundreds of full-scale pipe tests. It was based on the observations that surface-cracked pipes frequently fail in a more ductile manner than predicted by commonly used test specimens. Comparisons to pipe tests with surface-cracks in the base metal for A106B pipe were made in Reference 56. Comparison of SENT test results and predictions of SENT behavior from Charpy tests in old line pipe (1927 to 1946 vintage pipe) [57], as well as development of correlations to predict the transition temperature change with notch acuity for corrosion flaws were made in Reference 55.

The objective of the FITT Master Curve procedure is to determine the lowest temperature where the material has enough ductility to reach the upper-shelf failure stress. This behavior is illustrated in Figure 3-39 where the FITT is the temperature corresponding to the test where failure occurred just at the upper-shelf maximum load.

The FITT Master Curve accounts for test temperature, thickness, loading rate, specimen geometry, type of loading, and surface crack depth. There are built-in correlations that allow one to go from the transition temperature of any of these test specimens to the transition temperature of a full scale test. The different tests are:

- Charpy test (dynamic bend test with standard dimensions with a blunt notch – with the transition temperature corresponding to the temperature to have 85% shear area on the fracture surface),

- DWTT transition temperature (dynamic full-thickness bend test – with the transition temperature corresponding to the temperature to have 85% shear area on the fracture surface),
- Bend-bar or CT specimen test (full-thickness quasi-static bend test – transition temperature defined in Figure 3-39), and
- SENT tests (quasi-static full-thickness tension test with different crack to thickness ratios – transition temperature defined in Figure 3-39).

The corresponding relationship between the transition temperatures determined from these specimen types and full-scale behavior are:

- The Charpy test is a reference test used for quality assurance purposes,
- The DWTT test correlates well with predicting the lowest temperature that dynamic ductile crack propagation occurs in full-scale pipe fracture tests,
- The transition temperature from a bend-bar or CT specimen (used in standard CTOD or J-R curve testing) has been found to correlate well with the transition temperature for a through-wall crack in a pipe under quasi-static loading, and
- The transition temperature from a SENT test correlates well with the transition temperature for a surface crack in a pipe with the corresponding crack depth.

Hence, one can make predictions of the surface-cracked pipe FITT by knowing the Charpy transition temperature (or the transition temperature from the DWTT or quasi-static bend-bar/CT specimen test results).

The general shape of the FITT Master Curve is shown in Figure 3-40 for a material that has a Charpy 85% shear area transition temperature of -10 C. For other materials, all of the curves will move up or down with the difference of their Charpy 85% shear area transition temperature relative to this material case. In looking at this figure, it can be seen there are a series of curves for the temperature versus thickness plot. The upper curve is the lowest temperature at which the crack would dynamically propagate in a ductile manner (sometimes called the fracture propagation transition temperature or FPTT). The next lowest curve is the FITT for a through-wall crack in a pipe under quasi-static loading. The series of curves under that are for surface-cracked pipes under quasi-static loading with different crack depth-to-thickness ratios (a/t values). For surface cracks with a/t values of ~0.375 or greater, the FITT values are all about the same. Shallow surface cracks have lower constraint, so their FITT values are even lower. In the example in Figure 3-40, a vertical dashed line corresponds to a thickness of 12 mm, and for surface cracks with a/t of 0.375 or greater the FITT is about -90 C. If an operating condition is above all of the curves in Figure 3-40, then there would be ductile initiation, stable ductile crack growth, and dynamic ductile crack propagation. If the operating condition is below all the curves, then there would be brittle initiation and brittle propagation. If a surface crack or through-wall crack was operating at a temperature above its FITT curve but below the FPTT curve, then there would be ductile initiation but brittle propagation.

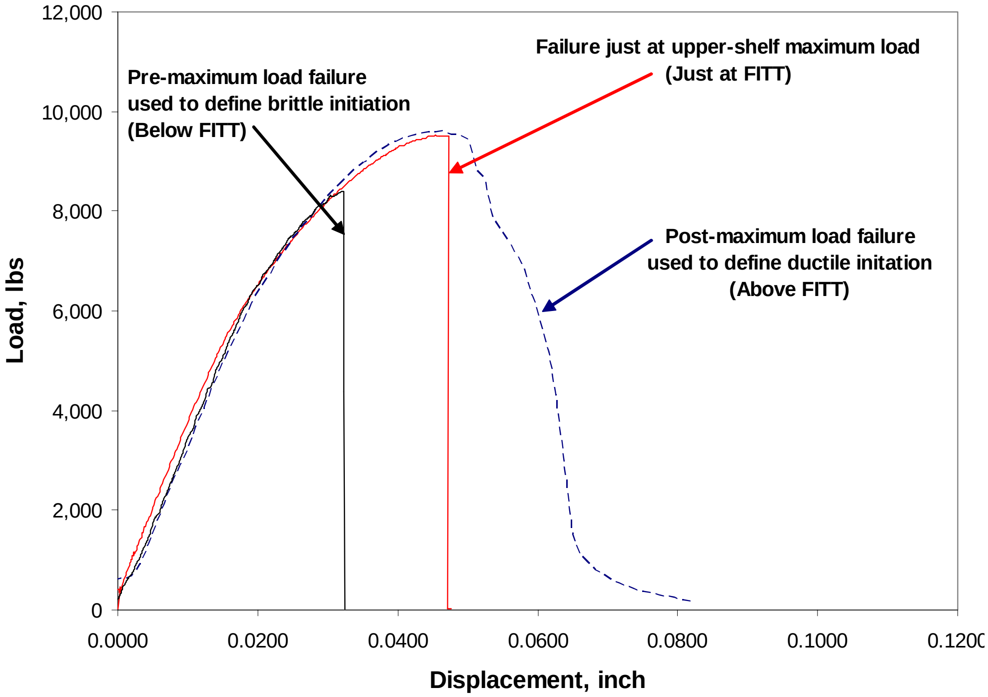

Figure 3-39 Example showing how brittle initiation and ductile initiation were defined for the FITT Master Curve method

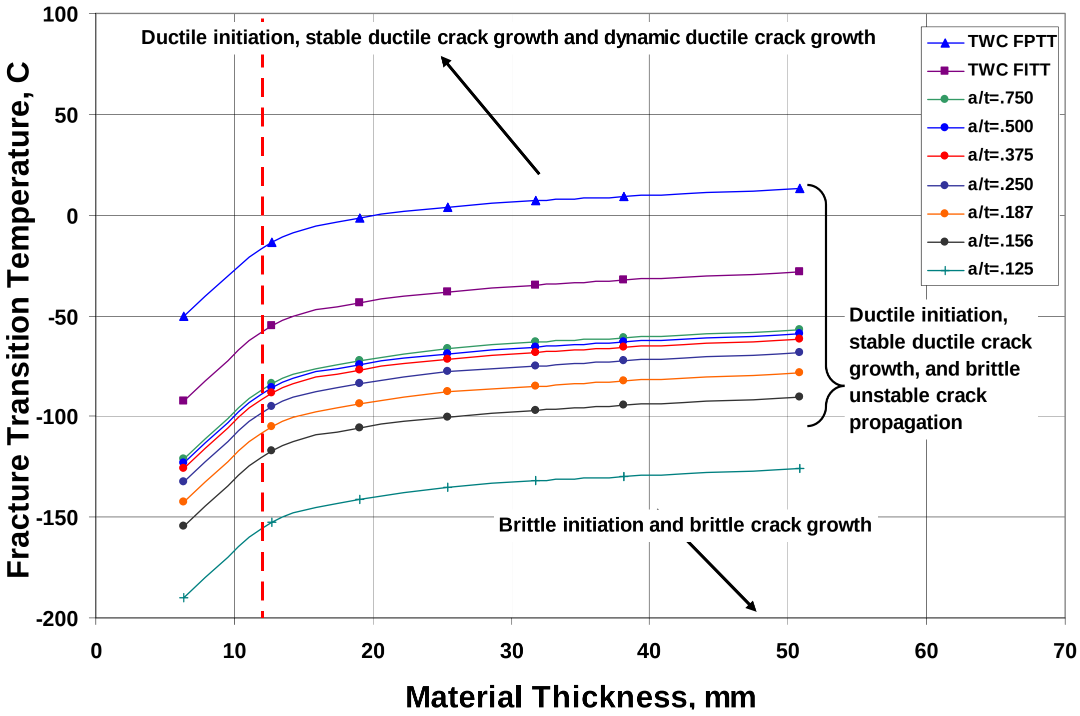

Figure 3-40 FITT Master Curve example for a material that has a Charpy transition temperature of -10 C

3.3.3.3.1.1 Application to Past Line-pipe Girth Weld Pipe Tests

An initial question is whether the FITT Master Curve works for weld metals, and in particular to high-grade X100 weld metals. Frequently it is seen that there can be more inherent scatter in welds and HAZ properties than in base metals. Additionally, in full-scale there will be weld residual stresses that cause through-thickness bending, which increases constraint and could increase the transition temperature. To address these questions, past pipe girth weld tests were first reviewed, and then SENT tests were conducted on the X100 weld (P108) used in this project.

From the original API 1104 pipe girth weld validation tests [58], a series of pipe tests were conducted on 30-inch diameter by 0.625-inch X60 pipe with inside circumferential surface cracks in the center of the welds. The tests were conducted at a temperature that corresponded to a lower-bound CTOD of 0.127 mm (0.005 inch). This was a very low test temperature of -95 C (-140 F). Brittle initiation occurred in both tests with circumferential cracks in the center of the weld being a/t = 0.4 and 2c = 5t, and a/t = 0.20 and 2c = 25% of circumference, see Figure 3-41. The Charpy 85% shear area transition temperature for this material was 7 C, and the predicted FITT for these surface cracks was -78 C (for a/w = 0.2 test) and -62 C (for a/w = 0.4 test). With the -95 C test temperature brittle initiation was correctly predicted.

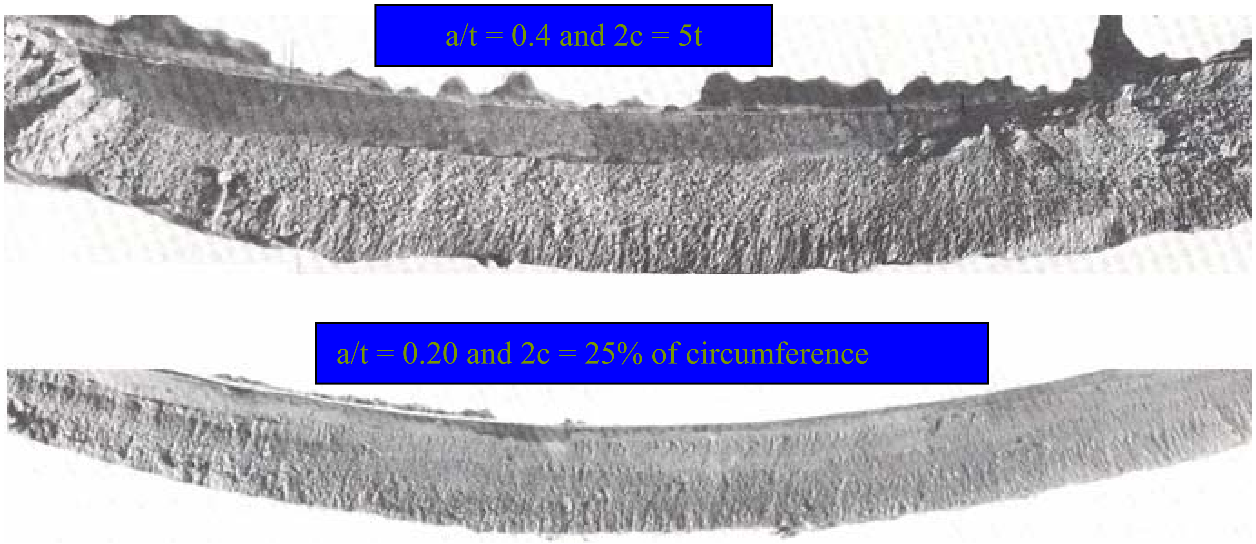

Figure 3-41 Brittle fracture surfaces in API girth weld pipe tests in Reference 58

3.3.3.3.1.2 Evaluation of recent X100 weld metal

For an X100 weld in this project, Charpy and CTOD versus temperature data were already available. In this project, a series of SENT tension tests were conducted with fatigue cracks in the center of the welds. From the past FITT work, there was a good correlation between the transition temperatures of Charpy, CTOD bend tests, and SENT tests. The Charpy 85% shear area was -10 C, and the tx2t SENB specimen actual transition temperature was -60 C (from transition of δ_c to δ_m fracture behavior), see Figure 3-42. The CTOD bend-bar specimens had a thickness of 11.5 mm (slightly less than the vertical dashed line in Figure 3-40), and with the Charpy transition temperature of -10 C, the predicted bend-bar transition temperature (same as TWC FITT curve) was -62 C. The agreement is excellent.

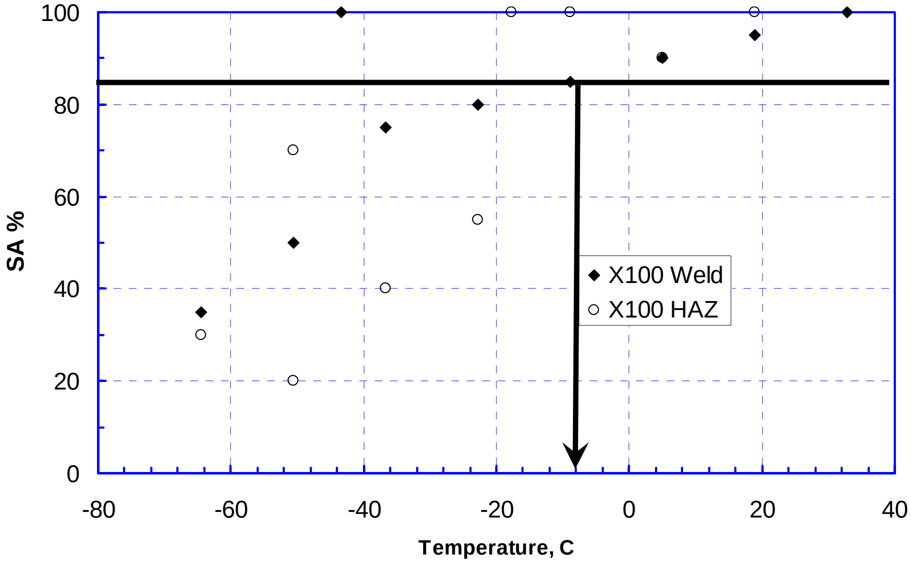

(a) Charpy 85% shear area transition temperature

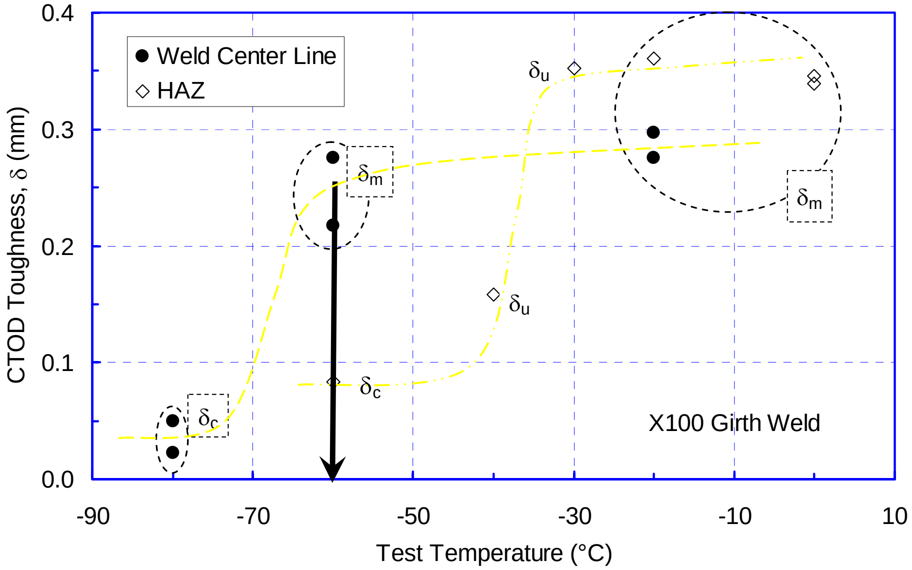

(b) CTOD tx2t bend-specimen transition temperature

Figure 3-42 Charpy and CTOD transition temperature for X100 weld (P108W)

The SENT tests conducted on that same X100 weld had crack a/t values from 0.4 to 0.75. This variability was because of fatigue precrack tunneling, and in later tests the d-c electric potential method was used to monitor the fatigue precrack depth. To keep the crack front as straight as possible, scans of the d-c electric potential across the crack front were made and the side-groove depth was adjusted to minimize the variability of the crack front using ASTM E1820 guidelines. Figure 3-43 shows the SENT in the Emc^2 MTS machine, and typical fracture surface.

Consequently, with the crack depths being different and the depth of the side groove being variable, it was necessary to normalize the load and load-line displacements to show all the data together. The load was normalized to the net-section stress and maximum load in the fully ductile tests, and the displacements were normalized so that they will have the same dimensionless elastic compliance (similar to the Key-Curve methodology [59]). Figure 3-44 shows the SENT results. Using the same FITT definition as in Figure 3-39, it can be seen that experimentally the SENT transition temperature is between -85 C and -95 C. The predicted FITT from the Charpy data for these SENT tests (thickness = 12 mm) is -90 C (see Figure 3-40) which again is excellent agreement.

From these results it is seen that the FITT Master Curve worked well for the X100 weld metal specimens. The FITT Master Curve also properly bounded the older X60 pipe full-scale brittle behavior. The last aspect to validate is to see how the FITT Master Curve method works for pipe tests conducted at a series of temperatures since the weld residual stresses might increase the constraint, which in turn could make the FITT warmer. With that final validation, the FITT Master Curve method could be readily implemented into codes and standards to ensure that the transition temperature is correctly predicted.

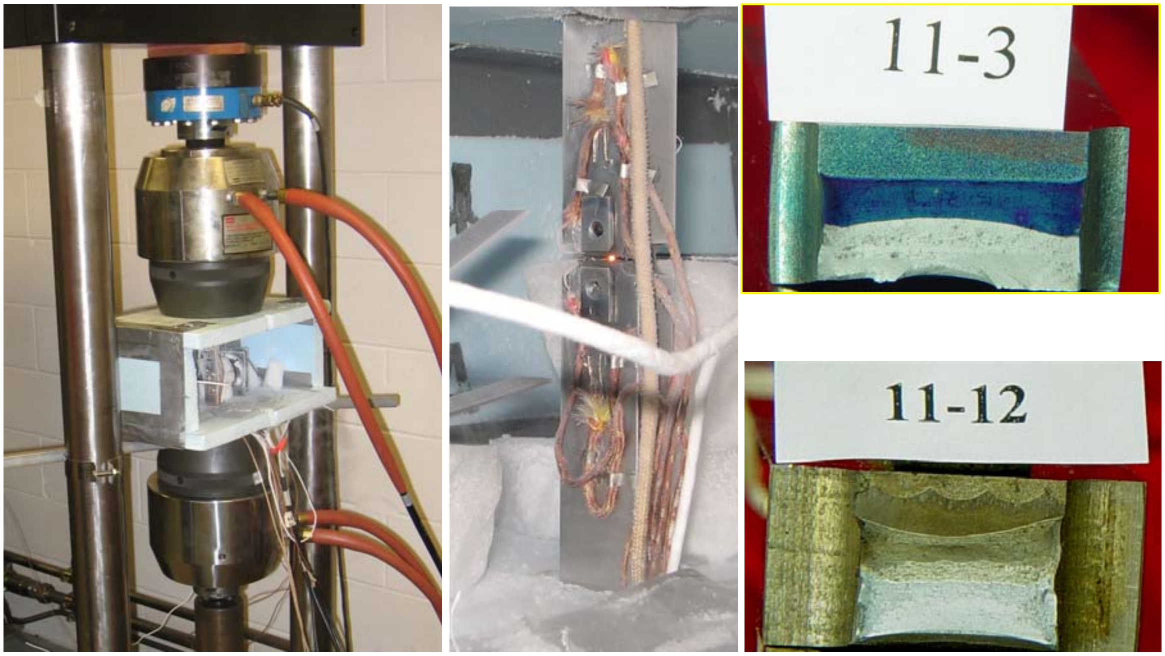

Figure 3-43 SENT specimen in test machine and fracture surfaces showing side-grooving, scalloped EDM notch for fatigue precracking fatigue crack (11-12), EDM notch (11-3), darker area is from ductile tearing during the test

An interesting comparison is the transition temperature of these fatigue-precracked SENT specimens compared to the back-bend specimens. Both are low-constraint tests. A further comparison can be made between the SENT and surface-cracked pipe tests. As shown in Section 3.3.3.1, the X100 weld back-bend specimen FITT transition temperature was lower than -126 C, whereas the SENT FITT was between -85 C and -95 C. Since there is reasonable comparison between SENT and surface-cracked pipe results (in the absence of weld residual stresses), it appears that the back-bend specimen either has too low of a constraint condition, or the EDM notch used in the back-bend tests produced a lower transition temperature than the fatigue-precracked SENT specimens.

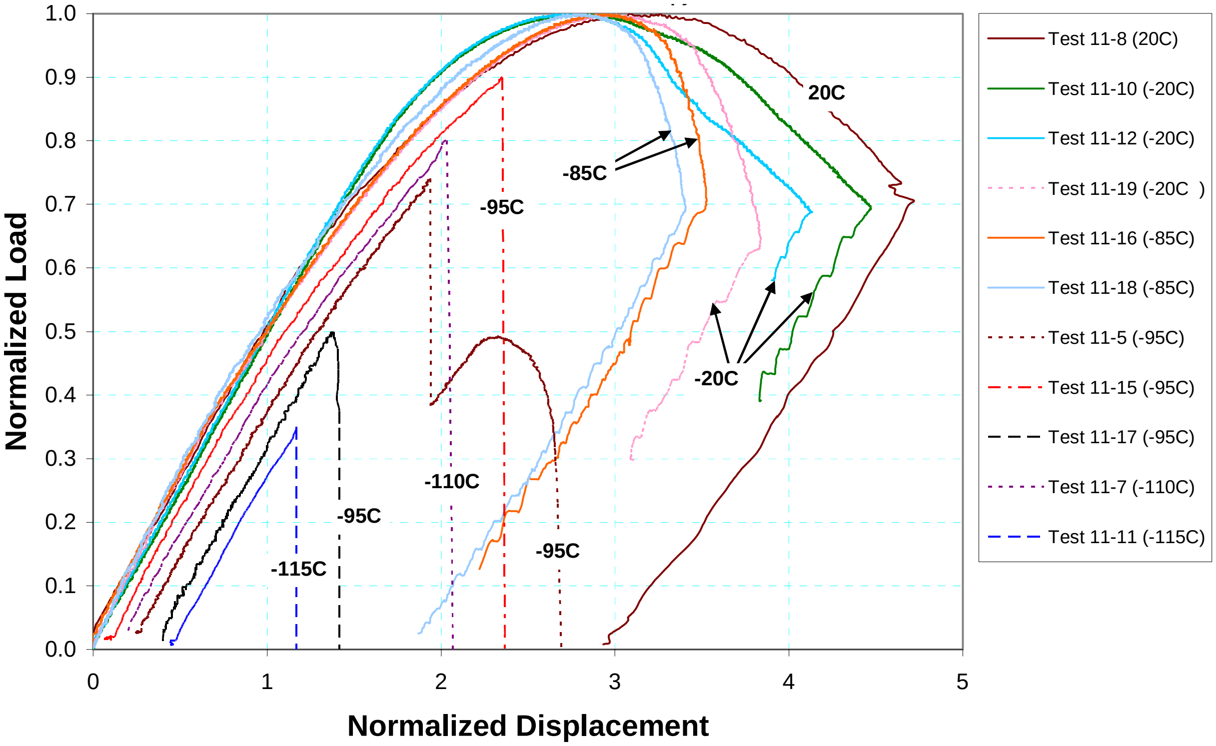

Figure 3-44 Normalized load versus normalized displacement curves from X100 weld SENT tests (lower-temperature tests offset to visualize easier – all specimens fatigue precracked)

3.3.3.3.2 Constraint Effects on Upper-Shelf Behavior for X100 Welds

In addition to the SENT tests conducted in the FITT study, several additional specimens in tension were tested with a fatigue and EDM notch. The EDM notch had the same notch acuity as used in the mini-wide-plate tests on the same welds. All tests were conducted at -20 C, which was the same temperature as many of the mini-wide-plate tests discussed earlier in this report. Standard bend-bar test results are given in Figure 3-42(b) for the same weld metal. The fatigue and EDM notch test results are shown in Table 3-6. These experimental data show that the EDM notch specimens have the start of ductile tearing occurring at a greater crack-mouth-opening displacement than the companion fatigue precracked specimens. The measured electric-potential data for these tests indicated that crack initiation was just past maximum load in the EDM notch. This was unusual, but possible. Since multiple specimen tests were not available to confirm this, the CMOD values at maximum load are referenced in Figure 3-45 and it was assumed that the same differences in CMOD at crack initiation occur. The EDM notch CMOD values at maximum load were about 1.3 times greater than those from the fatigue precracked specimens for the SENT specimens. The fact that the fatigue precracked specimen deviates from the blunter EDM notch is not surprising. Figure 3-46 from Reference [57] shows similar results from SENT specimens with fatigue precracks and a number of specimens with different radii notches. The more blunt the notch, the further it will progress up a power-law load-displacement curve that is a function of the material strain hardening until the ultimate strength in the ligament controls the failure stress.

Since there is not a standardized method to calculate CTOD in SENT tests (many proposed methods are in the literature including results from programs Emc^2 staff ran and are used in DNV-RP-F108), finite element analyses were conducted on these tests to assess the differences in the toughness at maximum load for tension versus bending, as well as assess the effects of fatigue precracked versus sharp-machined-notch specimens. The newly proposed constraint correction factor on the bend specimens in API 1104 says to multiply the average bend specimen CTOD by a factor of 2 to get the tension loaded CTOD constraint corrected value. There is evidence from other work that the effective toughness in a surface-cracked pipe can be 3 to 5 times that from a bend or CT specimen on the upper shelf [60, 61]. The finite element analyses used meshes that were similar to that shown in Figure 3-22. The CTOD values were extracted from the finite element results using the 45-degree method of Figure 3-23. Since the cracks are in the weld, the CTOD on both sides of the crack are symmetric.

The comparison of the fatigue versus EDM-notch specimens is an important consideration when using pipe specimen or wide-plate tests for validation of stress-based or strain-based analyses. In many projects, EDM or sharp-machined notches are used in pipe or wide-plate tests since the cost of fatigue precracking such large specimens can be high. Blunter flaws will effectively increase the initiation toughness of the material. Hence this should be taken into account in the validation analyses. In many past nuclear piping fracture programs [62, 63, 64, 65], if a pipe test was conducted with a sharp-machined notch, then lab tests (CT specimens) were conducted with the same notch acuity for comparison to the pipe test results, and CT tests were also conducted with fatigue precracks for material property database purposes. Figure 3-47 shows a comparison of J values at crack initiation from CT specimens with EDM notches and fatigue-precracked specimens. The EDM notches had a radius of 0.127 mm (0.005 inch), which is the same as used in the mini-wide plate tests on these same welds. These results show that the EDM notch gives a toughness value (based on J-integral) of 1.76 times the sharp crack toughness for this class of materials. For stress-based criteria, this toughness change will not greatly affect the failure stresses if the material is close to limit-load failure. However, for strain-based criteria, the strain at failure is linearly related to the CTOD, and hence pipe specimens with EDM notches could fail at much higher strains than a fatigue-cracked specimen. Hence, the notch acuity tests were conducted to see if X100 weld metal behaves similar to the nuclear piping steels in Figure 3-47.

The finite element results included the weld geometry and the stress-strain curves for the weld metal and base metal at -20 C. (Tensile test data are discussed above in this report.) Figure 3-45 shows a comparison of the load versus crack-mouth-opening displacements in the FE analyses and experiment. The FE analyses were for a stationary (non-growing) crack, so the deviation between the experiment and the FE analyses corresponds to crack initiation. As discussed above, the crack initiation point was also documented in the SENT tests by using the d-c electric potential method [66, 67], but the crack initiation point for the EDM notch specimens was past maximum load, which is unusual. Since multi-specimen tests did not exist to confirm that the d-c EP indicated initiation point, comparisons were made using the data at maximum load. Including the nonlinear geometry effects that occur near the crack tip did not affect results significantly although the results including large-strain effects compared a little better with the experimental data. The predictions compare very well with the test data up to crack initiation and maximum load here. Figure 3-48 shows the plastic-zone shape along with the blunted crack opening shape for the SENT cases at maximum load. Once good agreement with the experimental and FE load versus crack-mouth-opening displacement curves were verified then the key results from the FE analyses are CTOD values at crack initiation (J might also be of interest and is related to CTOD). As such, only values at maximum load for the stationary crack are presented in Table 3-6. These results are for the nonlinear geometry analysis case only although the linear geometry case produced similar results. A complete summary of the results of these analyses can be seen by studying Table 3-6 and Figure 3-45.

Table 3-6 Results summary of SENT FEM analyses of CTOD values at maximum load

Specimen	Notch type	CMOD Max Load	FE CTOD – 45° method	FE CTOD – Slope method	CTOD Ratio (EDM/Fatigue) – 45° method	CTOD Ratio (EDM/Fatigue) – Slope method
SENT	EDM	0.028	0.0192	0.0192	1.26	1.31
SENT	fatigue	0.024	0.0152	0.0146		

The CTOD values in Table 3-6 are much larger than the corresponding values reported in Figure 3-42 (which are about 0.3 mm or 0.011 inch) with fatigue precracked notches. Hence the ratio of the SENT to BEND specimen CTOD at maximum load is a subject that needs further study so that these results can be tied to results from References [62-65].

The ratio of the EDM notch to fatigue precracked notch was 1.26 (based on the 45-degree definition of CTOD) or 1.31 (for the CTOD slope definition) for the SENT specimen. The slope definition method simply extrapolates the crack profile back to the crack tip point, and is always slightly smaller than the CTOD method. It must be pointed out that the 45-degree method for defining CTOD is arbitrary but has been used for many years.

Two key points come from this section. (i) The use of bend type specimens to determine the toughness (based on CTOD or J) is conservative. For a surface crack in line pipe, the crack region is more likely to experience tension-like loading. Hence, it would be more accurate to develop toughness data from SENT-type specimen. (ii) The use of EDM-notched specimen to determine toughness should be avoided since this is not conservative, and accounted for if EDM notch full-scale data is used for validation of stress or strain-based flaw evaluation criteria (see further discussion in Section 5).

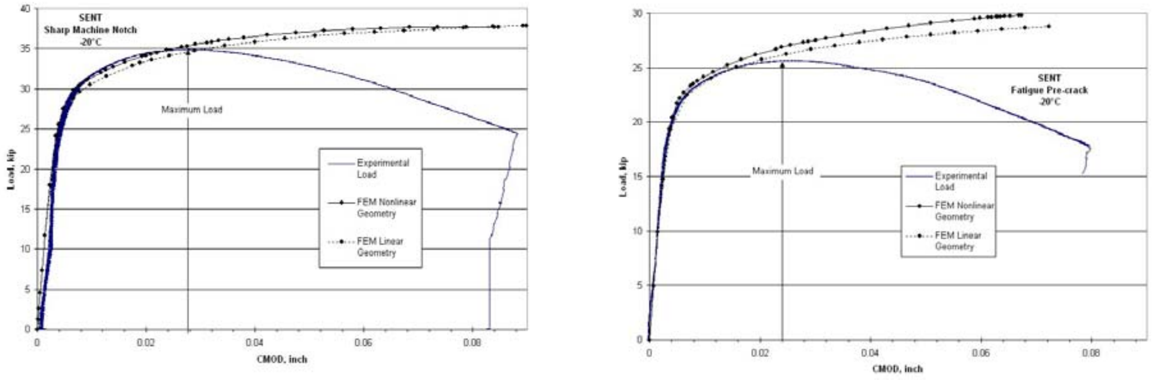

Figure 3-45 Experimental and FE analysis comparison of fatigue-precracked versus EDM-notched SENT specimens

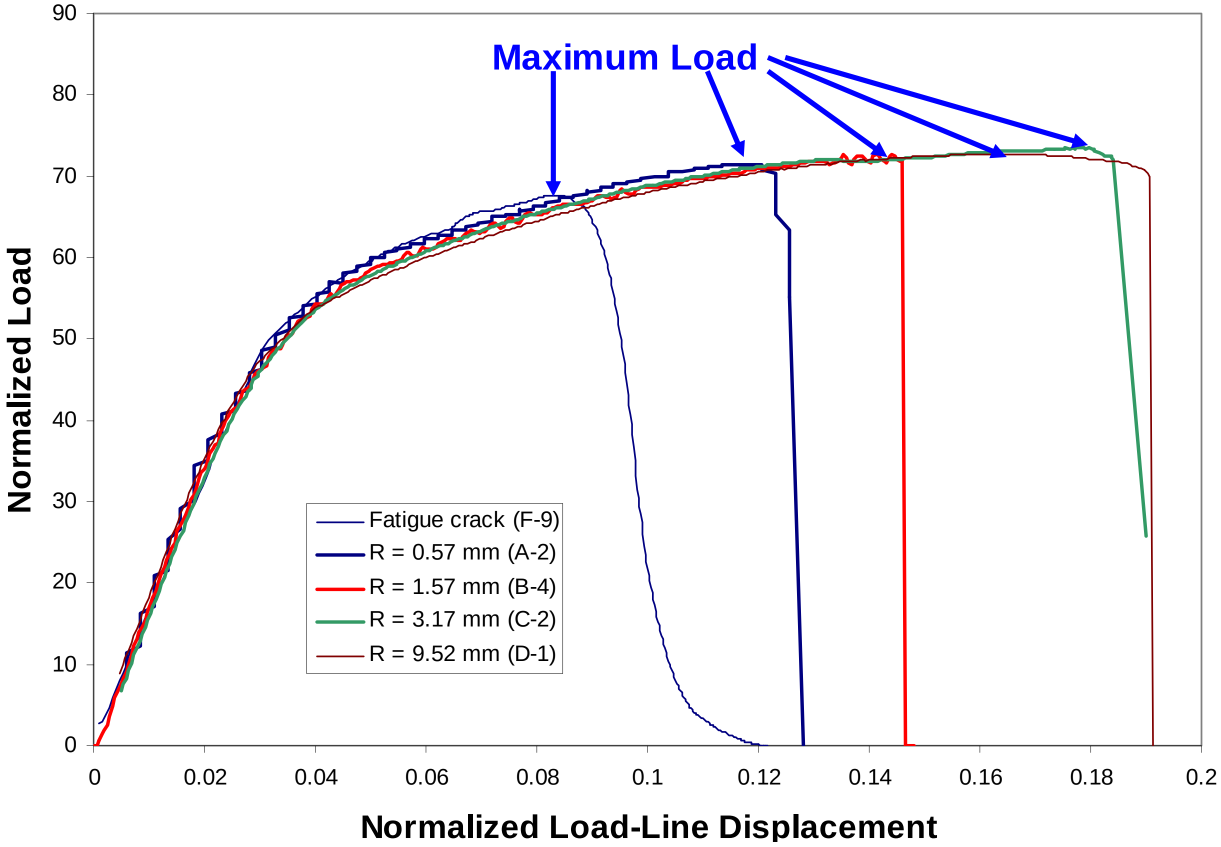

Figure 3-46 SENT results with fatigue-cracked notch and different machined radii notches

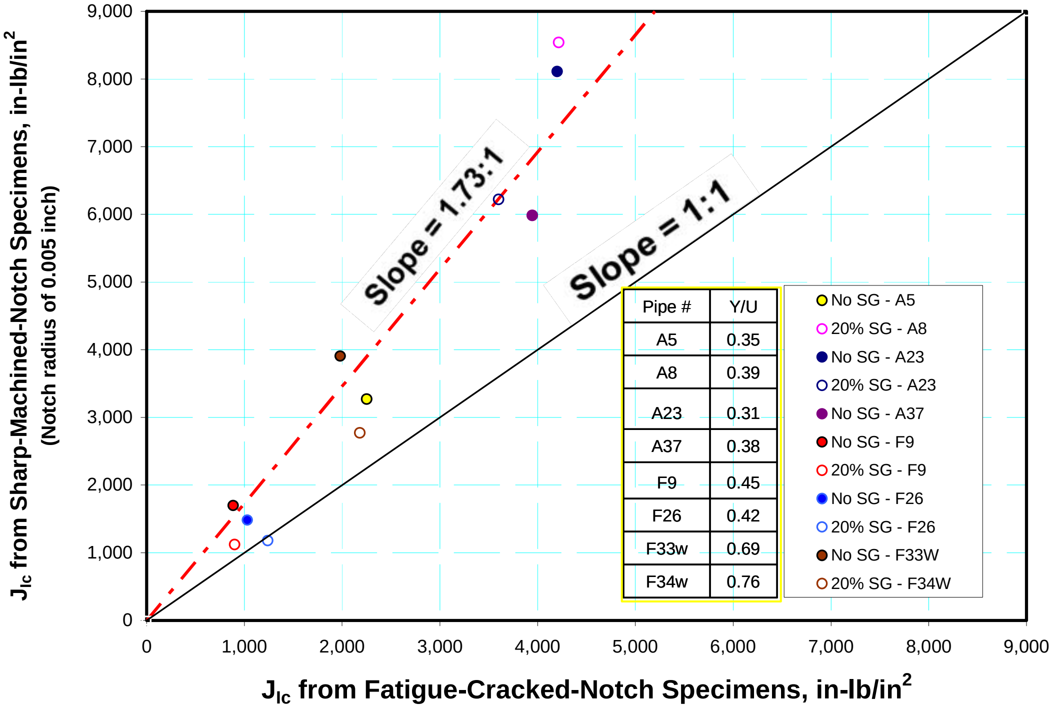

Figure 3-47 Effect of notch acuity from CT tests on large variety of nuclear-piping base metals and welds

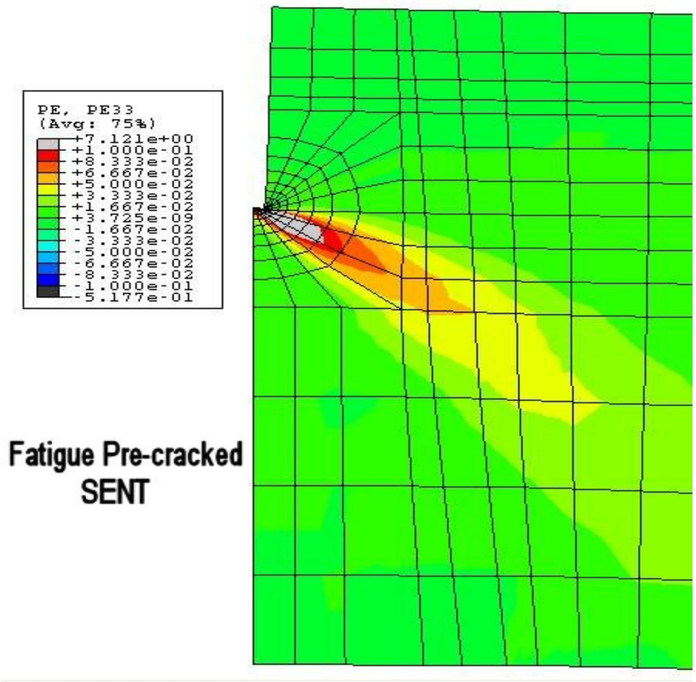

Figure 3-48 Equivalent-strain plastic-zone profile for fatigue-precracked SENT specimen near crack initiation (quarter model with symmetry at crack plane)

3.3.4 Advanced Modeling of Materials Anisotropy

Modern line-pipe steels made by thermo-mechanically controlled-roll processing (TMCP) can have significant anisotropic plastic properties due to the textures created in the rolling process of the plate product prior to pipe forming. Additionally, the transverse strains induced by pipe manufacturing can further modify the material properties through additional cold-working and the Bauschinger effect. For instance, the UOE process is commonly used to fabricate pipe from plate. UOE consists of crimping the rolled plate along its edges into a ‘U-shape’ and then pressing into an ‘O-shape’ between two semicircular dies. Finally, the pipe is welded closed and then circumferentially expanded ‘E-process’ to obtain a highly circular shape (hence UOE process). In addition, the construction and service conditions, such as offshore pipe-laying by reeling and service strains from frost heave and thaw settlement, can impose cyclic plastic strains. The strain-history affects mechanical properties in both the longitudinal and transverse directions.

The evolution of the anisotropic plastic properties is important to many aspects of pipeline integrity. For example, the collapse resistance to external pressure and buckling resistance to bending are sensitive to the cross-section ovality and stress-strain properties of the pipes. Internal pressure eliminates the ovalization effects, so that variation in the stress-strain curve is more important conventionally in welded pipe subjected to service bending loads after pressurization. The changing of the ovality during cyclic loading, on the other hand, is also affected by the evolution of the plastic properties. The accurate prediction of the material property evolution in all directions is beneficial and critical to the precise estimation of the load-carrying capacity of the line pipes with complex loading histories, especially under biaxial loadings. For this purpose, more representative material models rather than the isotropic model are required to simulate pipe behavior.

The next two subsections provide some details of attempts to consider anisotropic plastic behavior of line-pipe steels. First, phenomenological (classical) anisotropic hardening models are used and next recent crystal plasticity models are considered. It will be seen that some improvement is made using these models but completely satisfactory results are not obtained. This topic needs to be explored further to develop a pragmatic solution that can be implemented easily.

3.3.4.1 Classical Anisotropic Plasticity Models

The conventional anisotropic-hardening and kinematic-hardening plasticity models while simple to use, have certain limitations. There exist many anisotropic models among which the simplest and the most widely used is the classical Hill’s quadratic anisotropic model [68]. There are also many more recently developed non-quadratic anisotropic models [69, 70, 71]. The non-quadratic models give a better representation of the shape of yield surface, but require more effort in tuning the model parameters. Unfortunately, the anisotropic models in [68-71] can be used only for monotonic loadings. To simulate material behaviors under cyclic loading and loading-path change, a kinematic hardening model is often used. One of the most well-established kinematic models is the nonlinear isotropic/kinematic hardening model [72] and a form of the Lemaitre-Chaboche model [73] in which the yield surface translates in the stress space (kinematic component) and changes size (isotropic component) in terms of some internal variables (such as back stress and equivalent plastic strain) that characterize the stress/strain history. The pipe-forming procedures therefore are needed to accurately determine the internal variables of the materials in the post-manufacturing state.

Reference [74] describes applying a nonlinear isotropic/kinematic hardening model to represent the anisotropy of line-pipe steels and to study the effect of material's anisotropy on pipe-buckling resistance. Although the analyses showed the model works reasonably well for some line-pipe steels, a better model which accounts for both material anisotropy and kinematics is highly needed. In recent years, some new models combining Hill's quadratic-anisotropic-hardening model with the kinematic-hardening model have been developed. However, due to the phenomenological nature of these models (for instance Reference [75]), tedious experiments must be conducted in order to collect all the information required to tune the model parameters and hence this type of model was not considered.

3.3.4.1.1 Stress-Strain Curve Differences in Line Pipe

Consider an X100 TMCP line pipe made by the UOE process. Its tensile and compressive stress-strain relations measured in different directions are given in Figure 3-49(a) and (b), respectively [78]. Due to the large amount of cold working during the pipe manufacturing process, the material properties are quite different in different directions.

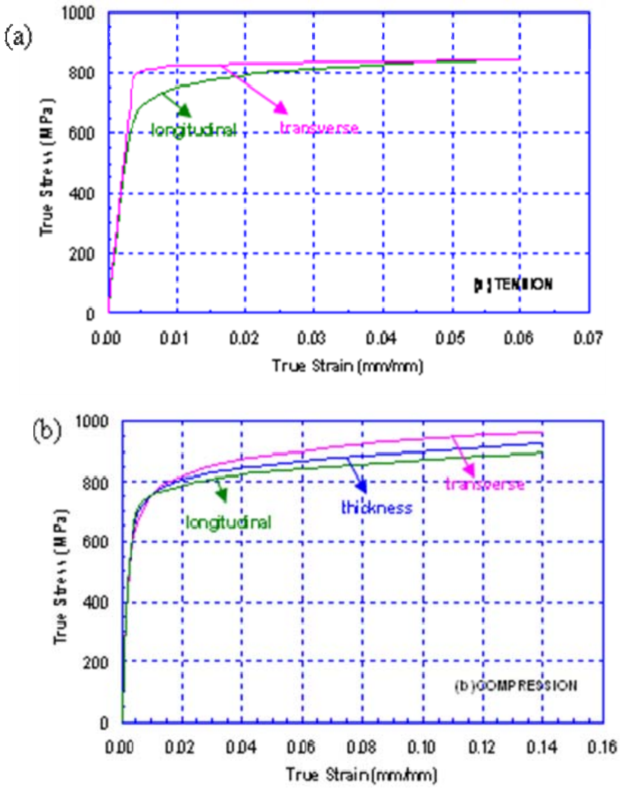

Figure 3-49 Experimentally measured tension and compression stress-strain relations for the X100 line pipe, from Reference [78]

Figure 3-49 (a) shows that the tensile yield strength is much higher while the strain hardening is much lower in the transverse direction than those in the longitudinal direction. The overall longitudinal stress-strain curve has a round-house shape without an obvious yield point while the transverse curve has a more obvious yield point. This is mainly caused by the pre-applied tensile strain in the transverse direction during the UOE process. The compressive stress-strain curves in Figure 3-49(b) on the other hand, are all of round-house shape and do not vary significantly in different directions. The compressive yield strengths are almost independent of the directions but the strain hardening in the transverse direction is higher than that in the longitudinal direction.

3.3.4.1.2 Buckling Response of X100 Pipe Including Anisotropic Effect

A finite element model of a pipe (outside diameter D = 36 inch, half length $l = 10D$ = 360 inch, thickness t = 0.5 inch) was developed to examine the effect of material anisotropy on buckling response of pipe. Shell elements using 7-point integration and 64 circumferential and 200 elements along the length direction were used (a half model taking advantage of symmetry was used). A 4% thickness reduction is created in the symmetry plane to initiate the buckling for all the cases.

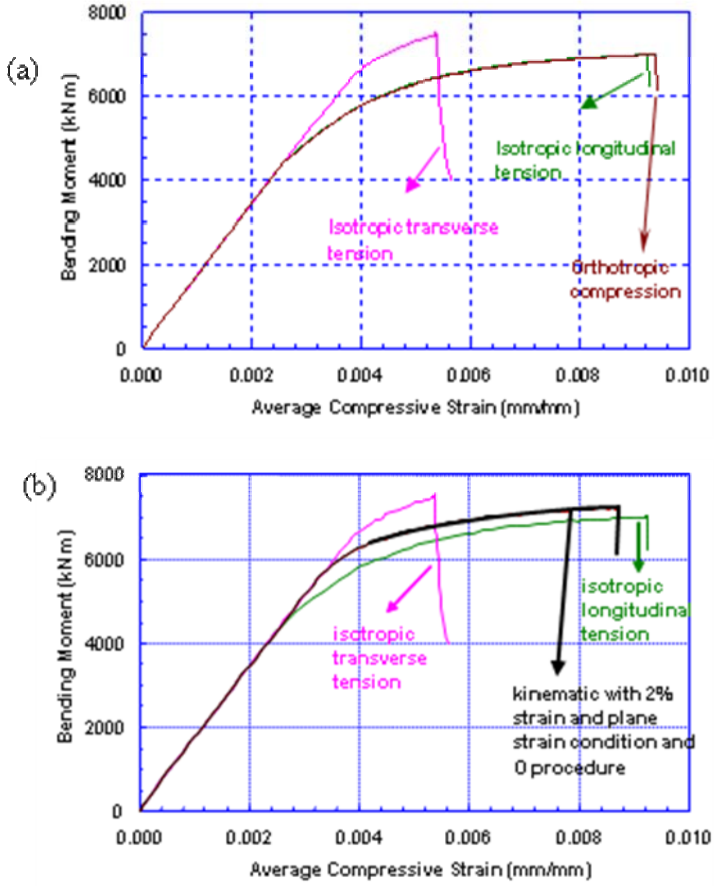

Figure 3-50 Predicted Buckling Strain Using Different Anisotropic Models; (a) Hill Model, (b) nonlinear kinematic and isotropic models

Figure 3-49(a) compares predictions of applied bending moment versus average compressive strain (defined as D/2Lθ with the gage length (L) on compression side and pipe rotation (θ) at gage length location) using classical isotropic plasticity and Hill theory. It is seen that the compression strain at failure using longitudinal stress-strain curves with isotropic hardening produces results close to Hill orthotropic theory [68]. Figure 3-50(b) shows the buckling-load predictions using the nonlinear-kinematic hardening model which included the pre-strain behavior caused by the UOE process. The isotropic hardening results are included here also. It is seen that both the load predictions and buckling strain between the Hill model and prestrain models are not significant, with the prestrain results having slightly smaller buckling strain and moment. When the buckling moment predictions are compared with conservative design buckling estimates from the literature and codes, all predictions are greater than these estimates. Reference [74] and [74] provide more details of this work.

3.3.4.2 Crystal Plasticity Models

The anisotropy of line-pipe steels resulting from rolling is mainly caused by the so-called texture, i.e., the preferred orientations of grains. Large plastic deformation induced during cold working can also change grain orientations and therefore modify material anisotropy. Numerous research works have been performed to model the behavior of the individual grains and their interactions based on theories of dislocations in crystals. Among them, the rate-dependent Taylor-type polycrystalline plasticity model [76] is simple and has been widely used (for instance by Kothari and Anand [77]). The model is physically more realistic and contains more details on the deformation mechanism in the micro/meso scale compared with the phenomenological models discussed in Section 3.3.4.1. The anisotropy is modeled by the experimentally measured microstructure texture and texture evolution due to plastic deformation. In addition, it has been shown that the kinematic-hardening behavior of the material can be represented reasonably well through the residual stress evolution developed in grains by the model without explicitly considering kinematic terms [78]. In this section, Taylor's polycrystalline plasticity model is used to study the evolution of material properties during simulated pipe forming, construction, and service processes. The capability of the crystal-plasticity model in modeling the anisotropy and plasticity evolution under cyclic strains is demonstrated using an X100 material as an example. More details can be found in Reference [79] and Appendices 6 and 10.

Metals are crystalline solids that consist of atoms arranged in a pattern (crystal lattice) repeated periodically. The lattice structure can be a number of shapes while the most common lattice types are face-centered cubic (FCC), body-centered cubic (BCC), and hexagonal close-packed (HCP). Most line-pipe steels are of BCC structure at normal construction and service conditions. In a single crystal, the entire crystalline solid contains one continuous crystal lattice unbroken to the sample edges. Line-pipe steels are polycrystalline, which is an aggregate of a great number of single-crystal grains with different orientations. The texture is the distribution of crystallographic orientations of single crystal grains within a solid and is represented by the orientation distribution function (ODF). The ODF is defined as the volume fraction of grains oriented along a certain direction. Line-pipe fabrication can orient grains in certain directions defining the texture. For BCC metals, the direction is normally identified using three Euler angles in a typical positive octant traditionally collected from X-ray diffraction. The plastic deformation occurs by slip on certain crystallographic planes (slip planes) and in certain crystallographic directions (slip directions). The combination of any one of the slip planes and any one of the slip directions is called the slip system. The only slip direction for BCC crystal is <111> direction, but the slip planes may be {110}, {112}, and {123}. Therefore, there are 48 total slip systems in a BCC crystal. Here we provide some results and attempt to shed light on the usefulness of these models compared with traditional anisotropic and isotropic models.

3.3.4.2.1 Polycrystalline Plasticity Constitutive Model

The polycrystal-plasticity model relates the macro-mechanical behavior of polycrystal metals to the fundamental mechanism of single-crystal deformation. The model assumes that each macroscopic material point contains a cluster of single-crystal grains of different orientations. The Taylor's theory assumes that the local deformation gradient ***F*** of each grain is homogeneous and identical to the macroscopic deformation gradient of the material point. However, due to the difference in orientations, the active slip system, hardening status, and stress of each grain are different. The stress at the material point is given by the volume average of the stresses of all grains in the volume. The details of the Taylor crystal plasticity model and detailed definitions of slip-planes and slip-directions, etc. can be found in References [73] and [79]. The Taylor model was implemented within a user subroutine (UMAT) and ABAQUS was used for all predictions. The focus here is on X100 steel.

The chemical compositions of the X100 steel specimen can be found in Table 3-1and a typical SEM microstructure is shown in Figure 3-9(b). It is seen that the X100 steel has a very fine grain structure with average grain about several micrometers. The measured pole figures are shown in Figure 3-51, where RD and TD stand for the rolling and transverse directions, respectively. The ODF is calculated from the pole figures using the program PopLA [80]. To reduce the computation effort in the crystal plasticity model, the ODF is discretized by 10-degree intervals in the Euler space. Therefore, considering the cubic symmetry, there are totally 729 grain orientations in the space. The ODF gives the volume fraction of grains aligned at each of the 729 orientations.

As detailed in References [74] and [73], unit cell models are used to calibrate and fit the model parameters and include the effect of the UOE process.

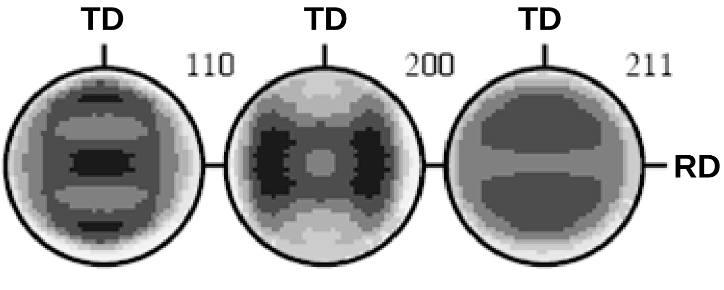

Figure 3-51 Experimentally measured texture of X100 line-pipe steel

3.3.4.2.2 Anisotropy and Full Pipe Reeling Simulation

The reel-lay method is a cost-effective method for offshore installation of small to medium size pipelines. However, the cyclic strains applied by the reel-lay process are well beyond the elastic range. The plastic strain will not only impact the integrity of the girth weld defects, but also affect the pipe resistance to collapse and buckling. One of the challenges in reeling simulation is the accuracy of the materials model. First of all, line-pipe has an initial anisotropy due to the rolling texture and cold work in the transverse direction. In addition, a large amount of cold work will be applied in the longitudinal direction by the reeling and it can further change the materials anisotropic property. The accurate prediction of the material anisotropy evolution in all directions is very important to pipe integrity assessment, since the pipe may experience bi-axial loading in construction and service. For instance, Reference [81] found that a 15% reduction of the compressive yield strength in the transverse direction can reduce the longitudinal strain resistance to buckling by as much as 50% when the pipe is bent with applied external pressure. The polycrystal plasticity model is a good candidate for reeling simulation since the change in the materials anisotropy can be automatically captured by the evolution of texture and residual stress of grains.

The deformation process of a full-size pipe during expansion (representing the E of the UOE process) and the reeling process is simulated. The pipe modeled was 18 inch outer diameter (OD) and 19.05-mm wall thickness, as illustrated in Figure 3-52(a). Considering the symmetry of the problem, only a quarter of the pipe is modeled. The total axial length of the model is taken to be 5 times the pipe diameter. A 5% thickness reduction is created at the symmetry plane of the longitudinal direction to expose the non-uniform pipe wall thickness effect. Close to the reduced-thickness cross section, 40 elements are used in the half circumference of the pipe and 8 elements are used through the thickness.

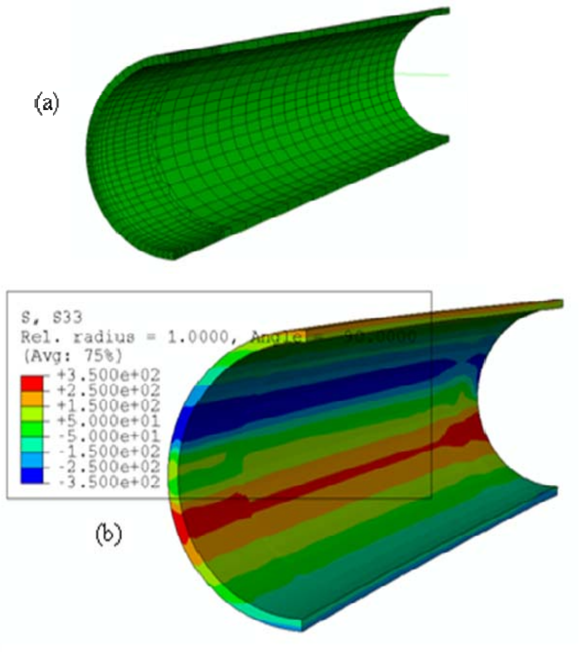

Figure 3-52 Quarter pipe model (due to symmetry) finite element model and residual stresses due to expansion during forming and pipe reeling

In the first step, a 1% strain in the transverse direction is applied by forcing expansion of all the nodes on the inner surface. The plane-strain condition in the longitudinal direction is maintained during the expansion. This process produces tensile longitudinal stress at outer surface of the pipe compressive residual stress of similar magnitude on the inner surface. The reeling process is then applied in five steps. Instead of applying the strain directly, rotation is applied at the remote end to simulate a pure bending. The longitudinal residual stress distribution at the end of reeling is shown in Figure 3-52(b). It shows that the reeling generated significant residual stress in the pipe. A large compressive residual stress exists in the 2-o'clock position and a large tensile residual stress exists in the 4-o'clock position. The model also predicted the pipe ovality as detailed in Reference [79].

Reeling not only alters the stress-strain properties of materials and creates cross-section ovalization, but also results in non-uniform residual stress distribution and non-homogeneous materials properties. The collapse resistance to external pressure and buckling resistance to bending will be affected by all the mechanisms resulting from the pre-strain and reeling effect. Due to the limitations of the conventional plasticity models, accurate modeling of the pre-strain effect is a challenging problem. The polycrystal plasticity model seems to be a promising method for this difficult problem. The polycrystal plasticity model has been proven successful in the simulation of sheet metal forming and stamping. By proper calibration, it could be used as a powerful tool for integrity assessment of offshore and onshore pipelines, especially for the circumstances involving complicated loading histories and biaxial loadings. However, the models need further refinement.

Finally, it is important to point out that finite element analysis using a polycrystal plasticity constitutive model is computationally intensive. In fact, some of the single analyses took weeks to complete. This renders the practical use of these models problematic at the present time.

3.3.5 Stress-Strain Property Predictions

The overall stress-strain curve is assumed to take the form that is suggested in CSA Z662,

$$\varepsilon_a = \frac{\sigma_a}{E} + \left(0.005 - \frac{\sigma_y}{E}\right)\left(\frac{\sigma_a}{\sigma_y}\right)^n \tag{3-1}$$

where σ_y is the nominal yield stress (SMYS) and E is the Young's modulus. There is a unique relation between applied stress σ_a and applied strain ε_a, if the strain-hardening exponent n is known. By assuming a pure power-law stress-strain relation, the strain-hardening exponent may be estimated as,

$$n = \frac{\ln(\varepsilon_t / 0.005)}{\ln\{1/(Y/T)\}} \tag{3-2}$$

Webster and Bannister examined the correlation of *Y*/*T* ratio and yield strength [82]. Two simple relationships were produced, one providing upper bound *Y*/*T* ratio, the other providing the best fit to the data. The relations were derived from theoretical and empirical considerations, and are applicable to many kinds of structural steels. Mannucci et al. found the relationships to be reasonable for pipeline steels tested in longitudinal direction [83]. The comparison of the line pipe test data and the upper bound and best-fit relationships is shown in Figure 3-53.

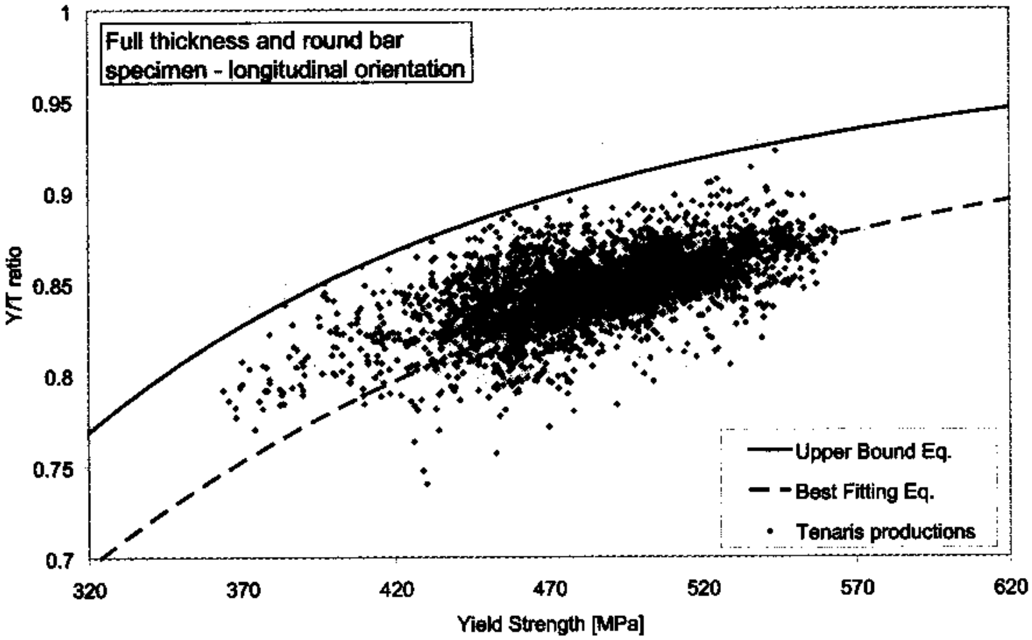

Figure 3-53 Comparison of line pipe longitudinal test data with the Webster and Bannister correlation equations

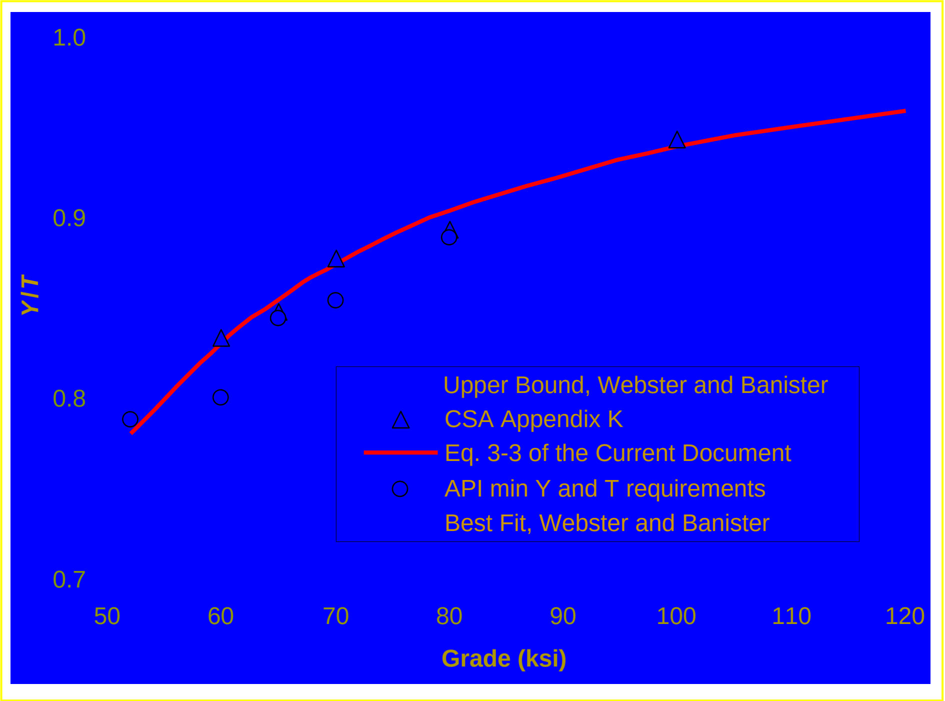

Figure 3-54 Comparison of the relations between *Y*/*T* ratio and pipe grades from estimation equations and codes

The relationships for the upper-bound and best-fit curves by Webster and Bannister are shown in Figure 3-54. Some reference points are added by computing the *Y*/*T* ratio from the API 5L minimum yield and tensile requirements. In addition, the plastic-collapse criterion of CSA Z662 Appendix K 2003 provides a reference table between pipe grade and flow stress. The implied *Y*/*T* ratio may be obtained when the flow stress is taken as the averaged value between yield and tensile strength. The API 5L and CSA Z662 values are also shown in Figure 3-54. A new equation in the same format as that of Webster and Banister, but providing the best fit to the API 5L and CSA Z662 Appendix K, is suggested as follows,

$$Y/T = \frac{1}{1+2\left(\frac{21.75}{\sigma_y}\right)^{2.25}} \tag{3-3}$$

The equation is also shown in Figure 3-54. The nominal yield stress σ_y is in the unit of ksi.

Estimating the strain at the ultimate tensile strength (UTS), often termed *uniform strain* or *tensile strain*, can be difficult. It is generally true that the uniform strain is inversely related to pipe grade. The following equation is suggested for grades up to X100 if no other proven estimation procedure is available.

$$\varepsilon_t = -0.00175\sigma_y + 0.22 \tag{3-4}$$

The nominal yield stress σ_y is in the unit of ksi. Reference [19] provides details of the above estimation procedure for stress-strain property prediction of line-pipe steels.

3.3.6 Toughness Prediction with Neural Network Model

Predictions of weld microstructure and mechanical properties are among the targets of mathematical modeling of weld phenomena. Weld integrity assessment requires the knowledge of the mechanical properties in the weld region. Significant progress has been made in numerical simulation of weld microstructure in the past decade. It is now possible to predict the microstructure of welds from their chemical composition and welding parameters. Most reported microstructure models are formulated using the fundamental phase-transformation thermodynamics and kinetics theories and can render predictions with reasonable accuracy. There are two major approaches to the predictions of weld mechanical properties; (i) predictions based on first principles, and (ii) empirical methods. Very limited advancement has been made in numerical modeling of weld mechanical properties, especially the predictions based on first principles. However, the empirical methods developed in recent years show promisingly fair predictability. The confidence of their predictions is attributed to the two main features of these empirical models. First, they employ modern computational techniques such as non-linear regression implemented with neural network; secondly, they incorporate large experimental databases.

Emc^2 acquired the neural network software package developed by Professor Bhadeshia, et al. of the University of Cambridge. A weld toughness database was also obtained along with the software. The database contains the experimental toughness data of ferritic steel welds. There are 879 data sets in the database. Each data set consists of chemical composition, welding conditions, Charpy test temperature, and toughness value. A neural network model was trained using the software and database. The input variables and output of the model are defined in Table 3-7. Charpy toughness is the output of the model. The model was employed to predict weld toughness using published experimental data. Figure 3-55 demonstrates one example of such prediction.

The neural network model developed at Emc^2 shows wide variation in predictions. The model is considered a preliminary model since its database does not incorporate enough data of pipeline steel welds, which are the primary materials researched in this program. More experimental data needs to be collected from the industry. A data collection template has been generated based on the preliminary study described above and sent to the industrial partners of this program for data collection. Such data will enable retraining of the neural network model and render toughness predictions for pipeline welds. The level of effort in compiling all the data needed as input to the neural network software to make it effective in predicting reliably material toughness information that would also be useful to the industry would be prohibitive. The effort was therefore limited to deterministic based approaches to characterize material toughness and fracture resistance of pipe-line steels and welds. Appendix 1 provides a complete description of this task.

Table 3-7 Input variables and output of the neural network model for weld toughness

	Data	Unit
Chemical Composition	C	wt%
	Si	
	Mn	
	S	
	P	
	Cr	
	Mo	
	Ni	
	Co	
	Cu	
	V	
	W	
	B	
	N	
	Nb	
	Ti	
	O	
Welding Conditions	Process Type	SMAW, FACW, SAW, etc
	Heat Input	kJ/mm or kJ/inch
	Interpass Temperature	^{0}C or ^{0}F
	PWHT Temperature	^{0}C or ^{0}F
	PWHT Time	hour
Charpy Test	Testing Temperature	^{0}C or ^{0}F
	Charpy Toughness	J

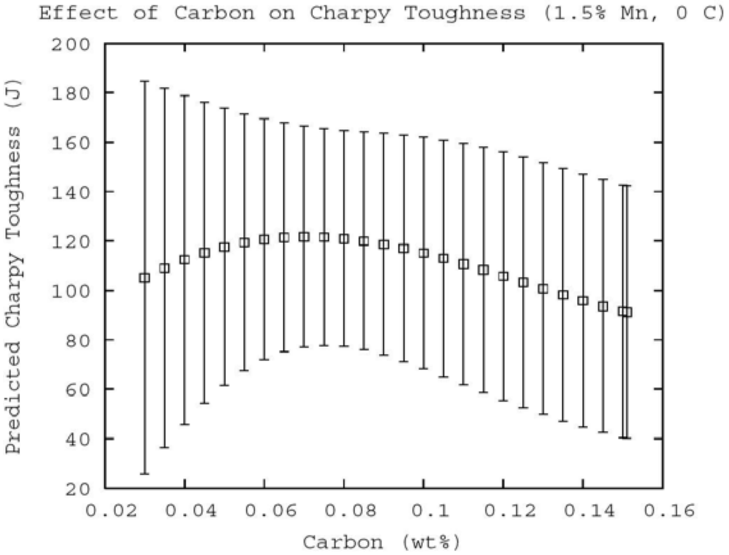

Figure 3-55 Predicted Charpy toughness with carbon content using neural network

3.3.7 Toughness Prediction with Damage Mechanics Model

3.3.7.1 Damage Mechanics Model

The failure of materials under high tensile strains may be determined by two approaches. The first uses a local criterion such as critical CTOD or J-integral to assess the onset of crack growth [84,85]. The CTOD-driving force is usually calculated by FE analysis without crack growth. Although more difficult, J-integral based calculations accommodate crack growth using the J-resistance curve for the material. However, it is well known that ductile failure of metals is generally preceded by some stable crack growth. Neglecting crack growth may induce some errors. The other approach is the so-called damage mechanics modeling. This approach utilizes special FE models where crack propagation can be simulated and it can render more insights into the fracture process

In this work, the application of the Gurson-Tvergaard-Needleman (GTN) model [13,14,15, 86, 87] (see Reference 88 for detailed equations) to low-constraint tests of high-strength line-pipe steels and weldments was investigated. Three different tests, i.e., uniaxial tension test, back-bend test, and mini-wide-plate test, were investigated as discussed above. For material properties, X100 line-pipe base metal (BM) and its weld metal (WM) were used. The GTN model contains eight parameters which are usually calibrated by FE calculations and experiments. Therefore, determining the parameters effectively and uniquely is always a big challenge and has been a research topic for many years. Thus, a simplified approach using both tension and back-bend tests was introduced to calibrate the GTN parameters consistently. Using the calibrated parameters, the CTOD at peak-load was predicted for various crack sizes in the back-bend and mini-wide-plate specimens.

3.3.7.2 Two-Stage Tuning Approach for Calibrating the GTN Model Parameters

As described in Reference [88], the GTN model uses 8 parameters: f_0, q_1, q_2, ε_N, s_N, f_N, f_c, and f_F. It is therefore a great challenge to determine all the parameters effectively and uniquely. Much work has been done to study the sensitivity of the damage model parameters [89, 90]. In this work, the insensitive parameters were determined by simple estimation and only the sensitive parameters were calibrated with FE calculations and experimental results. The two key sensitive parameters were volume fraction of nucleated voids (f_N) and critical void volume fraction at which void coalescence occurs (f_c). Since the parameters were not independent, it was very difficult to uniquely determine those parameters with one type of test specimen. To determine the two parameters consistently, calibrations were performed using different types of test specimens where different mechanisms were dominant. As a first stage of the two-stage calibration approach, void coalescence was disabled and f_N was varied to get the best fit to the experimentally measured uniaxial tension stress-strain curve up to the necking strain. In the tension test, since stress triaxiality and localization are relatively low, especially before necking, void growth and nucleation are the dominant mechanisms other than void coalescence. In this manner, f_N can be uniquely determined. In the second stage, one back-bend test was used to determine f_c. The parameters for both base and weld metals are given in Table 3-8**.** These parameters were used for all back-bend and mini-wide-plate test simulations.

Table 3-8 GTN parameters for X100 base and weld metal (mesh size 0.25 mm)

	f_0	f_c^*	f_F	f_N^*	ε_N	s_N	q_1	q_2
Base	0.002	0.025	0.20	0.01	0.018	0.014	1.359	0.998
Weld	0.002	0.015	0.14	0.01	0.020	0.015	1.347	0.994

***** Represents key fitting parameters

3.3.7.3 Peak-Load CTOD Predictions

The built-in GTN model in the commercial finite element software ABAQUS was used for FE simulations. Eight-node 3D elements were used in back-bend and mini-wide-plate simulations, and four-node axisymmetric elements were used in uniaxial tensile analyses. The typical FE models of back-bend and mini-wide-plate specimens are shown in Figure 3-56. The weld metal is shown in light grey and the base metal is shown in dark grey. The element size in the damage zone was fixed to 0.25 mm in all cases including tensile test analyses.

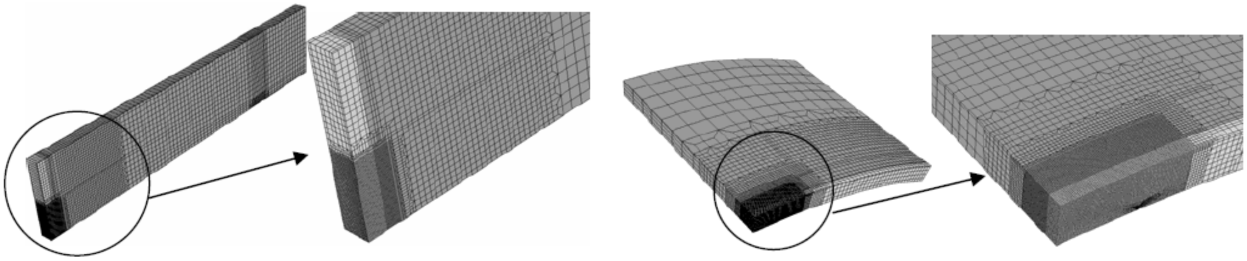

Figure 3-56 FE models of a back-bend and mini-wide-plate specimens

Figure 3-57 shows the measured and calculated load-displacement curves of the base metal back-bend tests (the test used to tune the model is not shown). The simulations overestimated the load, but properly predicted the displacement at the maximum load. The simulated and measured peak-load displacements as a function of ligament size are given in Figure 3-58. The calculated CTOD at the peak-load are also shown. The CTOD was always calculated on the symmetry plane perpendicular to the crack surface which is the mid-thickness plane for the back-bend specimen, and the plane containing the deepest point along the crack front for the mini-wide-plate specimen. The CTOD was calculated at the point 0.25 mm behind the crack tip on the crack surface. The GTN model predicted the relationship between the peak-load displacement and the ligament size very well. The predicted peak-load CTOD varied from 0.4 mm to 0.7 mm with an average of 0.6 mm. Figure 3-59 and Figure 3-60 show the results of the back-bend tests containing a weld metal crack. The GTN model again overestimated the load but predicted the displacement at the peak load very well. The predicted peak-load CTOD of the WM varied from 0.5 mm to 0.6 mm. The calibrated model parameters were then applied to the mini-wide plate simulations. Figure 3-61 shows the simulated and measured load versus gross strain curves for the mini-wide-plate tests containing a WM crack. The GTN prediction matched the measurement extremely well in terms of both load and strain. The peak-load CTOD and strain are shown in Figure 3-62 where the predicted data match the measured data very well. These results also verify that the same set of parameters can be transferred between back-bend and mini-wide-plate test specimens.

As demonstrated in this work, the damage mechanics model, i.e., the GTN model, can be used to simulate the ductile crack growth behavior of a crack in a girth weld. The two-stage tuning approach developed in this work provides a consistent and easy way to determine the model parameters. By using these calibrated GTN model, failure of materials under different constraint levels can be predicted more accurately. However, although the two-stage tuning approach can be used, the calibration of the GTN model parameters still requires extensive amount of experimental and numerical analyses. In this sense, analysis using the damage mechanics model is recommend for confirmatory type of analysis or to check unusual specific problems.

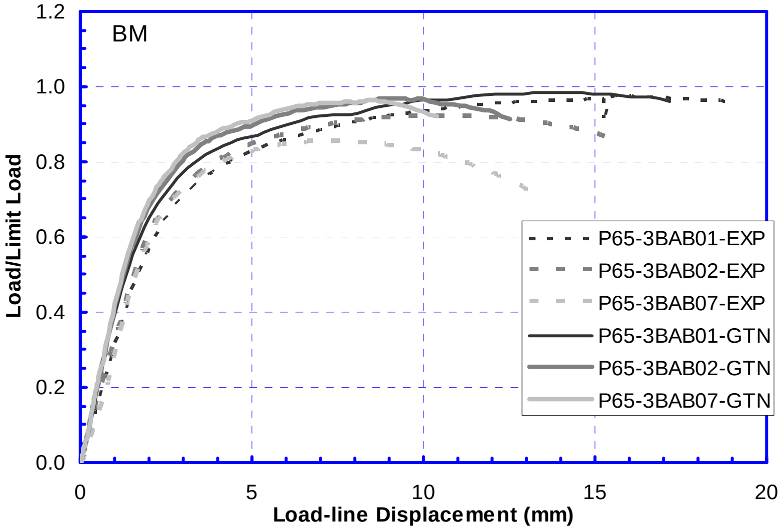

Figure 3-57 Normalized load versus load-line displacement of back-bend specimens with cracks in the base metal

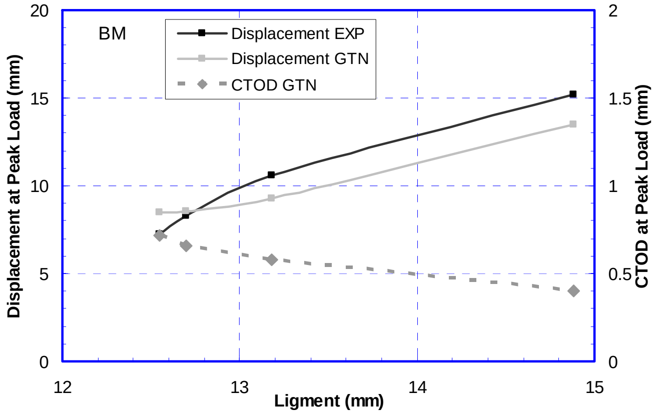

Figure 3-58 CTOD and load-line displacement at peak loads from experimental tests and FE simulation of back-bend specimens with cracks in X100 base metal

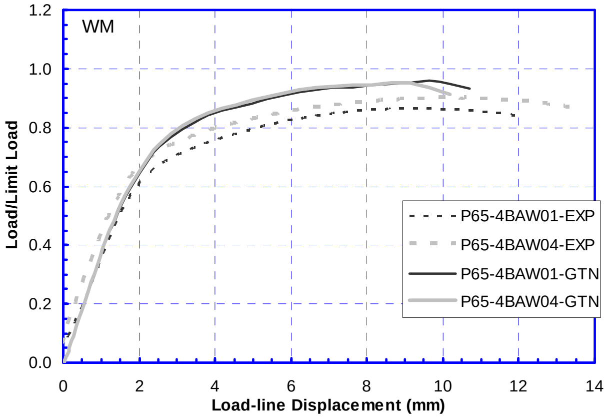

Figure 3-59 Normalized load versus load-line displacement of back-bend specimens with cracks in the weld metal

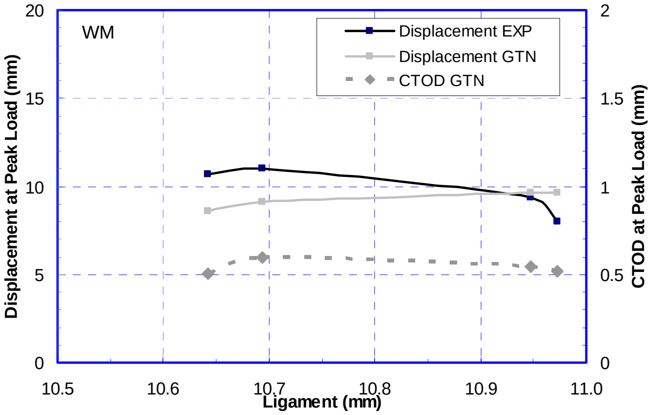

Figure 3-60 CTOD and load-line displacement at peak loads from experimental tests and FE simulation of back-bend specimens with cracks in the weld metal

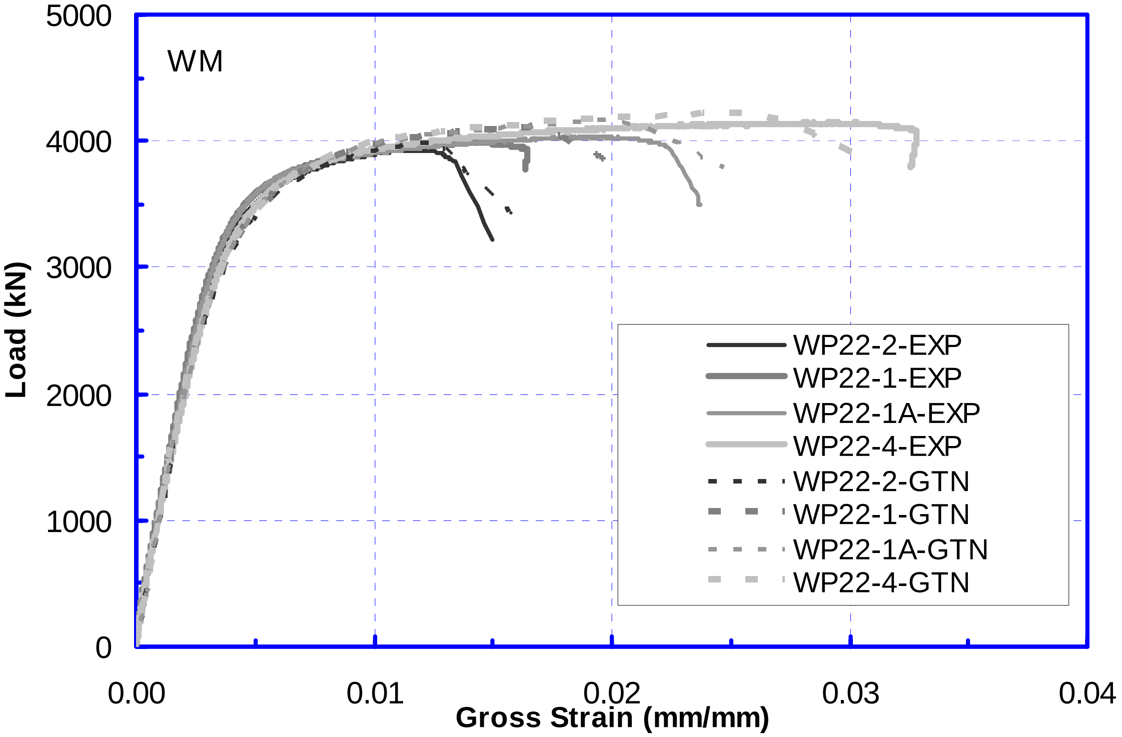

Figure 3-61 Load versus applied strain from experimental tests and FE simulation of mini-wide-plate specimens

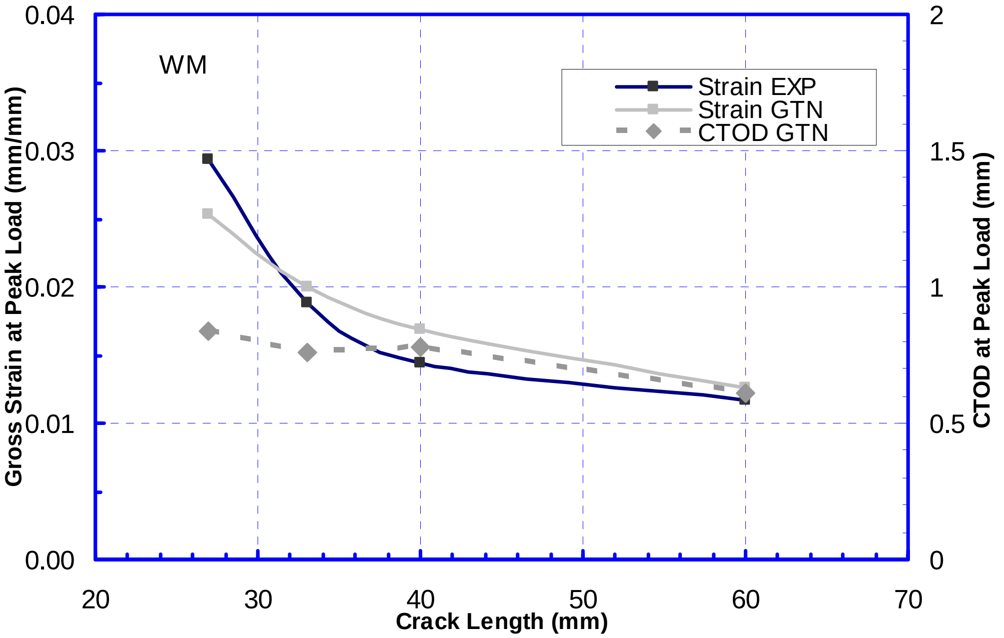

Figure 3-62 Gross strain and CTOD at peak loads from experimental tests and FE simulation of mini-wide-plate specimens

3.4 Implication of Results for Flaw Assessment Criteria for Girth Welds

Sections 3.2 and 3.3 of this report described work related to understanding the crack-driving force and measuring the resistance of X70 and X100 materials to fracture. This section shows how some of that work comes together to create improved stress-based or strain-based design criteria for girth weld flaw assessments, and then how those could be used to improve the current codes and standards for high-strength-steel pipeline construction.

3.4.1 Stress-Based Design

Traditional girthweld defect tolerance analysis is based on knowing the longitudinal stresses in the pipeline and knowing the strength and toughness of the material to determine the allowable flaw size. This approach is also called a *stress-based criterion*. There are many such circumferential flaw criteria in the world for different applications. The API 1104 criteria, Canadian Standards Association (CSA Z662), DNV, SINTAP, BS7910, etc. are standards or recommended practices used for buried or offshore transmission pipelines for oil or gas. The ASME Section XI of the Boiler and Pressure Vessel code is for above ground power plant piping, and perhaps proposed the first such standard for girth weld defect tolerance. There are French, Japanese, German, and British (R6) standards that are also used for power plant piping. The API-579 code was developed for chemical and refinery plant applications, but essentially uses criteria similar to the other above ground plant piping flaw acceptance criteria.

Many of these codes recognize that there are different failure conditions or analyses procedures for girth weld defect tolerance. They may also have several criteria that go from simple procedures to much more complicated analyses. The failure modes typically are;

- Limit-load analyses,
- Elastic-plastic fracture mechanics (EPFM), or
- Linear elastic fracture mechanics (LEFM).

Generally limit-load analysis means that the material is tough enough that the failure stress is governed by the pipe dimension, flaw size, type of loading (i.e., bending, tension), and material strength. This failure mode is independent of the material toughness, but it must be demonstrated that sufficient toughness exists to use this analysis procedure. The analysis is the simplest of the three failure modes.

Elastic-plastic fracture mechanics (EPFM) analysis generally occurs when the material has a reasonable amount of toughness, but not enough so that a limit-load analysis can be used. The toughness can be described by either the crack-tip-opening displacement (CTOD) analysis or the J-integral fracture parameters. These two parameters are related and could be used interchangeably with the proper relationship (usually a function of the material strength or strain-hardening exponent and possibly with some specimen or crack-size dependence). The CTOD parameter has traditionally been used in the oil and gas industries, whereas the J-integral crack growth resistance curve (J-R curve) has traditionally been used for nuclear and power plant piping applications.

LEFM is applicable when the material is brittle. It is highly desirable to avoid having such materials, so there are not as many practical applications for this failure mode. Stress intensity factors based on LEFM are usually used to address stress corrosion and fatigue crack growth in line pipe. In this failure mode, the weld residual stresses can be important in determining the failure stresses, where as in limit-load and EPFM there is enough ductility at the crack that the residual stress contribution to the crack-driving force is small or negligible compared to the material's fracture resistance. Hence virtually all standards for girth weld defect tolerance in the EPFM or limit-load regions neglect the effect of weld residual stresses.

The following describes how the output from this program affects these different analyses, and then affect the more pertinent girth weld defect tolerance standards.

3.4.1.1 Limit-Load Analysis

A number of limit-load analyses have been developed for girth weld defect tolerance analyses [91, 92, 93, 94]. Of these, the Net-Section-Collapse (NSC) analysis originally developed by Broek in [94] is the most commonly used limit-load solution. This solution is for circumferential cracks in piping under external bending, combined tension and bending (from internal pressure), and was later extended to pure tension [60]. The original work related the applied moment to determine the tolerable flaw size as a function of the material strength called the flow stress. The flow stress was determined from pipe tests and flat-plate tests on very tough materials to be approximately equal to the average of the yield and ultimate strength of the material. The key assumption is that the material is so tough that this flow stress value is reached throughout the pipe cross section as illustrated in Figure 3-63 and the relationship is given in Equation 5-1 (definition of symbols for Equation 3-5 are in Figure 3-63).

$$M_{nsc} = 4\ \sigma_f R_m^2 t\ \{\sin\beta - (a/t)\ [\sin\theta)]/2\} \qquad (3\text{-}5)$$

From the bending moment, one can then determine the bending stress at failure using the elastic definition of bending stress, i.e., $\sigma = M_{nsc}R_m/\pi R_m^3 t$, see Equation 3-6 when the Net-Section-Collapse moment equation is put in terms of stress.

$$\sigma_{nsc} = (4\sigma_f/\pi)\{\sin\beta - (a/t)\ [\sin\theta]/2\} \qquad (3\text{-}6)$$

For a pressurized pipe with a circumferential surface crack subjected to bending, that is, combined pressure and bending, an idealized bending stress was originally assumed in the plane of the crack as shown in Figure 3-63. A free-body analysis shows that the point of stress inversion in this case is

$$\beta = [\pi - (a/t)\theta]/2 - \pi R_i^2 p/(4R_m t\sigma_f) \qquad (3\text{-}7)$$

The end-cap-induced axial stress from pressure in the second term in Eq 3-6 could be replaced by any axial membrane stress contributions. These equations assume that the circumferential crack length, 2θ, is above the neutral axis location (β) in Figure 3-63. The NSC equations and flow stress definition have been validated by hundreds of pipe tests on tougher nuclear piping steels [95] where over 300 circumferentially cracked pipe tests were examined first. The pipes were screened to ensure the toughness was high enough that limit-load should be satisfied, and the statistical relationship of the actual material strengths (yield and ultimate) at the pipe test temperature were related to the flow stress calculated for the qualifying pipe tests. Hence, the NSC analysis and its limits were well qualified in the development of the ASME Section XI pipe flaw evaluation criteria.

In the work by Miller [93], he used the NSC equation, but with the fully plastic definition of the bending stress ($\sigma_{bending} = MR_m/4R_m^3t$) rather than the elastic solution ($\sigma_{bending} = MR_m/\pi R_m^3t$) used in all engineering stress analyses. Hence, the Miller equation differs from the Net-Section-Collapse equation by a factor of $4/\pi$ when talking in terms of bending stress. *This is a subtle but important point as will be shown in the following comparisons to line-pipe experimental data.*

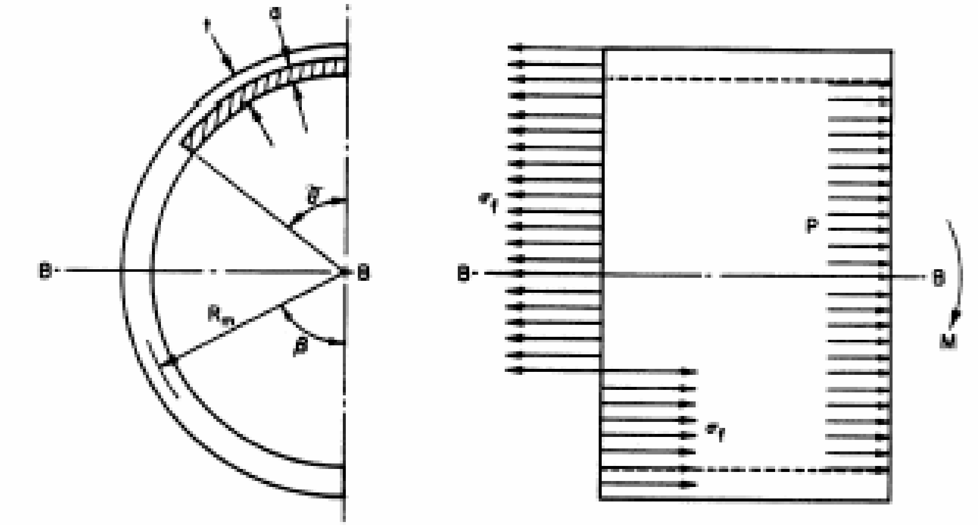

Figure 3-63 Illustration of Net-Section-Collapse assumption of flow stress being reached in the entire pipe cross-section

In a recently completed DOT/PRCI project on development of girth weld defect tolerance approaches [19], a limit-load solution was implemented from work by Wang [96]. This same limit-load equation was implemented into the 2007 API 1104 Appendix A [97]. It was found in Reference 19, that there was a large difference between the limit-load equations validated for mini-wide-plate tests versus that used for pipes in bending, see Figure 3-64. Forty mini-wide plate tests were compared to the flat plate limit-load solution in Reference [19] with the ratio of experimental/predicted stress being 1.07 with a coefficient of variance (standard deviation/mean) of 3 percent. This was excellent agreement. However, when using the Wang-modified/Miller limit-load equation, the experimental/predicted failure stress ratio was 1.43 which was a factor of 1.33 more conservative. Since there are other safety factors used in the API code, it was desirable to eliminate this degree of conservatism.

To investigate these differences, a detailed investigation of the equations and validation data used by Wang was conducted. The initial evaluation was a comparison of limit-load equations using the original Net-Section-Collapse (NSC), Miller's limit-load equation, and Wang's modification to the Miller limit-load equation. These comparisons are graphically shown in Figure 3-65 in the form of predicted bending stress at failure/flow stress versus the normalized crack length (θ/π). There are curves for a/t values of 0.1, 0.3, and 0.5 for each analysis. The NSC analysis gives the highest predicted failure stresses. It always used the elastically calculated bending stress, $\sigma_{bending} = M/(\pi R^2 t)$ as used in virtually all common design stress analyses. Note how the NSC analysis goes towards a value of 4/π (or 1.27) as the crack length goes toward zero, which comes from developing fully plastic stresses in the pipe cross section under bending since β=0 with no crack (see Figure 3-63).

The Miller equation is exactly the same form as the NSC equation, but it used the fully plastic definition of the bending stress, $\sigma_{bending} = M/(4R^2 t)$. This stress definition is not commonly used, but makes the failure stress/flow stress go toward a value of 1.0 as the crack length goes toward zero, see Figure 3-65. This would be the same trend from pure tension loading on a pipe or flat plate.

The Wang modification of the Miller equation has a function that gives a lower predicted failure stress as the crack size increases. It was a curve-fit correction to experimental results. It becomes lower than the Miller equation by a factor of π/4. The Wang modification on the Miller solution is given in the first term in Equation 3-8a. Hence the Wang equation is lower than the Miller equation by π/4 (79%) if fully plastic bending stress definition is used in the Wang equation. If the elastic bending stress is used in the Wang equation, then it is lower by an additional factor of π/4 (a total of 62% of the NSC predicted failure stress).

$$\frac{\sigma_L}{\sigma_f} = \left[\frac{\pi}{4} + 385\left[\left(0.05 - (a/t)(\theta/\pi\right)\right]^{2.5}\right]\left[\cos\left(\frac{(a/t)(\theta/\pi)}{2}\right) - \frac{(a/t)\sin(\theta)}{2}\right] \qquad \text{if } (a/t)(\theta/\pi) < 0.05 \qquad (3\text{-}8a)$$

$$\frac{\sigma_L}{\sigma_f} = \frac{\pi}{4}\left[\cos\left(\frac{(a/t)(\theta/\pi)\pi}{2}\right) - \frac{(a/t)\sin((\theta/\pi)\pi)}{2}\right] \qquad \text{if } (a/t)(\theta/\pi) \geq 0.05 \qquad (3\text{-}8b)$$

A final graphical comparison of the different limit-load solutions is given in Figure 3-66. This graph shows the Miller and Wang-modified/Miller limit-load solutions using failure stress/flow stress versus the cracked area, (a/t)*(θ/π). This cracked-area normalization was used for comparison to experimental results, but yields a unique single curve for all flaw depths only if the (a/t)*(θ/π) value is less than 0.04 for the Wang analysis and less than 0.02 for the Miller analysis. Hence care should be exercised when using this normalizing scheme.

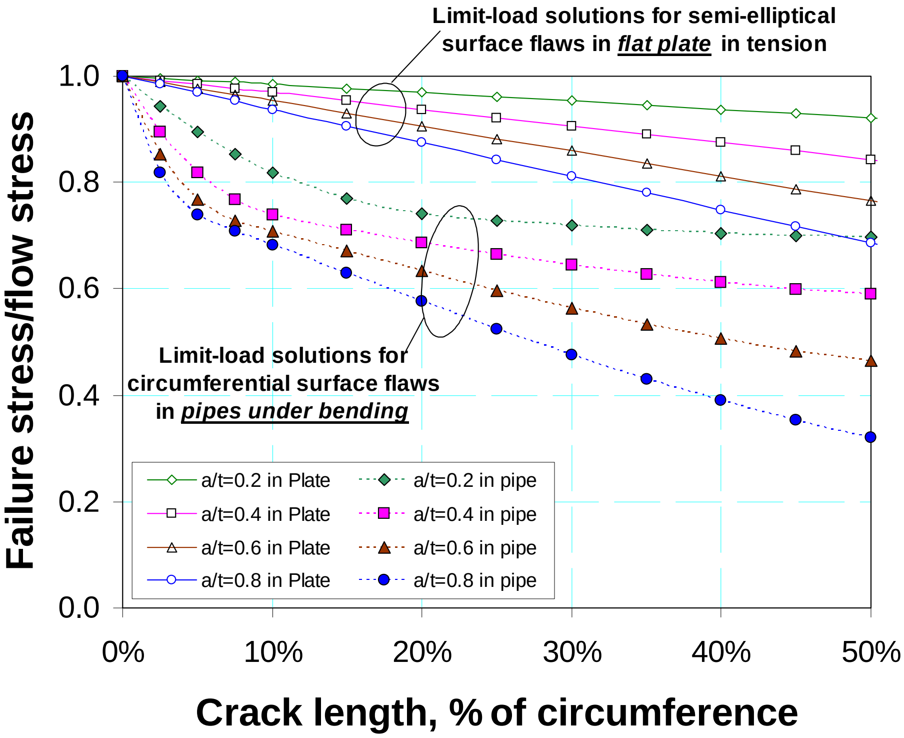

Figure 3-64 Comparison of X100 weld mini-wide plate test results to a flat-plate limit-load solution and the Wang-Modified/Miller pipe bending limit-load solution

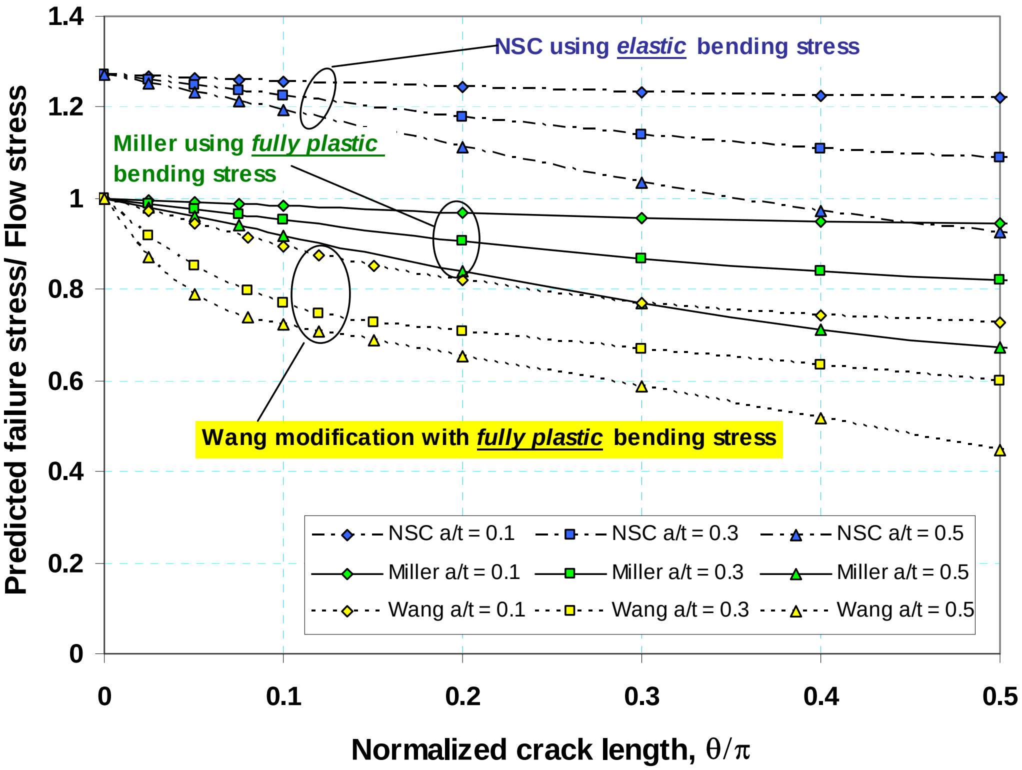

Figure 3-65 Comparison of different limit-load equations

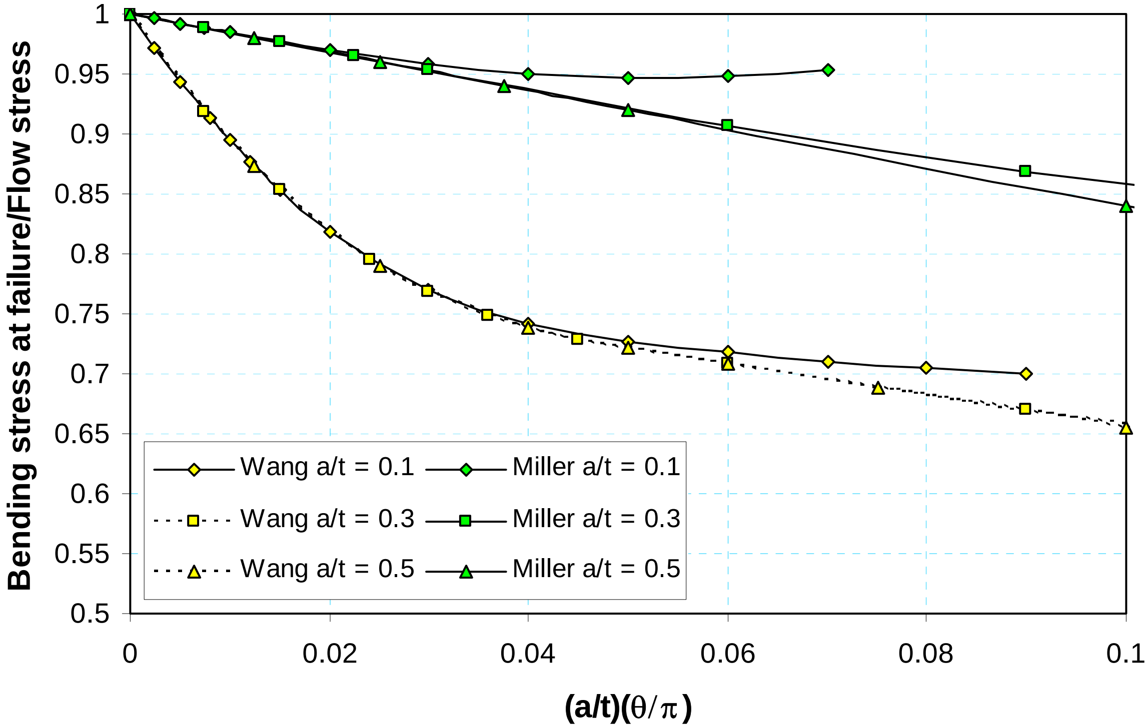

Figure 3-66 Comparison of Wang and Miller limit-load solutions using cracked area for x-axis

Additional comparisons were then made with the original experimental data used by Wang for validation of his modified limit-load solution. The data were pure bending tests (no internal pressure or axial stress) on line pipe with sharp cracks in the center of the girth welds. There were a few line-pipe tests with blunt circumferential flaws that should be at limit-load conditions, see Figure 3-67. The original database was compiled by Rosenfeld [98] for PRCI; additional data were input as part of this project. The final data set included;

- Glover data from Welding Institute of Canada [99,100],
- Erdogen [101],
- Worswick, Pick and Glover [102†],
- Hopkins EPRG tests [103],
- Wilkowski original API validation tests [58], and
- Wilkowski repair groove pipe tests (small and large-diameter pipe tests) [92].

The original reports for each of these data sets were obtained and reviewed to ensure that the starting database from Reference [98] was correct. Some minor changes were needed and those changes were cross checked if there were several publications having the same data reported. Some of the Hopkins, Worswick, and all of the Wilkowski data were added to the database after they were checked for quality assurance.

Figure 3-68 shows the experimental data divided by the predicted data versus the normalized cracked area [(a/t)(θ/π)]. The experimental bending stress at failure was ***elastically*** calculated

---

[†] Note, the official PRCI report for Reference 112 misspelled the names of Worswick and Pick as “Worlock and Piok” on the report cover page.

(not using the Miller fully plastic stress definition). The predicted stress was the Miller limit-load equation. Additionally, the lower red line shows how the Wang-modification would lower the Miller limit-load value. The Wang-modified lower line appears to bound most of the data except three points. However, none of these data were screened to ensure that they truly were limit-load failures. The data points that could be eliminated because they were not limit-load failures or for other reasons are discussed below, (also see Figure 3-68).

- Several of the Hopkins pipe tests were conducted at very low temperatures and had brittle initiation. The reported CTOD values from bend-bar specimen tests were less than 0.001 inch (0.025 mm).
- The Wilkowski repair groove tests included some tests that had a/t values of 0.69 to 0.75. It is well known that the basic NSC equations do not work well for deep flaws [60]. Additionally, the new API 1104 criterion limits flaw sizes to a/t < 0.5. Hence these deep flaw tests were eliminated from the database.
- The 4-inch diameter Wilkowski repair groove tests were on a heavily cold-worked material that had a yield of 94.5 ksi and ultimate of 95 ksi, so that it had very low toughness even with the blunt flaws used and ductile tearing rather than brittle fracture. These pipe tests were eliminated.
- The Wilkowski API girth weld pipe tests had brittle initiation (see discussion in Section 3.3.3.3.1.1), so they were eliminated for not being limit-load failures.
- The pipe tests with crack lengths longer than the limits within the new API 1104 Appendix A criterion were eliminated. The maximum allowable API flaw length is 12.5% of the circumference and the maximum depth is 50% of the thickness, hence $[(a/t)(\theta/\pi)] < 0.0625$. (Note, as shown in Figure 3-66, once $[(a/t)(\theta/\pi)] > 0.05$ then the failure stress curves for different a/t values diverge from a single common curve.)
- There are additional data from Glover and Worswick that also are less than limit-load cases.
    - 11 of the Glover tests had a/t values of 0.53 to 0.83 and one was a through-wall flaw. These were eliminated because of the API flaw depth restriction.
    - 7 of the Glover tests had CTOD values of 0.002 or 0.003 inch (0.051 mm or 0.076 mm), which is below the limits that can be used for the API Option 1 EPFM allowable flaw chart. Hence these are clearly not limit-load failures.
    - Out of the remaining Glover test data, all but one had CTOD values from bend specimen tests of 0.004 inch (0.102 mm). This toughness level is at the very bottom of the acceptable range for the EPFM analysis acceptable by the new API 1104 Appendix A Option 1 imperfection limit curve (Figure A-8 of the API 1104 Appendix A). Hence there really was only one Glover data point with a CTOD of 0.009 inch (0.229 mm) that may satisfy limit-load conditions. (In reality, some of those tests were done with natural defects that were not always sharp cracks, and the effective toughness from the blunter crack would be higher and they may reach limit-load conditions. However, there was not sufficient documentation in the reports reviewed to say what the notch acuity was and how to account for the effective toughness, see later discussion in this report on notch acuity effects on toughness).
    - For the Worswick data, one smaller flaw test buckled, while the others failed but had CTOD values of 0.004 inch (0.102 mm). Those data points could be eliminated, but in the interest of checking the API Option 1 EPFM versus limit-load procedures, it was found that the EPFM correction would be a factor of 1.06 and 1.08 for the two

> tests where fracture occurred. In those tests, strains were measured and stresses were calculated. Two of the tests had stresses and strains that were in good agreement with the base metal stress-strain curve. The third test was significantly out of line with the stress-strain curve, and was low by a factor of 1.12. These corrections were applied to the Worswick EPFM data to see where they would have fallen as limit-load corrected values, see Figure 3-69.

Using only the valid limit-load test data shows how the different limit-load expressions compare. The constant Y-axis value of 1.0 means there would be perfect agreement with the Miller limit-load equation. The constant Y-axis value of 1.27 (4/π) would give perfect agreement with the Net-Section-Collapse equation. The lower solid red curve would be perfect agreement with the Wang-modified/Miller equation, and finally the Wang modification was also shown as applied to the Net-Section-Collapse analysis.

First it is important to note that *the experimental stresses were the elastically calculated bending stresses at failure*. The Miller equation is actually for fully plastic bending stresses, whereas the Net-Section-Collapse equation uses the elastic bending stresses (same as the experimental data). Note that the Miller fully plastic bending stresses will always be larger than the elastic bending stress. Hence it is really more appropriate to compare the test data to the NSC relationship. Interestingly, what can be seen is that the Wang-modification could be applied to the NSC relationship and gives an excellent bound to the "valid" limit-load data. Hence the limit-load expression in the new API 1104 Appendix A criterion is conservative by a factor of 1.27 (4/π). This degree of conservatism explains why the mini-wide-plate tests were conservative by a factor of 1.33 on the average compared to the proper limit-load expression for a surface crack in a flat plate being conservative by a factor of 1.06. By not qualifying which data were valid limit-load tests, the Wang-modified/Miller limit-load expression actually bounds all the test data with CTOD ≥ 0.002 inch, and thereby also overcorrects in applying an EPFM correction using that limit-load expression.

Using the Wang modification on the Net-Section-Collapse equation will make it much easier for high-strength steel pipelines to have more tolerable imperfection limits. Section 5.1.2 further discusses how this factor of 4/π significantly changes the calculated imperfection sizes relative to the API workmanship flaw sizes for different grade pipes.

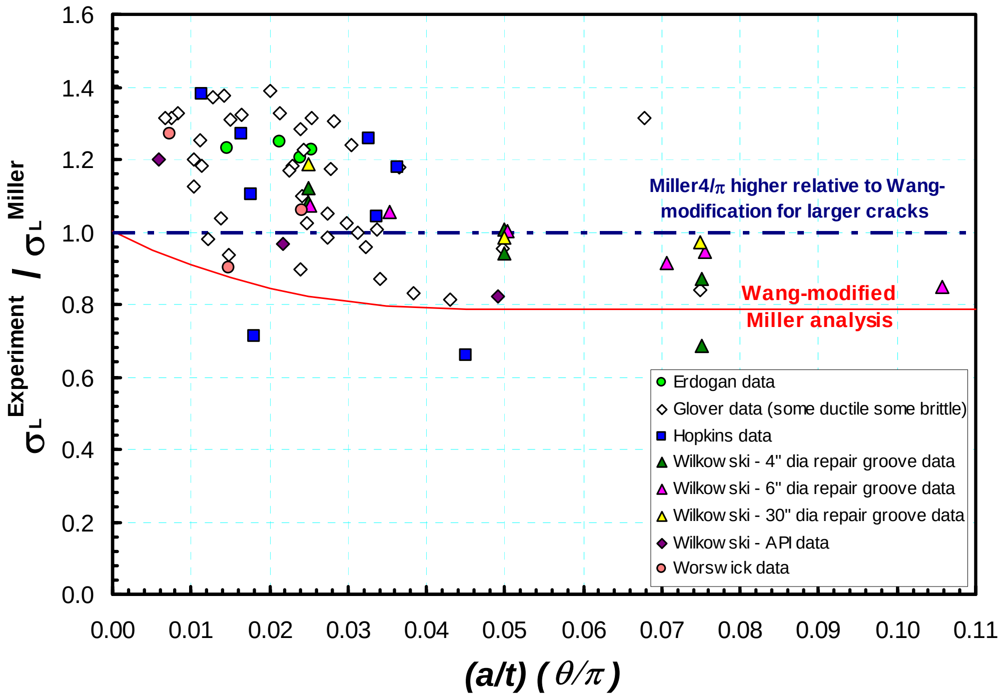

Figure 3-67 **Comparisons of unpressurized line-pipe bending tests (no internal pressure) to Wang-modified Miller equation and original NSC equation**

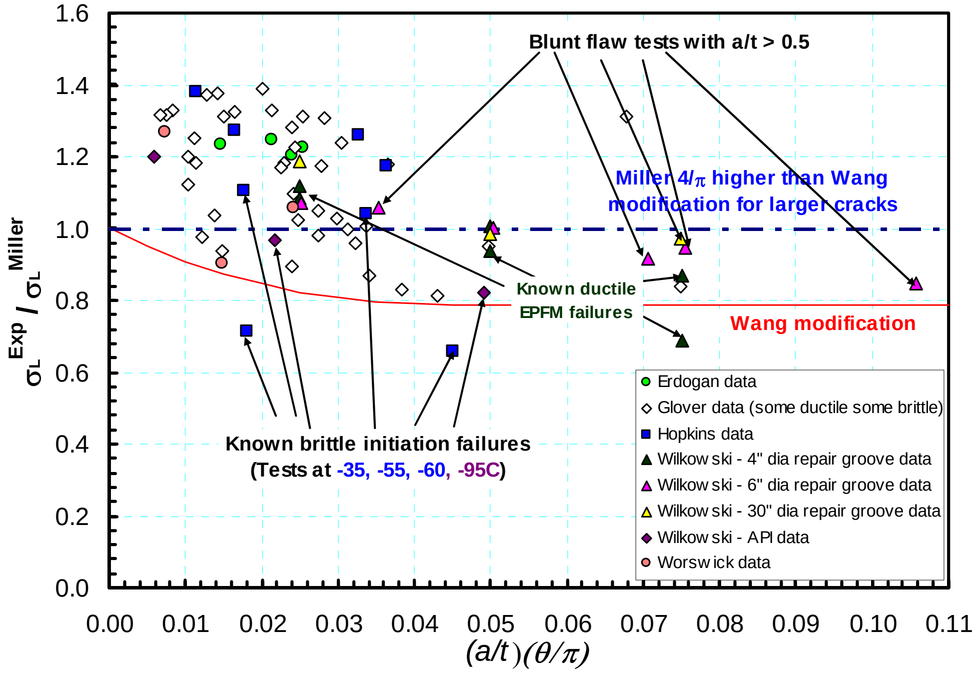

Figure 3-68 **Illustration of invalid limit-load data points from Hopkins and Wilkowski data (Note; virtually all the Glover data were not valid limit-load cases, as well as some of the Worswick tests.)**

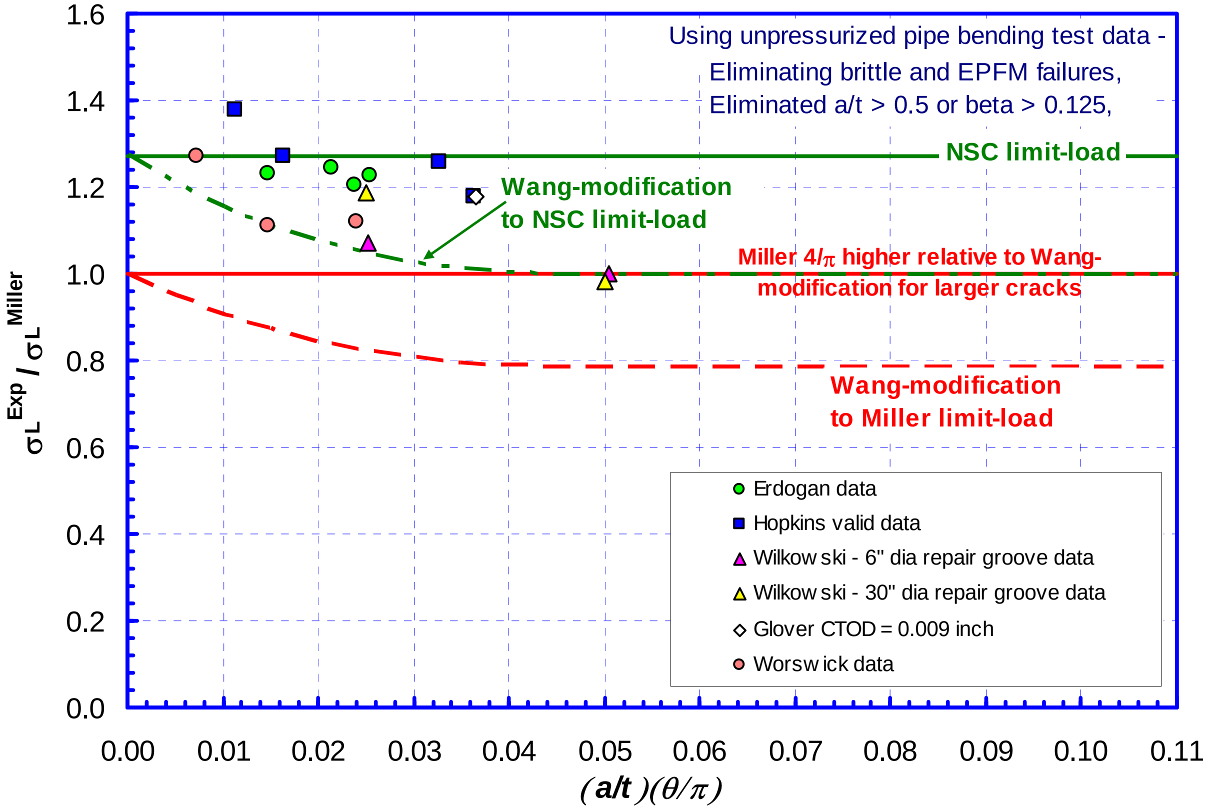

Figure 3-69 Comparison of valid limit-load test data to various limit-load equations

3.4.1.2 Elastic-Plastic Fracture Mechanics Analyses

Elastic-plastic fracture mechanics analyses can be conducted in a number of ways. A common but detailed analysis involves using a failure assessment diagram or FAD analysis. The FAD analysis is used in many pipe girth weld defect tolerance analyses, i.e., R6, Section XI of the ASME Boiler and Pressure Vessel Code, API 579, etc. It was also implemented recently into the 2007 API 1104 Appendix A approach. In the FAD approach, there is a curve that allows interpolation between a pure linear elastic solution and the limit-load solution. However, as was shown in Section 3.4.1.1, the API 1104 Appendix A limit-load solution is conservative by a factor of 1.27 (4/π). By not qualifying which data were "valid" limit-load tests, the Wang-modified/Miller limit-load expression actually bounded all the test data with CTOD ≥ 0.004 inch, and thereby also overcorrects in applying an EPFM correction using that limit-load expression, see Figure 3-70. FAD approach could be revalidated using the proper limit-load equation since the EPFM correction in API-1104 Appendix A is applied to the conservative Wang-Modified/Miller limit-load equation.

Another aspect in the EPFM analyses is the question of the validity of using CTOD bend specimen data to represent the toughness of a surface crack in a pipe. The difference is attributed to a factor called constraint, where the bend specimen has a gradient of tension to compression in the ligament, while the ligament in the surface crack is completely in tension. This constraint difference affects the upper-shelf toughness, as well as the brittle-to-ductile transition temperature. In Reference [19], it was suggested that the low-constraint CTOD value that is more appropriate for a surface crack in a pipe is 3 times the minimum value or 2 times the average value. For nuclear piping steels, this difference was up to a factor of 4 [104], while other test data on line-pipe base metals showed differences of 4 to 7 between standard bend-specimen CTOD values (a/w = 0.5) and SENT specimens (a/w of (0.15 and 0.5) [61]. Work at DNV [50] has shown that the SENT specimen had a CTOD of about 4 times larger than the bend-bar specimen. Hence the API recommendation of using a factor of 2 to 3 should be conservative.

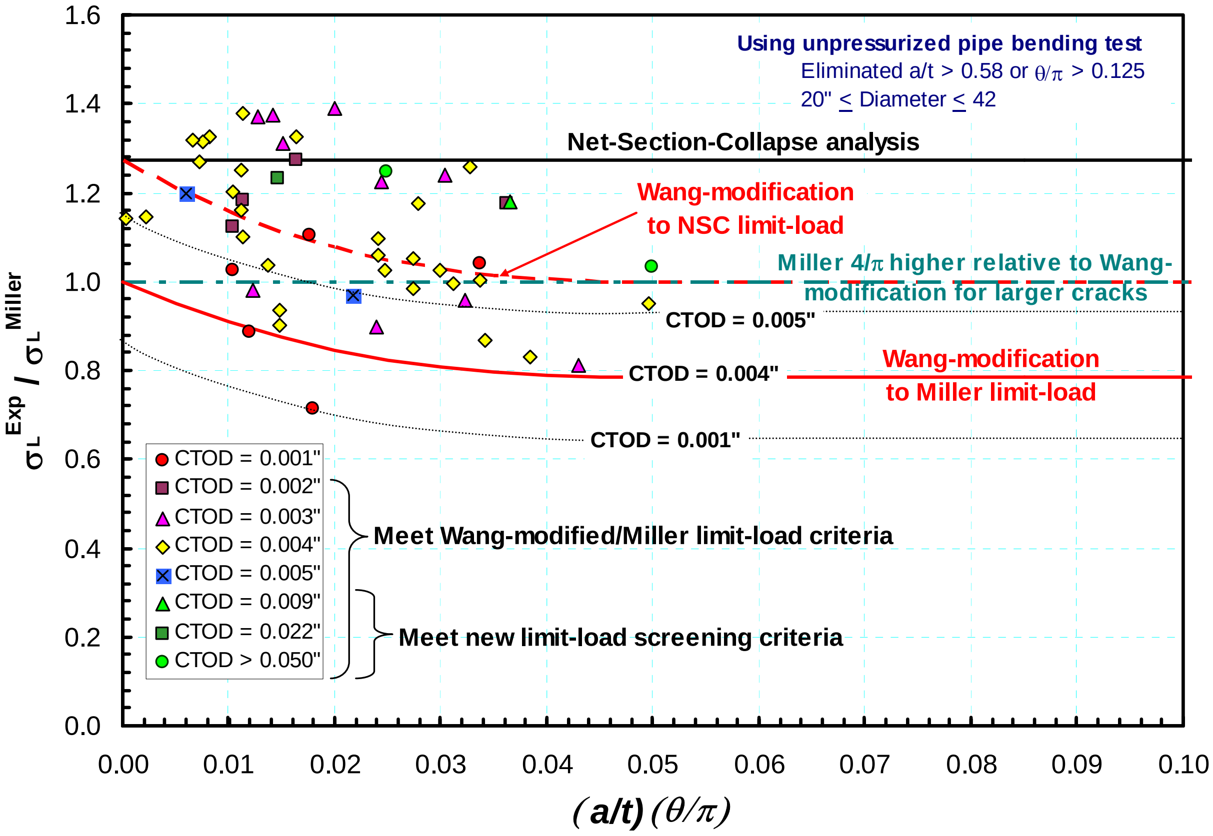

Figure 3-70 Comparisons of test data sorted by CTOD value from bend specimens to various limit-load equations

3.4.1.3 LEFM Analyses

Generally materials that fail in the Linear-Elastic Fracture Mechanics (LEFM) regime are considered rejectable since the material would be brittle. A question is how to properly judge if a material will be brittle or not. It is desired to be conservative on this aspect, but not too conservative. The existing codes and standards use bend-specimen tests and sometimes Charpy tests. Both are suggested in the 2007 API 1104 Appendix A procedure.

A series of Charpy, CTOD bend-bar, and SENT tests were conducted to assess the FITT Master Curve for the X100 weld in this program. Comparisons to the past API girth weld validation tests on X60 pipe were also made. The results were given in Section 3.3.3.3.1.2. These tests were the first results that involved comparisons between fracture tests on line-pipe girth welds and the FITT Master Curve approach [55]. The results are highly encouraging in that the X100 Charpy, bend-bar CTOD tests, and SENT transition temperatures all correlate well as predicted from the base-material correlations. All of the prior results for the development of the FITT Master Curve were performed on lower-strength line-pipe steels, and generally with cracks in the base metals.

In the pipe configuration, there are also much higher weld residual stresses than in specimen tests. Most of those stresses are relaxed when the test specimens are cut from a girth weld. The weld residual stresses increase the constraint that in turn could raise the brittle-to-ductile transition temperature. The comparison between the FITT Master Curve using the Charpy transition temperature for the weld metal and the original X60 API validation girth weld fracture tests were encouraging in that they correctly predicted brittle fracture initiation in those tests. Unfortunately there were no girth weld tests at warmer temperatures in that API validation program to obtain the full-scale transition temperature relative to the predicted FITT. Other data exist in the literature, but comparisons to those results have not been made yet since additional unpublished results are needed.

With further validation, the FITT Master Curve could be used in codes and standards for girth weld defect tolerance. For instance, the recent API 1104 Appendix A criterion recommends that Charpy tests on the weld metal should be conducted at the minimum operating temperature and that there should be a 50-percent or greater shear area in the fracture surface. For the X100 weld examined in this effort, the Charpy 50% shear area requirement is met at -60 C (see Figure 3-42a). Interestingly, the CTOD transition temperature from bend-bar tests was also -60 C (see Figure 3-42b). The SENT results showed this weld metal would have ductile initiation behavior between -85C and -95C, which agreed well with the FITT Master Curve prediction of -90 C (using the Charpy 85% shear area transition temperature). Hence this weld could be used at a lower temperature than the current API 1104 Appendix A and still have ductile initiation behavior for *stress-based* design analyses.

For *strain-based* design, the minimum temperature should be slightly above the FITT since some ductile tearing through the thickness is needed to have the margins for strain capacity. Figure 3-44, shows that fully ductile stable tearing could be achieved at -85 C for the same X100 weld (evident from the slow drop in the load-displacement curves).

Another consideration in pipeline design, which is key in nuclear piping, might be to ensure leak versus break behavior. In such analyses, one needs to understand the consequence of the entire pipe fracture event. As an example, if the material was just operating at the FITT temperature for a surface crack, then it would have good load-carrying capacity from a stress-based design, but once the surface crack propagates through the thickness, it could transition to a through-wall crack with brittle behavior and the pipe might completely break in two pieces. If the material was well above the FITT temperature, then the surface crack might transition to a ductile through-wall crack. The continued propagation of the through-wall crack would depend on the energy supplied by the pipe system relative to the energy absorbed by the fracture process. If the pipe is loaded in displacement-controlled bending (i.e., frost heave), then it is possible that only a large leak could develop rather than a full line break. If the pipe stresses were more load-controlled (i.e., offshore pipe laying), then the pipe is more likely to have a full break. This leak versus break behavior of piping under any combination of load-controlled stresses and displacement-controlled stresses is a relatively mature analysis procedure from work done on nuclear piping [60, 105].

Finally, the FITT Master Curve also supplies a basis for accounting for differences in thickness on the transition temperatures for specimens machined from pipes, versus the transition temperature for the actual pipe thickness.

From these results it is seen that the FITT Master Curve correlations worked well for the X100 weld metal specimens. These are encouraging results suggesting that the FITT Master Curve approach is applicable to high-strength weld metals as well as base metals. Additional testing and comparisons on other welds metals would give greater confidence in this approach. Another important aspect that should be validated is how the FITT Master Curve method works for pipe tests conducted at a series of different temperatures, since the weld residual stresses might increase the constraint, which in turn could make the full-scale FITT occur at higher values. The FITT Master Curve properly bounded the older API validation X60 pipe full-scale girth weld crack brittle behavior, but tests at warmer temperatures are needed to ensure the FITT was not significantly affected by the constraint from weld residual stresses.

3.4.2 Strain-Based Design Criteria

The development and validation of strain-based design criteria is currently under study. One of the aspects of interest is validation of criteria using experimental test data. In Reference [19], the mini-wide plate tests described in Section 3.3.3.2 were used to assess what the strain limits would be to insure safe pipeline operation. One of the difficulties in using mini-wide-plate tests is that the specimen size is small compared to that same flaw size in a large diameter pipe. Hence, one needs to scale the wide-plate tests results relative to the flaw size of interest in the pipe. That was addressed in Reference [19], but is an important aspect frequently overlooked and still needs additional validation.

3.4.2.1 Considerations in Validation of Strain-Based Criteria

Frequently wide-plate or pipe validation tests are conducted with sharp notches (i.e., EDM notches with a width on the order of 0.254 mm, (0.010 inch) rather than actual sharp cracks. As was discussed in Section 3.3.3.3.2, the notch acuity increases the apparent toughness of the material. SENT and bend-specimen tests were done on the X100 weld using the same notch acuity as in the mini-wide-plate test (EDM notches with 0.127 mm, 0.005 inch, radius at the notch tips). Those results showed that the CTOD at crack initiation was a factor of about 1.3 higher in the EDM notch specimens than in the fatigue-precracked specimens. This notch-acuity-correction factor was lower than a larger series of CT specimen tests with fatigue-precracked and very similar EDM notches in nuclear pipe steels where the EDM notch initiation toughness (based on J_{Ic}) was higher by a factor of 1.7 than the sharp fatigue crack. For a given material, there is a relationship between J and CTOD but it is not linear even in the elastic regime. Hence the 1.7 for J being larger than the 1.3 ratio for CTOD is expected (Figure 3-47).

To see how significant the correction factor of 1.3 on the CTOD is for the mini-wide-plate tests, a separate evaluation was conducted. The maximum stress and strain at failure in the mini-wide plate tests were determined with the reduction of 1.3 on the CTOD from the EDM-notched specimen to estimate the behavior of an identical fatigue-precracked specimen. This was done using the following four figures for one of the typical mini-wide plate tests described in Section 3.3.3.2. Figure 3-71 shows data from a typical mini-wide plate test, i.e., load versus ram displacement and crack-mouth-opening displacement (LVDT5) versus ram displacement. The red-dashed line shows how a stationary crack would behave, and the experimental deviation from that behavior determines when the EDM flaw in that test initiated. Figure 3-72 shows the crack-mouth-opening displacement (LVDT5) and CTOD (from FEA) versus the remote strain (LVDT3). This figure shows that the EDM-notched specimen initiated with a CTOD of 0.045 mm and the strain was 5.3 percent. From the SENT tests in this project, a fatigue crack would have an initiation toughness of 1.3 lower or a CTOD = 0.035 mm. This CTOD value corresponds to a strain of ~4.1 percent. The ratio of 5.3% to 4.1% is 1.3. Since strain is roughly linear with CTOD, this analysis confirmed the correction factor proposed.

Finally, Figure 3-73 illustrates the differences in the loads at crack initiation between the EDM notch and fatigue-cracked specimens. From Figure 3-71 it was shown that the CMOD (LVDT5) for the fatigue crack should be 0.074 mm at crack initiation. Using that value in Figure 3-72 gives a load at crack initiation that is extremely close to that for the EDM notch, i.e., 98 percent of the load at crack initiation in the EDM notch case. Since these mini-wide-plate tests agree extremely well with the limit-load predictions (using the proper limit-load equations for a surface crack in a flat plate), that means that slight changes in the toughness will not affect the failure loads much. These are also consistent results.

The conclusion from this work is that care needs to be made in using sharp-machined notch (EDM) plate or pipe test results for validation of failure criteria. For the surface-cracked mini-wide-plate tests on the X70 and X100 welds in this program, the toughness was sufficiently high that limit-load should be *valid for stress-based* failure criteria validation. However, the remote strain is approximately linear with CTOD, and if the EDM notch gives a higher CTOD than a fatigue precrack, *the fatigue versus EDM-notch toughness ratio will linearly affect the strain capacity of a fatigue-cracked specimen for validation of strain-based criteria*.

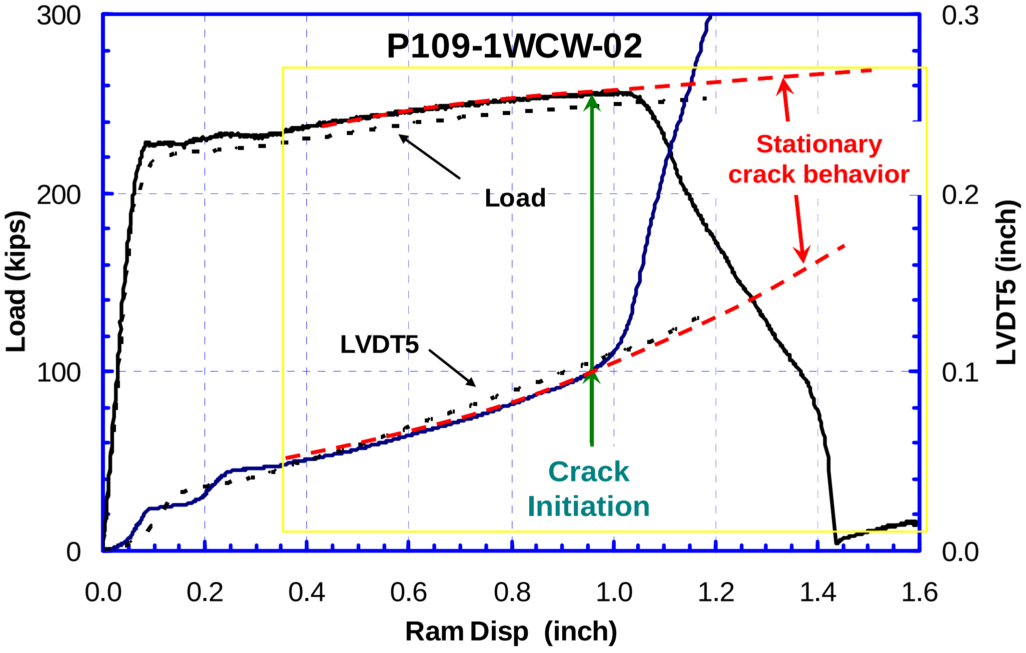

Figure 3-71 Determination of crack initiation for an EDM notch in a mini-wide-plate test

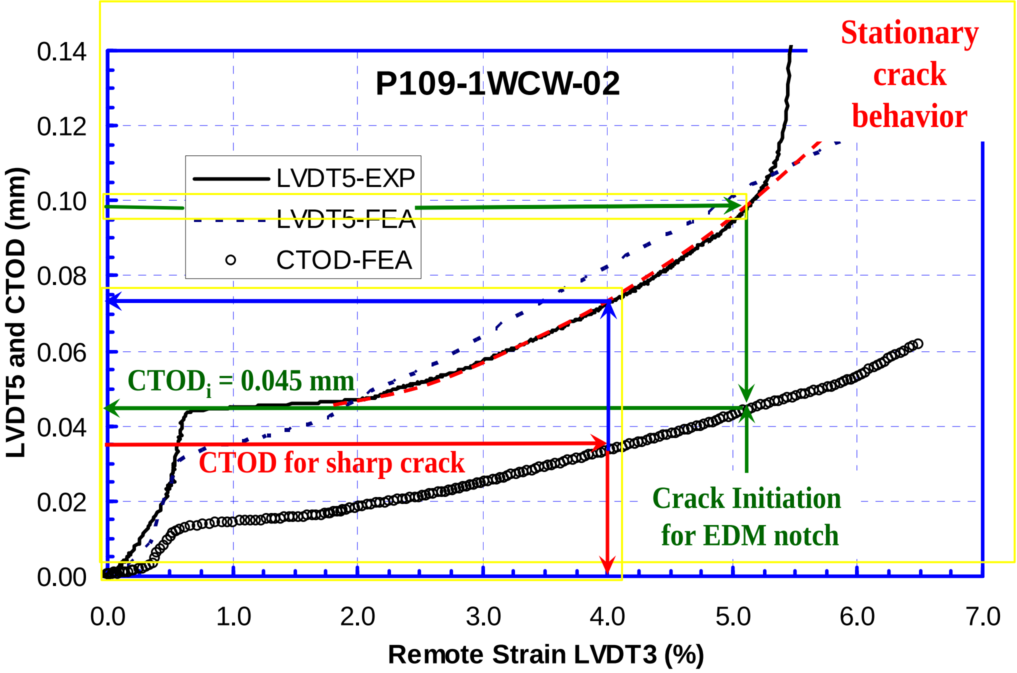

Figure 3-72 Mini-wide-plate data and FEA analyses results used to illustrate strains at crack initiation for fatigue crack versus sharp-machined notch that has initiation toughness higher than fatigue crack by factor of 1.3

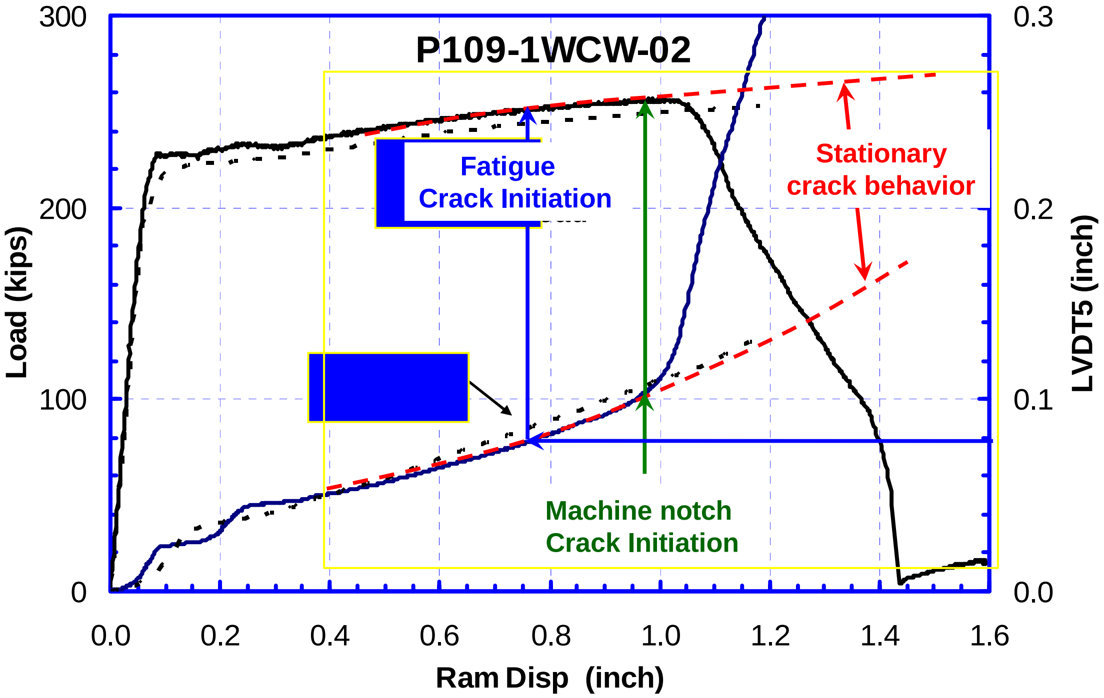

Figure 3-73 Mini-wide-plate data used to illustrate change in initiation loads for fatigue crack versus sharp-machined notch that has initiation toughness higher than fatigue crack by factor of 1.3

This effect of the notch acuity reducing the strain capacity between an EDM notch and fatigue-cracked specimen test applies to the strain-based analyses conducted in Reference 19 for the mini-wide-plate tests conducted described in Section 3.3.3.2. In that analysis, it was strongly pointed out that it is important to consider the scaling of the flaw length in the wide-plate test to the flaw in the full pipe circumference. The strain capacities for flaws that were 5-percent of the pipe or plate width were then given for the X70 (see Figure 3-74) and X100 (see Figure 3-75) welds. With the reduction factor of 1.3 on the CTOD from the EDM to a fatigue crack, the estimated drop in the strain capacity for the flaws 5 percent of the circumferences went to 6.85% strain for the X70 welds and 5.15% strain for the X100 welds. Of course conducting those same mini-wide plate tests with the fatigue-precracked flaws would be the ultimate proof of this prediction.

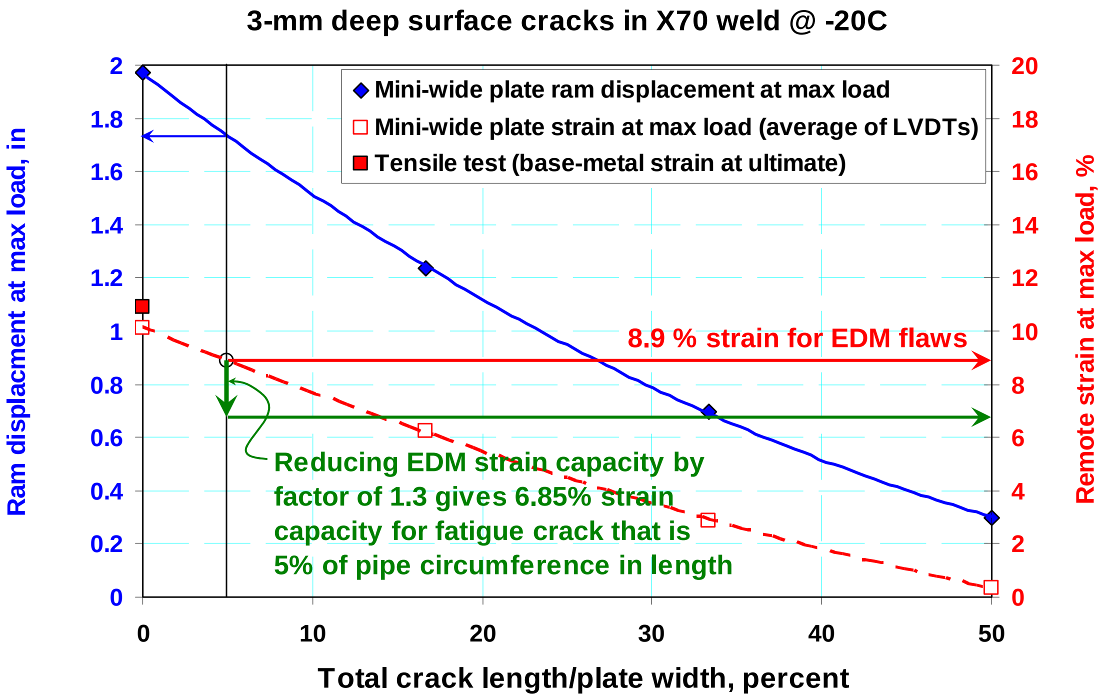

Figure 3-74 Effect of fatigue crack on strain capacity of X70 weld mini-wide-plate tests with a crack length of 5 percent of the pipe circumference or plate width

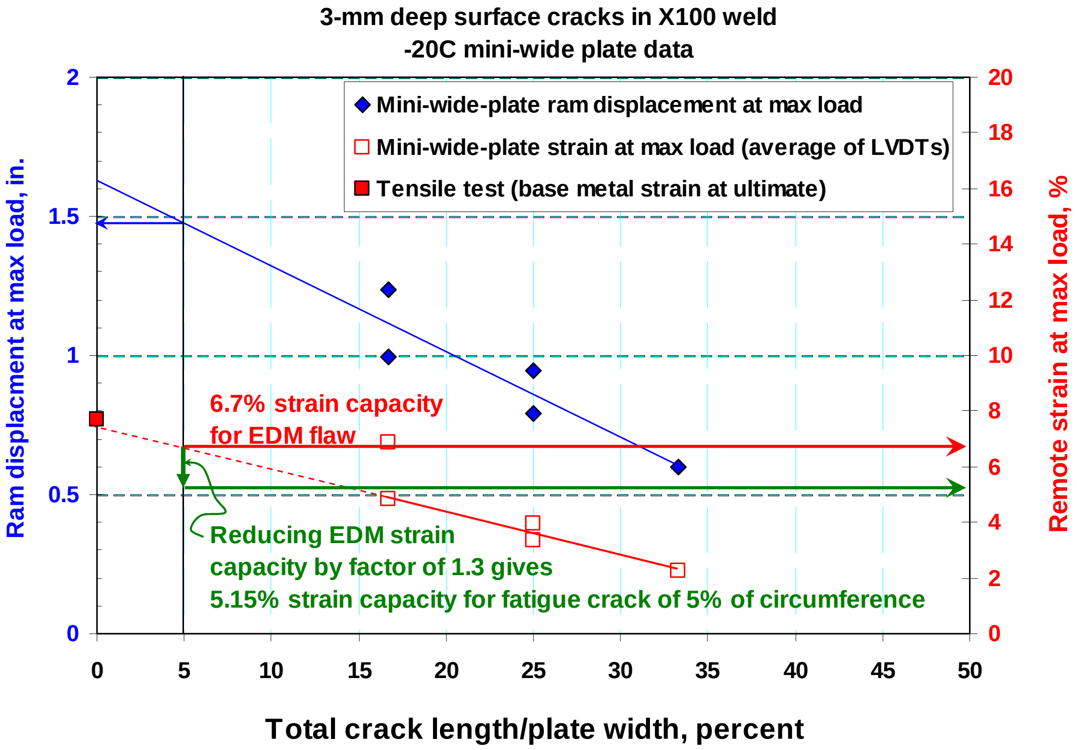

Figure 3-75 Effect of fatigue crack on strain capacity of X100 weld mini-wide-plate tests with a crack length of 5 percent of the pipe circumference or plate width

3.4.2.2 Hoop Stress Effects on Strain-Based Criteria

During the course of this project, it was determined that hoop stress can increase the crack-driving force for a pipe with a circumferential surface crack and the pipe under longitudinal loading [106]. This work showed that the crack-driving force increased as a function of the hoop stress, with the maximum effect occurring with hoop stress values between 60 and 80% of the yield strength. Interestingly, with the hoop stress at 100% of yield the magnification of the crack-driving force over unpressurized pipe was less than at 60 to 80% of yield. For lower grade pipe (X52) there is not much change with hoop stress values between 40 to 100% of yield, but the increased driving force (in terms of CTOD) was increased by 50 to 100 percent over the unpressurized cases with some sensitivity to flaw size. For the higher grade steel (X100), the hoop stress increased the crack-driving force by a factor of 100 to 300 percent over the unpressurized pipe cases, again with some sensitivity to surface flaw size.

The earlier work in this project [106] did not explicitly say in the published technical paper if the internal, pressure was also applied to the crack faces. An additional sensitivity calculation was conducted for one of those cases to examine the effect of crack-face pressure, see Figure 3-76 and Figure 3-77 as compared to Figure 2 of Reference 106. These results showed that there was negligible effect of the crack-face pressure on the increased crack-driving force from the internal pressure for this crack size. These results mean that the increased crack-driving force effects should also be applicable to buried and external surface cracks.

The results show that the crack-driving force, measured as CTOD toughness, increases with internal pressure at a given axial strain. This effect is not the same for stress based design where crack-driving force decreases with internal pressure compared to no pressure [107] and shows that strain-based and stress-based design have additional considerations between the two approaches. The reason for this can be explained in terms of the plastic-zone size at the crack tip. For the case considered in Figure 3-76 (X100 pipe, geometry and circumferential crack size listed in the figure), the CTOD values at a strain of 0.015 (1.5%) are 0.3 mm for the no pressure case and 0.7 mm for the pressure case (more than a factor of two). The corresponding far-field axial stress for these two cases is 749 MPa and 866 MPa for the no pressure and pressure cases, respectively. For the internal pressure case, the plastic zone size for the same value of far-field stress is much smaller. Figure 3-76(a) shows the plastic-zone size contours at the deepest point of the circumferential crack and the corresponding crack opening profile for an applied strain value of 1.5%. Figure 3-76(b) shows the same plastic-zone contour plot for the pressure case. While the far-field applied strains are identical for these two cases, the far-field loads are quite different ($\sigma = 750$ MPa for no pressure and $\sigma = 866$ MPa for the pressure case). Figure 3-76(c) shows the plastic-zone size contours for the pressure case at the same level of far-field stress (the far-field strain for this case is only 0.3%). For a strain-controlled loading, the corresponding far-field applied stress depends on the amount of crack-tip plasticity. The elastic case (no plasticity) will obviously produce the largest far-field applied stress. Comparing Figure 3-76(a) and (c), which have the same far-field stress applied, shows that the plastic zone for the no pressure case is much larger. This is due to the multi-axial nature of plasticity theory based on Von Mises stress. The pressure case has more constraint (in the form of higher hydrostatic stress) and hence, less plasticity. As illustrated in Figure 3-76(b), by the time the strain reaches 1.5%, the stress has reached 866 MPa. Recall that the CTOD is proportional to load to the ‘nth’ power, where "n" is the strain-hardening exponent, which is about 7.4 for X100 steel. This is the reason that pressure increases the CTOD-based crack-driving force for identical far-field applied strain. Reference [106] showed that for applied pressure producing a hoop stress greater than 0.6 SMYS, the CTOD decreases compared to this case (but is still higher than the no pressure case). The reason for this decrease in strain capacity as the pressure increases further is related to the Von Mises effective flow stress changes, and is the subject of other programs.

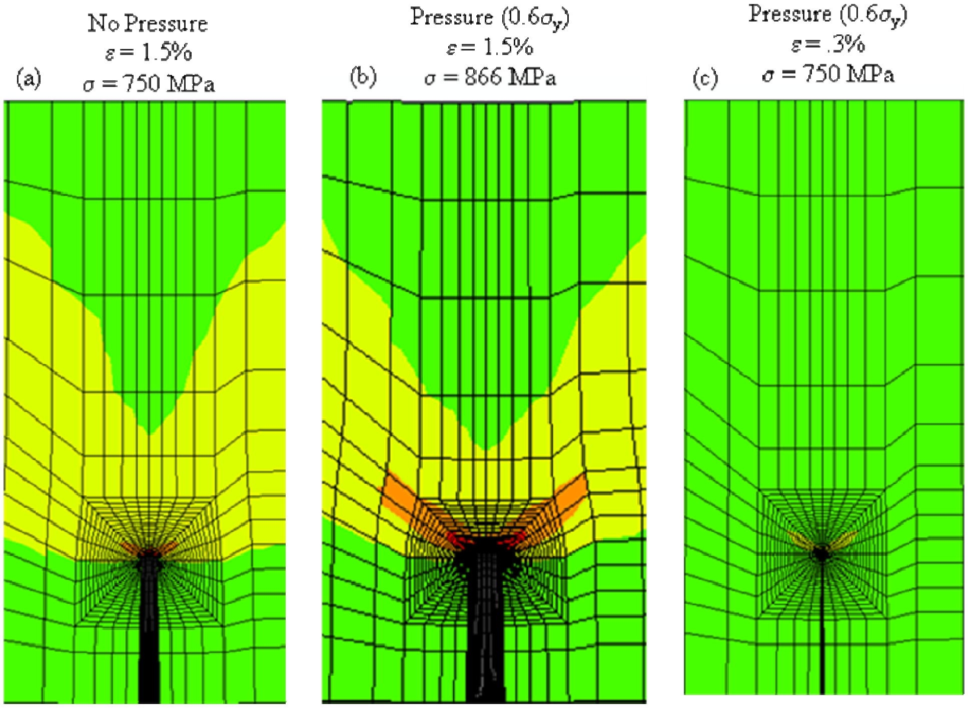

Figure 3-76 Plastic-zone sizes for pressure versus no pressure cases for applied strain to pipe

In terms of the significance to stress-based analyses, if the flawed-pipe situation is close to being a limit-load failure, then the increase in the CTOD-driving force is not very important. In fact from full-scale pipe tests conducted for the nuclear industry by Emc^2 staff, it was found that pipe tests with pressure plus bending were frequently more conservatively predicted than the bending only tests with similar flaws when using a number of different EPFM analyses [108]. This increase in load-capacity under combined hoop-stress and bending implied there are benefits to stress-based criteria, since the limit-load analyses were validated on bending only tests. The combined hoop-stress and bending stress gives an effective higher flow stress for the material, which is not currently considered in any code or standard flow acceptance criteria. Additionally, aluminum pipe tests with and without pressure and having similar lack of penetration (root) flaws had very similar remote failure strains of 1.7% without pressure and 1.6% with internal pressure [109].

To roughly assess the affects of the hoop stress on the strain capacity, one could take the approximate factor of 2 on the increased CTOD, and since strain is roughly linear with CTOD, the strain capacity would drop by that factor. Looking at the mini-wide-plate examples in Figure 3-74 and Figure 3-75, the actual tests with the EDM notches could be used to determine that a crack with length of 5% of the circumference would have a strain capacity in X70 and X100 pipes of 8.9 and 6.7 percent, respectively. Correcting for the notch acuity effects (factor of ~1.3) on a fatigue crack in the X70 and X100 welds gives strain capacities of 6.85 and 5.15 percent, respectively. Using an approximate factor of 2 for hoop stress[‡] on increasing the crack-driving force, the resulting strain capacities for the X70 and X100 welds would be 3.43 percent and 2.57 percent, respectively. To further explore these effects of hoop stress on the crack-driving force, there are on-going programs funded by PRCI and the US DOT [110].

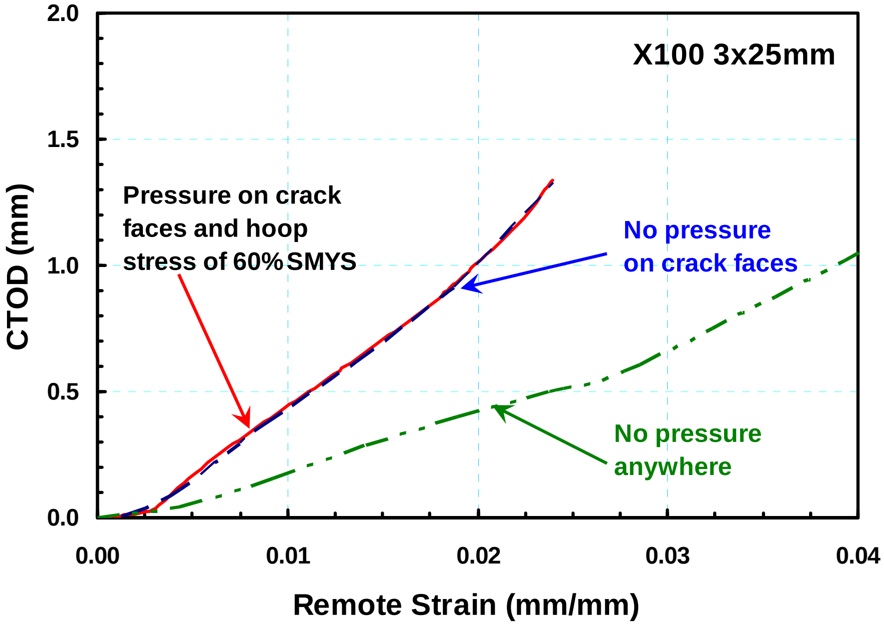

Figure 3-77 FEA analyses showing that the effects of crack-face pressure were not significant for the 36" diameter by 12.7-mm thick X100 pipe with a 3-mm deep and 25-mm long flaw

3.4.2.3 HAZ Softening Effects on Strain-Based Criteria

An additional concern for girth weld defect assessment is the effect of HAZ softening on the crack-driving force. High-grade steels like X100 are more prone to HAZ softening. The weld process microstructure modeling discussed in Section 3.2 describes methods to predict the hardness and microstructure in the HAZ. The empirical Kirkaldy or the more fundamental StructureR codes were used to make blind predictions of microstructures and hardness values in lower and higher grade line-pipe steels. Kirkaldy tended to over predict the HAZ hardness, while StructureR underpredicted it in the blind analyses using the same prior austenite grain sizes. There was also considerable sensitivity to how the austenite grain growth modeling was done, and if one knows the results ahead of time those parameters could be tweaked to get the right answer. Future work on the austenitic grain growth modeling is underway through a PhD dissertation effort as a result of the efforts in this project. Hence at this time, both the Kirkaldy and StructureR microstructure analyses should be conducted to bound the magnitude of the HAZ softening.

[‡] The hoop stress magnification factor on the CTOD-driving force should be less for the higher strain-hardening X70 steel than the X100 steel, but also depends on flaw size and hoop stress level.

From the efforts in [106] in this project, it was also shown that if there is a flaw in a softer HAZ, then the crack-driving force is further increased even with the hoop stress effects. When having a HAZ with a 15% lower stress-strain curve, the crack-driving force increased by a factor of 10 to 25 percent, depending on the hoop stress level and flaw size. As a cumulative effect with hoop stress this is an important aspect, but by itself it is not as important as the hoop stress effect.

Using the mini-wide-plate data discussed in the prior section, if there was a flaw in the HAZ softened region, and the region had the degree of softening in these example cases, then the strain capacity of the HAZ might be 15% lower than after the correction for the notch acuity and hoop stress. However, the X70 and X100 HAZ toughness from the standard CTOD bend specimens had slightly higher values than the weld metal. The HAZ mini-wide plate tests also performed better in terms of failure stress and failure strain than the weld metal tests, hence we conclude that the softened HAZ correction factor on the strain capacity can be less important once all the factors are considered.

3.4.3 Code Implications

Some of the work in this project has direct implications to codes and standards for pipeline design and evaluation. Of particular note is the API Standard 1104 on “Welding of Pipelines and Related Facilities”. Earlier work by Emc^2 staff led to the change in the “Alternative Acceptance Standards for Girth Welds”. The July 2007 edition includes a new Appendix A for the alternative acceptance standards for girth welds. There is an Option 1 approach with prescribed imperfection limit graphs, see Figure 3-78 [97]. There is also an Option 2 approach that is a more detailed Failure Analysis Diagram (FAD), which is much more detailed analysis.

Both the Option 1 and Option 2 approaches used the Wang-modified limit-load approach. As shown in detail in Section 3.4.1.1 of this report, there is an over conservatism in the Wang-modified/Miller limit-load solutions, which affects both the Option 1 and Option 2 approaches. That degree of conservatism came about because the experimental data used to establish the Wang-modified limit-load analysis included pipe tests that actually had CTOD values down to 0.051 mm (0.002 inch) which was a low enough toughness so that many of the pipe tests used were really EPFM failures, rather than limit-load failures.

3.4.3.1 Effect of Over Conservatism on Workmanship Flaw Sizes

The magnitude of the over conservatism in the 2007 API 1104 limit-load solutions was shown earlier to be a factor of $4/\pi$ (1.27) on the failure stress, which is a significant factor. To further assess the significance of this change, graphs similar to the current Option 1 graphs were created and comparisons were made to the workmanship imperfection acceptance standard in Section 9 of the main body of API 1104, see Figure 3-79a. For the workmanship flaw standards in the main body of API 1104, the maximum length for any imperfection is 8% of the circumference and the maximum depth of any imperfection is 25% of the thickness (by UT inspection). In Appendix A, the maximum imperfection length is 12.5% of the flaw length and no greater than 50% of the pipe thickness. The interesting comparisons are in Figure 3-79 and Figure 3-80 which show the workmanship flaw size superimposed on the existing Option 1 solution as well as using the properly validated limit-load solution from this project. Figure 3-79 shows the different flaw acceptance curves using the parameter P_r (axial stress/flow stress). Figure 3-80 used an axial stress of 100% SMYS for different grades of steel as per the limits in 2007 API 1104 Appendix A. Each of these figures has an upper and lower graph. The upper graph is the comparisons using the 2007 API 1104 Appendix A Option 1 approach, where the bottom graph shows a similar comparison but with the properly validated limit-load equation from this project. These results clearly show the over conservatism in the 2007 Appendix A limit-load equation cause the workmanship imperfection limits to be not acceptable, whereas the properly validated limit-load equation from this project shows there is no problem with the API workmanship imperfection limits. This will be brought to the attention of the API 1104 committee.

3.4.3.2 Over Conservatism in Appendix A Option II Approach

In the same way that the limit-load equation in the 2007 API 1104 Appendix A is overly conservative, this same over conservatism flows to the Option 1 EPFM results and the Option II failure assessment diagram. As a simple example, the Wang-modified limit-load equation used in the 2007 API 1104 Appendix A bounded all full-scale data with CTOD values down to 0.102 mm (0.004 inch), however Option II is applicable for CTOD values down to 0.1 mm (0.004 inch) and two figures (A-7 and A-8) are given in the API 1104 Appendix A for high and low toughness values. In reality, since the Wang-modified limit-load curve is so conservative, it was applicable to CTOD values even below the lowest toughness case in Option 1.

The FAD approach in Option II is said to be valid for CTOD toughness values down to 0.051 mm (0.002 inch). The FAD approach is a very detailed procedure. However, since the Wang-modified limit-load curve actually bounded full-scale experiments with CTOD values down to 0.102 mm (0.004 inch), the entire Option II FAD approach could have just been replaced with that limit-load equation. Alternatively, the properly validated limit-load equation could be used in the FAD approach (with additional checks for validity) to give more relief to users of Appendix A for Alternative Acceptance Standards for Girth Welds.

3.4.3.3 Alternative Simpler EPFM Analyses for 1104 Appendix A

There is another option that is much easier to implement than the FAD-curve approach. This would be parallel to the ASME Section XI Appendix C approach for flaw evaluation in nuclear piping. In that approach, there is a simple multiplier put on the limit-load equation for pipe materials of different toughnesses. From the above work it is seen that a multiplier of $\pi/4$ could be used on the proper limit-load equation if the CTOD was 0.102 mm (0.004 inch). Similar multipliers could be established for different toughness levels as illustrated by the dashed curves shown in Figure 3-70. The ASME Section XI multiplier approach, however, has this multiplier as a function of the pipe diameter. This pipe diameter effect is not discussed in the Option 1 approach in the 2007 Appendix A. For smaller diameter pipe, generally the required toughness needed to reach limit-load with the same dimensionless flaw size (a/t and θ/π) is much lower. There is currently no way to take advantage of that trend in the API 1104 Appendix A approach.

A semi-empirical approach that has been developed [104] is called the Dimensionless Plastic-Zone Parameter (DPZP) analysis, and is shown in Figure 3-81 for circumferential through-wall cracks and circumferential surface cracks in nuclear piping tests. The DPZP is simply the plastic-zone size relative to the distance from the crack tip to the neutral axis of the pipe, which is much easier to envision for a circumferential through-wall flaw, see Equation 3-9. The plastic-zone size was estimated by the Irwin plastic-zone parameter, but using J_{Ic} from a CT specimen (which has a similar constraint condition to a SENB specimen used for typical CTOD testing). The concept is that if the plastic zone is large enough to extend to the neutral axis for a pipe under bending, then fully plastic conditions exist in the pipe and limit-load is met. Although the precise definitions of the neutral axis were explored in Reference [104], it was found that the expression could be simplified using the pipe radius (actually D/2 was used in Equation 3-9). As can be seen in Figure 3-81, when the DPZP was 1.0 or greater, the circumferential through-wall-crack experimental failure stress was equal to the limit load. Hence there is good agreement for a circumferential through-wall flaw when predicting when limit-load was reached. As provided in Reference [104 and updated in 60], a relatively simple equation could also be fit to the data that failed below limit-load, see Equation 3-10. Hence a Section XI type multiplier could be determined from Equation 3-10. Although the J-integral parameter was used in that work, it could be readily converted to the CTOD parameter.

$$\mathrm{DPZP} = (2EJ_{Ic})/(\pi^2 \sigma_f^2 D) \tag{3-9}$$

$$\sigma_{\mathrm{failure}}/\sigma_{\mathrm{limit\text{-}load}} = (2/\pi) \arccos\left[e^{-\mathrm{DPZP}}\right] \tag{3-10}$$

For the circumferential surface-crack case as shown in Figure 3-81, it can be seen that limit-load is reached when DPZP is about 0.25 when using the CT specimen J_{Ic} values. This illustrates the effect of constraint on the apparent fracture toughness in a surface-crack in a pipe. These full-scale pipe tests suggest that the constraint difference could have an effect of about a factor of 4. However, there could also be some anisotropy effects in the factor of 4 since the CT specimens were always taken in the L-C orientation, where the surface crack is growing in the L-R orientation. Nevertheless, the full-scale line-pipe data used in Figure 3-70 could similarly be used to check the DPZP-type equation using CTOD rather than J_{Ic} to provide a simple EPFM analysis for an Option II approach as given in Equation 3-10. This approach would give more relief to users of smaller-diameter piping.

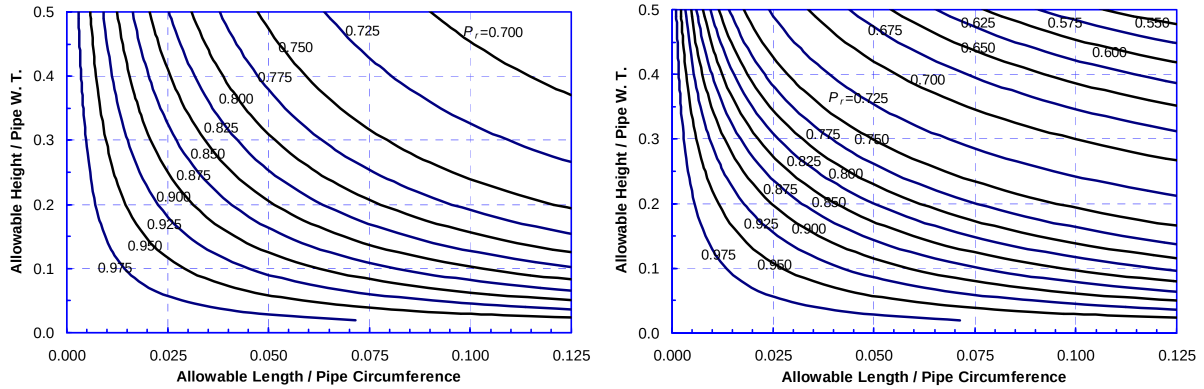

(a) For CTOD ≥ 0.010 inch (0.25 mm)

(b) For CTOD ≥ 0.004 inch (0.10 mm) and less than 0.010 inch (0.25 mm)

Figure 3-78 Option 1 defect acceptance level at various applied load levels as given in Appendix A of 2007 API (Note P_r = applied stress/flow stress)

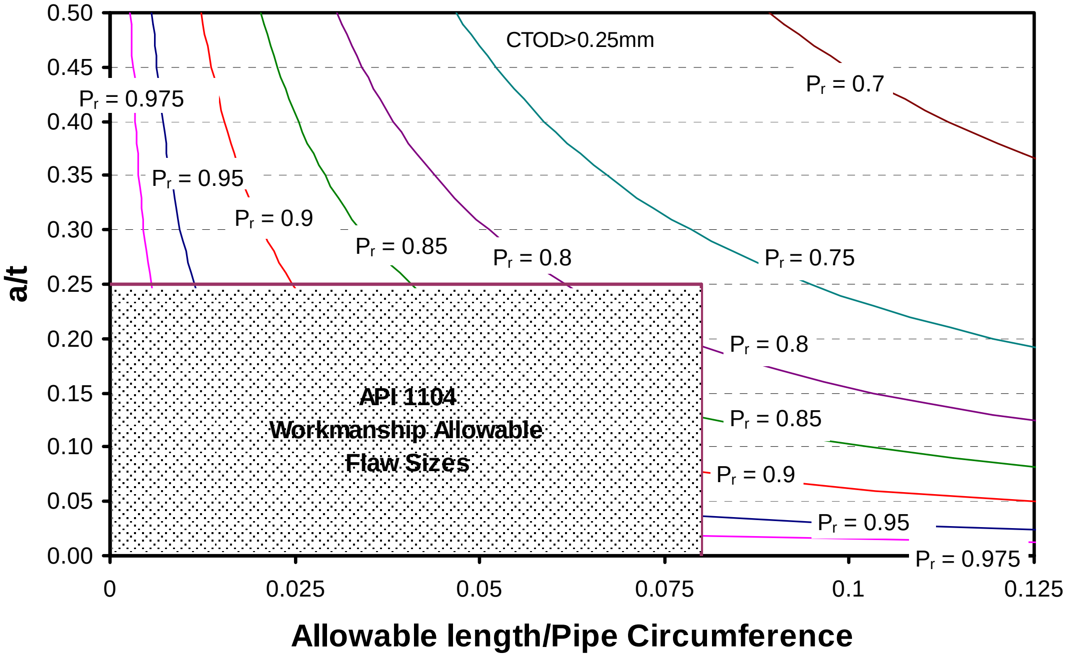

(a) Using 2007 API 1104 Appendix A limit-load equation

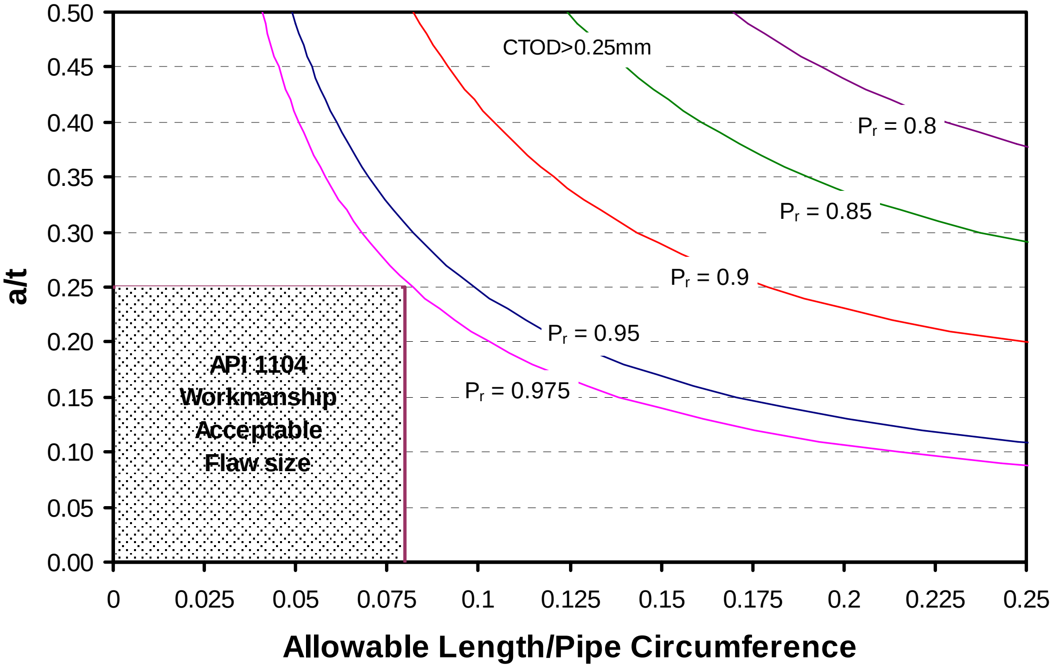

(b) Using properly validated limit-load equation from this project

Figure 3-79 Comparison of API Workmanship flaw sizes (in Section 9 of API 1104 main body) to Option 1 criteria in Appendix A and properly validated limit-load equation from this project (Note; P_r = axial stress/flow stress)

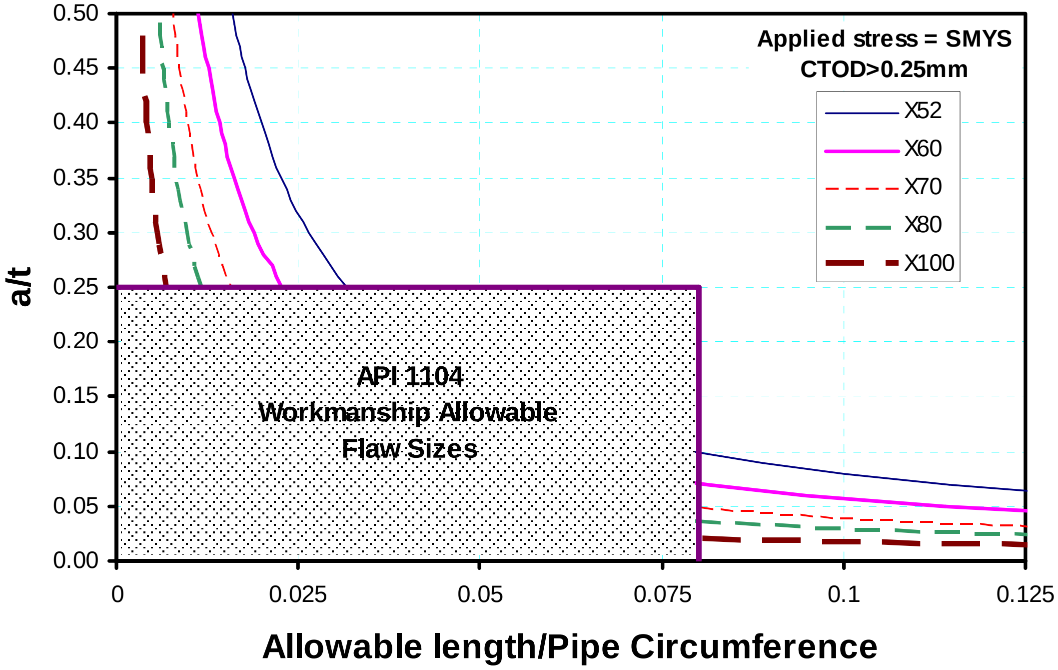

(a) Using recent 2007 API 1104 Appendix A limit-load equation

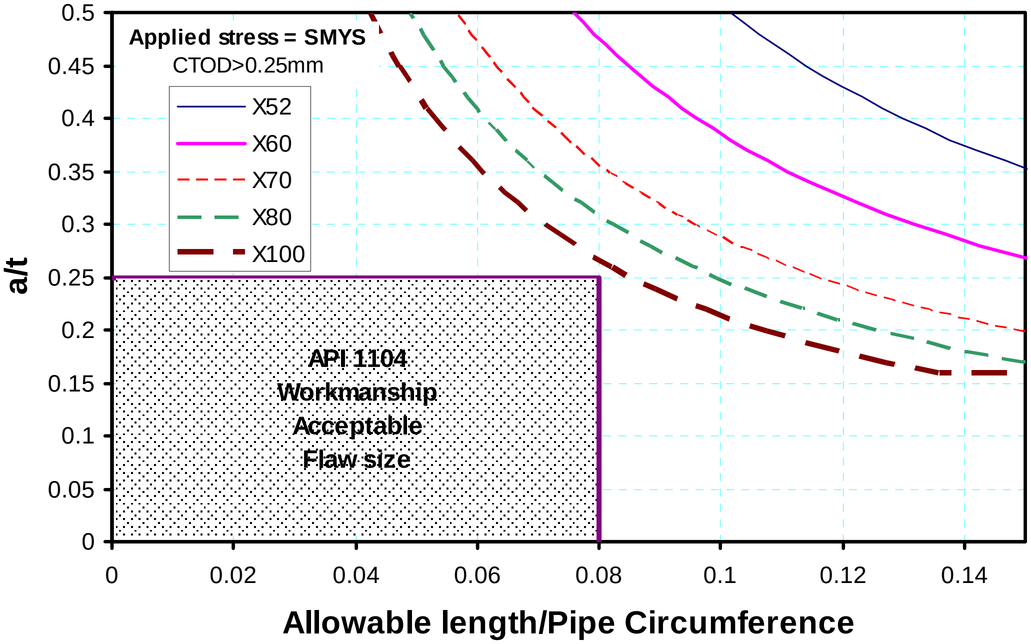

(b) Using properly validated limit-load equation from this project

Figure 3-80 Comparison of API Workmanship flaw sizes (in Section 9 of API 1104 main body) to Option 1 criteria in Appendix A and properly validated limit-load equation from this project – with axial stress equal to 100% SMYS limit of API 1104

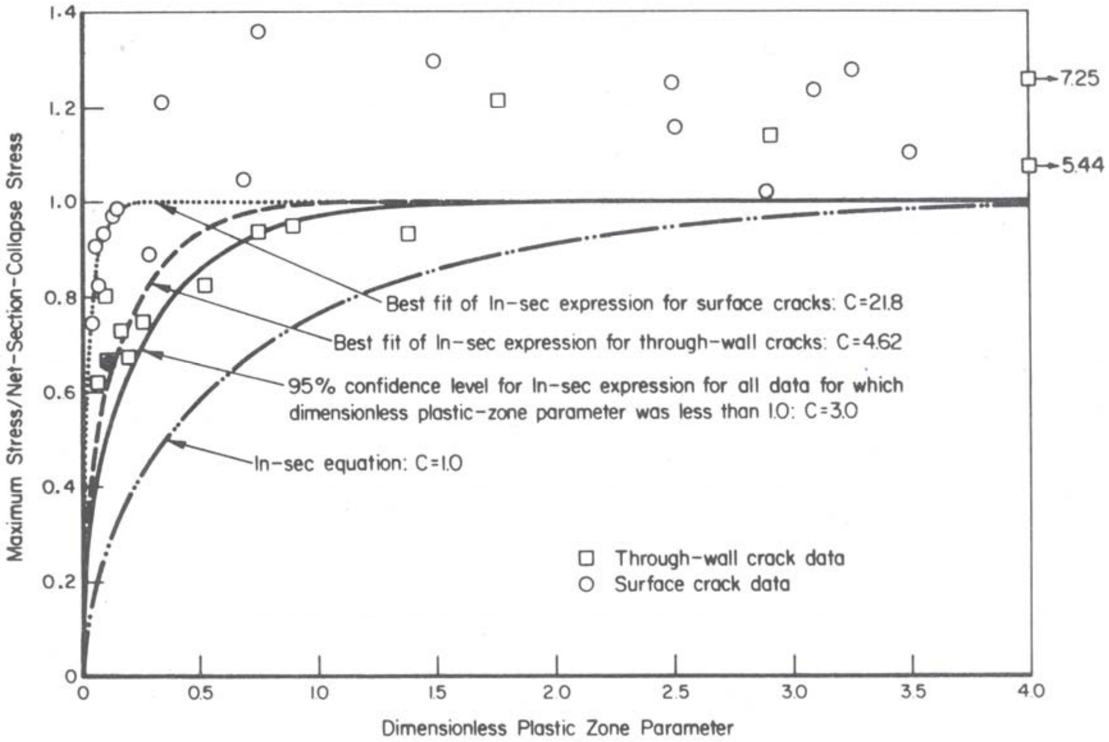

Figure 3-81 Dimensionless Plastic-Zone Parameter (DPZP) analysis fit to circumferentially cracked full-scale nuclear pipe test results

3.4.4 Other Flaw Stability Considerations

3.4.4.1 Effects of Loading Rates

The 2007 API 1104 documents discuss different stress components. Included in those are dynamic and sustained-load cracking.

Dynamic loading could occur for sudden closing of check valves, or rapid soil movement during settlement or seismic loading. The dynamic loading will tend to shift the material brittle-to-ductile transition temperature to a higher temperature [55], and raise the upper-shelf toughness for ferritic steels operating at temperatures below their dynamic strain-aging temperature (typically dynamic strain-aging effects on toughness at different loading rates occurs above 150 C, [111]). Hence the only deleterious effect of the dynamic loading rate occurs if the material is operating close to the fracture initiation transition temperature, see Section 3.3.3.3.1.2.

API 1104 discusses sustained load effects, but for stress corrosion cracking (SCC) from sour gas. Another aspect of the sustained-load effect is that there can be some primary creep crack growth that can reduce the failure stress or strain capacity. Primary creep crack growth can occur at any temperature if the stresses are close to the failure stress (that is, stress-induced primary creep [112, 113]). The effect of hold-time on hydrostatic testing has been a concern for decades for axial flaws in pipelines. Consequently, the applied safety factors for stress-based design and strain-based design should account for the sustained-load deleterious effects.

3.4.4.2 Leak-Before-Break Behavior for Circumferential Flaws

Throughout most of this report and other similar girth weld defect tolerance work for the oil and gas industry, generally the concern has been with determining the maximum load or when ductile tearing starts from the surface crack. From experimental data, Emc^2 staff is aware that the applied stress at the start of ductile tearing from a surface crack is typically 95 to 98 percent of the maximum load [60], so the start of ductile tearing is relatively simple to estimate once maximum load is known. Another consideration is how will the resulting flaw fail, that is, will the pipe fracture into two pieces, or will the surface crack pop through the wall thickness and result in a large leak. Either way the pipeline has to be shut down for repair, but the leak-before-break case would result in a much quicker repair process, with much less damage to the resulting site, and could make the pipeline safer.

The leak-before-break (LBB) stability behavior for circumferentially cracked pipe is a topic of long-standing research effort in the nuclear piping industry. Hundreds of pipe tests and different levels of sophisticated analyses have been developed to determine the stability of a cracked nuclear pipe even under dynamic loading such as seismic events [60,114,115].

The stability of a circumferentially cracked pipe depends on how much energy can be absorbed by the pipe fracture process, versus the energy that is supplied by the pipeline. The energy supplied depends on the type of stresses, i.e., load-controlled versus displacement-controlled. Displacement-controlled stresses are akin to frost heave and ground settlement, whereas offshore pipe laying stresses are closer to load-controlled. The energy absorbed from the pipe fracture process depends on the pipe geometry, flaw geometry, material stress-strain curve, and the material fracture toughness. These energies can be balanced to assess the instability by a relatively simple procedure [105], or by using sophisticated finite element evaluations [114,115]. For quasi-static loading like frost-heave cases, the Energy Balance Approach in Reference [105] should be sufficient. In this approach, J-integral analyses for circumferential surface and through-wall-cracked pipe are used, that predict not only crack initiation and maximum load, but also the shape of the load-displacement (or moment-rotation) curves for cracked pipes with large amount of crack growth. These EPFM analyses are well established and validated from nuclear pipe fracture work [60], but may need some improvements for lower strain-hardening X100 material using the approach given in Reference [116].

A further illustration of how the Energy Balance Approach works is given in Figure 3-82. Energy absorbed by the surface crack growth and the energy applied by the pipe system are illustrated at the top figures, while the bottom figure shows how the energies balance for a surface crack that transitions to a through-wall crack. Typically when a surface crack tears through the thickness, there is a rather rapid drop in the load until it becomes a circumferential through-wall crack. The length of the surface crack determines the resulting through-wall crack length. The example case in Figure 3-82 is for a very long surface crack. Shorter length surface cracks will have much higher through-wall-crack curves which will absorb more energy to assist in crack stability. In general, as the pipe-system compliance (1/stiffness) increases, the crack is more likely to become unstable. These examples are for pipe systems under bending, where the cracks are more likely to be stable than under pure axial tension. If the pipe was loaded under pure load-controlled stresses, then the compliance is just a horizontal line in Figure 3-82 and full break would occur once maximum load is reached. For the medium and low compliance cases in

Figure 3-82, the pipe would not break entirely in two pieces, but there would be a large leakage (which could be calculated). Although not illustrated here, it is also possible to apply this method with any combination of load-controlled and displacement-controlled stresses, as well as with combination of bending stress and axial membrane stress [115].

One of the key material aspects to determining the fracture resistance involves knowing if the pipe material will behave in a brittle or ductile manner during the instability. If brittle behavior occurs then the material resistance becomes negligible and a complete break will occur. Earlier in this report the Fracture Initiation Transition Temperature (FITT) Master Curve was discussed. The FITT for the surface crack could be determined from any number of specimens (with the proper transition temperature shift correlation). This temperature is the lowest temperature where ductile initiation occurs so that the failure stress would correspond to upper-shelf behavior. However, at this temperature, there would be brittle propagation. For strain-based design, some small amount of ductile tearing is needed to reach the appropriate strains so the minimum operating temperature should be slightly above the FITT of that weldment. To achieve LBB behavior, there needs to be ductile tearing behavior for large amounts of crack growth possibly at some higher loading rate than just standard material testing conditions. Base metals that have better than 85% shear area on the DWTT, would behave fully ductile, and this is a typical design condition. However, the weld metals and HAZ need to have dynamic brittle-ductile transition temperatures below the minimum operating temperature to provide sufficient fracture resistance for circumferential LBB behavior to have a chance.

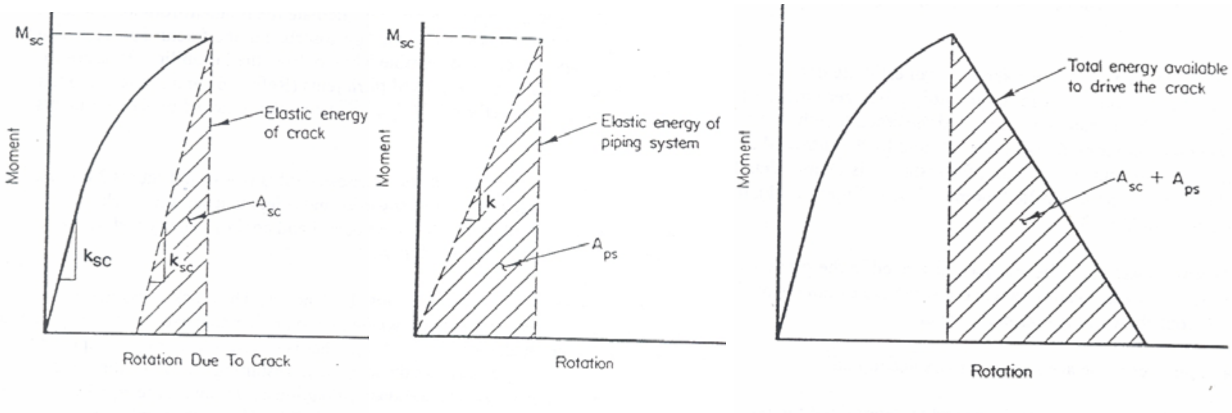

(a) Surface crack behavior (b) Pipe-system behavior (c) Combined energy

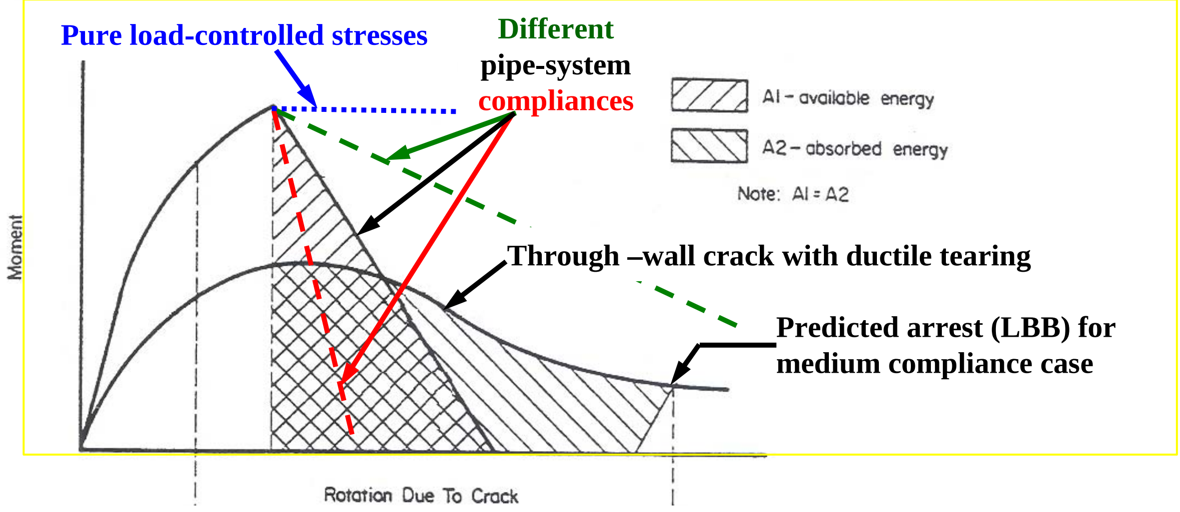

(d) Combination of curves for energy absorbed versus different system compliances

Figure 3-82 Detailed illustration of energy balance approach for predicting if a pipe will leak or completely break (LBB occurs for medium and low compliance cases in this illustration)

3.5 Probabilistic Procedure Development

3.5.1 Introduction

In traditional girth weld engineering critical assessments (ECA) or flaw evaluations, lower or upper bound values are used in the assessment to achieve "conservative" predictions. For instance, only the lowest toughness value from a set of multiple specimens may be used in determining the allowable defect size in a girth weld. No consideration is given for the other toughness values or the distribution of toughness that may exist in the line. These types of assumptions can lead to results with an unknown degree of conservatism. In addition, the cumulative effects of these uncertainties are unquantified. Reliability-based approaches allow for the treatment of uncertainties within the ECA framework.

In order for the reliability-based approach to be efficient, an appropriate definition of the relevant limit states is necessary. A limit state may be defined as a boundary between safe and unsafe or desirable and undesirable. However, for use in reliability-based analyses, the limit state should accurately predict the true limit state and not one with an unknown safety factor. In addition, the uncertainty and distributions in the input parameters for the limit-state definition need to be clearly and appropriately defined. Work in past programs and in this program aimed at defining accurate limit-state definitions and quantifying uncertainty in both the limit state and the input parameters.

Therefore, in this Chapter, recent reliability assessment programs conducted prior to this program will be reviewed. In Section 3.5.2, two PRCI-funded reports will be reviewed. The first is based on the further development of a reliability, stress-based ECA procedure. The second is based on the initial development of a reliability, strain-based assessment procedure for girth weld defects. The basis of each approach and the status of the procedures will be discussed. Finally in Section 3.5.3, a description of how the work conducted in this project could be used to further advance these procedures will be discussed.

3.5.2 Review of Current Reliability-Based Assessments for Girth Weld Defects

Currently, two programs have been conducted to continue to develop reliability-based procedures for assessment of girth weld defects. Each of the programs discussed in this section were funded by PRCI and were conducted by Emc^2 in the 2004-2005 timeframe. The first, entitled "Reliability Assessment Using the Improved ECA Procedures," looks at stress-based reliability procedures, while the second, entitled "Reliability-Based Strain Design," focuses on strain-based design. The report from this effort is provided in Appendix 2. The second program discussed here was also used as cost-sharing as part of this project.

3.5.2.1 Summary of Reliability Assessment Using Improved Stress Based Procedures

In this effort [18], a software program, termed *GirthRel* [117], was modified with several deterministic improvements. These improvement included updates to the circumferential crack K-solutions, the limit-load equations and the definition of fracture toughness. Each of these updates is briefly described below:

- Updated limit-load solution. The limit-load solution adopted in this effort follows the recommendation of Wang [118]. The basis of the recommendation has been covered extensively in prior publications. The limit-load solution is due to Miller [93], with a defect correction factor proposed by Wang [119]. The modified Miller solution is the basis of the revised limit-load criterion in CSA Z662 Appendix K 2003 Edition. The acceptance criteria of CSA Z662 Appendix K have a safety factor of 2 on the defect length computed from this criterion. This limit-load equation was also implemented into the 2007 API 1104 Appendix A criterion. This safety factor is consistent with historical recommendations.

- Updated K-solution. Originally, the stress intensity solutions by Chapuloit [120] were curve fit using a polynomial functional form and included in the *GirthRel* software. However, the curve fits used created undesirable oscillations (due to the polynomial form used) in the stress intensity solution for certain crack sizes. In order to improve the reliability of the solutions, a new curve-fit equation was developed which removed the polynomial functions. These new solutions improved the reliability of the K-solutions.

- Updated Failure Assessment Curve. The formulation of the FACs in the previous version of *GirthRel* is cumbersome as the FACs are converted from the GE/EPRI *J* estimation scheme. The new FACs are functions of material's strain-hardening exponent (which is related to the Y/T ratio) and defect length, and include a cut-off on the collapse portion of the FAC.

- A relationship was incorporated that related the strain hardening to the pipe grade. If a defect is located in weld metal, the yield strength used in the calculations is taken as the weld yield strength. If the defect is located in the HAZ, the higher value of the yield strength between the weld metal and the base metal is taken so a conservative value of n and Y/T ratio can be obtained.

- Updated Mismatch Correction Factors. The mismatch correction factors in PR-185-9831 are based on the extensive numerical and analytical work at GKSS [121]. These factors proved very accurate by the finite element results in PR-185-9831 [119].

- Definition of fracture toughness. In the original code, the fracture toughness was defined as K_c; however, in the updated code, the critical crack-tip-opening displacement (CTOD) is used as the toughness parameter.

These deterministic modifications were made to the *GirthRel* software along with other user-friendly improvements.

From the project report in Appendix 2, some of the continued work needed in this effort included:

- Further confidence may be gained by validating the output of the software with field data. Such data are generally expensive to collect. However, persistent efforts in collecting such data will have a long-term beneficial impact on the industry.
- The other needed improvement is developing weld mismatch correction factor for defects of finite length.

3.5.2.2 Summary of Reliability Based Strain Design

In this effort, a Windows-based software code, termed RSD, was developed to aid in conducting ECA for high longitudinal strain loadings. The details of this effort can be found in the final report, which is provided in Appendix 2.

In another PRCI effort [122], parametric finite element analyses were conducted for both surface-breaking and embedded girth-weld defects in order to determine the tensile strain limits for a variety of line-pipe steels. In the effort described in Appendix 2, the results from this parametric study were curve fit for use in reliability analyses. The input data in the development of the parametric equations was over a wide range of material properties, including X52, X60, X65, X70, and X80. The *Y/T* values varied with the pipe grade and had a range of 0.788 to 0.841 for X52 and from 0.889 to 0.917 for X80.

For the surface-breaking defects, the pipe wall thickness (*t*) had 5 different values: 0.25, 0.375, 0.5, 0.75, and 1.0 inch. The defect height (*a*) was fixed at 3 mm which corresponds to one weld pass height. The ratio of defect height to wall thickness therefore varied from 12% to 47%. The defect length (2*c*) varied from 12.5 mm to 100 mm. For the buried defects, the pipe wall thickness (*t*) had 4 different values: 0.250, 0.375, 0.500, and 0.750 inch. The defect depth (*d*) or distance from the surface to the buried flaw had different values depending on the pipe wall thickness. It had a value of 1.5 mm for 0.250 inch wall thickness, 3.0 mm for 0.375-inch and 0.500-inch wall thickness, and 3.0 or 6.0 mm for 0.750-inch wall thickness. The buried defect height (2*a*) ranged from 3 mm to 6 mm and the defect length (2*c*) varied from 12.5 mm to 75 mm. For the surface breaking defects the maximum value of the CTOD toughness (δ) was set at 1 mm, while for the embedded defects it was set at 0.6 mm due to data limitations.

The longitudinal strain limit for surface breaking defects is given as,

$$\varepsilon_{\lim it} = \delta^{(2.36-1.58\lambda-0.101\xi\eta)}\left(1+16.1\lambda^{-4.45}\right)\left(-0.157+0.239\xi^{-0.241}\eta^{-0.315}\right) \tag{3-11}$$

where $\lambda \equiv Y/T$, $\xi \equiv 2c/t$, and $\eta \equiv a/t$ and 2c/πD varied between 1 to 5 %. The apparent CTOD toughness has a unit of mm in Eq. (3-11). The units of other parameters need to be consistent to produce the non-dimensional parameters. The strain limit ($\varepsilon_{\text{limit}}$) is in percent (%). The minimum apparent CTOD (δ) value to use in Eq (3-11) is 0.1 mm.

The strain limits of rectangular-shaped defects are given as,

$$\begin{aligned}\varepsilon_{\text{limit}} = {} & \delta^{1.08-0.612\eta-0.0735\xi+0.364\psi}\left(12.3-4.65\sqrt{t}+0.495t\right)\\ & (11.8-10.6\lambda)\left(-5.14+\frac{0.992}{\psi}+20.1\psi\right)\left(-3.63+11.0\sqrt{\eta}-8.44\eta\right)\\ & \left(-0.836+0.733\eta+0.0483\xi+\frac{3.49-14.6\eta-12.9\psi}{1+\xi^{1.84}}\right)\end{aligned} \tag{3-12}$$

The strain limits of the elliptical-shaped defects are given as,

$$\begin{aligned}\varepsilon_{\text{limit}} = {} & \delta^{1.00-0.511\eta-0.0507\xi+0.364\psi}\left(5.62-2.30\sqrt{t}+0.260t\right)\\ & (13.6-12.1\lambda)\left(-9.95+\frac{0.189}{\psi}-19.2\psi\right)\left(-4.21+12.3\sqrt{\eta}-9.14\eta\right)\\ & \left(-0.180+7.28\eta-0.0321\xi+\frac{0.785-7.82\eta+0.0237\psi}{1+\xi^{-1.97}}\right)\end{aligned} \tag{3-13}$$

where $\lambda \equiv Y/T$, $\xi \equiv 2c/t$, $\eta \equiv a/t, \psi \equiv d/t$. The wall thickness and the apparent CTOD toughness have the unit of mm in Eqs. (3-12 and 3-13). The units of other parameters need to be consistent to produce the non-dimensional parameters. The strain limit ($\varepsilon_{\text{limit}}$) is in percent (%). The minimum apparent CTOD (δ) value to use in these equations is 0.1 mm.

An example of the accuracy of the equations above is shown in Figure 3-83. In this figure, the failure strains as a function of the apparent CTOD toughness are compared. The symbols represent the FE results from Reference 122, while the solid lines represent the curve-fit equation above. As noted in Appendix 2, the errors in these curve fits can be as large as 30%, and decrease as the wall thickness decreases. These errors (uncertainties) in the equations used are not accounted for in the current version of the RSD software.

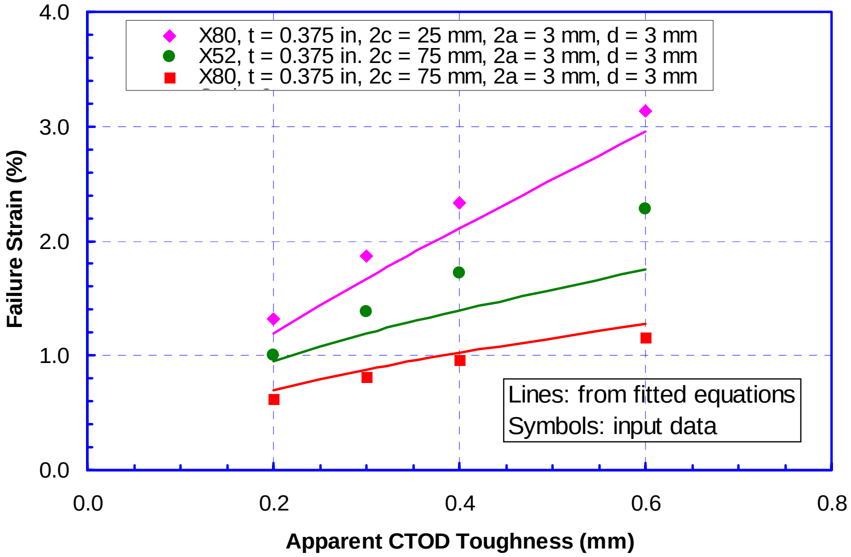

Figure 3-83 Comparison of failure strains as a function of CTOD toughness between input data and the fitted equation for elliptical-shaped buried defects (lines: fitted equation; symbols: input data)

The program considers two types of defects: surface-breaking defects and buried defects. For surface-breaking defects, the input parameters for the computation of the distribution of the strain limits are CTOD, yield strength of the pipe material, *Y*/*T* ratio, pipe wall thickness, defect length, and defect height. For buried defects, the input parameters for the computation of the distribution of the strain limits are CTOD, *Y*/*T* ratio, pipe wall thickness, defect length, defect height, and defect depth. Only the rectangular-shaped buried defects are considered in the current software. The rectangular-shaped defects provide lower (thus conservative) values of strain limits. To evaluate failure probability, the distribution of design strain is entered as an input parameter.

Some areas for future work described in Appendix 2 include:

- The data which formed the basis for the fitted Eqs. (3-11), (3-12), and (3-13) were obtained from large-diameter pipes with relatively short defects. These short defects were considered necessary to have high longitudinal strain limits, i.e., strain-based design. The validity of these equations to small diameter pipes, such as those in offshore applications, needs to be examined.
- No residual stress was considered in obtaining the data. Residual stresses may affect the constraint conditions and affect the apparent toughness.
- Experimental validation of the reliability-based procedure presented is necessary before the procedure can be put to practical use.

3.5.3 Updating Reliability Procedures

The research conducted in this project can be used in future efforts to update the current reliability based ECA programs. Some of these future improvements may include:

- Update of strain-hardening relationship. Through this program, longitudinal stress-strain curves have been developed for the relevant materials as a function of temperature. The strain-hardening relationships developed and discussed above can be validated and updated as needed. This will aid in reducing the uncertainty associated with the pipe strength properties.
- Better representation of crack-driving force. In probabilistic codes discussed above, technical issues such as HAZ softening, hoop stress, and mismatch effects for finite length flaws, which were developed in this effort, were not included. Updating the driving-force solution to include these issues will decrease the uncertainty in capturing the crack-driving force.
- Better representation of fracture toughness. As noted in previous references, the material toughness developed from 3-point bend specimens (J or CTOD) will be much lower than the apparent toughness of a circumferential surface crack in a pipe due to differences in constraint. As discussed in this effort, lower constraint test specimens such as the back-bend and SEN(T) were used to more accurately capture the apparent toughness. The apparent toughness in the surface-cracked pipe can be 4 to 7 times greater than from standard CTOD bend-bar specimen tests.
- Better limit-load predictions. As noted in Section 3.4.1.1 the equations currently embedded in the probabilistic codes contain a $4/\pi$ level of conservatism. By removing

this conservatism from the probabilistic code, the uncertainty in the stability of the flaw is greatly reduced

- More defined material distributions. With a properly trained neural network, predictions of material properties and their associated distributions can be made. This will allow the prediction of failure probabilities with high confidence levels.
- Updated stochastic methods. Currently, the probabilistic codes use Monte Carlo simulations for prediction of failure probability. This method is relatively inefficient when large sample sizes are required on problems with a large number of random variables. Therefore, implementing other stochastic procedures, such as the First Order Reliability Method (FORM) or the Second Order Reliability Method (SORM) could greatly increase the code efficiency if the deterministic equations become more computationally intensive.
- The strain-based code needs a number of improvements. For instance, the curve-fit equations should also have a $2c/\pi D$ limitation. Hoop stress effects, as well as HAZ and weld strength effects could be included with stochastic variability of the weld/HAZ/base metal strength variations. Flaw location also becomes important.

4 ACCOMPLISHMENTS

Many of the major accomplishments from this program resulted in papers presented at national and international meetings, publications authored in peer reviewed journals, and presentations and reports prepared for project and review meetings of the team and advisors. A list of the significant documents is presented below.

4.1 Papers

Proceedings of the Seventeenth (2007) International Offshore and Polar Engineering Conference, ISOPE-2007-SBD10 "Microstructure Modeling of HAZ Softening in Microalloyed High Strength Line-Pipe Steels," Chen, Y. and Wang, Y.-Y., Emc^2.

Proceedings of OMAE2005, 24th International Conference on Offshore Mechanics and Arctic Engineering, (OMAE 2005), June 12-17, 2005, Halkidiki, Greece, paper OMAE2005-67039, "Significance of HAZ Softening on Strain Concentration and Crack Driving Force in Pipeline Girth Welds," Liu, M., Wang, Y-Y, Emc^2, Horsley, D, TransCanada Pipelines Ltd.

Proceedings of the 26th International Conference on Offshore Mechanics and Arctic Engineering, OMAE2007, June 10-15, 2007, San Diego, California, USA; paper OMAE2007-29415, "Significance of Biaxial Stress on the Strain Concentration and Crack Driving Force in Pipeline Girth Welds with Softened HAZ," Liu, M., Wang, Y-Y., Emc^2.

Proceedings of the Sixteenth (2006) International Offshore and Polar Engineering Conference San Francisco, California, USA, May 28-June 2, 2006, ISBN 1-880653-66-4 (Set); ISSN 1098-6189 (Set), "Modeling of Anisotropy of TMCP and UOE Line Pipes," Liu, M. and Wang, Y.-Y., Emc^2.

Proceedings of the Seventeenth (2007) International Offshore and Polar Engineering Conference ISOPE, 2007-SBD-12, "Advanced Modeling of Plasticity of Line-Pipe Steels with Anisotropic Texture and Complex Loading History," Liu, M. and Wang, Y.-Y. Emc^2.

Proceedings of IPC 2006, 6th International Pipeline Conference (IPC 2006), September 25-29, 2006, Calgary, Alberta, Canada, paper IPC2006-10416, "Applying Gurson Type of Damage Models to Low Constraint Tests of High Strength Steels and Welds," Liu, M. and Wang, Y.-Y., Emc^2.

Proceedings of EPRG-PRCI-APIA 15TH Joint Technical Meeting on Pipeline Research, Orlando, FL U.S.A., MAY 17-19, 2005, "Some Aspects of Material and Welding Specifications for Strain Based Design of Pipelines," Liu, M., Wang, Y.-Y. (Emc^2), Horsley, D. (TransCanada Pipelines).

Proceedings of IPC 2004, International Pipeline Conference, October 4 - 8, 2004 Calgary, Alberta, Canada, paper IPC04-0558, "Weld Microstructure and Hardness Prediction for In-

Service Hot-Tap Welds," Cheng, W., Wang, Y.-Y.(Emc^2), Amend, W. (Southern California Gas), Swatzel, J. (Columbia Gas Distribution).

Proceedings of IPC2004, 5th International Pipeline Conference 2004, Calgary, Alberta, Canada, October 4-October 8, 2004, paper IPC04-0524, "Tensile Strain Limits of Buried Defects in Pipeline Girth Welds," Wang, Y.-Y., Cheng, W. (Emc^2), Horsley, D. (TransCanada Pipelines).

Proceedings of IPC 2006, 6th International Pipeline Conference (IPC 2006), September 25-29, 2006, Calgary, Alberta, Canada, paper IPC2006-10414, "Low-Constraint Back-Bend Test of High Strength Steels: Crack Driving Force Calibration," Liu, M., Wang, Y.-Y. (Emc^2).

Proceedings of IPC2006, 6th International Pipeline Conference 2006, Calgary, Alberta, Canada, September 25- 29, 2006, paper IPC2006-10474, "A Quantitative Approach to Tensile Strain Capacity of Pipelines," Wang, Y.-Y., Liu, M. (Emc^2), Horsley, D., Zhou, J. (TransCanada Pipelines).

Proceedings of IPC2006, 6th International Pipeline Conference 2006, Calgary, Alberta, Canada, September 25- 29, 2006, paper IPC2006-10491, "A Tiered Approach to Girth Weld Defect Acceptance Criteria for Stress-Based Design of Pipelines," Wang, Y-Y, Liu, M. (Emc^2), Horsley, D. (TransCanada Pipelines), Bauman, G. (Pipeline and Hazardous Materials Safety Administration, US DOT).

Proceedings of IPC 2006, 2006 International Pipeline Conference, September 25-29, 2006, Calgary, Alberta, Canada, paper IPC2006-10492, " Low-Constraint Testing of Pipeline Girth Welds," Rudland, D., Wang, Y.-Y. (Emc^2).

Proceedings of IPC2006, 6th International Pipeline Conference 2006, Calgary, Alberta, Canada, September 25- 29, 2006, Paper IPC2006-10496, "An Updated Cooling Rate and Microstructure Model for Pipeline In-Service Hot-Tap Welds," Chen, Y., Wang, Y-Y (Emc^2), Horsley, D. (TransCanada Pipelines).

Proceedings of IPC2006, 6th International Pipeline Conference 2006, Calgary, Alberta, Canada, September 25- 29, 2006, paper IPC2006-10497, "Effects Of Geometry, Temperature, And Test Procedure On Reported Failure Strains From Simulated Wide Plate Tests," Wang, Y.-Y., Liu, M., Chen, Y. (Emc^2), Horsley, D. (TransCanada Pipelines).

Proceedings of IPC2008 - 7th International Pipeline Conference, September 29-October 3, 2008, Paper IPC2008-64658, "Predicting The Brittle-To-Ductile Transition Temperatures For Surface Cracks In Pipeline Girth Welds - It's Better Than You Thought," Wilkowski, G. M, Rudland, D., Shim, D.-J., (Emc2) and Horsley, D. (BP),

There will also be several future presentations at the October 2009 Pipeline Technology Conference for work done near the end of this project.

4.2 Reports/Thesis

Submitted to Department of Mechanical Engineering in partial fulfillment of the requirements for Doctor of Philosophy in Mechanical Engineering at the Massachusetts Institute Of Technology, June 2007, "Plastic buckling in gas transmission line-pipes, cold formed from thermo-mechanically-controlled rolling of low-alloy steel plates," by Vaibhaw Vishal.

5 CONCLUSIONS

The major important conclusions emanating from these studies included:

- From the microstructure modeling and predictive efforts, it was found that both the Kirkaldy (overpredicts the HAZ hardness) and StructureR (underpredicts the hardness) models are acceptable in cases where the hardness may increase in the HAZ, i.e., hot-tapping of older line pipe steels. For cases where there could be softening in the HAZ, such as for newer X100 steels, it is currently necessary to both models to bound the actual hardness in the HAZ, i.e., Kirkaldy overpredicts the HAZ hardness and StructureR underpredicts HAZ softening for higher grade steels like X100.
- A methodology developed in prior work, the Fracture Initiation Transition Temperature (FITT) Master Curve properly predicts surface-cracked pipe brittle-to-ductile initiation temperature. It has value in developing Codes and Standards to better correlate full-scale behavior from either CTOD or Charpy test results with the proper temperature shifts from the FITT master curve method.
- For stress-based flaw evaluation criteria, the new circumferentially cracked pipe limit-load solution in the 2007 API 1104 Appendix A approach is overly conservative by a factor of 4/π, which has additional implications. For instance, the Wang-modified/Miller limit-load equation that was used actually bounds full-scale pipe test data that had CTOD toughness values of equal to or greater than 0.10 mm (0.004 inch), hence the EPFM analyses in the 2007 API 1104 Appendix A criteria were not really needed. A more simplified EPFM was suggested than the FAD-curve approach in API 1104 Appendix A. This simpler approach would be parallel to girth weld flaw evaluation procedures in ASME Section XI pipe flaw evaluation procedures that have been in place for decades.
- For strain-based design of girth weld defects, the hoop stress effect is the most significant parameter impacting CTOD-driving force and can increase the crack-driving force by more than a factor of 2 depending on the material strain-hardening, the pressure level as a % of SMYS, and the flaw size.
- The ability to predict weld metal and HAZ Charpy energy (toughness) by neural network analyses showed promise, but much more development is required before the neural network method becomes a practical tool to provide reliability analyses input.
- The Taylor polycrystal plasticity model for anisotropy effect assessment took a large amount of computational time, so that in a realistic sense it is useable on small specimen studies, but currently not practical for large structural analyses.
- From our years of experience in circumferential fracture analyses and experimentation, there has not been sufficient integration of work performed for other industries into analogous problems facing the oil and gas pipeline markets. Some very basic concepts and problems solved previously in these fields could have circumvented the inconsistencies seen in the stress-based and strain-based analysis efforts to date. For example, in nuclear utility piping work, more detailed elastic-plastic fracture analyses were always validated in their ability to predict loads ***and*** displacements (stresses and strains) together.

The eventual implementation of these methodologies will result in an acceleration in the industry and rapid adoption of the next generation, higher-strength line-pipe steels. The use of high strength steels (X100) in turn results in energy savings across the spectrum, from manufacturing of the pipe itself to transportation to the field and fabrication, including welding of pipeline in the field resulting in higher productivity and improved quality assurance as a result of the technologies developed in this project.

Elementary examples of energy savings include more the 25 trillion BTUs saved annually based on lower energy costs to produce the thinner walled high strength steel pipe, with the potential for the US part of the Alaskan pipeline alone saving more than 7 trillion BTU in production and much more in transportation and assembling. Annual production, maintenance and installation of just US domestic transmission pipeline is likely to save 5 to 10 times this amount based on current planned and anticipated expansions of oil and gas lines in North America. From an operations and maintenance standpoint, installation of the higher strength steels could save more than $1 billion on the Alaska Gas Pipeline from just reduction in weld costs. These uses of high-strength steels and the methodologies used will also eventually spinoff to other industries in such areas as building and construction, military, naval, and aerospace applications.

6 RECOMMENDATIONS

Based on the studies discussed in this project, the following recommendations are made for future work:

1. It is suggested that both the Kirkaldy (overpredicts the HAZ hardness) and StructureR (underpredicts the hardness) models be used to bound the actual hardness in the HAZ if softening is an issue to be explored.
2. There is a need to develop integrated process-microstructure-performance models capable of predicting microstructure and properties as a function of material and process parameters. These improved integrated process models must permit robust calculation of weld metal microstructure as well as taking into account inclusion characteristics. The models must seamlessly integrate thermal distortion, residual stress, and microstructure properties for the HAZ.
3. There is a need to develop weld metal consumables that produce more favorable HAZ hardening characteristics. The proposed models from 2 above could aid in this development..
4. The ability to predict weld metal and HAZ Charpy energy (toughness) by neural network analyses approach is a sophisticated method to develop empirical correlations for complicated problems. The method looks promising, but much more development is required before the neural network method becomes a practical tool to provide reliability analyses input. Upwards of 100 additional references were collected, but there was not sufficient time to train the neural network, and contact the authors for some of the many variables that undoubtedly were not in the technical papers that were needed for complete training of the network.
5. To improve the Codes and Standards for determining the lowest operating temperature for ductile fracture initiation behavior, the following could be done; (a) Additional SENT test data and comparison with bend and Charpy data for weld metals is desirable, since the FITT Master Curve method was developed more from base metal tests, and (b) further validation of the FITT Master Curve method by comparison of fracture full-scale pipe tests with girth weld defects where the pipe tests were conducted with identical flaws over a series of temperatures to give full-scale brittle versus ductile fracture initiation behavior.
6. For stress-based girthweld defect tolerance analyses, the limit-load equation, FAD approach, and properly accounting for pipe diameter effects are all aspects that can and should be modified in API 1104 and CSA Z662 to enhance the usability of high-strength steel pipelines.
7. Strain-based reliability analysis was developed in a PRCI/GRI effort using empirical curve-fit equations that do not account for hoop-stress effects (in software called *RSD*). This will need updating when the more detailed hoop stress evaluations are completed in an on-going PRCI/DOT program. There are a number of other improvements that could also be implemented, such as making sure there is consistency in the parameters between stress-based and strain-based analyses, i.e., limits on the flaw length relative the percent of the pipe circumference.

8. There should be some consistency between stress-based and strain-based criteria, for example; (1) draft strain-based criteria recognize that surface-cracked pipe have lower constraint so that the bend specimen CTOD could be multiplied by a factor of 2 to 3, but that is not incorporated into the stress-based criteria; (2) hoop stress can increase the CTOSD driving force for strain-based analyses, but the load capacity increases from the hoop stress for stress-based considerations, (3) stress-based criteria have the crack-driving force as a function of the crack length as percent of the pipe circumference, where draft strain-based criteria do not.

7 REFERENCES

1 “Welding-Related Expenditures, Investments, and Productivity Measurements in U.S. Manufacturing, Construction, and Mining Industries,” American Welding Society and Edison Welding Institute, May 2002, www.aws.org .

2 Silberglitt, R. and Mitchell, J., “Industrial Materials for the Future (IMF) R&D Priorities,” Sept, 2001. http://www.oit.doe.gov/imf/pdfs/imfdb364.pdf.

3 “Welding Technology Roadmap,” Final Draft, September 2000. DOE, Office of Industrial Technologies, www.oit.doe.gov/related/related.shtml.

4 Scheinbergy, P., “Pipeline Safety,” United States General Accounting Office, GAO/RCED-00-128, May, 2000.

5 Eisenhauer, J., etc., “Natural Gas Supply and Utilization for the 21st Century, Understanding Technology Need in Emerging Gas Markets,” U.S. Department of Energy, Office of Fossil Energy, July, 1999.

6 Coote, R. I. and Stanistreet, M. G., “Fracture Mechanics and Workmanship Rules for Girth Weld Defects in the Canadian Pipeline Standard,” in *Circumferential Cracks in Pressure Vessels and Piping* – Vol. I, PVP Vol. 94, G. Wilkowski Ed., 1983.

7 “Steel Industry Technology Roadmap”, DOE OIT, December, 2001.

8 “Minimum Federal Safety Standards for Liquid Pipeline,” *Code of Federal Regulations*, Title 49 Transportation, Part 195, Office of the Federal Registry, National Archives and Records Service, General Services Administration (Revised October 1, 1975).

9 *API Standard 1104*, "Welding of Pipelines and Related Facilities," 19th Edition, September 1999.

10 *API RP 579*, “Fitness-for-Service,” First Edition, January 2002.

11 Hilton, P. D. and Mayville, R. A., “An Evaluation of Girth Weld Defect Acceptance Criteria,” Final report to U. S. Department of Transportation, Research and Special Projects Administration, November, 1985.

12 Gurson, A. L., “Continuum Theory of Ductile Rupture by Void Nucleation and Growth-I,” *ASME Journal of Engineering Materials and Technology*, Vol. 99, 1977, pp. 2015.

13 Tvergaard, V., “Influence of Void on Shear Band Instabilities under Plane Strain Condition,” *International Journal of Fracture Mechanics*, Vol. 17, 1981, pp. 389-407.

14 Tvergaard, V., “On Localization in Ductile Materials Containing Voids,” *International Journal of Fracture Mechanics*, Vol. 18, 1982, pp. 237-251.

15 Needleman, A., Tvergaard, V., “An Analysis of Ductile Rupture in Notched Bars,” *Journal of the Mechanics and Physics of Solids*, Vol. 32, 1984, pp. 461-490.

16 Shih, C. F., Xia, L., Hutchinson, J. W., “A Computational Approach to Ductile Crack Growth under Large Scale Yield Conditions,” *Journal of the Mechanics and Physics of Solids*, Vol. 43, 1995, pp. 389-413.

17 Haq, F., McClintock, F. A., Parks, D. M., and Bass, M. K., “Fully-Plastic Back-Bend Tests for Low-Triaxiality Plane Strain Crack Growth,” ASME Drucker Medal Symposium in honor of Frank A. McClintock, November 2004.

18 Wang, Y-Y., Chen, Y., and Carrasco, C., “Reliability Assessment Using the Improved ECA Procedure,” final report for Gas Research Institute (GRI), GRI-04/0145, February 2005.

19 Wilkowski et al., “A Comprehensive Update in the Evaluation of Pipeline Weld Defects,” U.S. DOT Agreement No. DTRS56-03-T-0008, PRCI Contact No. PR-276-04503, final report submitted for approval Feb 2008.

20 Babu, S. S., et al., 1999, “A model for inclusion formation in low alloy steel welds,” *Science and Technology of Welding and Joining,* Vol. 4, pp. 276-284.

21 David, S. A., Babu, S. S., and Vitek, J. M., 2003, “Overview – Welding: Solidification and Microstructure,” *JOM-J MIN MET MAT*, Vol. 55, pp. 14-20.

22 Bhadeshia H. K. D. H. and Svensson, L. E., 1993, “Modeling the evolution of microstructure in steel weld metal,” *Mathematical Modeling of Weld Phenomena*, Eds. H. Cerjak and K. E. Easterling, Institute of Materials, London, pp. 109-182.

23 Shome, M., Gupta, O.P., and Mohanty, O. N., 2004, “Effect of Simulated Thermal Cycles on the Microstructure of the Heat-Affected Zone in HSLA-80 and HSLA-100 Steel Plates,” *Metallurgical and Materials Transactions A*, Vol. 35A, pp. 985-996.

24 Chan, B., Bibby, M., and Goldak, J., 1992, “A software system for determining the preheat temperature required to avoid under bead cracking-1,” *Canadian Metallurgical Quarterly*, Vol. 31, pp. 195-202.

25 Chan, B., Bibby, M., and Goldak, J., 1992, “A software system for determining the HAZ hardness after post weld heat-treatment 2,” *Canadian Metallurgical Quarterly*, Vol. 31, pp. 203-209.

26 Chen, Y., and Wang, Y., 2007, “Microstructure Modeling of HAZ Softening in Microalloyed High Strength Line-Pipe Steels,” *ISOPE Conference Proceedings.*

27 Brust, F. W., and Kim, D., “Mitigating Welding Residual Stress and Distortion,” Chapter 8 in *Processes and Mechanisms of Welding Residual Stress and Distortion,* pp. 264 – 294, Woodhead Publishing, July 2005.

28 Brust, F., W., and Cao, Z., “Virtual Fabrication Technology (VFT^{TM}) computer code,” Theory Manual, Distributed by Battelle and Engineering Mechanics Corporation of Columbus.

29 Cao, Z., Yang, Z., and Chen, X. L., “Three-Dimensional Simulation of Transient GMA Weld Pool with Free Surface,” *American Welding Society (AWS) Supplement*, June, 2004.

30 Goldak, J., Chakravarti, A., and Bibby, M., 1984. “A new finite element model for welding heat sources,” *Metallurgical, Transactions B* 15B: pp. 299-305.

31 Kirkaldy, J. S., 1991, “Diffusion-controlled phase transformations in steels – Theory and Applications,” *Scandinavian Journal of Metallurgy*, Vol. 20, pp. 50 – 61.

32 Watt, D.F., Coon, L., Bibby, M., Goldak, J., and Henwood, C., 1988, “An Algorithm for Modeling Microstructure Development in Welding Heat-Affected Zones (Part A) Reaction Kinetics,” *Acta Metall.*, Vol. 36, No. 11, pp. 3029-3035.

33 Li, M.V., et al., 1998, “A Computational Model for the Prediction of Steel Hardenability,” *Metallurgical and Materials Transaction B,* Vol. 29B, No. 6, pp. 661-672.

34 Jones, S. J. and Bhadeshia, H. K. D. H., 1997, “Kinetics of the Simultaneous Decomposition of Austenite in to Several Transformation Kinetics,” *Acta Matall.*, Vol. 45, No. 7, pp. 2911-2920.

35 Ashby, M.F., and Easterling, K.E., 1982, “A First Report on Diagrams of Microstructure and Hardness for Grain Growth in Welds,” *Acta Metall.*, Vol. 30, No. 11, pp. 1969-1978.

36 Ion, J. C., Easterling, K. E., and Ashby, M. F. 1984. "A second report on diagrams of microstructure and hardness for heat-affected zones in welds," *Acta. Metall.*, Vol. 32, pp. 1949-1962.

37 Miranda, R.M., and Fortes, M.A., 1989, "Austenite Grain Growth, Microstructure and Hardness in the Heat-Affected Zone of a 2.25Cr-1Mo Steel," *Mater. Sci. Eng*, Vol. 108A, pp. 1-8.

38 Moon J., Lee, J., and Lee, C., 2007, "Prediction for the austenite grain size in the presence of growing particles in the weld HAZ of Ti-microalloyed steel," *Materials Science and Engineering A*, Vol. 459, pp. 40-46.

39 Kirkaldy, J. S. and Venugopalan, D., "Prediction of Microstructure and Hardenability in Low Alloy Steels," in *Phase Transformations in Ferrous Alloys*, eds. A. R. Marder and J. I. Goldstein, pp. 125-148, AIME, Philadelphia, PA, 1984.

40 Henwood, C., Bibby, M. J., Goldak, J. A., and Watt, D. F., "Coupled Transient Heat Transfer-Microstructure Weld Computations. Part B," *Acta Metallurgica*, Vol. 36, 1988, pp. 3037-3046.

41 Zhang, W., Boring, M. A., and Chen, Y., "Incorporation of Enhancements to PRCI Thermal Analysis Model for Hot Tap Welding – Version 5.0", Final Report to Pipeline Research Council International (PRCI), Arlington, VA, Contract No. PR-185-05409, EWI Project No. 48478CSP, Edison Welding Institute, Columbus, OH, November, 2007.

42 Wang, Y.-Y. and Orth, F., "Development of Fracture Assessment and Testing Procedures for HAZ Cracks, Progress Report – Fracture Toughness Testing of Through-Thickness Notched HAZ Cracks," EWI Project No. 06224CPG, September 17, 1997.

43 Liu, M., Wang, Y.-Y., and Horsley, D., "Significance of HAZ Softening on Strain Concentration and Crack Driving Force in Pipeline Girth Welds", *Proceedings of OMAE2005, 24th International Conference on Offshore Mechanics and Arctic Engineering* (OMAE 2005).

44 Wang, Y.-Y., Liu, M., and Horsley, D. J., "Some Aspects of Material and Welding Specifications for Strain-Based Design of Pipelines", *Proc. of EPRG-PRCI-APIA 15th Joint Technical Meeting on Pipeline Research*, Orlando, FL, USA, May 17-19, 2005.

45 Jayadevan, K.R., Ostby, E., and Thaulow, C., "Fracture response of pipelines subjects to large plastic deformation under tension" *Int. J. Pressure Vessels and Piping*, Vol. 81, pp. 771-783, 2004.

46 Liu, M., and Wang, Y.-Y., "Significance of Biaxial Stress on the Strain Concentration and Crack Driving Force in Pipeline Girth Welds with Softened HAZ," *Proceedings of the 26th International Conference on Offshore Mechanics and Arctic Engineering*, OMAE2007-29415, OMAE2007, June 10-15, 2007, San Diego, California, USA.

47 Fan, J. H., and Hao, S., "A Design-Centered approach in developing Al-Si-based light weight alloys with enhanced fatigue life and strength," accepted for publication by *J. Computer-Aided Materials Design,* 2004.

48 Hao, S., et al., "Multi-Scale Modeling and Simulation for Computational Alloys Design and a Quasi-Particle Dynamics Approach," *The 6th World Congress of Computational Mechanics*, 2004.

49 Hao, S., et al., "Multi-Scale Constitutive Model and Computational Framework for the Design of Ultra-High Strength, High Toughness Steels," *International Conference on the Mechanics of Heterogeneous Materials*, Chungchin, China, 2004.

50 Nyhus, B., Polanco, M. L., and Ørjasæther, O., "SENT Specimens An Alternative To SENB Specimens For Fracture Mechanics Testing Of Pipelines," paper #OMAE2003-37370, *Proceedings of OMAE03, 22nd International Conference on Offshore Mechanics and Arctic Engineering*, June 8–13, 2003, Cancun, Mexico.

51 Rudland, D. and Wang, Y.-Y., "Low-Constraint Testing of Pipeline Girth Welds," IPC2006-10492, Proceedings of IPC 2006, *2006 International Pipeline Conference*, September 25-29, 2006, Calgary, Alberta, Canada.

52 McClintock, F. A., "Slip Line Fracture Mechanics: A New Regime of Fracture Mechanics," Professor Jerry L. Swedlow Memorial Lecture, in *Fatigue and Fracture Mechanics*, Vol. 33, ASTM STP 1417, W. G. Reuter and R. S. Piascik, Eds., American Society for Testing and Materials, West Conshohocken, PA 2002.

53 Haq, F., "Fully-Plastic Back-Bend Tests for Low-Triaxiality Plane Strain Crack Growth," MIT Master's Thesis, 2002.

54 Liu, M., and Wang, Y.Y., "Low-Constraint Backbend Test Of High Strength Steels: Crack Driving Force Calibration," *6th International Pipeline Conference*, Paper IPC2006-10414, September 25-29, 2006, Calgary, Alberta, Canada.

55 Wilkowski, G., Rudland, D. and Wolterman, R., "Predicting The Brittle-To-Ductile Fracture Initiation Transition Temperature For Surface-Cracked Pipe From Charpy Data," Paper PVP2005-71199, *Proceedings of ASME-PVP 2005 ASME/JSME Pressure Vessels And Piping Conference*, Denver Colorado, July 17-21, 2005.

56 C. Williams, F. Brust, P. Scott, D. Rudland, and G. Wilkowski, "Validation of an Estimation Procedure to Predict the Quasi-static Brittle-to-Ductile Fracture Initiation Transition Temperature (FITT) for Ferritic Piping," *Proceedings of ASME-PVP 2005 ASME/JSME Pressure Vessels And Piping Conference*, Denver Colorado, July 17-21, 2005.

57 Wilkowski, G., Rudland, D., Mincer, P., Rider, D., and W. Sloterdijk "When Old Line Pipe Initiates Fractures in a Ductile Manner," paper # IPC2006-10326, *2006 International Pipeline Conference*.

58 Wilkowski, G. and Eiber, R. "Evaluation of the Inherent Safety Factors in the Tentative API Girth Weld Defect Tolerance Approach," American Gas Association, Catalog No. L51385, June 1977.

59 Joyce, J. A., Ernst, H., and Paris, P.C., "Direct Evaluation of J Resistance Curves for Load Displacement Records," *Fracture Mechanics: Twelfth Conference*, ASTM STP 700, 1980, pp. 222-236.

60 Wilkowski, G., Olson, R., and Scott, P., "State-of-the-Art Report on Piping Fracture Mechanics," U.S. Nuclear Regulatory Commission report NUREG/CR-6540, BMI-2196, February 1998.

61 Wilkowski, G., Barnes, C., Scott, P., and Ahmad, J., "Development of Analyses to Predict the Interaction of Fracture Toughness and Constraint Effects for Surface Cracked Pipes," report to A.G.A. Welding Supervisory Committee, April 25, 1985.

62 Wilkowski, G., and others, "Degraded Piping Program - Phase II, Summary of Technical Results and Their Significance to Leak-Before-Break and In-Service Flaw Acceptance Criteria," March 1984-January 1989, NUREG/CR-4082, Vol. 8, March 1989.

63 Wilkowski, G., Krishnaswamy, P., Brust, F., Francini, R., Ghadiali, N., Kilinski, T., Marschall, C., Mohan, R., Rahman, S., Rosenfield, A., Rudland, D., Scott, P., "Key Results

for the NRC's Short Cracks in Piping and Piping Welds Research Program," NUREG/CP-0139, October 1994.

64 Wilkowski, G., Schmidt, R., Scott, P., Olson, R., Marschall, C., Kramer, G., and Paul, D., "International Piping Integrity Research Group (IPIRG) Program", NUREG/CR-6233 Vol. 4, June 1997.

65 Hopper, A., Mayfield, M., Olson, R., Scott, P. and Wilkowski, G., "Overview of the IPIRG-2 Program - Seismic Loaded Cracked Pipe System Experiments," *13th SMiRT Conference*, August 1995.

66 Wilkowski, G. and Maxey, W., "Applications of the Electric Potential Method for Measuring Crack Growth in Specimens, Flawed Pipes, and Pressure Vessels," *ASTM 14th National Symposium on Fracture Mechanics*, Los Angeles, California, ASTM STP 791, June 30, 1981.

67 Wilkowski, G., Wambaugh, J., and Krishnaswamy, P., "Single Specimen J-Resistance Curve Evaluations Using the Direct-Current Electric Potential Method and a Computerized Data Acquisition System," *ASTM 15th National Symposium on Fracture Mechanics*, ASTM STP 833, June, 1982, pp. 553-576.

68 Hill, R., "A theory of yielding and plastic flow of anisotropic metals," *Proc. Roy. Soc. London A*, Vol. 193, 1948, pp. 281-97.

69 Barlat, F. and Lian, J., "Plastic behavior and stretchability of sheet metals. Part I: a yield function for orthotropic sheets under plane stress conditions," *Int. J. Plasticity*, Vol. 5, 1989, pp. 51-66.

70 Hill, R., "Constitutive modeling of orthotropic plasticity in sheet metals," *J. Mech. Phys. Solids*, Vol 38, 1990, pp. 405-17.

71 Hill, R., "A user friendly theory of orthotropic plasticity in sheet metals," *Int. J. Mech. Sci.*, Vol. 35, 1993, pp. 19-25.

72 Mahbadi, H. and Eslami, M. R., "Cyclic loading of thick vessels based on the Prager and Armstrong-Frederick kinematic hardening models," *Int. J Pressure Vessels and Piping*, Vol. 83, 2006, pp. 409-419.

73 Lemaitre, J., and Chaboche, J. L., "Mechanics of Solid Materials", Cambridge University Press, 1985.

74 Liu, M. and Wang, Y.-Y. "Modeling of anisotropy of TMCP and UOE line pipes," *Proceedings of the 16th International Offshore and Polar Engineering Conference*, San Francisco, CA, May 28 – June 2, 2006, pp. 221-227.

75 Martinez, M. and Brown, G., "Evolution of pipe properties during reel-lay process: experimental characterization and finite element modeling," *Proc. of 24th Int. conf. Offshore Mech. Arctic Engg.,* Halkidiki, Greece, June 12-17, 2005, OMAE2005-67074.

76 Taylor, G., "Plastic strains in metals," *J. Inst. Metals*, Vol. 62, 1938, pp. 307-324.

77 Kothari, M. and Anand, L., "Elasto-viscoplastic constitutive equations for polycrystalline metals: application to Tantalum," *J. Mech. Phys. Solids*, Vol. 46, pp. 51-83, 1998.

78 Tang, H., Banerjee, A., and Parks D. M., "An investigation on the mechanical behavior of X100 pipe-steels under monotonic loading conditions: experiments and simulations," (submitted for publication in 2008).

79 Liu, M., and Wang, Y. -Y., "Advanced Modeling of Plasticity of Line Pipe Steels with Anisotropic Texture and Complex Loading History," *ISOPE 2007*, Paper No. 2007-SBD-12, 2007.

80 Kallend, J. S., Kocks, U. F., Rollett, A. D., and Wenk, H. R. (1989), “PopLA: the preferred orientation package from Los Alamos,” Los Alamos National Laboratory, TMS, Warrendale, PA.

81 Bruschi, R., Bartolini, L., Spinazzè, M., Torselletti, E., and Vitali, L., “A numerical lab to predict the strength capacity of offshore pipelines,” *Proc. of 24th Int. Conf. Offshore Mech. Arctic Engg.,* Halkidiki, Greece, June 12-17, 2005, OMAE2005-67482.

82 Webster, S. and Bannister, A., *Engineering Fracture Mechanics*, Vol. 67 (2000), pp. 481-514.

83 Mannucci, G., Di Vito, L., Malatesta, G., Izquierdo, A., and Cumino, G., “Evaluation of the Effect of Yield-to-Tensile Ratio on the Structural Integrity of an Offshore Pipeline by a Limit-State Design Approach,” *Proceedings of the 4th International Conference on Pipeline Technology*, May 9-13, 2004, Ostend, Belgium, pp. 1283.

84 Shih, C. F., deLorenzi, H. G., and Andrews, W. R., “Studies on crack initiation and stable crack growth,” in *Elastic-Plastic Fracture*, ASTM STP 668, 65-120, ASTM, Philadelphia, PA, 1979.

85 Wang, Y.-Y., Cheng, W., McLamb, M., Horsley, D., Zhou, J., and Glover, A., “Tensile Strain Limits of Girth Welds with Surface-Breaking Defects Part I An Analytical Framework,” in *Pipeline Technology, Proceedings of the 4th International Conference on Pipeline Technology,* Edited by Rudi Denys, Ostend, Belgium, May 9-13, 2004.

86 Needleman, A. and Tvergaard, V., “An analysis of ductile rupture modes at a crack tip,” *J. Mech. Phys. Solids*, 35, pp. 151-183, 1987.

87 Xia, L. and Shih, C.F., “Ductile crack growth – I: A numerical study using computational cells with microstructurally-based length scales,” *J. Mech. Phys. Solids*, 43, pp. 233-259, 1995.

88 Liu, M. and Wang, Y-Y., “Applying Gurson Type of Damage Models to Low Constraint Tests of High Strength Steels and Welds,” *Proceedings of IPC 2006, 6th International Pipeline Conference* (IPC 2006), September 25-29, 2006, Calgary, Alberta, Canada, Paper IPC2006-10416.

89 Faleskog, J., Gao, X., and Shih, C.F., “Cell model for nonlinear fracture analysis – I. micromechanics calibration,” *Int. J. Fract.*, 89, pp. 355-373, 1998.

90 Gao, X., Faleskog, J., and Shih, C.F., “Cell model for nonlinear fracture analysis – II. Fracture-process calibration and verification,” *Int. J. Fract.*, 89, pp. 375-398, 1998.

91 Eiber, R., Maxey, W., and Duffy A., “Investigation of the Initiation and Extent of Ductile Pipe Rupture,” BMI Report 1908 to AEC, 1971.

92 Wilkowski, G. and Eiber, R., “Evaluation of Tensile Failure of Girth Weld Repair Grooves in Pipe Subjected to Offshore Laying Stresses,” *ASME Journal of Energy Technology*, March, 1981, pp. 48-57.

93 Miller, A., "Review of Limit Codes of Structure Containing Defects," *International Journal of Pressure Vessels and Piping*, Vol. 32, 1988, pp. 191-327.

94 Kanninen, M. F., Broek, D., Marschall, C. W., Rybicki, E. F., Sampath, S. G., Simonen, F. A., and Wilkowski, G. M., “Mechanical Fracture Predictions for Sensitized Stainless Steel Piping with Circumferential Cracks,” EPRI Report NP-192, September 1976.

95 Scott, P. and Wilkowski, G., “Development and Application of a Database of Pipe Fracture Experiments,” in *Fatigue and Fracture - 1996* - Volume 1, PVP - Vol. 323, July 1996, pp. 13-26.

96 Wang, Y.-Y., Rudland, D., and Horsley, D., "Development of a FAD-Based Girth Weld ECA Procedure, Part II Experimental Verification," *Proceedings of the 4th International Pipeline Conference*, Calgary, Alberta, Canada, September 29-October 3, 2002.

97 *Welding of Pipelines and Related Facilities*, API Standard 1104 Appendix A, July 2007.

98 Rosenfeld, M. J., "Serviceability of Corroded Girth Welds," PRCI Catalogue No. L51742, May 1996.

99 Glover, A. G., "Effects of Real Defects on Girth Weld Fracture Behavior," PRCI Catalogue No. L51457e, June 1984.

100 Glover, A. G., "Small and Full Scale Fracture of Thick Section Girth Weldments," PRCI Catalogue No. L51533e, March 1987.

101 Erdogan, F., "Theoretical and Experimental Study on Fracture in Pipelines Containing Circumferential Flaws," DOT Report DOT-RC-82007, by Lehigh University, August 1982.

102 Worolok, M. J., Piok, R. J., and Glover, A. G., "The Effect of Misalignment on the Fracture Behavior of Girth Welds," PRCI Catalogue No. L51489e, August 1985.

103 Hopkins, P., Demofonti, G., Knauf G., and Denys, R., "An Experimental Appraisal of the Significance of Defects in Pipeline Girth Welds," Paper 20, *Proceedings of the EPRG/NG18 Eighth Biennial Joint Technical Meeting on Line Pipe Research*, Paris, May 14-17, 1991.

104 Wilkowski, G., and Scott, P., "A Statistical Based Circumferentially Cracked Pipe Fracture Mechanics Analysis for Design on Code Implementation," *Nuclear Engineering and Design*, Vol. III, 1989, pp. 173-187.

105 Wilkowski, G., and Kramer, G., "An Energy Balance Approach to Estimate the Initiation and Arrest of Ductile Fracture Instability in Circumferentially Cracked Pipe," ASME Special Technical Publication, Vol. 167, July 1989, pp. 103-114.

106 Liu, M., and Wang, Y.-Y., "Significance of Biaxial Stress on the Strain Concentration and Crack Driving Force in Pipeline Girth Welds with Softened HAZ," *OMAE 2007*, paper # OMAE2007-29415, June 2007.

107 Shen, G., and Tyson, W. R., "Effect of Biaxial Stress on Crack Driving Force", *Proceedings of PVP2006-ICPVT-11*, July 2006.

108 Krishnaswamy, P., Wilkowski, G., Mohan, R., Scott, P., Rahman, S., Choi, Y., and Ghadiali, N., "Improvements to Surface-Cracked Pipe J-estimation Schemes, Validation by Experiments, and Proposed Modification of the ASME Section XI Pipe Flaw Evaluation Criteria," *21st MPA Seminar*, October 1995.

109 Mohr, W., "Weld area mismatch and pressure effects in strain-based design," *Proceedings of 4th International Conference on Pipeline Technology*, Volume 1, May 2004, pp. 279-290.

110 "Validation and Documentation of Tensile Strain Limit Design Models for Pipelines – Project No. 1," (PRCI Project Ref: ABD-1, Contract No. PR-276-064507), DOT OTA No. DTPH56-06-000014, (on-going project).

111 Rudland, D. L., Scott, P. M., and Wilkowski, G. M., "The Effect of Cyclic and Dynamic Loads on Carbon Steel Pipe," NUREG/CR-6438, February 1996.

112 Brust, F. and Leis, B., "Primary Creep Crack Growth at Room Temperature in Surface Cracked Pipes," *Int. Journal of Pressure Vessels and Piping*, Vol. 52, pp 273-298, 1992.

113 Brust, F.W, and Leis, B.N.," A New Model for Characterizing Primary Creep Damage," *Int. Journal of Fracture*, Vol. 54, pp 45-63, 1992.

114 Hopper, A., Wilkowski, G., Scott, P., Olson, R., Rudland, D., Kilinski, T., Mohan, R., Ghadiali, N., and Paul, D., "*The Second International Piping Integrity Research Group (IPIRG 2) Program - Final Report*," NUREG/CR-6452, February 1997.

115 Olson, R., Wolterman, R., and Wilkowski, G., "FEM Predictions of the HDR Circumferentially Cracked Pipe Experiments," ASME PVP Vol. 280, June 1994, pp. 165-182.

116 Rudland, D., Wang, Y.-Y., and Wilkowski, G., "Developing Dynamic Steady-State Ductile Fracture Toughness Test Procedures from a DWTT-Size Specimen," *Proceedings of 2000 IPC Conference*, Calgary Alberta, Canada, October 8, 2000.

117 Warke, R.W., Wang, Y.-Y., Ferregut, C., Carrasco, C., and Horsley, D.J., "A FAD-Based Method for Probabilistic Flaw Assessment of Strength-Mismatched Girth Welds," in *Probabilistic and Environmental Aspects of Fracture and Fatigue*, ASME PVP Vol. 286, 1999.

118 Wang, Y.-Y., Rudland, D., Horsley, D., "Development of a FAD-Based Girth Weld ECA Procedure, Part I Theoretical Framework," *Proceedings of the 4th International Pipeline Conference*, Calgary, Alberta, Canada, September 29-October 3, 2002.

119 Wang, Y.-Y., Rudland, D., and Crompton, J. "Development of Structural Integrity Assessment Procedures and Software for Girth-Welded Pipes and Welded Sleeve Assemblies," PRCI Contract PR-185-9831, final report, March 2002.

120 Chapuloit, S., Lacire, M. H., and Le Delliou, P., "Stress Intensity Factors for Internal Circumferential Cracks in Tubes over a Wide Range of Radius over Thickness Ratios," PVP Vol. 365, ASME 1998, pp. 95-106.

121 Schawable, K.-H., et al., EFAM ETM-MM 96, "The ETM Method for Assessing the Significance of Crack-Like Defects in Joints with Mechanical Heterogeneity (Strength Mismatch)," GKSS 97/E/9, Geesthacht, 1997.

122 Wang, Y.-Y., and Chen, W., "Guidelines on Tensile Strain Limits," GRI-8658, September 2003.

Appendix 1

Summary Report
on

Weld Metal Toughness Prediction Using Neural Network Methods

Summary Report

on

Weld Metal Toughness Prediction Using Neural Network Methods

May 5, 2005

Engineering Mechanics Corporation of Columbus
3518 Riverside Drive
Suite 202
Columbus, OH 43221

This page is intentionally left Blank.

Table of Contents

1.0 Introduction 1
1.1 Background 1
1.2 Mechanical Property Predictions Based on First Principles 1
1.3 Empirical Methods 3
2.0 Literature Review on Weld Metal Toughness and its Prediction 3
2.1 Weld Metal Toughness 3
2.2 Factors Influencing Charpy Toughness 4
2.2.1 Alloying Elements 4
2.2.2 Microstructure 8
2.2.3 Other Factors 11
2.3 Prediction Based on Microstructural Characteristics 12
2.4 Traditional Empirical Methods 12
2.5 Neural Network Model 13
2.5.1 Principle of Neural Network 13
2.5.2 Applications in Toughness Prediction 15
3.0 Toughness Prediction Using Neural Network at Emc2 20
4.0 Concluding Remarks 23
5.0 References 23

List of Figures

Figure 1: Effect of niobium on 55 J transition temperature of weld metal [20]............... 6

Figure 2: Effect of molybdenum on 55 J transition temperature of weld metal [20]....... 7

Figure 3 Influence of weld metal nickel and manganese contents on Charpy toughness in J at -50^0C [23] 7

Figure 4 Effect of chromium on 50 J transition temperature of weld metal [30]............ 8

Figure 5: Impact toughness at -60^0C as a function of acicular ferrite content [39]....... 10

Figure 6: The relationship between ferrite grain size and Impact toughness at -60^0C [52].. 11

Figure 7: Variation of 47 J transition temperature with overall MFP [53] 11

Figure 8: Illustration of a neural network. (a) Overall architecture; (b) A single neuron/hidden unit [66].. 15

Figure 9: Comparison of predicted and measured Charpy toughness [70] 18

Figure 10: Combined effect of Mn and Ni on the calculated weld toughness at -40^0C [75] 18

Figure 11: Comparison of predicted and measured T_{27J} [71]... 19

Figure 12: Computed T_{27J} contour lines in °C [71]. (a) Neural network predictions; (b) Predictions using the empirical formula given in Equation 4......................... 19

Figure 13: Variations of Charpy toughness values at –18 and –51°C as functions of oxygen concentration [73] 19

Figure 14: Sensitivity analysis of neural network model [53] 20

Figure 15: Predicted variation of weld toughness with oxygen content 22

Figure 16: Comparison of predicted and measured weld toughness................................ 22

1.0 Introduction

1.1 Background

Predictions of weld microstructure and mechanical properties are among the targets of mathematical modeling of weld phenomena. Weld integrity assessment requires the knowledge of the mechanical properties in the weld region. Significant progress has been made in numerical simulation of weld microstructure in the past decade. It is now possible to predict the microstructure of welds from their chemical composition and welding parameters. Most reported microstructure models are formulated using the fundamental phase transformation thermodynamics and kinetics theories and can render predictions with reasonable accuracy. There are two major approaches to the predictions of weld mechanical properties: predictions based on first principles and empirical methods. Very limited advancement has been made in numerical modeling of weld mechanical properties, especially the predictions based on first principles. However, the empirical methods developed in recent years show promisingly fair predictability. The confidence of their predictions is attributed to the two main features of these empirical models. First, they employ modern computational techniques such as non-linear regression implemented with neural network; secondly, they incorporate large experimental databases.

1.2 Mechanical Property Predictions Based on First Principles

Theoretically, prediction of weld mechanical properties can be achieved through applying first principles such as physical metallurgy principles to numerical modeling. However, it becomes a daunting task due to the complexity inherent in welds. The approach can be demonstrated on predicting yield strength, which is easier to be computed than other properties such as toughness. The computation can be established on microstructure-property relationships. It starts with calculating the yield strength of individual microstructural constituent as a function of its morphology and strengthening mechanisms. The relationship is expressed in the following equation [1].

$$\sigma = \sigma_{Fe} + \sum_{i} x_i \sigma_{SS_i} + \sigma_C + K_L (\overline{L})^{-1} + K_D \rho_D^{0.5} \qquad \text{Equation 1}$$

where σ_{Fe} is the strength of pure iron; x_i is the concentration of a substitutional solute represented by a subscript i; σ_{SSi} is the substitutional solute (i) strengthening; σ_C is the solid solution strengthening due to carbon; K_L is the coefficient for strengthening due to lath size; $\overline{L}$ is the measure of ferrite plate size; K_D is the coefficient of strengthening due to dislocations; and ρ_D is the dislocation density. After obtaining the yield strength of each microstructure in a weld using the equations similar to Equation 1, the yield strength of the weld is expressed as a function of those of the microstructural constituents using rule of mixture [2,3], as described in Equation 2.

$$\sigma_{YS} = \sum_i \sigma_i V_i \qquad \text{Equation 2}$$

where V_i is the volume fraction of phase i and σ_i is the corresponding strength.

It is very difficult, if not impractical to apply the property prediction method described above. As stated by Bhadeshia and Svensson [4] the mechanical property modelling based on first principles has seen very slow progress and encountered tremendous difficulties. One difficulty would be determining all the coefficients in Equation 1 for each phase present in a weld. Another drawback of the microstructure-property relationships using the theoretical prescription is they fail to address the inherent complexity in real welds. For example, the variations in mechanical properties are prevailing phenomena in welds and cannot be quantified using any theoretical formulation. There are many influencing factors contributing to the variations and there is no satisfactory theory available to cope with them.

It is known that measured Charpy toughness values exhibit the widest variations among the weld mechanical properties, and consequently it is even more difficult to predict the weld Charpy toughness than the other properties such as yield strength and hardness. Large scatter in the weld toughness is due to the microstructural and mechanical inhomogeneity associated with welds. The inhomogeneity of weld metal is considerably greater than that of base metal and the corresponding scatter in experimental toughness values is greater.

Compared to the Charpy toughness, it is easier to compute the hardness in welds based upon first principles. There has been significant advancement in modeling microstructure and hardness in weld metal and HAZ during the pass twenty years. The complex transformation in the HAZ were modeled by Ion, Easterling and Ashby in 1984 [5]. The model contained a distributed heat source to represent the welding arc, adapted from Rosenthal’s theory of heat flow. A key feature of the model was the concept of kinetic strength, a parameter which, by combining time and temperature, enables the effect of continuous heating or continuous cooling on the kinetics of transformation to be modeled. They were therefore able to calculate the dissolution and growth rates of carbides and nitrides during the heating part of the thermal cycle, and hence the effect of microalloying elements on the growth of austenite grains in the HAZ. Transformations during cooling were modeled using a representation of experimental continuous cooling transformation diagrams within a loose Avrami formulation. Finally, the hardness was related to the microstructure using a rule of mixture, the hardness of the individual phases being estimated from empirical equations containing chemical composition and cooling rate as variables.

1.3 Empirical Methods

Empirical methods have been utilized to predict weld mechanical properties for more than three decades. For example, there are number of empirical hardness estimation formulae available in the open literature since the 1970s [6,7,8,9,10,11,12,13]. Yield strength was also calculated using close-formed empirical equations and frequently expressed as a function of hardness, i.e. according to the following equation from Reference 14.

$$\sigma_{YS} = \frac{9.8}{3} HV(0.1)^n \qquad \text{Equation 3}$$

where σ_{YS} is the yield strength in MPa; HV is the Vickers hardness number, and n is the strain hardening coefficient, which is 0.09 for steel.

Empirical methods were widely used on weld toughness prediction and will be reviewed in the subsequent section. The empirical methods developed in recent years show promisingly fair predictability. The confidence of their predictions is attributed to the two main features of these empirical models. First, they employ modern computational techniques such as non-linear regression implemented with neural network; secondly, they incorporate large experimental databases.

2.0 Literature Review on Weld Metal Toughness and its Prediction

2.1 Weld Metal Toughness

The measure of material toughness investigated in this study is the Charpy toughness. The Charpy test involves impacting a square section notched bar with a pendulum under specified temperatures. The energy of separation in notched specimens is taken as a measure of toughness, which is also referred to as the absorbed energy. The Charpy test is often mentioned as impact test and the Charpy toughness as impact toughness. The Charpy toughness lacks the mathematical rigor and predictive capabilities of the toughness parameters formulated with fracture mechanics methods, i.e. K_{IC} [15]. However, the Charpy test is one of the most common tests used to estimate material toughness and widely applied to structural materials including pipeline steels. It is specified in many international standards. It is a vital material screening and quality control indicator in pipeline welding operations and in this sense it is the subject of this investigation.

The Charpy toughness provides a qualitative indication of material toughness. The test is usually conducted at different temperatures to obtain the Charpy transition curve characterizing the ductile-to-brittle fracture transition. It is well known that large scatter exists in the Charpy data of weld region including weld and HAZ; thus a sufficient number of tests are needed to capture the entire statistical distribution of the material toughness [16,17]. The statistical scatter in weld metal toughness is caused by many factors, which will be elaborated on in the next section. Some of the scatter is nevertheless attributed to the inherent characteristics of welding such as non-uniform heating and cooling. Welding is a thermal-mechanical-metallurgical fabrication process and introduces variations of microstructure, properties and, residual stresses in the weld region.

Based on the observation that steel undergoes a ductile to brittle transition as the temperature of Charpy impact test is reduced, Charpy toughness is frequently characterized by the transition temperature corresponding to a certain value of the absorbed impact energy. Higher toughness values translate into lower transition temperatures.

2.2 Factors Influencing Charpy Toughness

The Charpy toughness of a weld depends on a large number of factors, such as chemical compositions of base and filler metal, welding parameters, post-weld heat treatment, and testing temperature. Extensive research efforts were made to investigate the effects of these influencing factors on weld metal toughness. The factors are categorized into four groups and the their effects on the toughness are reviewed accordingly in the following contexts. Note that there often exist correlations and interactions between the effects of different factors and therefore it is impossible to separate one factor from another. For example, the microstructure in a weld determines its toughness and almost all other factors affect the toughness through altering its microstructure.

2.2.1 Alloying Elements

Svensson and Gretoft [18] investigated the effect of carbon and manganese on the impact toughness of C-Mn weld metals. It was found that the low-temperature toughness could be improved through balancing carbon and manganese in several combinations. Proper C-Mn combinations resulted in the microstructure with high portion of acicular ferrite that was essential to obtain the toughness improvement at low temperatures. Surian and de Vedia [19] reached the same conclusion in their study.

The effects of alloying elements on toughness were not straightforward but rather complex under some circumferences. Niobium was used in line pipe steels to improve strength and low-temperature toughness. When pipes were manufactured using submerged arc welding (SAW), which was a high-dilution process, niobium pick-up from the base plate into weld metal might degrade the weld metal toughness [20]. The study in Reference 20 indicated that niobium above 0.03% in the weld metal was strongly deleterious to the toughness, as illustrated in Figure 1. Note that the transition temperature was used as an indicator of toughness and lower transition temperatures corresponded to higher toughness values. The metallurgical examination revealed the deleterious effect was caused by the precipitation of niobium carbon-nitrides in the weld metal during cooling. The effect of carbon was also demonstrated in Figure 1. The transition temperature increased with the increasing carbon concentration. The toughness was improved when the alloying elements such as nickel and molybdenum were added to the weld metal, because these elements favored the formation of acicular ferrite. Figure 2 showed the effects of molybdenum and welding flux on toughness. Use of a moderate basic flux (flux A) produced the welds with lower transition temperatures than those made with a acid flux (flux B) in that the former reduced the oxygen level in the weld metal.

Research efforts were directed toward determining the effects of nickel and manganese on the microstructure and toughness of weld metals, especially the effect of their interactions [21,22,23,24,25]. Zhang and Farrar performed a systematic investigation on the microstructure and toughness of shielded metal arc (SMA) weld metals [23]. Their investigation was focused on 1) how a wide range of nickel and manganese contents influenced the toughness, 2) the interaction between nickel and manganese and the correlation with the microstructure and toughness, and 3) their effect on the morphologies of the microstructure components and other microstructural features, and how this could be related to toughness. It was found that both alloying elements promoted acicular ferrite at the expense of proeutectoid ferrite. The beneficial effect of acicular ferrite on toughness will be addressed in the subsequent section. The most significant finding in Reference 23 was that there was an optimum combination range of nickel and manganese for optimum toughness. Figure 3 showed the optimum combination range was 0.6~1.4% manganese and 1.0~3.7% nickel. Additions beyond the optimum range promoted the formation of martensite and other microstructural components that might be detrimental to toughness.

A number of authors researched the effect of chromium on the microstructure and toughness of C-Mn SMA welds [19,26,27,28,29]. They noticed that chromium promoted an increase in the volume fraction of acicular ferrite at the expense of primary ferrite. However, chromium impaired toughness even in the welds with large amounts of acicular ferrite. Such observation contradicted the common sense that high acicular ferrite content in the microstructure was beneficial to the weld toughness. Jorge et al. [30] further pointed out that the toughness was adversely affected by an increase in the chromium content, especially when the weight percentage of chromium exceeded 0.5%, as demonstrated in Figure 4. This study concluded that the increasing chromium content generated the higher volume fraction of martensite-austenite (M-A) constituent that led to the decreasing toughness.

Numerous studies indicated that the increasing oxygen or nitrogen content was detrimental to weld metal toughness [31,32,33,34,35,36,37,38]. Surian et al. [36] studied C-Mn-Ni SMA weld metal with 3% nickel to demonstrate the effect of oxygen content on the toughness of the these welds. The oxygen contents beyond 200~250 ppm greatly impaired the toughness of C-Mn-Ni weld metal. The toughness reduction was clearly associated with a larger size and greater number of oxide inclusions in the high-oxygen weld metal. In this study, magnesium powders were added to the electrode coatings and effectively reduced oxygen level in the weld metal. Magnesium was among the deoxidants frequently employed to control the oxygen content in the weld metal. However, different deoxidants might have different effects on the toughness. North et al. [37] investigated such effects in their study of the toughness of low oxygen content submerged arc (SA) welds. They found that the use of aluminum, rare-earth elements, manganese, silicon, and magnesium for deoxidizing welds below 220 ppm oxygen impaired the toughness, on the other hand, titanium and vanadium as deoxidants improved the toughness in welds with 200 ppm oxygen. Shinada et al. [38] demonstrated that improved toughness were attained in SA pipeline welds by retaining an appropriate amount of titanium after the oxidation of aluminum while keeping a low level of oxygen and nitrogen.

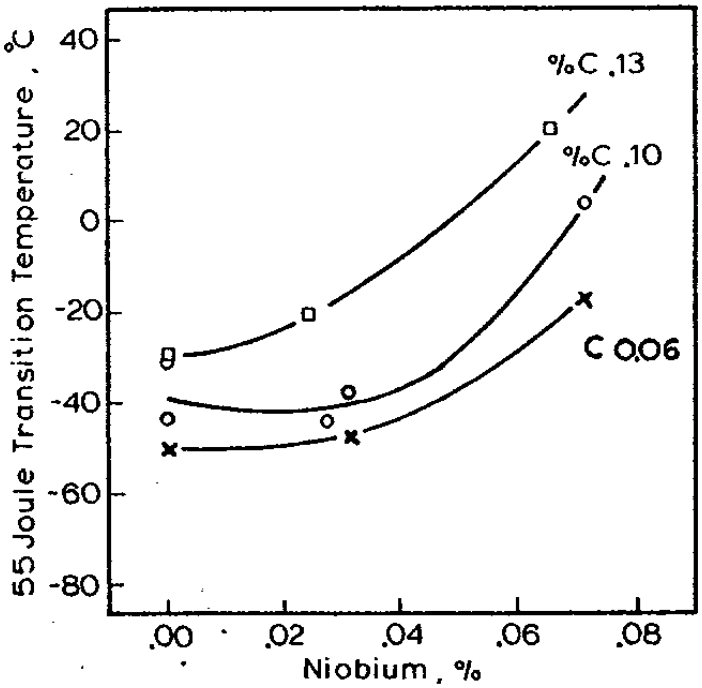

Figure 1: Effect of niobium on 55 J transition temperature of weld metal [20]

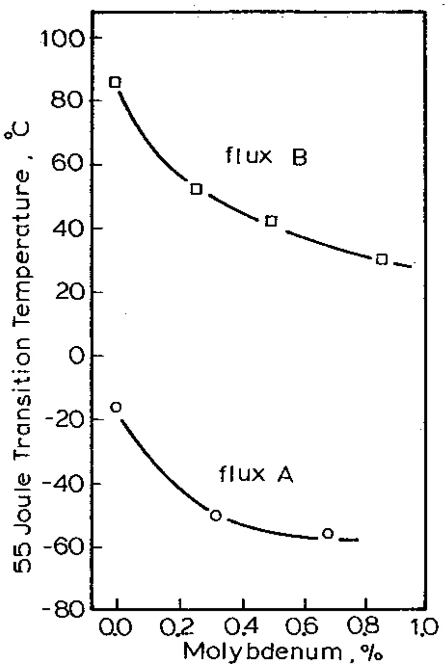

Figure 2: **Effect of molybdenum on 55 J transition temperature of weld metal [20]**

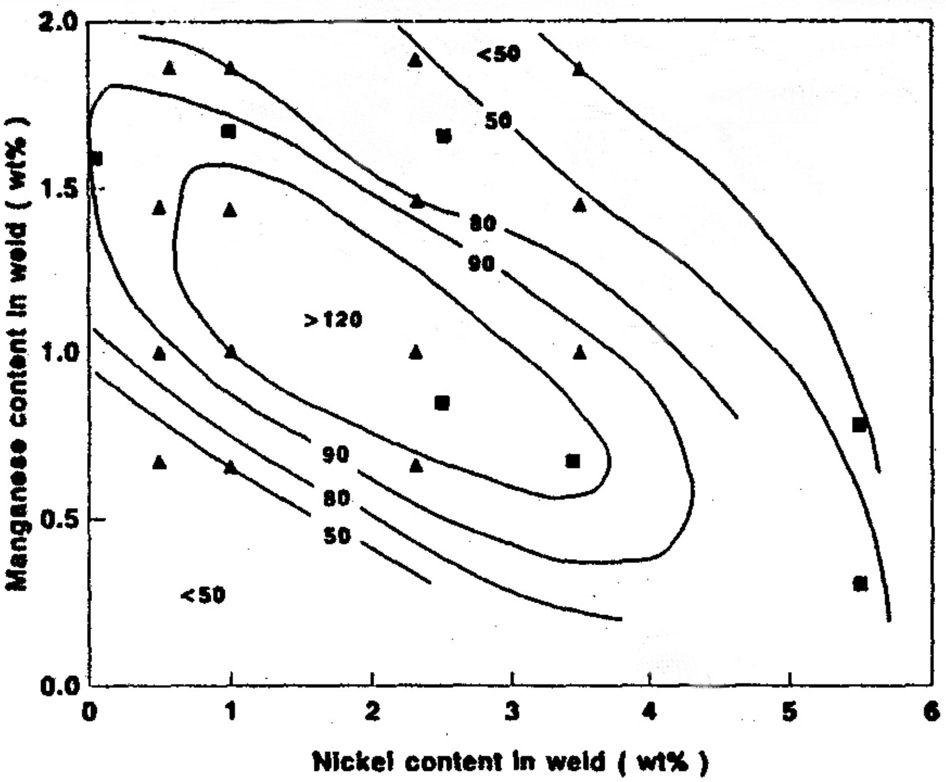

Figure 3 **Influence of weld metal nickel and manganese contents on Charpy toughness in J at –50^{0}C [23]**

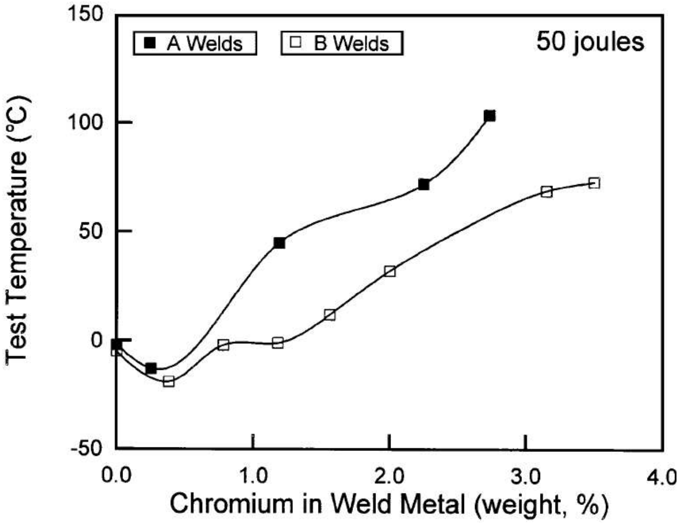

Figure 4 Effect of chromium on 50 J transition temperature of weld metal [30]

2.2.2 Microstructure

The effect of various alloying elements on the weld toughness has been the subject of many investigations. The effect was often examined through evaluation of the microstructure of weld metal. Microstructure evaluation was employed to establish two critical correlations: 1) chemical composition and microstructure, and 2) microstructure and toughness. Among the microstructural components of low carbon steel and high-strength low-alloy (HSLA) steel welds, acicular ferrite was found to be very important with respect to the toughness behavior. As discovered in the many investigations on low carbon and HSLA steel welds, the weld metal microstructure consisted of the following major components: grain boundary ferrite, ferrite side plates (Widmannstätten ferrite), acicular ferrite, and martensite. It was commonly believed that a high amount of acicular ferrite should be present in the microstructure to obtain good low-temperature impact toughness through the effect of fine grain size [39,40,41,42,43].

For low carbon and HSLA steels, it was generally believed that increasing amounts of acicular ferrite improved weld metal toughness and 80~90% acicular ferrite in the weld microstructure was necessary to obtain satisfactory toughness at low temperatures [40]. However, other investigations indicated the toughness did not always improved with the increasing acicular ferrite contents. Evans [39] and Svensson et al. [18] found that the toughness decreased if the contents were in excess of 70%, as shown in Figure 5. Zhang and Farrar [23] demonstrated the best toughness was associated with the microstructures containing 50~75% acicular ferrite. The mechanisms of the toughness reduction phenomenon mentioned above were debated among the researchers. Evans [39] argued that the decreasing toughness was due to increasing yield strength without a corresponding decrease in grain size. Other researchers pointed out a finer microstructure might not be always beneficial to the toughness when the deposits were overalloyed [18,23,42]. They provided the following reasoning:

> *Very high concentrations of acicular ferrite were achieved through adding high contents of alloying elements to the weld metal. High alloying contents produced increased amount of acicular ferrite as well as other microstructure components such as segregated microphases. These microstructure components might offset the beneficial effect of finer grains in acicular ferrite.*

The segregated microphases might appear as grain boundary carbides and dispersed regions of martensite or retained austenite. Grain boundary carbides might facilitate propagation of cleavage cracks across grain boundaries [44]. Martensite and retained austenite as microphases had detrimental effects on toughness by facilitating the nucleation of cleavage cracks [42]. When the microphases formed segregated bands, as in high-carbon and high-manganese welds, the situation was even worse, since cleavage cracks easily nucleate and propagate [18].

Addition of nickel and molybdenum suppressed proeutectoid ferrite (grain boundary ferrite and ferrite side plates) and upper bainite and favor acicular ferrite [20].

It was known that nonmetallic inclusions influenced acicular ferrite formation and certain types of inclusions were better nuclei for acicular ferrite than others [45,46]. However, it was also common knowledge that inclusions were detrimental to toughness. For ductile fracture, the increasing oxide inclusion content lowered the upper shelf energy in the Charpy toughness transition curve of the weld metal because the inclusions were easily debonded from the metal matrix [47,48]. For brittle fracture, the inclusions acted as cleavage initiation sites [49,50].

As mentioned above, the ferrites with different morphologies are the major microstructural components in low carbon and HSLA steel welds. The ferrite ‘grain size’ was considered a key factor in determining the weld metal toughness [51]. Higher toughness was usually associated with the microstructure with smaller grain size, as demonstrated in Figure 6 [52]. For example, acicular ferrite was believed to provide improved toughness over other types of ferrites such as packets or sheaves of bainitic ferrite because the grain size of acicular ferrite is smaller than those of the other types. The measurement of ferrite grain size is not straightforward due to the complexity of the microstructure in weld metal. In order to take account of such complexity, mean free path (MFP) was proposed and utilized as an index of ferrite grain size [53,54]. MFP gauges the average separation of boundaries between ferrite grains or crystals, regardless of the morphology of the ferrite. It was also described as mean linear intercept grain size or the characteristic distance between ferrite grain boundaries. Tsuei et al. [53] found that there existed apparent linear correlation between the weld metal MFP and tensile strength, but no definite relationship between the MFP and toughness. As shown in Figure 7, there was no consistent variation in the values of T_{47J} with MFP.

Some investigators demonstrated that reheated microstructure, or more precisely reautenized regions significantly affected the toughness in multipass welds [52,55,56]. In the multipass C-Mn weld metal, the weakest region where the cleavage crack initiated was just the region having the lowest toughness among various reheated zones [52]. The toughness of the weld metal depended upon the toughness of this weakest region. Heat input and alloying elements affected the toughness of the weakest region in the multipass weld.

It was generally recognized that the martensite-austenite (M-A) constituent in the weld metal seriously reduced its toughness [30,57,58,59]. The M-A constituent was found to form preferentially at the grain boundary region, at which stresses were more liable to be concentrated than at the intragranular region [57]. The M-A constituent was detrimental to the toughness because it acted as the starting point of a cleavage crack. It might facilitate propagation of the cleavage crack across the grain boundary if it had a slender morphology, i.e. its aspect ratio was greater than four [18].

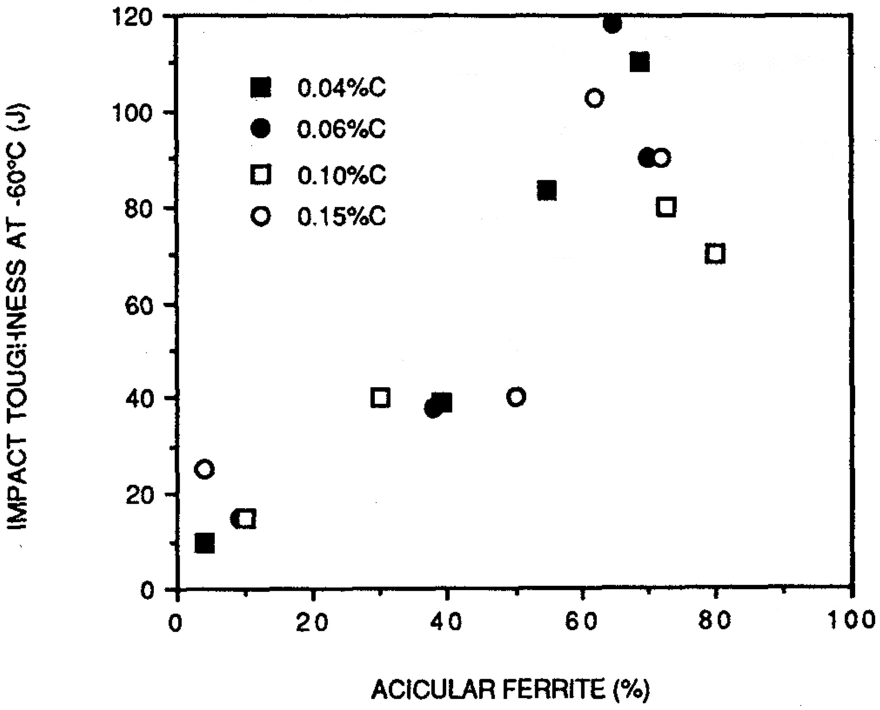

Figure 5: Impact toughness at –60^{0}C as a function of acicular ferrite content [39]

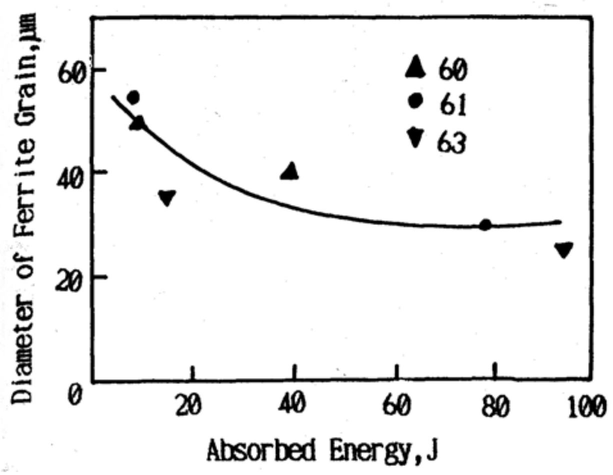

Figure 6: The relationship between ferrite grain size and Impact toughness at –60^{0}C [52]

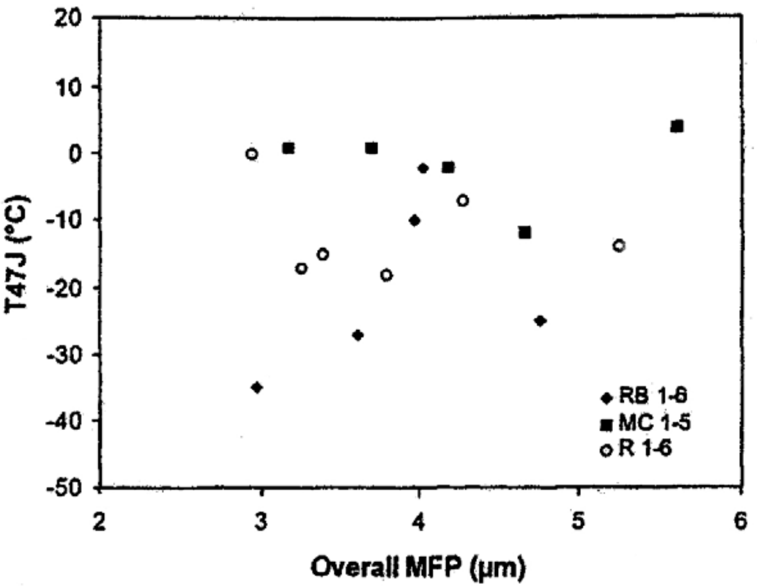

Figure 7: Variation of 47 J transition temperature with overall MFP [53]

2.2.3 Other Factors

In addition to the factors described above, there are many others more or less influencing the toughness of weld metal, such as post-weld heat treatment [60,61,62], welding procedure (i.e. heat input and welding position) [56,58,63], and weld metal mis-matching [19,64]. In summary, weld metal toughness is affected by many factors. They more or less contribute to the large scatter in measured toughness. Research efforts were attempted to generalize the relationships between weld toughness and various influencing factors. However, the established relationships were qualitative at best. It is extremely difficult, if not impossible to correlate toughness with the factors quantitatively.

2.3 Prediction Based on Microstructural Characteristics

Theoretically, weld toughness can be predicted based on the microstructure of weld metal. However, there are tremendous difficulties associated with such prediction due to the complexity of weld toughness phenomenon and lack of knowledge of the physics underlying the phenomenon. For example, the toughness improvement in ferritic steel welds can be achieved through adding nickel as an alloying element. Nevertheless, the increasing nickel concentration beyond a critical amount induces chemical segregation upon solidification and in turn leads to hard zones in the weld and reduced toughness. There is no rigorous thermodynamic algorithm correlating such metallurgical phenomenon to toughness. Indeed, no published research on such prediction was found in the literature review.

Tremendous efforts are needed to develop the toughness-prediction models based on the metallurgical principles. It will be long time before such models can be used to yield quantitative predictions.

2.4 Traditional Empirical Methods

In traditional empirical methods, the Charpy data were often correlated with particular variables using linear regression analysis. Although such methods may yield useful results, they could not describe the effects of various factors on mechanistic bases.

As described in section 2.1, Charpy toughness is often expressed in terms of a transition temperature that corresponds to a particular toughness value. There are many published empirical formulas for calculating the transition temperature. In a recent experimental study on toughness of multipass welds, French [65] expressed the temperature T_{27J} as a function of the yield strength, oxygen content, and the microstructure. The relationship is described in the following empirical equation:

$$T_{27J} = 0.007(YS) + 550(O) + 0.034(R) - 0.31(AF) - 74 \ {}^{\circ}\mathrm{C} \qquad \text{Equation 4}$$

Where T_{27J} is the transition temperature corresponding to a measured Charpy impact energy of 27 J, *YS* is the yield strength in MPa, *O* is the oxygen concentration in wt%, *R* is the reheated microstructure in area percentage, and *AF* is acicular ferrite as area percentage.

An empirical equation was presented in Reference 20 to calculate the 55-J transition temperature for pipeline seam welds. The equation is given below:

$$\begin{aligned} T_{55J} &= 1950C^2 - 8Ni + 12Cr + 1900Al + 3750(1+11C)Nb^2 \\ &\quad - 56Mo^{0.5} - 680\mathrm{Ti} - 7\mathrm{V}^{0.5} - 60 \ {}^{\circ}\mathrm{C} \end{aligned} \qquad \text{Equation 5}$$

C, Ni, Cr, Al, Nb, Mo, Ti, and V were the weight percentages of carbon, nickel, chromium, aluminum, niobium, molybdenum, titanium, and vanadium respectively. It was divulged in Equation 5 that niobium had significant deleterious effect on the toughness while other elements such as nickel and molybdenum were beneficial to the toughness. The applicable range of the formula was rather narrow since it was generated using linear regression analysis on the experimental data of the pipeline welds that were made with particular welding procedure, namely SAW with moderate basic flux.

2.5 Neural Network Model

As mentioned in the previous section about traditional empirical methods, when calculating weld mechanical properties empirically, many researchers utilize linear regression analysis where a property is correlated to input data through best-fitting exercises and the relationship is linear. While it is easy to formulate and use linear regression analysis, there are some difficulties associated with the method: (1) A linear relationship or pseudo-linear relationship with non-linear terms needs to be determined before analysis; (2) It is difficult to apply the regression equation across the entire input space if it spans widely; (3) The error of prediction cannot be precisely estimated if the input data are outside the input space, or in other words, beyond the range of fitted data. Obviously, linear regression analysis is not suitable for predicting weld metal Charpy toughness, which is affected by many variables with wide ranges and has large scatter in measured values. Neural network analysis is a better alternative to bypass the above-mentioned difficulties in that it can perform non-linear regression in addition to linear regression.

2.5.1 Principle of Neural Network

A brief introduction to neural network analysis is given here for the purpose of illustration. Full description of the method can be found elsewhere in abundant references. A neural network is a mathematical model formulated with learning algorithms which enable it to function as a memory. The terminology “neural” arise from the fact that this type of mathematical models is intended to emulate biological memories and simulate the process taking place in human nervous systems, with the hope of garnering some of the brain power. If presented in a simple mathematical expression, a neural network implements a function given in the following equation [66].

$$y = f(X;W) \qquad \text{Equation 6}$$

where y is the output of the network and is a non-linear function of the input variables X, and W are the weights used to parameterize the function f. As revealed in above mathematical presentation, the architecture of a neural network comprises input variables and output as well as their relationships which are defined through neurons or also called hidden units. Activity rules are assigned to neurons to constitute their activities in response to the perturbation to input variables. Learning rules are constructed within the network to make it chase the target values of the output, namely specifying the behavior of the weights in Equation 6. The principle of neural network is also demonstrated in the following example.

A schematic illustration of a typical two-layer neural network is given in Figure 8. The architecture of a single neuron/hidden unit is also shown in the same figure. Since a neural network consists of neurons, the implementation of the network is described using the single neuron. As illustrated in Figure 8b, the neuron has the inputs x_i and one output y. Each input is assigned a random weight w_i. The activity rule can be prescribed in the following equations:

$$a = \sum_i w_i \cdot x_i \qquad \text{Equation 7}$$

$$y = f(a) \qquad \text{Equation 8}$$

In Equation 7, each input x_i is multiplied by a random weight w_i and the products are summed together to compute the activation of the neuron a. In Equation 8, the output y is calculated as a function of the activation. The activation function $f(a)$ can be either linear or non-linear. The weights are systematically changed so that the output meets the target value, in other words, a best-fit description of the output with respect to the target is obtained. The learning rule specifies how the weights are changed. The operation is also called learning or training of a neural network.

Training of a neural network is achieved by searching the optimum relationship between the inputs and outputs. Network training is generally computationally intensive. After the network is trained, a set of equations is obtained along with a set of weights. The outputs are related to the inputs through combination of the equations and weights. Once training is completed, estimation of the outputs for any given inputs is very rapid [67].

In summary, a neural network is a non-linear regression analysis by nature. The non-linear regression is implemented through a non-linear function. The accuracy of the network is determined by the flexibility of the non-linear function, which augments with as the number of neurons/hidden units increases. Multiple input variables can be incorporated into the network and the interactions between them can be analyzed. Besides the predicted average values, the predictive errors can be estimated if a proper probability method is integrated with the network. Data collection and training of the network are needed before it can be used.

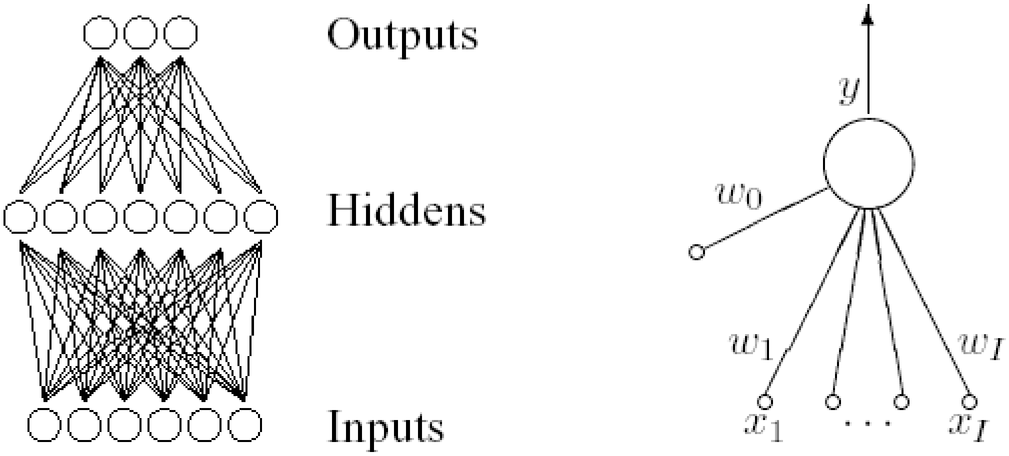

(a) (b)

Figure 8: Illustration of a neural network. (a) Overall architecture; (b) A single neuron/hidden unit [66].

2.5.2 Applications in Toughness Prediction

Neural network analysis has been recently used to predict weld mechanical properties including Charpy toughness [16,68,69,70,71,72,73,74,75,76,]. Most of the published researches reviewed in this study were conducted by Professor Bhadeshia of University of Cambridge and his collaborators [16,68-76]. The neural network model developed by this group of researchers will be referred to as the Cambridge model in the following context.

In the Cambridge model, hyperbolic tangent function was chosen as the activation function. This type of functions provides high flexibility, and moreover it can fit almost arbitrarily non-linear relationships by altering the weights and combining several functions. The model was integrated with a probability model, namely a Bayesian framework so that the predictive errors could be estimated. The method recognized that there were many functions which could be fitted or extrapolated into uncertain regions of the input space, without unduly compromising the fit in adjacent regions which were rich in accurate data. Instead of calculating a unique set of weights, a probability distribution of sets of weights was used to define the fitting uncertainty. The predictive errors expressed as error bars represented the uncertainty in the fitting parameters. The error bars were large when the input variables were in the uncertain regions of the input space where data were sparse or noisy. The predictive errors indeed indicated how accurate the prediction could be. For instance, large errors signified unreliable predictions.

Reference 70 presented training and application of a Charpy toughness model for ferritic steel welds. The neural network was built and training with a database containing 3142 experiments. The database was the largest among the published databases. The model was developed with 22 input variables including chemical compositions, welding heat input, interpass temperature, post-weld heat treatment temperature and time, and Charpy test temperature. The predicted Charpy toughness values were compared with the measured ones in Figure 9. The comparison indicated reasonably accuracy of the neural network model. The discrepancies between the prediction and measurement were evident, especially large error bars associated with certain data points. The discrepancies could be attributed to the large scatter in the measured Charpy toughness of weld metal and uneven distribution of the measured values over the entire input space. The model was utilized to study the effects of various factors on toughness.

The Cambridge model was utilized to investigate the interactions between the variables controlling Charpy toughness [74,75]. For example, the combined effect of manganese and nickel on the weld toughness was calculated, as illustrated in Figure 10 [75]. Contrary to the common belief that increasing the nickel concentration could improve the toughness of ferritic steel welds, the prediction revealed that more nickel reduced the toughness when the manganese concentration was high. The toughness could be increased in 7 – 9 wt. % nickel weld metal by reducing the manganese concentration. The trend in the calculated results was verified with experimental data in References 74 and 75.

As illustrated in the above example, the neural network analysis can be utilized to evaluate weld toughness in terms of interactive effects among multiple variables. Because of its flexibility, the neural network is capable of discovering more complex relationships in data than the traditional empirical method, which generally assumes a particular dependence of the predicted toughness on the given input variables. With respect to modeling the interaction between variables, the following example gives a comparison of the neural network and traditional empirical method.

The transition temperature T_{27J} was analyzed using the neural network [71]. The input variables of the model were yield strength, oxygen concentration, reheated microstructure, and acicular ferrite. The output was T_{27J} of multipass ferritic steel welds. Figure 11 showed the comparison of predicted and measured values of T_{27J}. The analysis results were also compared with those calculated using the empirical formula given in Equation 4, as illustrated in Figure 12. The figure displayed the contour plots of T_{27J} as a function of the acicular ferrite and oxygen concentrations while the values of yield strength and reheated microstructure were fixed. The results of empirical formula (Figure 12b) suggested that the lowest T_{27J} could be achieved with maximum amount of acicular ferrite and zero oxygen concentration. However, such suggestion was not justified since oxides were needed for the nucleation of acicular ferrite. The neural network predictions indicated that there existed an optimum combination of acicular ferrite and oxygen concentrations. As marked in Figure 12a, the region ‘A’ designated the optimum combination for the lowest T_{27J}. Note that finite oxygen concentrations were encompassed within the region ‘A’. The advantage of the neural network over the traditional method using linear regression was evident in that the former correctly demonstrated the dependence of T_{27J} on a particular variable was influenced by other input variables, on the other hand the latter could not capture the combined effects of multiple variables.

The quality of experimental greatly affects the accuracy of toughness predictions using either linear regression analysis (conventional empirical method) or non-linear regression analysis (neural network). The database quality deteriorates when the following conditions exist: 1) there is high level of noise in the experimental data, 2) the database is not sufficiently large, and 3) the experimental data are segregated over the input space, in other words, there exist the regions of input space with no or very sparse data points. In general, the traditional empirical method does not cope well with the poor-quality databases. The empirical formulas generated on such databases have low coefficients of determination and correlation, and furthermore, they are not capable of revealing any trends in data. The advantage of neural network over traditional empirical method is exhibited in dealing with the experimental databases with poor quality. One example can be found in Reference 73, in which the neural network model was formulated and employed to evaluate the weld toughness of HSLA steels for shipbuilding. There were only 189 data points in the database in this investigation and the level of data noise was high. However, use of the neural network made it possible to recognize the reasonable trends in data and quantify the uncertainties of predictions. For example, the analysis results indicated that increasing oxygen concentration led to a non-linear reduction in toughness. The trend was demonstrated in Figure 13. The large error bars denoted the high uncertainties associated with the predictions, which was an inherent result of noisy data. The plausible trend was nevertheless reflected in the predictions. The capability of neural network in analyzing noisy and segregated data was ascribed to the treatment of neural network in a Bayesian framework. As described earlier in this section, such treatment allowed the calculation of predictive errors representing the uncertainty in the fitting parameters.

The Cambridge model or its derivatives were utilized in the applications of neural network in toughness prediction reviewed above. The neural network model developed by a different group of researcher is reviewed in the following contexts. Tsuei et al developed a model to evaluate factors that are beneficial or detrimental to the low temperature impact toughness of flux cored arc steel welds [53]. Three main fields of input variables were incorporated into the training of the neural network: chemical composition, microstructural features, and non-metallic inclusions. Hardness and test temperature were also included as input variables. The microstructural features were described by the variables that define the volume fraction and characteristic dimension of the microstructure, such as volume fraction of AF and overall ferrite mean free path. The variables that define non-metallic inclusions included volume fraction of inclusions, mean particle diameter, and number of particles per unit volume. The model was used to conduct the sensitivity analysis that calculated the sensitivity of toughness to fluctuations in any input variables. The sensitivity analysis is very helpful in providing practical guidance on improving toughness, for example, its results indicate which of the inputs has the greatest effect on toughness. Figure 14 showed the average sensitivity of each input variable of the model. The analysis results demonstrated the two most significant factors were the test temperature and volume fraction of AF.

The neural network model reported in Reference 53 yielded reasonably accurate toughness predictions. However, it was not as comprehensive as the Cambridge model. It was trained using only 83 experimental data while the Cambridge model was developed on more 3000 data. Yet another drawback of the model in Reference 53 was lack of the capability of estimating the predictive errors. Unlike the Cambridge model, it was not treated with any probability algorithm that computes the prediction uncertainties based on data noise and segregation in distribution.

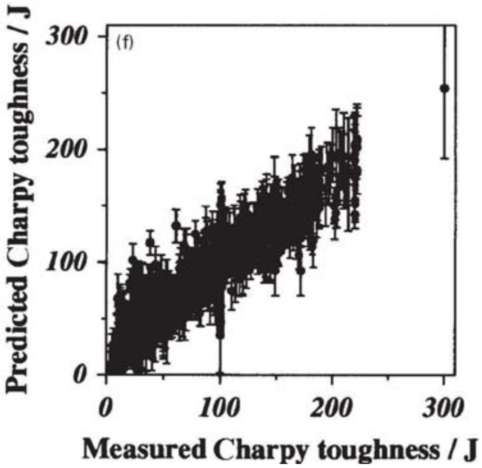

Figure 9:   Comparison of predicted and measured Charpy toughness [70]

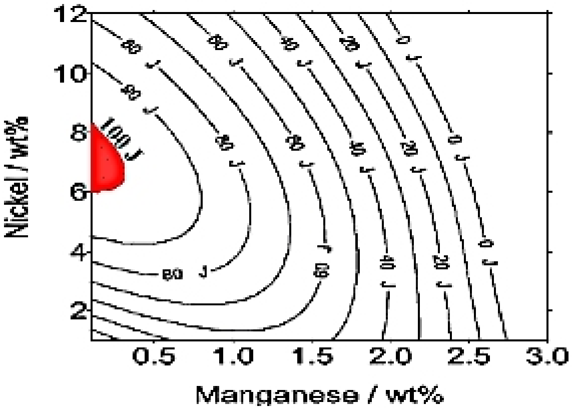

Figure 10: Combined effect of Mn and Ni on the calculated weld toughness at –40^{0}C [75]

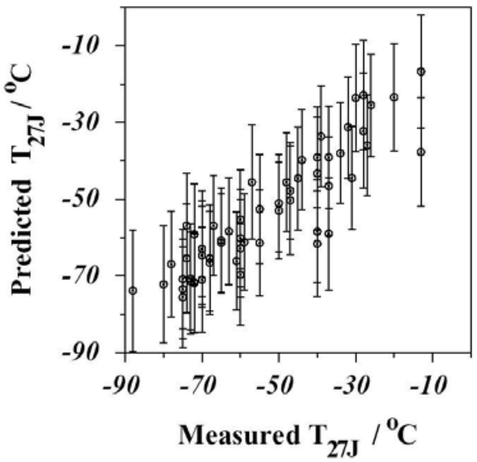

Figure 11: Comparison of predicted and measured T_{27J} [71]

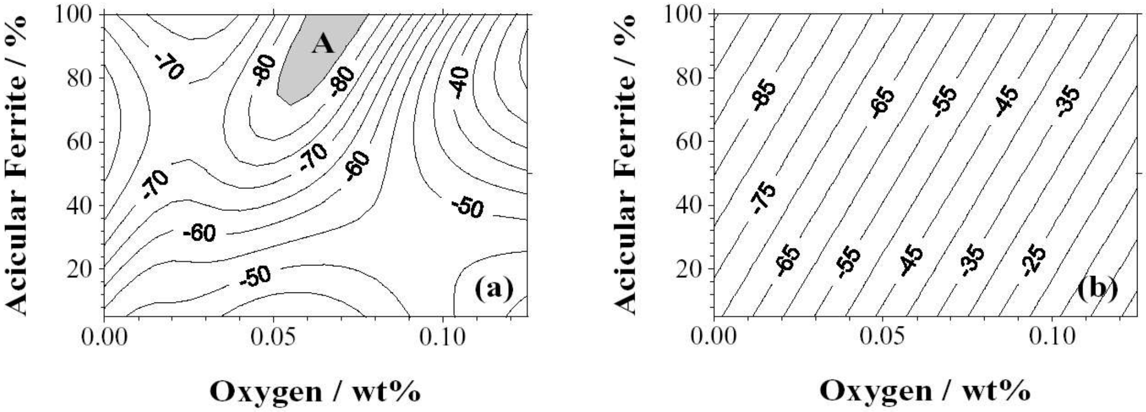

Figure 12: Computed T_{27J} contour lines in °C [71]. (a) Neural network predictions; (b) Predictions using the empirical formula given in Equation 4.

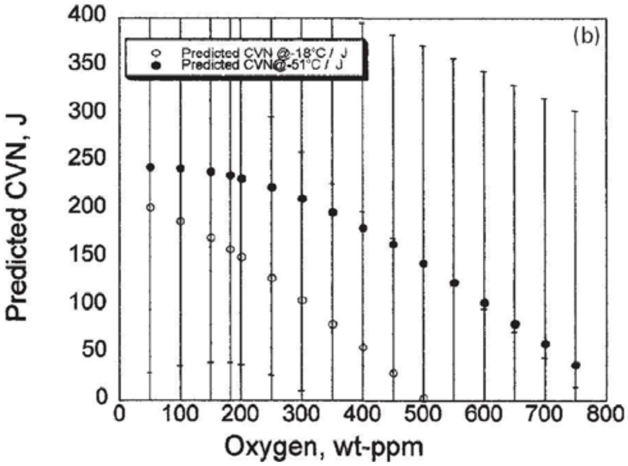

Figure 13: Variations of Charpy toughness values at –18 and –51°C as functions of oxygen concentration [73]

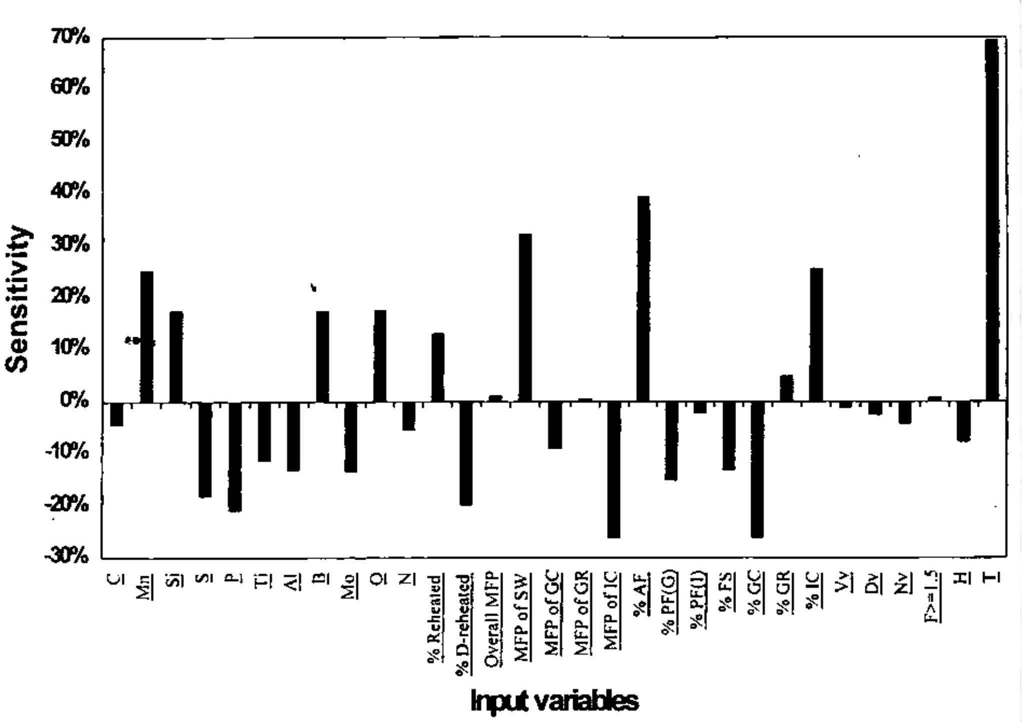

Figure 14: Sensitivity analysis of neural network model [53]

3.0 Toughness Prediction Using Neural Network at Emc2

Emc2 acquired the neural network software package developed by Professor Bhadeshia et al at University of Cambridge. A weld toughness database was also obtained along with the software. The database contains the experimental toughness data of ferritic steel welds. There are 879 data sets in the database. Each data set consists of chemical composition, welding conditions, Charpy test temperature, and toughness value. A neural network model was trained using the software and database. The input variables and output of the model are defined in Table 1. Charpy toughness is the output of the model. The model was utilized to investigate the effects on toughness of various input variables, for example, the effect of oxygen content in weld metal, as shown in Figure 15. The error bars in the analysis results represent the uncertainties of predicted values. Large prediction errors are associated with high oxygen concentrations because there are few data points in the high oxygen range in the database. The model was also employed to predict weld toughness using published experimental data. Figure 16 demonstrates one example of such prediction. The experimental data were taken from reference 18.

The neural network model developed at Emc2 shows reasonable accuracy. The model is considered a preliminary model since its database does not incorporate enough data of pipeline steel welds, which are the primary materials researched in this program. More experimental data of pipeline welds need to be collected from the industry. A data collection template has been generated based on the preliminary study described above and sent to the industrial partners of this program for data collection. Such data will enable re-training of the neural network model and render toughness predictions for pipeline welds.

Table 1: Input variables and output of the neural network model for weld toughness prediction at Emc2

	Data	Unit
Chemical Composition	C	wt%
	Si	
	Mn	
	S	
	P	
	Cr	
	Mo	
	Ni	
	Co	
	Cu	
	V	
	W	
	B	
	N	
	Nb	
	Ti	
	O	
Welding Conditions	Process Type	SMAW, FACW, SAW, etc
	Heat Input	kJ/mm or kJ/inch
	Interpass Temperature	^{0}C or ^{0}F
	PWHT Temperature	^{0}C or ^{0}F
	PWHT Time	hour
Charpy Test	Testing Temperature	^{0}C or ^{0}F
	Charpy Toughness	J

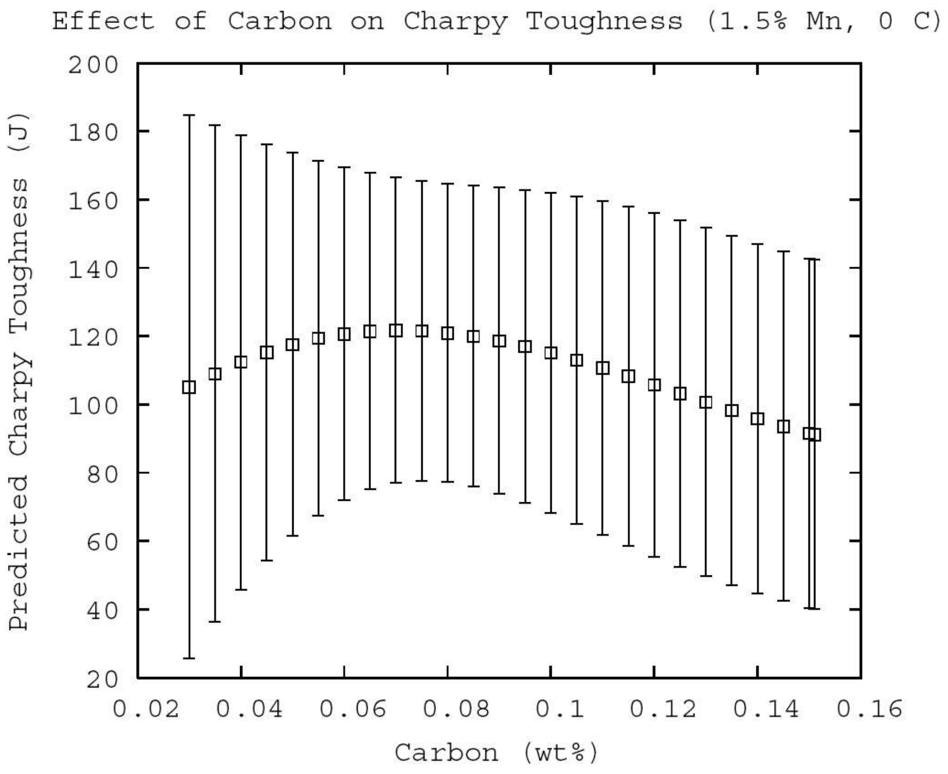

Figure 15: Predicted variation of weld toughness with oxygen content

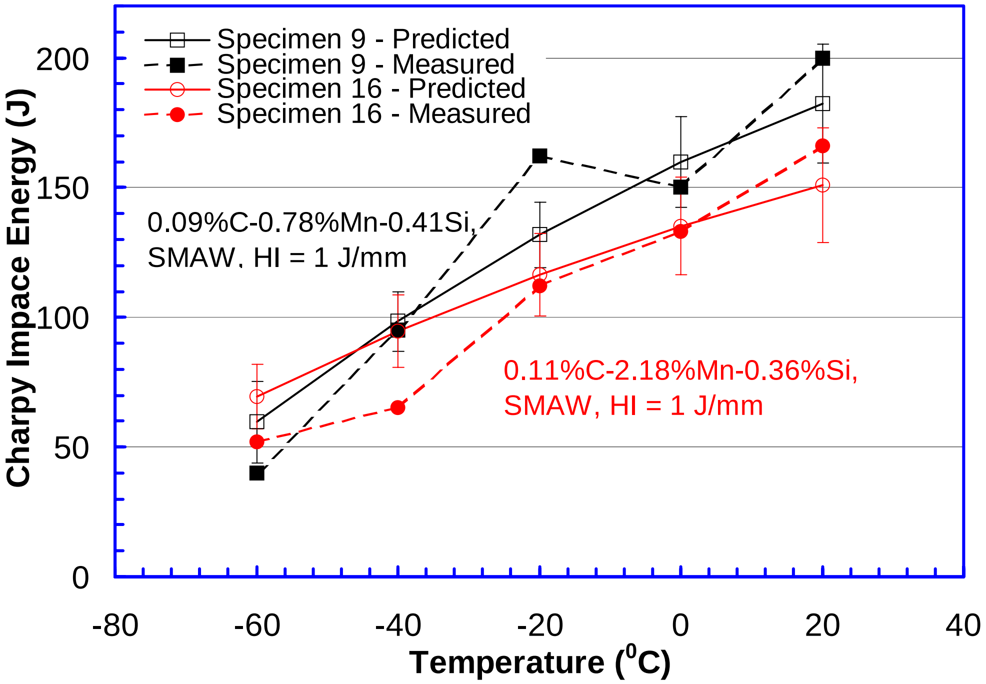

Figure 16: Comparison of predicted and measured weld toughness

4.0 Concluding Remarks

Past research efforts on weld metal toughness are review in this study. Weld toughness is a very complex physical phenomenon. The complexity is reflected in many aspects of the phenomenon, such as large scatter in measured toughness values and wide range of influencing factors. There are tremendous difficulties associated with the toughness prediction based on metallurgical principles due to the complexity of weld toughness phenomenon and lack of knowledge of the physics underlying the phenomenon. Such prediction cannot be achieved at least for now. On the other hand, empirical methods have been widely applied to the toughness prediction. Neural network analysis has been increasingly utilized for predicting weld toughness. The neural network models have shown advantages over the traditional empirical methods, such as the promising predictability and the capability of processing data scatter. A neural network model has been developed in this study and rendered reasonably accurate predictions. The future work will be focused on collecting more experimental data on pipeline steel welds and therefore a more comprehensive model can be established for pipeline welds.

5.0 References

1 Honeycombe, R. W. K. and Bhadeshia, H. K. D. H., “Steels: Microstructure and Properties,” Butterworth-Heinemann, London, 1995, pp. 311-312.

2 Sugden, A. A. B. and Bhadeshia, H. K. D. H., Metall. Trans. A, Vol. 19A, 1988, pp. 1597-1602.

3 Tomita and Okabayashi, Metall. Trans. A, Vol. 14A, 1983, pp. 485-492.

4 Bhadeshia, H. K. D. H. and Svensson, L.-E., “Modelling the Evolution of Microstructure in Steel Weld Metals,” Mathematical modelling of weld phenomena 1, The institute of Materials, London, 1993, pp. 109-182;

5 Ion, J. C., Easterling, K. E., and Ashby, M. F., Acta Metall., 32, 1984. pp. 1949-1962.

6 Bechert, M. and Holz, R., “Use of carbon equivalent and prediction of the weld heat affected zone hardness,” Schweiss Technik (Berlin), 23(8), 1973, pp. 344-346.

7 Lorenz, K. and Duren, C., “Evaluation of large diameter pipe steel weldability by means of the carbon equivalent”, Proceedings of Conference on Steels for Pipe and Pipeline Fittings, TMS, 1981, pp. 322-332.

8 Yurioka, N., Okumura, M., Kasuya, T., and Cotton, H. J. U., “Prediction of HAZ hardness of transformable steels,” Metal Construction, 19(4), 1987, pp. 217R-223R.

9 Yurioka, N., Ohshita, S., and Tamehiro, H., "Study on carbon equivalent to assess cold cracking tendency and hardness in steel welding," Proc. Pipeline Welding in the 80s, 1981, Melbourne.

10 Suzuki, H., "A new formula for estimating HAZ hardness in welded steels," IIW DOC IX-1351-85, 1985.

11 Terasaki, T., Akiyama, T., and Serino, M., "Chemical compositions and welding procedures to avoid cold cracking," Proc Int. Conf. on Joining of Metals, Nelsingor, Denmark, 1984, pp. 381-386.

12 Cotrrell, C. L. M., "Hardness equivalent may lead to a more critical measure of weldability," Metal Construction, 16, 1984, pp. 740-744.

13 Mayoumi, M. R., "Towards a prediction of the hardness of the heat-affected zone of steel weldments," Journal of Materials Science, 26, 1991, pp. 2716-2724.

14 Cahoon, J. R., Broughton, W. H., and Kutzak, A. R., Met. Trans., 2, 1971, pp. 1979-1983.

15 Anderson, T. L., "Fracture Mechanics Fundamentals and Applications," CRC Press, Boca Raton, FL, 1991, pp. 470-471.

16 Bhadeshia, H. K. D. H., "Complex weldment properties: trends in predictive power," Proceedings of the 6th International Conference on Trends in Welding Research, ASM International, Atlanta, GA, USA, 2002.

17 Wang Y.-Y. and Cheng, W., "Guidelines on tensile strain limits," PRCI Contract No. GRI-8656, 2003.

18 Svensson, L.-E. and Gretoft, B., "Microstructure and impact toughness of C-Mn weld metals," Welding Journal, 1990, pp. 454s-461s.

19 Surian, E. S. and de Vedia, L. A., "All-weld-metal design for AWS E10018M, E11018M and E12018M type electrodes," Welding Journal, 1999, pp. 217s-228s.

20 Yoshino, Y. and Stout, R. D., "Effect of microalloys on the notch toughness of line pipe seam welds," Welding Journal, 1979, pp. 59s-67s.

21 Svensson, L.-E., "Control of microstructure and properties in steel arc welds," CRC Press, 1994, pp. 69.

22 Zhang, Z. and Farrar, R. A., "Columnar grain development in C-Mn-Ni low alloy weld metals and the influence of nickel," Journal of Materials Science, 30, 1995, pp. 5581-5588.

23 Zhang, Z. and Farrar, R. A., "Influence of Mn and Ni on the microstructure and toughness of C-Mn-Ni weld metals," Welding Journal, 1997, pp. 183s-196s.

24 Murugananth, M., Bhadeshia, H. K. D. H., Keehan, E., Andren, H. O., and Karlsson, L., "Strong and tough ferritic steel welds," Proceedings of the 6th International Seminar on Numerical Analysis of Weldability, Austria, 2001.

25 Keehan, E., Karlsson, L., Murugananth, M., Andren, H. O., and Bhadeshia, H. K. D. H., “High strength steel weld metals – development with Ni and Mn,” Proceedings of the 7th International Welding Symposium, Kobe, Japan, 2001, pp. 797-802.

26 Evans, G. M., “The effect of chromium on the microstructure and properties of C-Mn all-weld metal deposits,” Weld Metal Fabrication, 57(7), 1989, pp. 346-358.

27 Jorge, J. C. F., Rebello, J. M. A., and Evans, G. M., “Microstructure and toughness relationship in C-Mn-Cr all weld metal deposits,” IIW document II-A-880-93, 1993.

28 Surian, E., Trotti, J., Cassanelli, A., and de Vedia, L. A., “Influence of chromium on mechanical properties and microstructure of weld metal from a high strength SMA electrode,” IIW document II-A-868-92, 1992.

29 Babu, S. S. and Bhadeshia, H. K. D. H., “Transition from bainite to acicular ferrite in reheated Fe-Cr-C weld deposits,” Materials Science and Technology, 6(12), 1990, pp. 1005-1020.

30 Jorge, J. C. F., Souza, L. F. G., and Rebello, J. M. A., “The effect of chromium on the microstructure/toughness relationship of C-Mn weld metal deposits,” Materials Characterization, 47, 2001, pp. 195-205.

31 Abson, D. J. and Evans, G. M., “A study of the manganese-oxygen system in low hydrogen MMA all-weld metal deposits,” IIW document II-77O-89, 1989.

32 Cochrane, R. C. and Kirkwood, P. R., “The effect of oxygen on weld metal microstructure,” International Conference on Trends in Steels and Consumables for Welding, London, November 13-16 1987, pp. 103-122.

33 North, T. H., Bell, H. B., Nowicki, A., and Craig, I., “Slag/metal interaction, oxygen and toughness in submerged arc welding,” Welding Journal, 57(3), 1978, pp. 63s-75s.

34 Craig, I., North, T. H., and Bell, H. B., “Deoxidation during submerged arc welding,” International Conference on Trends in Steels and Consumables for Welding, London, November 13-16 1987, pp. 249-263.

35 Koukabi, A., North, T. H., and Bell, H. B., “Flux formulation, sulphur, oxygen, and rare-earth additions in submerged arc welding,” International Conference on Trends in Steels and Consumables for Welding, London, November 13-16 1987, pp. 281-297.

36 Surian, E. S., Trotti, J. L., and Boniszewski, T., “Effect of oxygen content on Charpy V-notch toughness in 3% Ni steel SMA weld metal,” Welding Journal, 71(7), 1992, pp. 263s-268s.

37 North, T. H., Bell, H. B., Koukabi, A., and Craig, I., “Notch toughness of low oxygen content submerged arc deposits,” Welding Journal, 58(12), 1979, pp. 343s-354s.

38 Shinada, K., Horii, Y., and Yurioka, N., “Development of weld metal with high toughness and low hardenability,” Welding Journal, 1992, pp. 253s-262s.

39 Evans, G. M., “The effect of carbon on the microstructure and properties of C-Mn all-weld-metal deposits,” IIW document II-A-546-81, 1981.

40 Vuik, J., “Effects of carbon on the properties and microstructure of weld metal,” IIW document IX-1375-85, 1985.

41 Evans, G. M., “Effect of manganese on the microstructure and properties of all-weld-metal deposits,” IIW document II-A-432-77.

42 Garland, J. G. and Kirkwood, P. R., “Towards improved submerged arc weld metal,” Metal Construction, 7, 1975, pp. 275-283.

43 Evans, G. M., “The effect of molybdenum on the microstructure and properties of C-Mn all-weld-metal deposits,” IIW document II-A-666-86.

44 Curry, D. C. and Knott, J. F., “Effects of microstructure on cleavage fracture stress in steel,” Metal Science, 12, 1978, pp. 511.

45 Bhadeshia, H. K. D. H., “Bainite in steels,” The Institute of Materials, London, 1992.

46 Babu, S. S., David, S. A., Vitek, J. M., Mundra, K., and DebRoy, T., “Model for inclusion formation in low alloy steel welds,” Science and Technology of Welding and Joining, 4(5), 1999, pp. 276-284.

47 Tuliani, S. S., Boniszewski, T., and Eaton, N. F., “Notch toughness of commercial submerged arc weld metal,” Welding and Metal Fabrication, 37(8), 1969, pp. 327-339.

48 Dieter, G. E., “Mechanical metallurgy,” McGraw Hill Book Co., London, UK, 1988, pp. 372-374.

49 McRobie, D. E. and Knott, J. F., “Effects of strain and strain aging on fracture toughness of C-Mn weld metal,” Materials Science and Technology, 1(5), 1985, pp. 357-365.

50 Tweed, J. H. and Knott, J. F., “The effect of preheat temperature on the microstructure and toughness of a C-Mn weld metal,” Metal Construction, 19(3), 1987, pp. 153R-158R.

51 Easterling, K., “Introduction to the physical metallurgy of welding,” Butterworths, Oxford, UK, 1992, pp. 183-187.

52 Chen, J. H., Xia, T. D., and Yan, C., “Study on impact toughness of C-Mn multiplayer weld metal at –600C,” Welding Journal, 1993, pp. 19s-27s.

53 Tsuei, H., Dunne, D., and Li, H., “Neural network analysis of impact properties of flux cored arc weld metals for structural steels,” Science and Technology of Welding and Joining, 8(3), 2003, pp. 205-212.

54 Underwood, E. E., “Quantitative stereology,” Addison-Wesley, London, UK, 1970, pp. 30-33.

55 Yougyuth, P., Ghosh, P. K., Gupta, P. C., Patwardhan, A. K., and Prakash, S., “Influence of macro/microstructure on the toughness of ‘all weld’ multipass submerged are welded C-Mn steel deposits,” ISIJ Int, 32(6), 1992, pp. 771-778.

56 Peng, Y., Chen, W., and Xu, Z., “Study of high toughness ferrite wire for submerged arc welding of pipeline steel,” Materials Characterization, 47, 2001, pp. 67-73.

57 Matsuda, F., Fukada, Y., Okada, H., Shiga, C., Ikeuchi, K., Horri, Y., Shiwaku, T., and Suzuki, S., “Review of mechanical and metallurgical investigations of martensite-austenite constituent in welded joints in Japan,” Welding in the World, 37(3), 1996, pp. 134-154.

58 Yurioka, N., “TMCP steels and their welding,” Welding in the World, 35(6), 1995, pp. 375-390.

59 Ikawa, H., Oshige, H., and Tanoue, T., “Effect of martensite-austenite constituent on HAZ toughness of a high strength steel,” IIW document IX-1156-80, 1980.

60 Shiga, C., Gotoh, A., Kojima, T., Horii, Y., Fukada, Y., Ikeuti, K., and Matsuda, F., “State of the art review on the effect of PWHT on properties of steel weld metal,” Welding in the World, 37(4), 1996, pp. 163-176.

61 Smith, C., Pistorius, P. G. H., and Wannenburg, J., “The effect of a long post weld heat treatment on the integrity of a welded joint in a pressure vessel steel,” Int. J. Pres. Ves. & Piping, 70, 1997, pp. 183-195.

62 Utterberg, B. and Svensson, L.-E., “Effect of nomalising heat treatment on microstructure and properties of nickel alloyed C-Mn weld metals,” Science and Technology of Welding and Joining, 7(6), 2002, pp. 363-373.

63 Ramini de Rissone, N. M., Bott, I. De S., de Vedia, L. A., and Surian, E. S., “Effect of welding procedure (welding position, number of layers, arc energy, and shielding gas type) on ANSI/AWS A5.20-95 E71T1 flux cored wire deposits,” Science and Technology of Welding and Joining, 8(2), 2003, pp. 113-122.

64 Spurrier, J., Hancock, P., and Chubb, J. P., “An assessment of weld mis-matching,” Engineering Fracture Mechanics, 53(4), 1996, pp. 581-592.

65 French, I. E., Australian Welding Journal, 44, 1999, pp. 44-46.

66 MacKay, D. J. C., “Information Theory, Inference, and Learning Algorithms,” Cambridge University Press, Cambridge, UK, 2003.

67 Cool, T., Bhadeshia, H. K. D. H., and MacKay, D. J. C., “Modelling the Mechanical Properties in the HAZ of Power Plant Steels,” Mathematical Modelling of Weld Phenomena III, Institute of Materials, London, 1997, pp. 403-442.

68 Cool, T., Bhadeshia, H. K. D. H., and MacKay, D. J. C., “The yield and ultimate tensile strengths of steel welds,” Materials Science and Engineering, Vol. A223, 1997, pp. 186-200.

69 Lalam, S. H., Bhadeshia, H. K. D. H., and Mackay, D. J. C., “Estimation of mechanical properties of ferritic steel welds. Part 1: yield and tensile strength,” Science and Technology of Welding and Joining, 5(3), 2000, pp. 135-147.

70 Lalam, S. H., Bhadeshia, H. K. D. H., and Mackay, D. J. C., “Estimation of mechanical properties of ferritic steel welds. Part 2: elongation and charpy toughness,” Science and Technology of Welding and Joining, 5(3), 2000, pp. 149-160.

71 Lalam, S. H., Bhadeshia, H. K. D. H., and Mackay, D. J. C., “The Charpy impact transition temperature for some ferritic steel welds,” Australasian Welding Journal, Vol. 45, 2000.

72 Metzbower, E. A., DeLoch, J. J., Lalam, S. H., and Bhadeshia, H. K. D. H., “Neural network analysis of strength and ductility of welding alloys for high strength low alloy shipbuilding steels,” Science and Technology of Welding and Joining, 6(2), 2001, pp. 116-124.

73 Metzbower, E. A., DeLoch, J. J., Lalam, S. H., and Bhadeshia, H. K. D. H., “Analysis of toughness of welding alloys for high strength low alloy shipbuilding steels,” Science and Technology of Welding and Joining, 6(6), 2001, pp. 368-374.

74 Keehan, E., Karlsson, L., Murugananth, M., Andren, H.-O., Bhadeshia, H. K. D. H., “High strength steel weld metals: developments with Ni and Mn,” Proceedings of the 7th International Welding Symposium, Japan Welding Society, 2001.

75 Keehan, E., Andren, H.-O., Karlsson, L., Murugananth, M., Bhadeshia, H. K. D. H., “Microstructural and mechanical effects of nickel and manganese on high strength steel weld metals,” Proceedings of the 6th International Conference on Trends in Welding Research, ASM International, Atlanta, GA, USA, 2002.

76 Metzbower, E. A., DeLoch, J. J., Lalam, S. H., and Bhadeshia, H. K. D. H., “Secondary effects in neural network analysis of the mechanical properties of welding alloys for HSLA shipbuilding steels,” Mathematical Modelling of Weld Phenomena - VI, Maney, London, 2002, pp. 231-242.

Appendix 2

Final Report

on

Reliability Based Strain Design

GRI-04/0146

Reliability Based Strain Design

Prepared by:

Yong-Yi Wang, Yaoshan Chen, and Ming Liu
Engineering Mechanics Corporation of Columbus
3518 Riverside Drive, Suite 202
Columbus, OH 43221

Prepared for:

GRI
1700 South Mount Prospect Road
Des Plaines, IL 60018
Contract No. 8666

GRI Project Manager
Steve Foh

September 2005

LEGAL NOTICE

This report was prepared by the Engineering Mechanics Corporation of Columbus as an account of work sponsored by Gas Research Institute (GRI). Neither GRI, members of GRI, nor any person acting on behalf of either:

a. **MAKES ANY WARRANTY OR REPRESENTATION, EXPRESS OR IMPLIED WITH RESPECT TO THE ACCURACY, COMPLETENESS, OR USEFULNESS OF THE INFORMATION CONTAINED IN THIS REPORT, OR THAT THE USE OF ANY INFORMATION, APPARATUS, METHOD, OR PROCESS DISCLOSED IN THIS REPORT MAY NOT INFRINGE PRIVATELY OWNED RIGHTS, OR**

b. **ASSUMES ANY LIABILITY WITH RESPECT TO THE USE OF, OR FOR ANY AND ALL DAMAGES RESULTING FROM THE USE OF, ANY INFORMATION, APPARATUS, METHOD, OR PROCESS DISCLOSED IN THIS REPORT.**

Reference to trade names or specific commercial products, commodities, or services in this report does not represent or constitute an endorsement, recommendation, or favoring by GRI or its contractors of the specific commercial product, commodity, or service.

Table of Contents

List of Figures iii
Executive Summary iv
1.0 Introduction 1
  1.1 Background 1
  1.2 Need for Reliability-Based Procedures 1
  1.3 Structure of the Report 2
2.0 Review of Strain Design Procedures 2
  2.1 Overview of Strain-Based Design of Pipelines 2
  2.2 Fracture Mechanics Approach to Strain-Based Design of Pipelines 3
    2.2.1 DNV Offshore Standard OS-F101 and BS 7910 3
    2.2.2 Strain Design Related to Pipeline Installation by Reeling 3
    2.2.3 U.S. MMS and OPS Guidance 3
    2.2.4 Wide Plate Test Database 4
3.0 Deterministic Procedures for Strain-Based Design 5
  3.1 Background of PRCI Deterministic Procedures 5
  3.2 General Approach of the PRCI Deterministic Procedures 6
  3.3 Basic Assumptions 6
  3.4 Assumptions on Material Properties 7
  3.5 Finite Element Model 10
    3.5.1 Surface-Breaking Defects 10
    3.5.2 Buried Defects 10
  3.6 Sample Deterministic Results 13
4.0 Parametric Equations of Tensile Strain Limits 15
  4.1 Background 15
  4.2 Strain Limits of Surface-Breaking Defects 15
    4.2.1 Geometry and Material Property Parameters 15
    4.2.2 Input Data for the Development of Parametric Equations 15
  4.3 Strain Limits of Buried Defects 16
    4.3.1 Geometry and Material Property Parameters 16
    4.3.2 Input Data for the Development of Parametric Equations 16
  4.4 Comparison between Parametric Equations and Original Input Data 17
5.0 Reliability Procedure for Strain-Based Design 19
  5.1 Background on Limit State- and Reliability-Based Design 19
  5.2 Fundamental of the Reliability Procedure 19
  5.3 Numerical Integration by Monte Carlo Simulation 20
  5.4 Software of the Reliability Procedure 21
    5.4.1 Input Parameters 21
    5.4.2 Output Parameters 22
    5.4.3 File Saving Options 22
  5.5 Understanding the Significance of the Results 23
  5.6 Limits of the Procedures 23

6.0 Concluding Remarks 23
    6.1 Understanding Input Parameters 23
    6.2 Need for Future Work 24
7.0 Acknowledgement 25
8.0 References 25

List of Figures

Figure 2-1 Tensile failure strains of girth welds measured from a large number of wide plate tests [13]....4
Figure 3-1 Assumed stress strain curves of the X70 pipe materials with three *Y*/*T* ratios [16]....9
Figure 3-2 A typical FE model with a surface-breaking root-side defect [16]....9
Figure 3-3 A typical FE mesh with a surface-breaking defect [16]....10
Figure 3-4 A typical FE model with a buried defect [18]....11
Figure 3-5 A typical buried defect with an elliptical defect shape [19]....11
Figure 3-6 A typical buried defect with a rectangular defect shape [19]....12
Figure 3-7 FE mesh of a typical buried defect with an elliptical defect shape [18]....12
Figure 3-8 FE mesh of a typical buried defect with a rectangular defect shape [18]....13
Figure 3-9 Relations among three key variables for an X70 pipe with surface-breaking defects, one wall thickness, and three pipe diameters [16]....14
Figure 3-10 Relations among three key variables for an X70 pipe with buried defects [19]....14
Figure 4-1 A girth weld with a surface-breaking defect and the relevant dimensions....15
Figure 4-2 A girth weld with a buried defect and the relevant dimensions....16
Figure 4-3 Comparison of failure strains as a function of CTOD toughness between input data and the fitted equation for surface-breaking defects (lines: fitted equation; symbols: input data)....18
Figure 4-4 Comparison of failure strains as a function of wall thickness between input data and the fitted equation for surface-breaking defects (lines: fitted equation; symbols: input data)....18
Figure 4-5 Comparison of failure strains as a function of CTOD toughness between input data and the fitted equation for elliptically-shaped buried defects (lines: fitted equation; symbols: input data)....19
Figure 5-1 User interface of the software for reliability-based strain design....22

Reliability Based Strain Design

Executive Summary

Certain pipelines or sections of a pipeline may experience high longitudinal strains under displacement-controlled loading. For onshore pipelines, the high longitudinal strains are often associated with soil movement, such as seismic activity, slope instability, frost heave, mine subsidence, et al. For offshore pipelines, the highest longitudinal strains typically occur in the pipe laying operation. There are no generally accepted industry standards for the design and integrity assessment of pipeline girth welds under these high longitudinal strain conditions. Most ECA (Engineering Critical Assessment) procedures are stress-based and cannot be used when the longitudinal stress is greater than the specified minimum yield stress (SMYS).

There have been a number of PRCI and GRI funded projects aimed at developing girth weld ECA procedures for high longitudinal strain loadings. The major outcome of these projects is deterministic procedures that relate girth weld strain limits with linepipe and weld properties and defect size. These procedures may be used to obtain girth weld strain limits or weld defect acceptance limits by assuming *conservative* values of input parameters. In reality, almost all input parameters have certain variations or distributions. Taking conservative values of the input parameters leads to assessment results of unknown degree of conservatism. In comparison, a reliability-based approach considers the uncertainties of the input parameters. Therefore the overall safety and reliability of a structure can be determined.

In two previous projects, GRI-8656 and GRI-8509, the strain limits of girth welds with surface-breaking and buried defects were tabulated for a range of material properties, pipe dimensions, and defect sizes. Parametric equations that correlate those parameters are developed in this project. These equations provide “supply side” of the limit state functions. Together with specified design strain, i.e., “demand side,” they form the basis of the reliability-based procedure. Monte-Carlo simulation, which is implemented in a piece of software with Windows® user interface, is performed to compute the statistical distribution of the strain limits. When the distribution of the design strain is given, the software also provides estimates of failure probability based on user-specified distributions of input parameters, such as material properties, pipe dimensions, and defect size.

The reliability-based procedure similar to that presented in this report is useful in risk-informed design and maintenance of pipelines. It allows more effective use of new materials, construction practice, and maintenance procedures. However, the reliability-based procedure presented in this report should be viewed as preliminary. Further experimental validation is necessary if it were to be used in practice.

Key words: pipeline, girth weld, strain-based design, reliability-base design, defect acceptance criteria, engineering critical assessment (ECA), fitness-for-service (FFS)

1.0 Introduction

1.1 Background

Pipelines may experience high longitudinal strains under displacement-controlled loading. For onshore pipelines, the high longitudinal strains are often associated with soil movement, such as seismic activity, slope instability, frost heave, mine subsidence, et al. For offshore pipelines, the highest longitudinal strains typically occur in the pipe laying operation.

There are no generally accepted industry standards for the design and integrity assessment of pipeline girth welds under these high longitudinal strain conditions. Most ECA (Engineering Critical Assessment) procedures are stress-based and cannot be used when the longitudinal stress is greater than the specified minimum yield stress (SMYS). Since the SMYS is typically defined at 0.5% total strain, the stress-based ECA is often limited to a maximum longitudinal strain of 0.5%.

There have been significant research efforts to develop girth weld ECA procedures for high longitudinal strain loading. These efforts are reviewed in details in Section 2.0. The major outcome of these efforts is deterministic procedures that relate girth weld strain limits with material properties and defect size. These procedures may be used to obtain girth weld strain limits or weld defect acceptance limits by assuming conservative values of input parameters.

1.2 Need for Reliability-Based Procedures

In a traditional deterministic girth weld ECA, the input parameters, such as fracture toughness and load, are assumed to have single lower- or upper-bound values to achieve what is perceived as a "conservative" assessment. For instance, only the lowest toughness value from a set of multiple specimen tests is used in determining the allowable girth weld defect size in API Standard 1104 Appendix A and CSA Z662 Appendix K [1,2]. No consideration is given to the toughness values of the other tests. This simplistic treatment of the fracture toughness and other input parameters leads to assessment results of unknown degree of conservatism. The cumulative effect of various uncertainties, hence the overall reliability and safety of structures, remains un-quantified in the traditional deterministic approach. Compared with the deterministic approach, a reliability-based approach considers the uncertainties of input parameters. Therefore the overall safety and reliability of the structures can be determined. A further incentive of using the reliability-based approach is that certain structural loads, such as those from an earthquake, are frequently described in probabilistic terms.

All reliability-based procedures rely on the appropriate definition of relevant limit states. A limit state may be interpreted as a boundary between safe and unsafe or desirable and undesirable states. An appropriately formulated ECA procedure enables the construction of limit state(s). However, not all deterministic ECA procedures are appropriate for the construction of limit state(s). For instance, most codified deterministic ECA procedures are based on the philosophy of failure avoidance, not failure prediction [3]. In other words, if a failure is predicted using these procedures, the structure may or may not fail. If a safe condition is predicted, it can be stated with high confidence that the structure is safe. When a limit state function from the failure avoidance philosophy is used as the basis of a reliability-based ECA, the prediction would exaggerate the possibility of failure; therefore defeat the very purpose of applying the reliability-based ECA. To the extent possible, a limit state function in the reliability-based assessment should represent a true limit state, not a limit state with an unknown degree of safety factor.

The work presented in this report builds upon the deterministic procedures specifically developed for pipeline girth welds under high longitudinal strain conditions. These deterministic procedures were meant to predict true limit states. They are used as the basis in the reliability procedure that takes into account of the natural variations and distributions of various influencing factors. The combined effects of these factors are represented in the assessment results.

1.3 Structure of the Report

The strain design procedures, both standardized and non-standardized, are reviewed in Section 2.0. Section 3.0 provides an overview of the development of the deterministic procedures from mainly two completed GRI projects. Section 4.0 covers the development of parametric relations of the deterministic procedures. In Section 5.0, the results of Section 4.0 are cast in a reliability format with user-selectable distributions of input parameters. This main deliverable of the project is incorporated into a piece of software with Windows® user interface. Section 6.0 summarizes the current work, its limitations, and future research directions.

2.0 Review of Strain Design Procedures

2.1 Overview of Strain-Based Design of Pipelines

There can be many levels of sophistications in the strain-based design of pipelines. They can be broadly classified into three categories: (1) experience-based design, (2) case-specific design and analysis, and (3) general and through analysis based on the principles of ECA and fracture mechanics. A review of these design methods is given by Wang and Horsley [4]. The fracture mechanics approach is the most comprehensive and can be applied to various pipeline projects under a wide range of loading conditions. It affords a systematic understanding of various factors affecting the strain limits of girth welds. This understanding leads to optimal selection of linepipe materials, welding procedures, and defect acceptance levels. The development of this understanding requires sophisticated analytical/numerical procedures coupled with well-designed experimental validations. Some of these new developments, except that of PRCI, are reviewed below. The PRCI approach, which is the basis of this work, is presented in Section 3.1 in conjunction with the overview of the deterministic procedures of this current work.

2.2 Fracture Mechanics Approach to Strain-Based Design of Pipelines

2.2.1 DNV Offshore Standard OS-F101 and BS 7910

The DNV offshore standard F101 [5] provides broad guidance on girth weld defect acceptance criteria for longitudinal strain conditions from elastic to highly plastic. The standard stipulates that an ECA should be performed as per the Level 3 procedure of BS 7910:1999 [6] if the *accumulated plastic strain* is greater than 0.3%. The significance of the *accumulated plastic strain* is attributable to the effects of prior strain history on material properties, such as tensile properties and fracture toughness. It is not clear, however, from the language of the standard whether this *accumulated plastic strain* should be the nominal strain of a pipeline or the local strain in the vicinity of the welds where the defects are located. The more relevant local strain history can be extremely difficult to track, particularly with the weld strength mismatch and the spatial variation of properties in the heat-affected zone (HAZ). At the present time, using the nominal strain history appears to be the only feasible option.

As far as published standard in the area of strain-based design of pipelines, the DNV standard is perhaps the most advanced. There are certain limitations to the DNV standard. One of the most fundamental limitations is the reference to the Level 3 procedure of BS 7910:1999. The Level 3 procedure is in the form of a failure assessment diagram (FAD). The FAD format was developed and well-suited for stress-based design. The results from the FAD format are not particularly sensitive to the magnitude of post-yield strains, particularly in low strain hardening (high Y/T ratio) materials which are typical of modern micro-alloyed TMCP linepipe materials and their welds.

2.2.2 Strain Design Related to Pipeline Installation by Reeling

A recently completed joint industry program (JIP) focused on pipeline installation by reeling [7]. The objective of the project was to develop a procedure for the assessment of girth weld defects of pipelines and risers during installation processes that involve cyclic plastic straining. The low-constraint SENT (single edge notched tension) specimen is suggested as the preferred toughness test specimens. This recommendation is consistent with the constraint-sensitive fracture mechanics and historical experience in fossil energy and nuclear power generation industries [8,9].

2.2.3 U.S. MMS and OPS Guidance

The Minerals Management Service (MMS) of the U.S. Department of Interior and the Office of Pipeline Safety (OPS) of the U.S. Department of Transportation funded a project at the Edison Welding Institute (EWI) to produce a guidance document for strain-based design of pipelines [10]. One particularly interesting issue raised in the report was the effects of internal and external pressure on the axial strain concentration. The results were based on welds with very large softened HAZ and root region. Two experimental tests were conducted on aluminum cylinders with the intent to demonstrate the effects of hoop stress on girth weld axial strain limits. The girth welds were produced with partial penetration welds and the property of the weld region was not quantified. The effects of hoop stress on axial failure strains were not evident in these tests.

The EWI work introduces intriguing questions about the effects of softened HAZ on the strain limits of pipeline girth welds under biaxial loading. There is little conclusive experimental evidence to suggest the degree of such influence. Further investigation, particularly experimental testing, is highly desirable.

2.2.4 Wide Plate Test Database

A large database on the failure strains of girth welds has been accumulated from wide plate tests [11]. Although the test data on their own do not constitute a systematic strain design procedure similar to the DNV standard or the PRCI procedure under development, the database is a valuable source for procedure validation and reality check. The database contains test data for a wide range of pipeline girth welds. Figure 2-1 shows the tensile failure strains measured from 238 wide plate tests [12]. The failure strains range from less than 0.5% to nearly 10%.

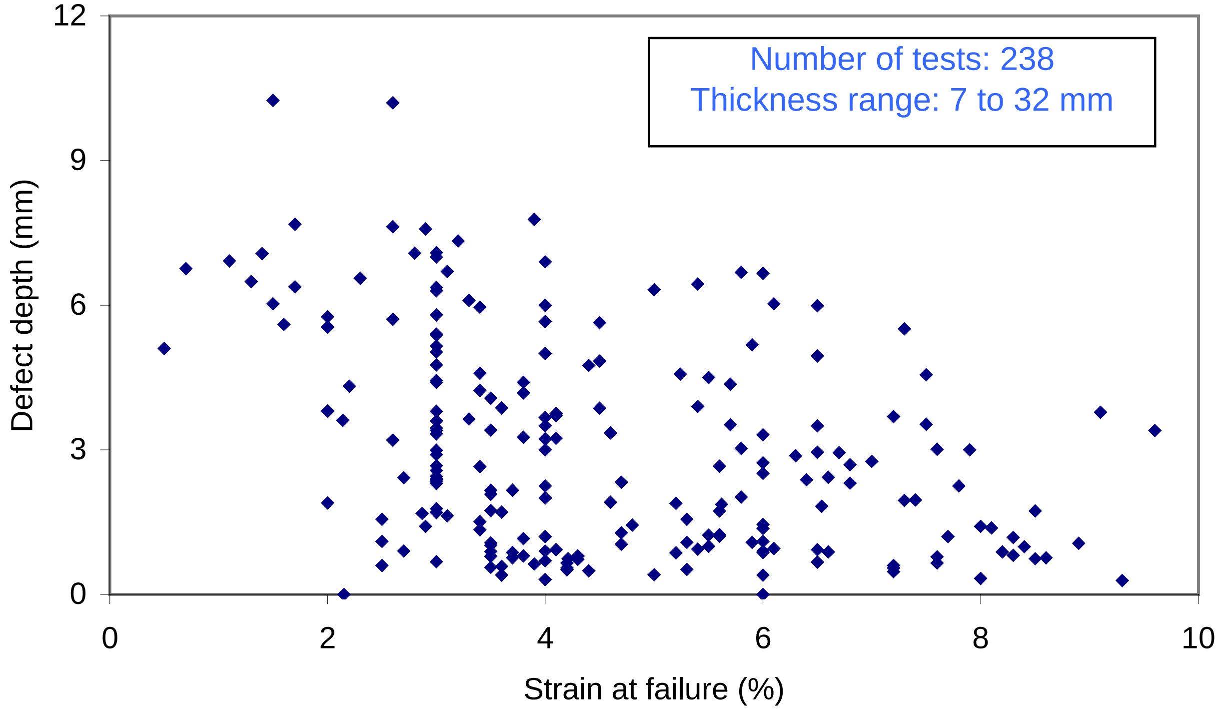

Figure 2-1 Tensile failure strains of girth welds measured from a large number of wide plate tests [12]

There can be a significant variability in wide plate test data. This variability may result from the natural variation of material's strain limits or test method or both. The earlier test data do not have corresponding full stress-strain curves of the pipe materials and welds which limit the use of such data. However, more recent tests often contain full characterization of material properties, thus making the database much more useful as a potential prediction tool.

3.0 Deterministic Procedures for Strain-Based Design

3.1 Background of PRCI Deterministic Procedures

The deterministic procedures which form the basis of this current work are the result of a multi-year PRCI effort aimed at developing systematic approach to strain-based design of pipelines. This effort started in the late 1990's and is still continuing. In its first project of this effort, a set of preliminary strain design guidelines was established [13]. The guidelines were presented in the form of parametric relations that relate strain limits with a number of input parameters, including defect size, CTOD toughness, and weld strength mismatch ratio. The comparison between the predicted strain limits and the experimentally measured failure strains showed that almost all predictions were conservative. Most predicted strains were within a factor of 2 of the experimental values.

One of the most significant contributions of the initial PRCI work is the use of the crack driving force method in estimating the girth weld tensile strain limits. In contrast to the FAD format, the crack driving force method is very sensitive to the post-yield material behavior. However, there were some serious omissions in the initial work. The defect length was not a variable in the finite element (FE) analysis, as all analyses were done using axisymmetric models. A defect length correction factor was added to the guidelines based on the comparison of numerical results and the full-scale experimental data. The correction factor was probably not very accurate for short defects. Furthermore, the effects of strain hardening were not examined in the initial work.

Subsequent to the initial work, two projects were initiated under GRI funding and PRCI direction. In GRI-8656, the major omissions of the initial PRCI were addressed [14]. In particular, the effects of defect length, material strain hardening capacity, and pipe wall thickness were thoroughly examined. The baseline tensile strain limits of girth welds containing *surface-breaking defects* were established for a wide range of pipe grade, wall thickness, defect size, and material toughness. The strain limits were presented in three formats representing varying degrees of complexity and flexibility. The most flexible format provided graphical relations among three key variables: (1) defect length, (2) strain limit, and (3) apparent toughness for a given pipe grade and wall thickness. These graphical relations could be used to determine any third variable from the other two known variables. The second format was the tabulation of strain limits for defects of predetermined length and toughness. These tabular forms enable the consolidation of all essential data into a few tables that cover a wide range of pipe grade and wall thickness. The third format was in the form of parametric equations. These equations provided the strain limits that are most relevant to the seismic design guidelines with varying degree of implied conservatism. An abbreviated version of the work and further experimental validation has been published in 2004 [15,16].

In GRI-8509, a systematic investigation of various factors affecting the tensile strain limits of *buried defects* has been conducted [17,18]. By using the same concept of crack driving and apparent toughness as in GRI-8656, baseline tensile strain limits of buried defect have been established for a wide range of pipe grade, wall thickness, defect size, and material toughness.

In view of the central role of the deterministic procedures for this current work, the general approach and basic assumptions in the development of the deterministic procedures are reviewed below.

3.2 General Approach of the PRCI Deterministic Procedures

In general terms a failure event occurs when the driving force reaches material's resistance to such failure. This general concept is applied in fracture mechanics terms, i.e., in the form of crack driving force and fracture toughness, to develop the deterministic procedures. The approach was to first develop the crack driving force relations under various materials, defects, and geometric conditions. The strain limits were obtained by equating the driving force with material's apparent toughness. The crack driving force approach is a modern and more specific version of the CTOD design curve [19]. It shares some similarity with the crack driving force (CDF) curve approach of SINTAP [20]. The concept of the apparent toughness is related to crack-tip constraint and explained in reference [16].

3.3 Basic Assumptions

There are a large number of factors that affect the crack driving force of a girth weld containing a planar defect, including material properties, geometric dimensions, and the interaction of the two. Some basic assumptions were made to reduce the problem to a tractable level.

1. Weld strength overmatching or even-matching exists for all welds. Flaws within overmatching welds are shielded to some extent from global applied strain. The weld joint is conservatively treated as having uniform tensile properties of the base metal.
2. The weld cap height is negligible, i.e., assuming zero weld cap height. The weld cap provides some reinforcing effects to the weld. However, the weld cap height can vary around the circumference of a pipe and is process dependent. Assuming zero weld cap height leads to conservative results.
3. The weld bevel geometry has no influence on crack driving force when the weld joint is assumed to have uniform tensile properties.
4. The defect location (weld metal or HAZ) has no influence on crack driving force when the weld joint is assumed to have uniform tensile properties. However, the defect location will affect the selection of material's fracture toughness.

With respect to most actual girth weld conditions, the above assumptions should lead to conservative estimations of the tensile strain limits of girth welds.

3.4 Assumptions on Material Properties

Material’s strain hardening capacity has a strong influence on the accumulation of strains in a cracked plane, therefore, affecting the crack driving force. Generally speaking, the higher the pipe grade, the lower the strain hardening rate and uniform strain. Using the API 5L minimum yield and tensile requirements as the baseline, generic relations among pipe grade, *Y*/*T* ratio, and uniform strain can be established.

The stress strain curve is assumed to obey the CSA Z662 [2] relation,

$$\varepsilon = \frac{\sigma}{E} + \left(0.005 - \frac{X_g}{E}\right)\left(\frac{\sigma}{X_g}\right)^n \tag{1}$$

where σ and ε is the stress and strain, respectively. And E is the elastic modulus, X_g is the pipe grade or yield stress at 0.5% strain, and n is the strain hardening exponent. This stress strain relation has a continuous yield (no Lűders extension). One of the useful features of this relation is that the strain is always 0.5% when the stress is at the pipe grade level ($\sigma = X_g$).

The uniform strain, ε_T, is related to the strain hardening exponent by,

$$\varepsilon_T = 2/n. \tag{2}$$

The above relation is based on the observation of a wide range of linepipe materials and is shown to be reasonable. For a given pipe grade, one can use the minimum specified values for yield and tensile per API 5L. These yield and tensile values, together with Eqs. (1) and (2), completely define the full stress strain curve.

Table 1 Pipe grade and associated lower bound, middle level, and upper bound strain hardening rates and uniform strains

Grade		API Min. Yield		API Min. Tensile		API Min. Requirements, Lower Bound *Y*/*T*			Middle *Y*/*T*			Upper Bound *Y*/*T*		
(ksi)	(MPa)	(ksi)	(MPa)	(ksi)	(MPa)	*Y*/*T*	Strain Hardening Exponent, *n*	Uniform Strain	*Y*/*T*	Strain Hardening Exponent, *n*	Uniform Strain	*Y*/*T*	Strain Hardening Exponent, *n*	Uniform Strain
52	359	52	359	66	455	0.788	15.38	13.0%	0.841	19.88	10.1%	0.894	27.95	7.2%
60	414	60	414	75	517	0.800	16.43	12.2%	0.850	21.19	9.4%	0.900	29.70	6.7%
65	448	65	448	77	531	0.844	20.84	9.6%	0.883	26.72	7.5%	0.922	37.33	5.4%
70	483	70	483	82	565	0.854	22.16	9.0%	0.890	28.33	7.0%	0.927	39.42	5.1%
80	552	80	552	90	621	0.889	28.69	7.0%	0.917	36.44	5.5%	0.944	50.32	4.0%

Equations (1) and (2) provide a convenient and reasonable approximation of the full stress strain curves for different grades of linepipe materials. They capture the essential relations between pipe grade and material’s strain hardening capacity. The actual material tensile properties are almost certainly different from those described in Eqs. (1) and (2). It is important to recognize that the assumed stress strain relations of Eqs. (1) (2) are meant to provide a general description, not as a replacement for the actual stress strain curves of the materials of interest. A few important limitations are worthy noting:

(1) Lűders extension is sometimes observed in the stress strain curves of linepipe materials and frequently in the girth welds. It is believed that the crack driving force at high strains is more significantly influenced by the overall strain hardening behavior than the extent of the Lűders extension.

(2) The actual *Y*/*T* ratio of a pipe material can be different from that computed using the API 5L minimum requirements. Since the strain limits are reduced with increasing *Y*/*T* ratio, a non-conservative prediction may result if the actual *Y*/*T* ratio is higher than that from the API 5L minimum requirements. For each pipe grade, an upper bound and a middle level *Y*/*T* ratio are also included. The lower bound *Y*/*T* ratio is computed from API 5L minimum yield and tensile requirements. The upper bound *Y*/*T* ratio is taken as the average of the lower bound *Y*/*T* ratio and unity. The middle level *Y*/*T* ratio is the averaged value of lower bound and upper bound *Y*/*T* ratios. The respective *Y*/*T* ratio, strain hardening exponent, and uniform strain are given in Table 1. For each pipe grade, the UTS for the three levels of *Y*/*T* ratios were set to the same value as the API minimum requirement. The upper bound and middle level *Y*/*T* ratios were achieved by increasing the yield stress levels. The stress strain curves of X70 pipe with the assumed three *Y*/*T* ratios are shown in Figure 3-1.

(3) The actual yield and ultimate tensile strength are almost certainly higher than the API specified minimum values. As far as developing crack driving force relations beyond the elastic strain range, the strain hardening rate is much more influential than the magnitudes of the yield and ultimate tensile strength. For each pipe grade, the assumed strain hardening range was wide enough to cover most practical possibilities.

(4) There can be certain degree of anisotropy in modern control rolled linepipe materials, affected by rolling process, pipe forming, cold expansion, and even corrosion protection coating. For example, Grade 690 (X100) UOE pipe was observed to have longitudinal yield strength as low as 590 MPa (85.6 ksi). The current model does not consider the effects of anisotropy.

(5) Seamless pipes may have very different stress strain relations than those assumed by Eqs. (1) and (2).

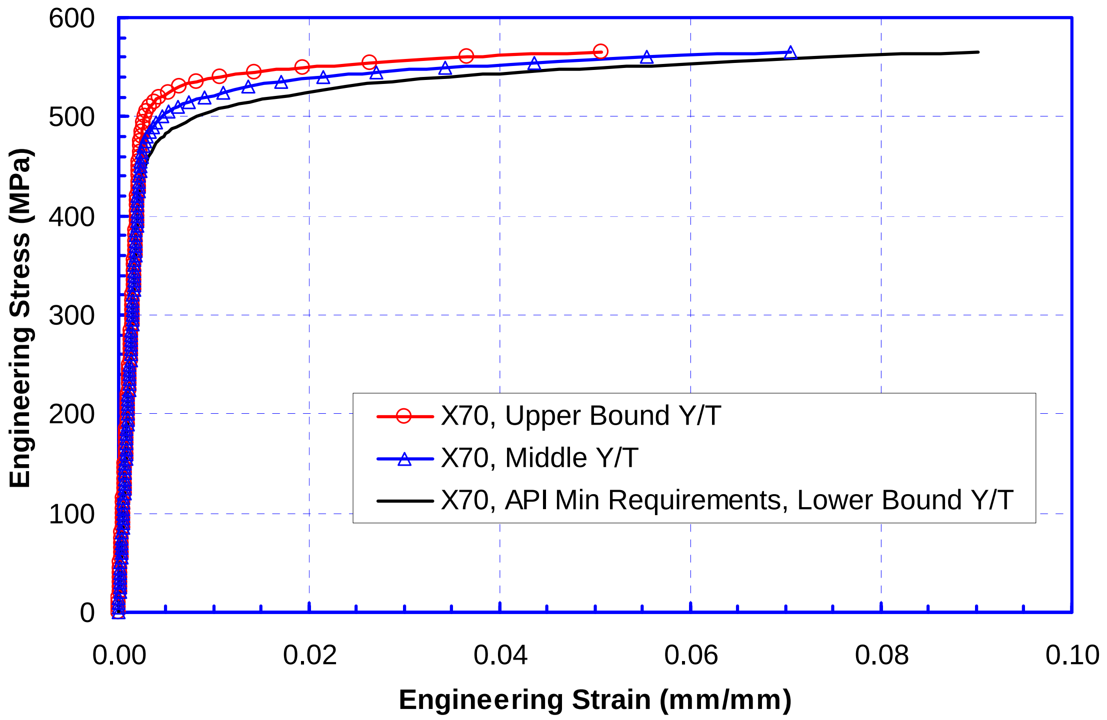

Figure 3-1 Assumed stress strain curves of the X70 pipe materials with three *Y*/*T* ratios [15]

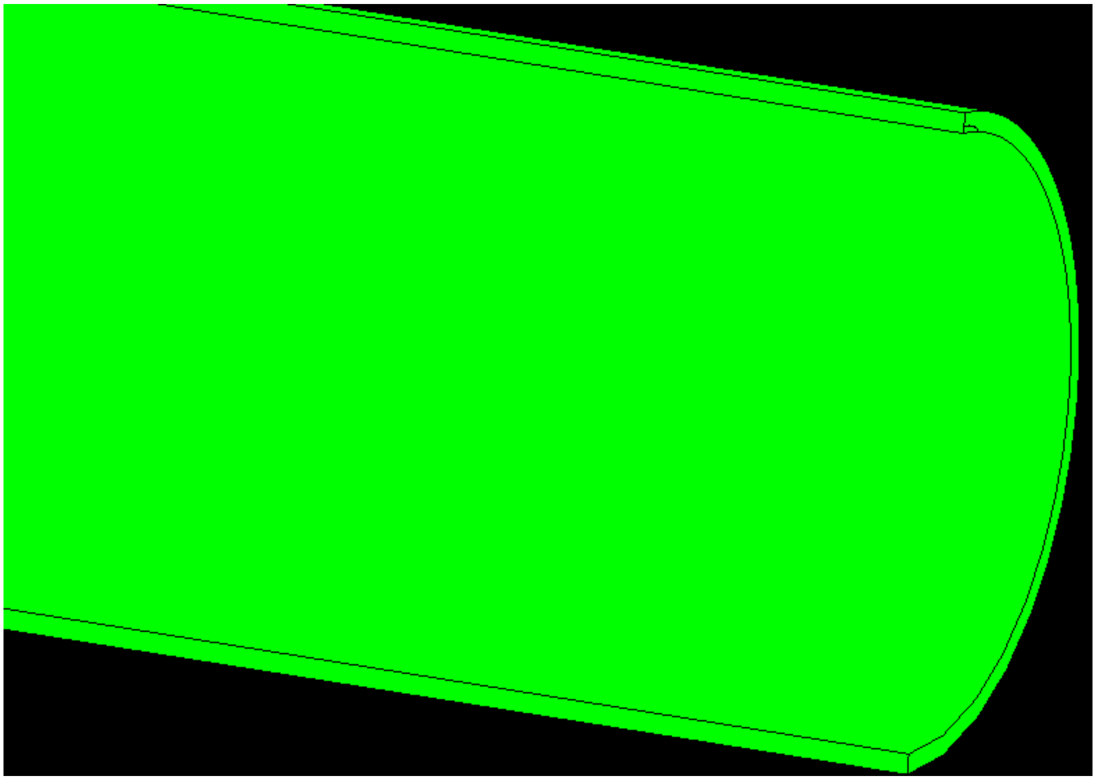

Figure 3-2 A typical FE model with a surface-breaking root-side defect [15]

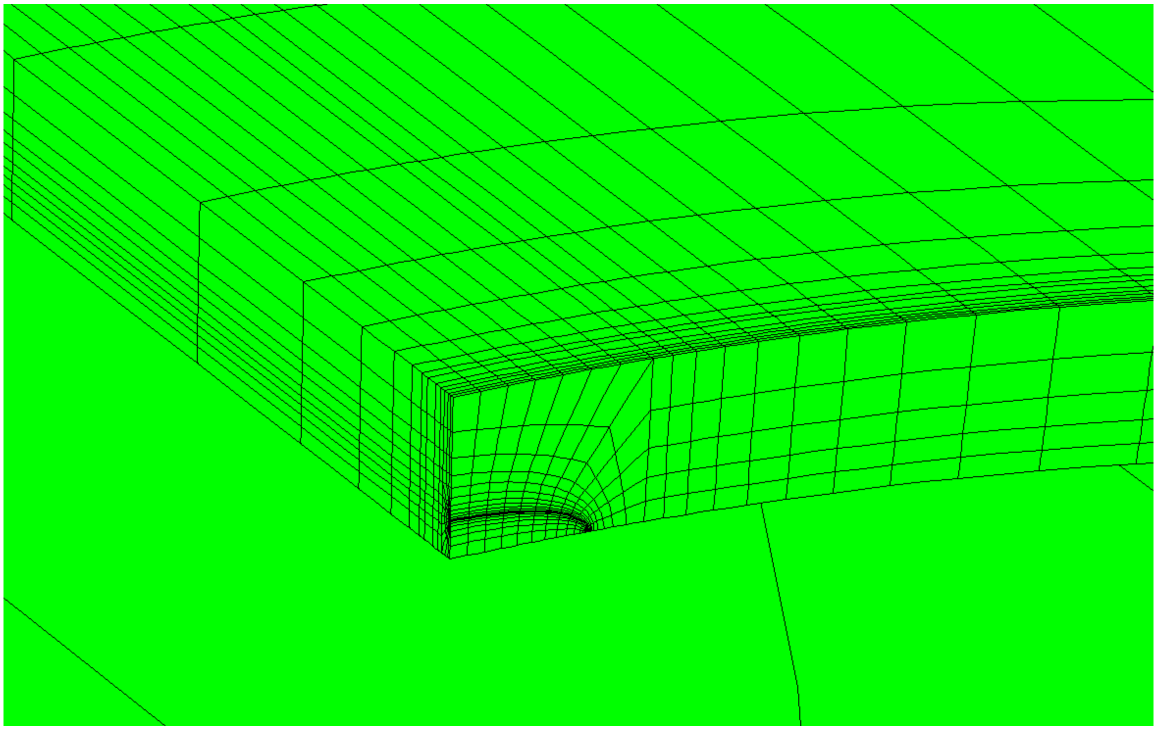

Figure 3-3   A typical FE mesh with a surface-breaking defect [15]

3.5 Finite Element Model

3.5.1 Surface-Breaking Defects

Three-dimensional FE models simulating a section of pipe with a planar root-side defect were generated. Due to the symmetry conditions, one quarter of the pipe is represented by the FE model to simulate the full pipe behavior.

The outline of a typical FE model with a surface-breaking defect is shown in Figure 3-2. The axial extent of the model was always 5 times the pipe diameter. A typical FE mesh is shown in Figure 3-3.

3.5.2 Buried Defects

The outline of a typical FE model with a buried defect is shown in Figure 3-4. The axial extent of the model was 5 times the pipe diameter.

The shape of the buried defects is either elliptical or rectangular as shown in Figure 3-5 and Figure 3-6. To accommodate the meshing requirements, the end of the rectangular defects is not perfectly squared. However, its effects on strain limits should be minimal as the length of this end section is much smaller than the overall length of the defect. The corresponding finite element meshes are shown in Figure 3-7 and Figure 3-8.

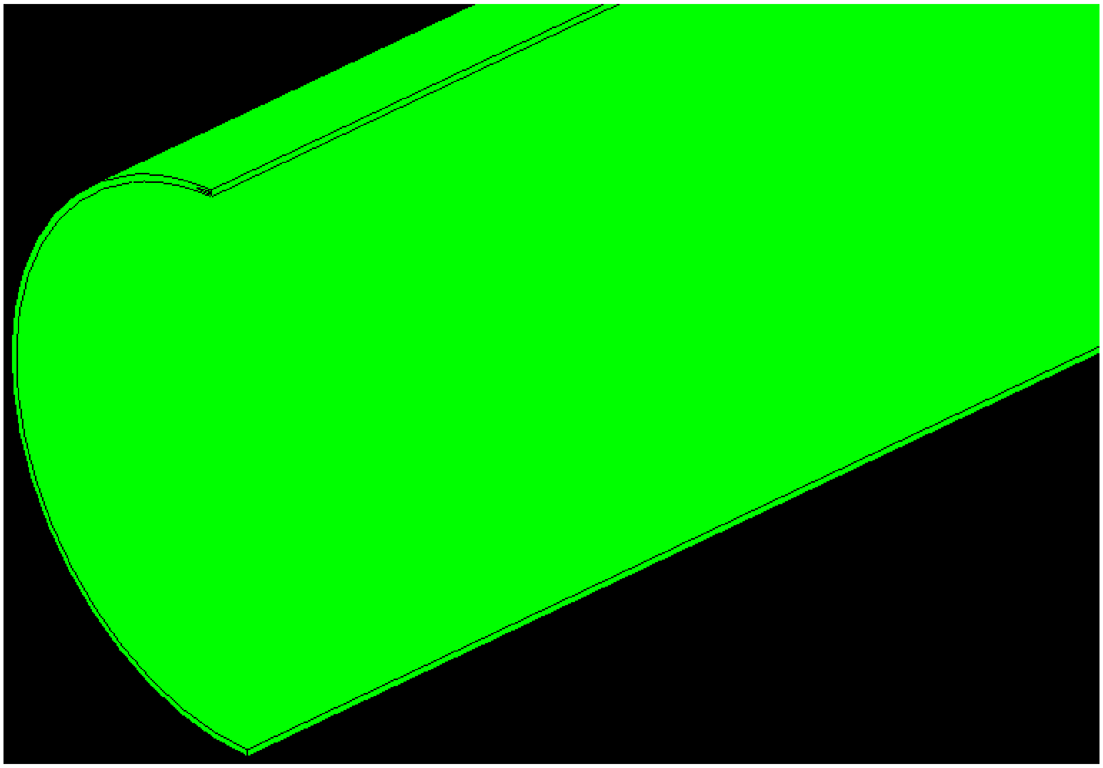

Figure 3-4   A typical FE model with a buried defect [17]

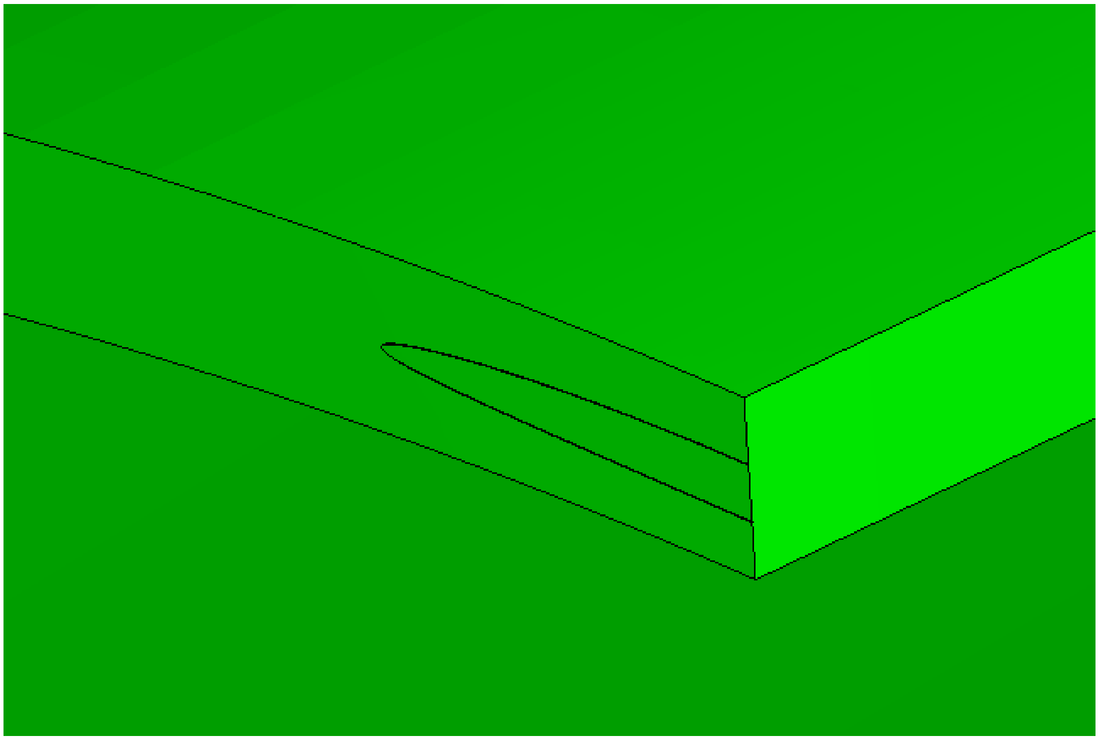

Figure 3-5   A typical buried defect with an elliptical defect shape [18]

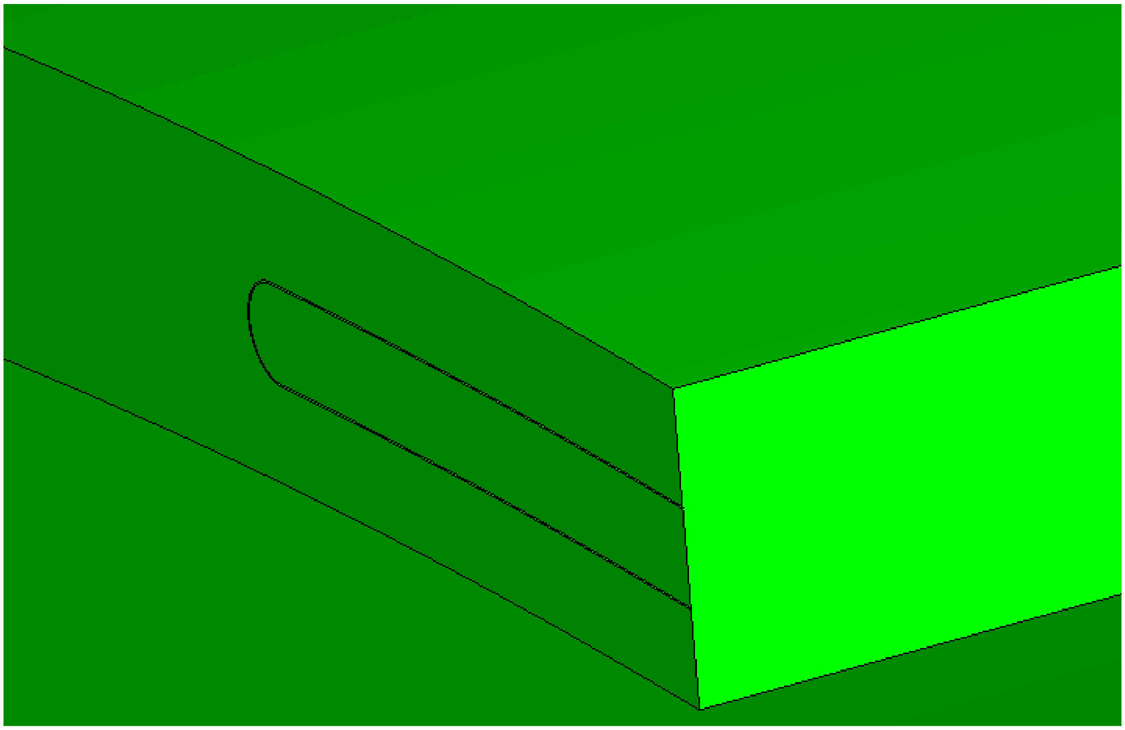

Figure 3-6 A typical buried defect with a rectangular defect shape [18]

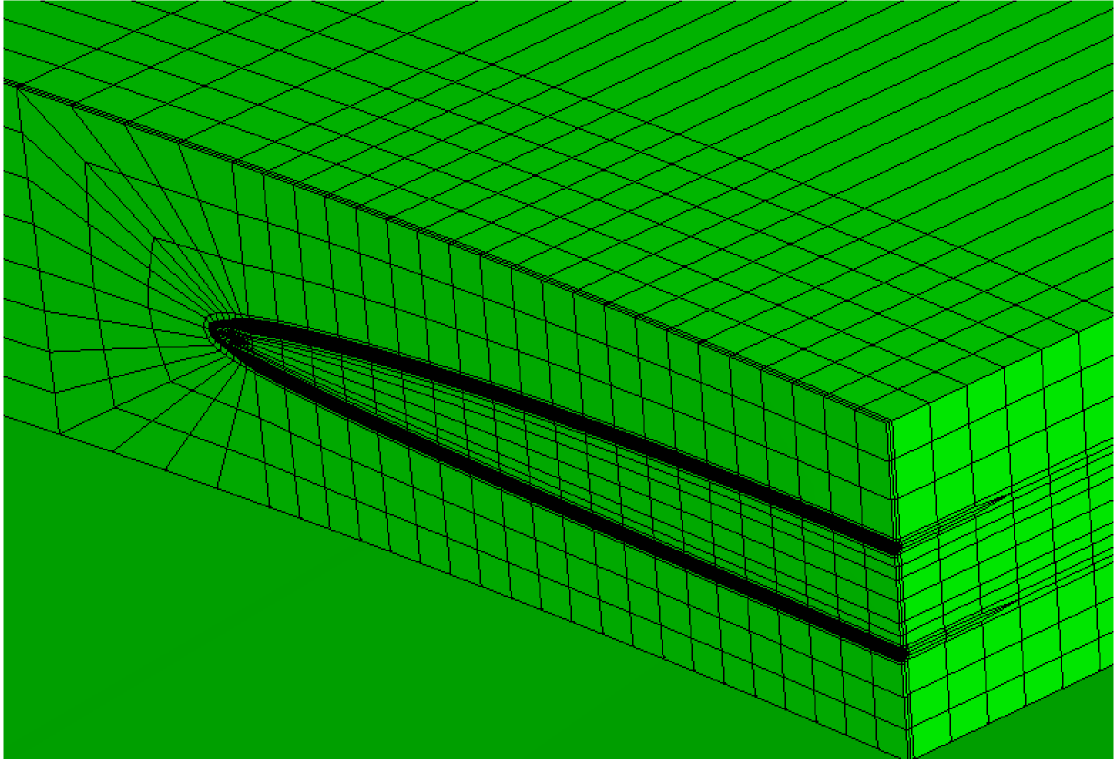

Figure 3-7 FE mesh of a typical buried defect with an elliptical defect shape [17]

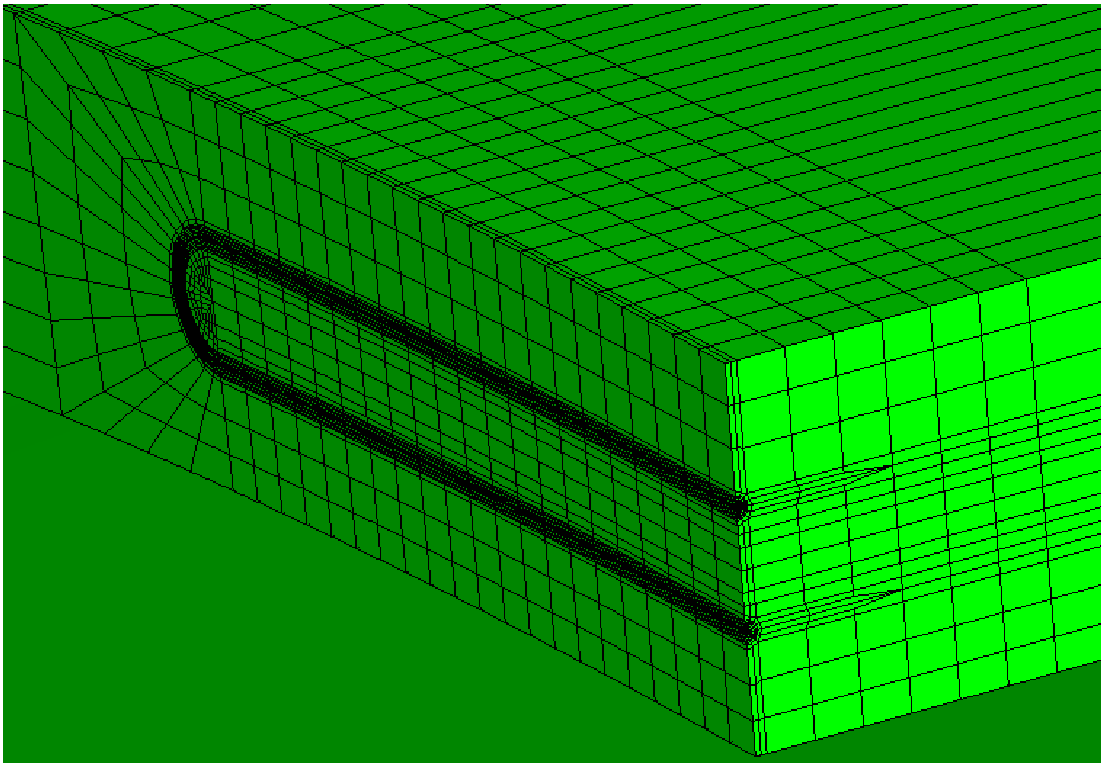

Figure 3-8 FE mesh of a typical buried defect with a rectangular defect shape [17]

3.6 Sample Deterministic Results

The failure of a girth weld is assumed to occur when the CTOD driving force reaches material's resistance, or "apparent CTOD toughness." By equating this CTOD driving force with this apparent toughness, the relations among three key variables, (1) defect length, (2) toughness, and (3) applied strain, are defined. When any two variables are known, the third variable can be determined. An example of these relations for surface-breaking defects is given in Figure 3-9. Similar relations for buried defects are shown in Figure 3-10. The difference between the solid and dashed lines in Figure 3-10 illustrates the effects of ligament thickness. The thinner ligament, on the ID side in this case, results in higher driving force.

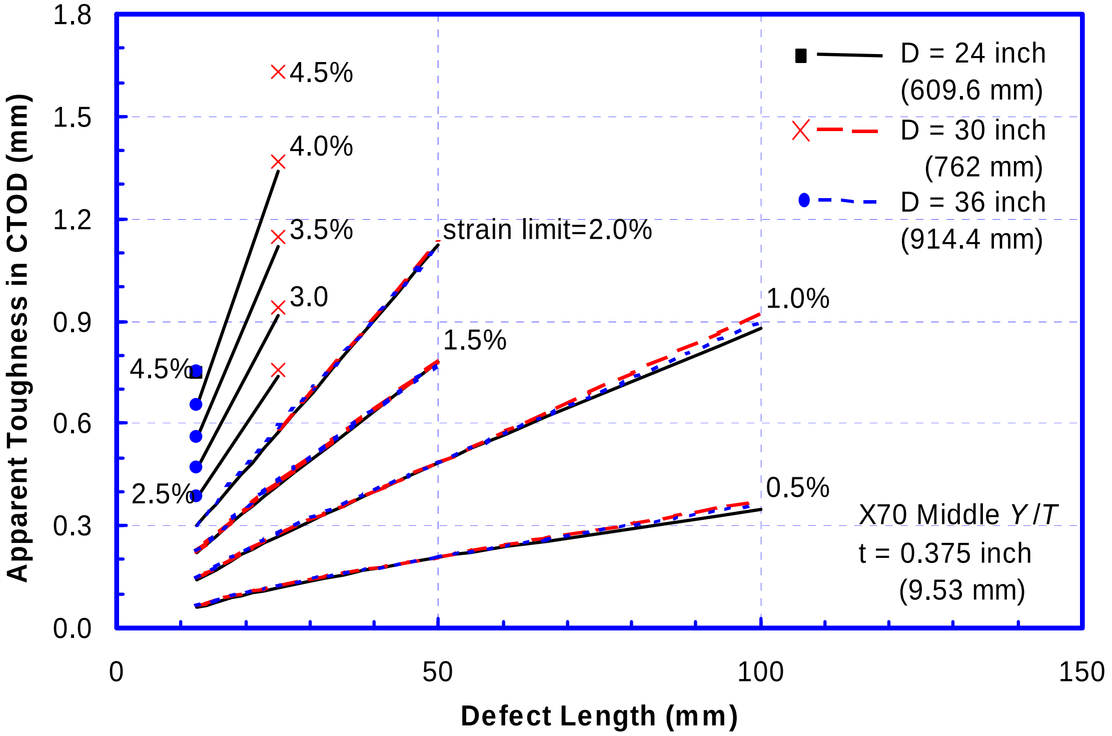

Figure 3-9 Relations among three key variables for an X70 pipe with surface-breaking defects, one wall thickness, and three pipe diameters [15]

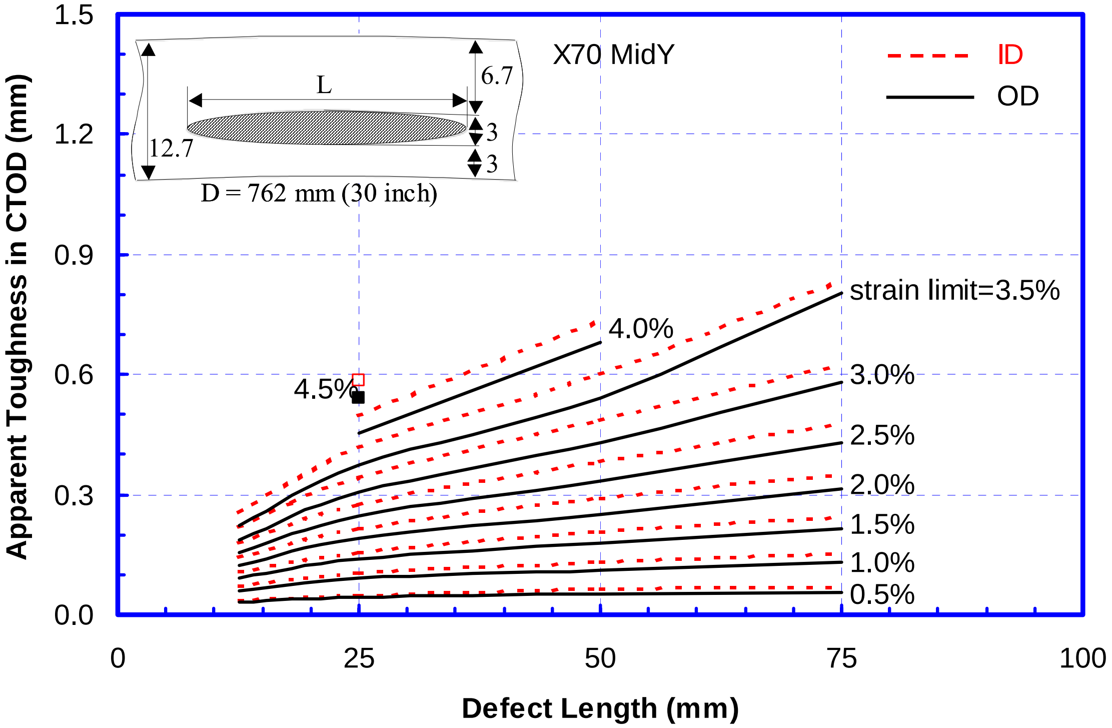

Figure 3-10 Relations among three key variables for an X70 pipe with buried defects [18]

4.0 Parametric Equations of Tensile Strain Limits

4.1 Background

The strains limits were tabulated with respect to material properties, pipe dimensions, and defect sizes in GRI-8656 and GRI-8509 for surface-breaking and buried defects, respectively. Parametric equations of longitudinal strain limits are developed in this section. These equations are the key elements of the limit state functions that form the basis of the reliability-based procedures.

4.2 Strain Limits of Surface-Breaking Defects

4.2.1 Geometry and Material Property Parameters

A girth weld with a surface-breaking root-side defect is schematically shown in Figure 4-1. The defect has a semi-elliptic shape and is located on the ID side of the pipe. The geometric parameters required to define the pipe and the defect dimensions include: pipe wall thickness *t*, defect surface length 2*c*, and defect height *a*. Prior results showed that the pipe diameter had a negligible effect on crack driving force over a pipe diameter range of 16 to 48 inches [14]. Therefore, pipe diameter is not a variable in this study. In addition to the geometric dimensions, the material parameters are: pipe grade *G*, apparent CTOD toughness δ, and *Y*/*T* ratio λ. Here *Y* is material's yield strength which is typically taken as the pipe grade and *T* is material's ultimate tensile strength (UTS).

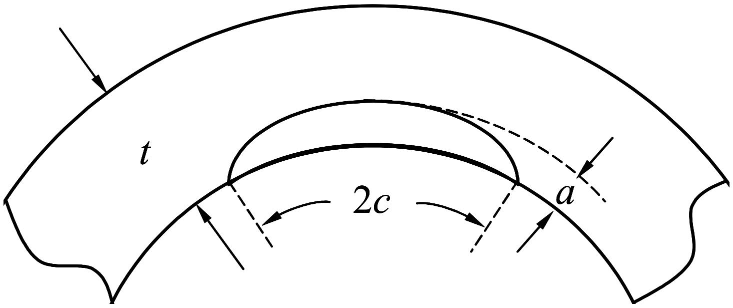

Figure 4-1 A girth weld with a surface-breaking defect and the relevant dimensions

4.2.2 Input Data for the Development of Parametric Equations

The input data in the development of the parametric equations was over a wide range of material properties, including X52, X60, X65, X70, and X80. The *Y/T* values varied with the pipe grade and had a range of 0.788 to 0.841 for X52 and from 0.889 to 0.917 for X80.

The pipe wall thickness (*t*) had 5 different values: 0.25, 0.375, 0.5, 0.75, and 1.0 inch. The defect height (*a*) was fixed at 3 mm which corresponds to one weld pass height. The ratio of defect height to wall thickness therefore varied from 12% to 47%. The defect length (2*c*) varied from 12.5 mm to 100 mm.

The strain limit was fitted as a function of material property, pipe dimension, and defect size. The maximum value of apparent CTOD toughness (δ) used in the fitting was 1.0 mm due to data limitations. Only the data of middle *Y*/*T* ratio in GRI-8656 were used in the fitting. The longitudinal strain limit is given as,

$$\varepsilon_{\mathrm{lim}it} = \delta^{(2.36-1.58\lambda-0.101\xi\eta)}\left(1+16.1\lambda^{-4.45}\right)\left(-0.157+0.239\xi^{-0.241}\eta^{-0.315}\right), \tag{3}$$

where $\lambda \equiv Y/T$, $\xi \equiv 2c/t$, and $\eta \equiv a/t$. The apparent CTOD toughness has a unit of mm in Eq. (3). The units of other parameters need to be consistent to produce the non-dimensional parameters. The strain limit ($\varepsilon_{\mathrm{limit}}$) is in percent (%). The minimum apparent CTOD (δ) value to use Eq. (3) is 0.1 mm.

4.3 Strain Limits of Buried Defects

4.3.1 Geometry and Material Property Parameters

The schematic of a buried defect is given in Figure 4-2. The defect was assumed to have either an elliptic or a rectangular shape. The geometry parameters are: pipe wall thickness *t*, defect length 2*c*, defect height 2*a*, and defect depth *d*. Similar to the surface-breaking defects, the material parameters include: material grade *G*, CTOD toughness δ, and *Y*/*T* ratio λ.

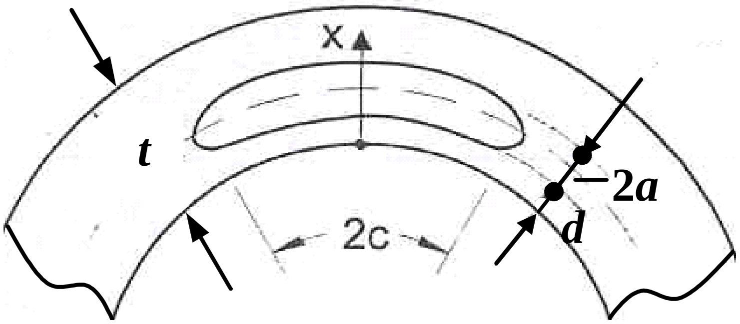

Figure 4-2 A girth weld with a buried defect and the relevant dimensions

4.3.2 Input Data for the Development of Parametric Equations

The material grade (*G*) ranged from 52 ksi (X52) to 80 ksi (X80). The *Y/T* ratio (λ) was fixed for each material grade at 0.841 (X52), 0.85 (X60), 0.883 (X65), 0.89 (X70), and 0.917 (X80), respectively. Those values were determined by the middle level *Y/T* ratios and were believed to be the most reasonable estimation for the materials.

The pipe wall thickness (*t*) had 4 different values: 0.250, 0.375, 0.500, and 0.750 inch. The defect depth (*d*) had different values depending up pipe wall thickness. It had a value of 1.5 mm for 0.250 inch wall thickness, 3.0 mm for 0.375-inch and 0.500-inch wall thickness, and 3.0 or 6.0 mm for 0.750-inch wall thickness. The defect height (2*a*) ranged from 3 mm to 6 mm and the defect length (2*c*) varied from 12.5 mm to 75 mm.

The strain limits were fitted to a parametric equation with a maximum value of apparent CTOD toughness of 0.6 mm due to data limitations. The strain limits of rectangular-shaped defects are given as,

$$\varepsilon_{\text{limit}} = \delta^{1.08-0.612\eta-0.0735\xi+0.364\psi}\left(12.3-4.65\sqrt{t}+0.495t\right)$$
$$\left(11.8-10.6\lambda\right)\left(-5.14+\frac{0.992}{\psi}+20.1\psi\right)\left(-3.63+11.0\sqrt{\eta}-8.44\eta\right) \tag{4}$$
$$\left(-0.836+0.733\eta+0.0483\xi+\frac{3.49-14.6\eta-12.9\psi}{1+\xi^{1.84}}\right)$$

The strain limits of the elliptical-shaped defects are given as,

$$\varepsilon_{\text{limit}} = \delta^{1.00-0.511\eta-0.0507\xi+0.364\psi}\left(5.62-2.30\sqrt{t}+0.260t\right)$$
$$\left(13.6-12.1\lambda\right)\left(-9.95+\frac{0.189}{\psi}-19.2\psi\right)\left(-4.21+12.3\sqrt{\eta}-9.14\eta\right) \tag{5}$$
$$\left(-0.180+7.28\eta-0.0321\xi+\frac{0.785-7.82\eta+0.0237\psi}{1+\xi^{-1.97}}\right)$$

where $\lambda \equiv Y/T$, $\xi \equiv 2c/t$, $\eta \equiv a/t, \psi \equiv d/t$. The wall thickness and the apparent CTOD toughness have the unit of mm in Eqs. (4-5). The units of other parameters need to be consistent to produce the non-dimensional parameters. The strain limit ($\varepsilon_{\text{limit}}$) is in percent (%). The minimum apparent CTOD (δ) value to use Eq. (3) is 0.1 mm.

4.4 Comparison between Parametric Equations and Original Input Data

The comparison between the input data and the fitted parametric equations for surface-breaking defects is given in Figure 4-3 and Figure 4-4. Figure 4-3 shows the relationship between the failure strains and the apparent CTOD toughness for different materials and defect sizes. Figure 4-4 shows the relationship between the failure strain and the pipe wall thickness. The fitted equations predicted the failure strains reasonably well as shown in those figures. The maximum error between the fitted functions and the input data was approximately 30%. In general, the higher the wall thickness, the bigger the maximum fitting error. The average error was about 10%.

The comparison between the input data and the fitted parametric equations for elliptical-shaped buried defects is given in Figure 4-5, which showed the relationship between the failure strains and the CTOD toughness for different materials and defect sizes. The fitted functions predicted the failure strain very well. The maximum error was less than 20% and the average fitting error was about 5%.

Similar agreement was found for the rectangular-shaped defects. The maximum fitting error was less than 25% with an average value of 7%.

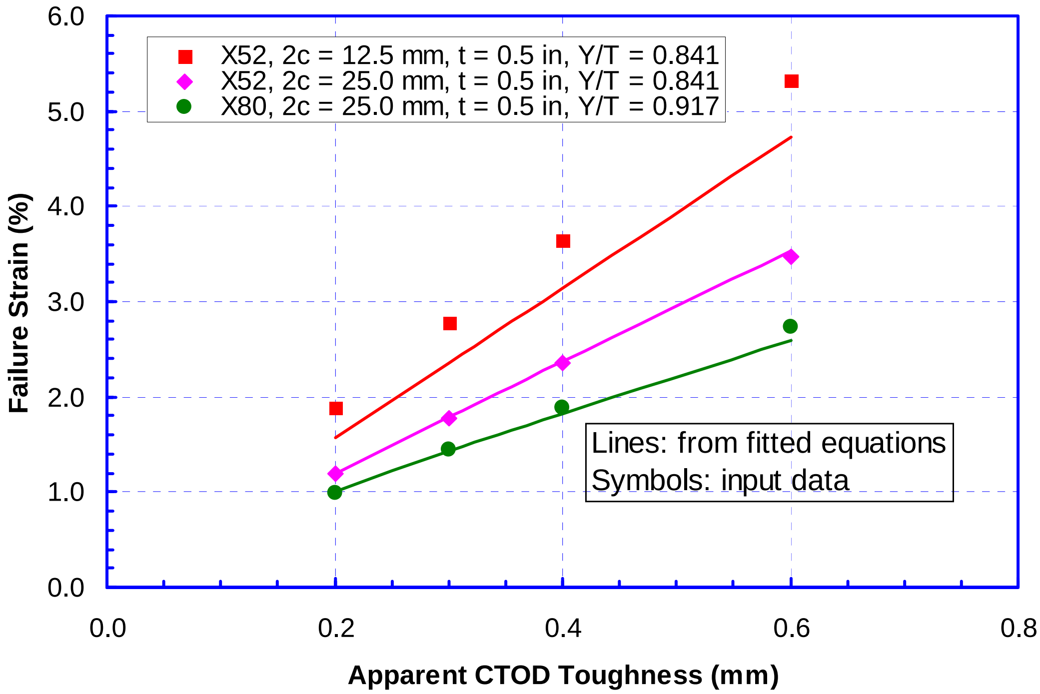

Figure 4-3 Comparison of failure strains as a function of CTOD toughness between input data and the fitted equation for surface-breaking defects (lines: fitted equation; symbols: input data). All defects have a 3-mm height.

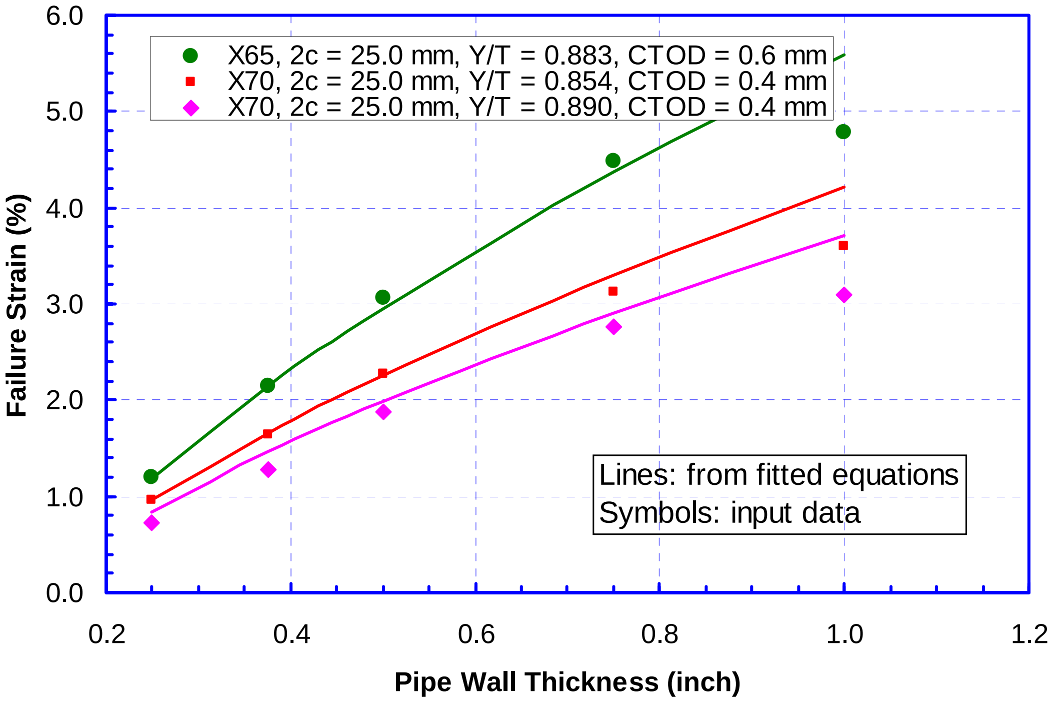

Figure 4-4 Comparison of failure strains as a function of wall thickness between input data and the fitted equation for surface-breaking defects (lines: fitted equation; symbols: input data). All defects have a 3-mm height.

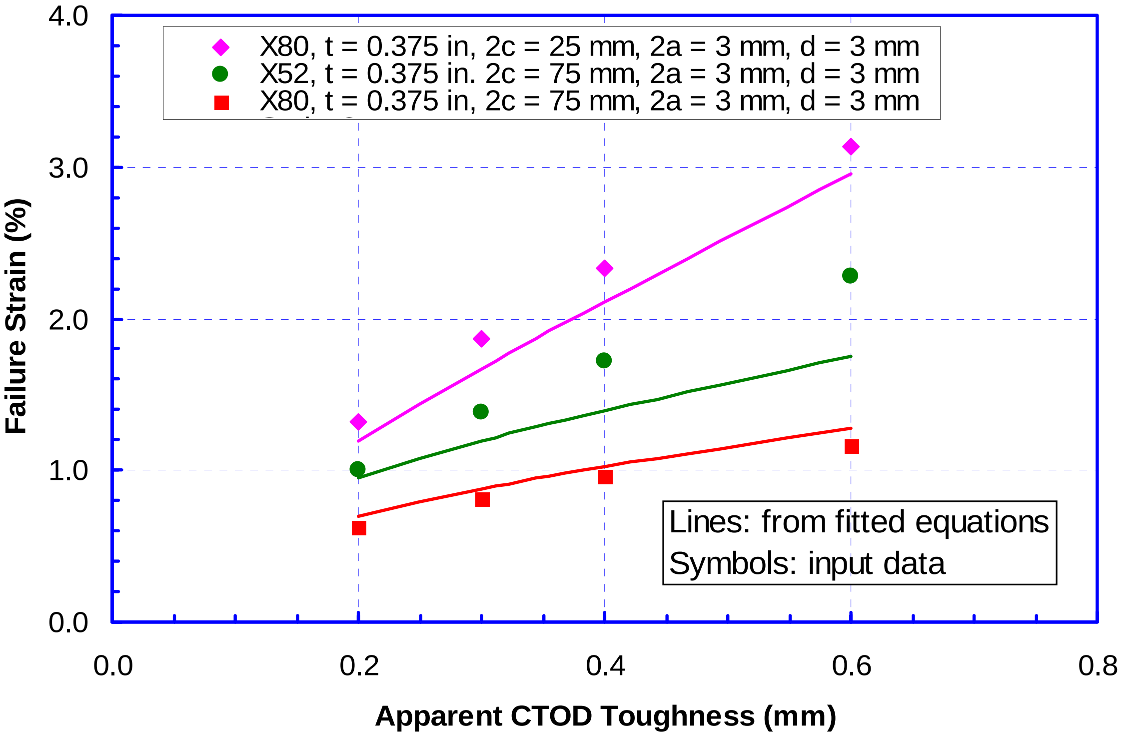

Figure 4-5 Comparison of failure strains as a function of CTOD toughness between input data and the fitted equation for elliptically-shaped buried defects (lines: fitted equation; symbols: input data)

5.0 Reliability Procedure for Strain-Based Design

5.1 Background on Limit State- and Reliability-Based Design

Limit states design (LSD) is gaining acceptance in the pipeline industries [2,21,22]. For instance, the increase of operating pressure of the UK National Transportation System (NTS) was justified on the basis of limit state design [23,24]. The use of LSD for onshore pipelines in the U.S. is rather limited. The term LSD is often synonymous with reliability-based design. Limit states can be broadly divided into several categories based on failure consequences. A buckling is generally considered a serviceability limit state, not a safety limit state, as immediate failure may not occur. However it may become a safety limit if, overtime, a rupture is resulted from other time-dependent failure mechanisms, such as fatigue and corrosion.

5.2 Fundamental of the Reliability Procedure

The parametric equations of Section 4.0 shows that the strain limits depend on geometric and material parameters. These parameters are alternative referred to as *basic variables*. A general form of the strain limit functions of Eqs. (3), (4), and (5) is given as,

$$\varepsilon_{\text{limit}} = G(X), \tag{6}$$

where X is a vector for the basic variables. As in many other engineering applications, these variables can vary in a certain range. The type of the distributions for each of these basic variables can be different. The distribution of a basic variable is determined by its mean value, coefficient of variance (COV), and the type of variation. The typical types of distributions used in reliability engineering assessment are normal distribution, lognormal distribution, extreme value distribution, Weibull distribution, et al. Since the strain limits are a function of the basic variables in a deterministic form, its distribution must also depend on the distributions of the basic variables.

To compute the distribution of the strain limits, the so-called direct numerical integration, or Monte-Carlo simulation is employed [25]. This method simply calculates the strain limits based on the values of the basic variables obtained by random sampling,

$$\varepsilon_{\text{limit},i} = G(X_i), i = 1,2,3,...n\,, \tag{7}$$

where X_i is the ith sampling of the basic variables, and n is the size of the sample. The random samplings of the basic variables are carried out according to their distribution types. To get an accurate statistical representation of the strain limits, the number of samples of the basic variables, n, must be sufficiently large. After the discrete evaluation of the strain limits, its distribution is represented by a discrete distribution density function $f_s(\varepsilon)$, or its accumulative function $F_s(\varepsilon)$, which gives the number of evaluated strain limits out of the total number n for the range of $\varepsilon_{limit} < \varepsilon$.

The computed distribution of strain limits can itself be used a design parameter. However, when the distribution of the design strain (also termed “demand”) is known, the failure probability can be computed by combining the demand and with “supply,” i.e., the achievable strain limits based on the distribution of the basic input parameters.

Assume the distribution density function of design strain (demarnd) is $f_d(\varepsilon\,)$ and the accumulative distribution of the strain limits (supply) is $F_s(\varepsilon)$, the probability of failure for the given distributions is calculated as,

$$P_f = \int f_d(\varepsilon) F_s(\varepsilon) d\varepsilon\,. \tag{8}$$

5.3 Numerical Integration by Monte Carlo Simulation

The Monte-Carlo simulation for the calculation of the distribution of the strain limits is carried out in the following steps:

1. Upon the choosing of the input parameters, i.e., their distribution types, their mean values and their COV, the parameters are randomly sampled according to their distribution types.
2. The random values of the basic variables are fed into the strain limit function of Eqs. (3), (4), or (5) . One random value of the limit strain is calculated.
3. Repeat Steps 1 and 2 for the entire population of sample size n.
4. Calculate the discrete distribution function for the limit strain.

5. Calculate the failure probability by numerical integration of Eq. (8).

5.4 Software of the Reliability Procedure

The software for the reliability-based strain design is a Windows® program. It also provides graphic charts for the visualization of the distributions of the basic variables and the distribution of the strain limits.

5.4.1 Input Parameters

The program considers two types of defects: surface-breaking defects and the buried defects. For the surface-breaking defects, the input parameters for the computation of the distribution of the strain limits are:

- CTOD,
- Yield strength of the pipe material,
- *Y*/*T* ratio,
- Pipe wall thickness,
- Defect length, and
- Defect height

For the buried defects, the input parameters for the computation of the distribution of the strain limits are:

- CTOD,
- *Y*/*T* ratio,
- Pipe wall thickness,
- Defect length,
- Defect height, and
- Defect depth

Only the rectangular-shaped buried defects are considered in the current software. The rectangular-shaped defects provide lower (thus conservative) values of strain limits.

To evaluation failure probability, the distribution of design strain needs to be entered as input parameters.

For each input parameter, four types of distribution are available for selection:

- Normal distribution,
- Lognormal distribution,
- Extreme value distribution type I, and

- Exponential distribution.

For each input parameter, its actual distribution is plotted graphically when a user clicks on any of the input field related to that parameter.

The software lets user to control the size of the Monte-Carlo simulation. By the sample size, the accuracy of the simulation is improved. The Monte-Carlo simulation can be started by clicking on the "*Simulation*" button.

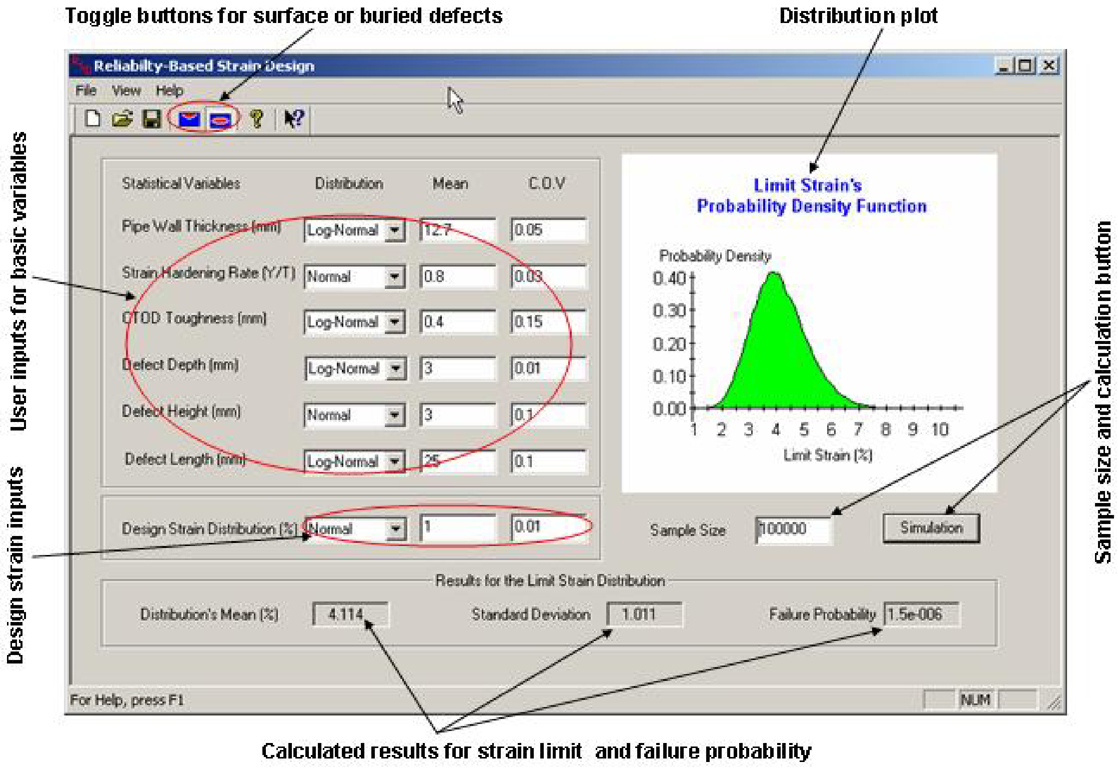

Toggle buttons for surface or buried defects

Distribution plot

User inputs for basic variables

Design strain inputs

Sample size and calculation button

Calculated results for strain limit and failure probability

Statistical Variables	Distribution	Mean	C.O.V
Pipe Wall Thickness (mm)	Log-Normal	12.7	0.05
Strain Hardening Rate (Y/T)	Normal	0.8	0.03
CTOD Toughness (mm)	Log-Normal	0.4	0.15
Defect Depth (mm)	Log-Normal	3	0.01
Defect Height (mm)	Normal	3	0.1
Defect Length (mm)	Log-Normal	25	0.1
Design Strain Distribution (%)	Normal	1	0.01

Sample Size 100000

Results for the Limit Strain Distribution

Distribution's Mean (%) 4.114

Standard Deviation 1.011

Failure Probability 1.5e-006

Figure 5-1 User interface of the software for reliability-based strain design

5.4.2 Output Parameters

At the completion of the simulation, the distribution of the strain limits is plotted graphically. The mean and standard deviation of the strain limits, along with the failure probability, are given at the bottom of the output window. The Windows® user interface of the software is shown in Figure 5-1.

5.4.3 File Saving Options

The software allows users to save the set of inputs to a file with an extension of "rsd". This file can be opened and modified later. The software also allows the export of all inputs and outputs to a Microsoft® Excel® spreadsheet file. This spreadsheet file retains the details of the user inputs, results, and graphical illustration of the results.

5.5 Understanding the Significance of the Results

An ideal Monte-Carlo simulation needs to have a huge sample size so that the same results (in this case the distribution of strain limits) can be repeated. The computational time increases with this sample size, especially when the number of basic variables is large. So a user needs to choose the proper sample size based on the expected level of confidence. The relation among the target probability, the confidence level, and the sampling size is given as [26],

$$N = \frac{-\ln(1-C)}{P_f}, \tag{9}$$

where C is a given confidence level, P_f the target probability, and N the required sample size. Thus, for a 95% confidence level and P_f=10^{-3}, the required number of sample is more than 3000.

5.6 Limits of the Procedures

Several limits of the procedure exist and we only identify two of them here for future improvement.

1. Limits on the types of distributions for input variables. Currently, only 4 types of distributions are included in the software. Other types may not more appropriate in certain situation.
2. Computational efficiency. It is known that Monte-Carlo simulation is slow for large sample size. This is especially true if the number of basic variables is large. Simplified procedures, such as First-Order Second-Moment (FOSM) procedure, can be implemented for performance improvement and other reliability calculation, such as sampling optimization or sensitivity study.

6.0 Concluding Remarks

6.1 Understanding Input Parameters

As evident in Section 4.0, the strain limits of a girth weld are strongly influenced by materials strain hardening capacity. This capacity is represented by the *Y*/*T* ratio in the present formulation. This representation is valid given the assumed stress strain curve. It should be understood, however, that *Y*/*T* ratios taken directly from a mill certificate or actual test of the linepipe material may not provide adequate representation of material’s strain hardening capacity. *A user should make sure that the Y/T ratio used in the actual calculation is a valid representation of material’s strain hardening capacity*. Some situations that may raise question about the use of the *Y*/*T* ratio from mill certificates in the calculation are given below.

1. Pipes made from modern micro-alloyed TMCP steels may have substantial differences in yield strength between longitudinal and hoop direction. The tensile

property measured in hoop direction is often reported for medium to large diameter pipes. However, the relevant property in assessing girth welds under longitudinal loading is the longitudinal property.

2. The longitudinal stress strain curves from pipes of modern micro-alloyed TMCP steels frequently exhibit “round-house” shape. Furthermore, the stress strain relations can exhibit nonlinear behavior at stress levels well below SMYS. Consequently, the reported values of yield strength can vary significantly, depending on how yield strength is defined. For high grade pipes (X80 and above), the present standard tests can underestimate the true yield strength. This can result in uncharacteristically low Y/T ratio. Since strain limits increase with the decrease of the Y/T ratio, using the low Y/T ratio can result in overly optimistic estimation of strain limits.

The apparent CTOD toughness is the toughness measured from specimens with similar constraint conditions as pipeline girth welds. Ideally, the apparent toughness should be determined directly from testing specimens with low constraint conditions. However, there are no codified test standards to measure the toughness of low constraint specimens. A number of research projects are under way with the aim of developing and validating test procedures for low constraint specimens [27,28]. In the absence of test procedures that can be used to measure the apparent toughness, it is useful to estimate the apparent toughness from the large library of CTOD toughness from the standard CTOD specimens (high constraint). Some discussions on this conversion procedure and a review of the constraint-based fracture mechanics and its implications in the assessment of girth weld defects are given in references [17,29].

6.2 Need for Future Work

In two previous projects the strains limits of girth welds were tabulated with respect to material properties, pipe dimensions, and defect sizes for surface-breaking and buried defects, respectively. Parametric equations that correlate those parameters are developed in this project. These equations are the key elements of the limit state functions that form the basis of the reliability-based procedures. Monte-Carlo simulation, which is implemented in a software program with Windows® user interface, is performed to compute the distribution of strain limits. When the distribution of the design strain is given, the software also provides estimates of failure probability based on user-specified distributions of input parameters, such as material properties, pipe dimensions, and defect size.

The data which formed the basis for the fitted Eqs. (3), (4), and (5) were obtained from large diameter pipes with relatively short defects. There short defects were considered necessary to have high longitudinal strain limits, i.e., strain-based design. The validity of these equations to small diameter pipes, such as those in offshore applications, needs to be examined. Furthermore, no residual stress was considered in obtaining the data. The minimum apparent toughness in using Eqs. (3), (4), and (5) is 0.1 mm. This roughly translates to a minimum required CTOD of 0.05 mm from standard bend specimens due to the constraint effects.

The reliability-based approach similar to that presented in this report is useful in risk-informed design and maintenance of pipelines. It allows more effective use of new materials and construction and maintenance procedures that are safer and more economical than those using the traditional deterministic approach.

Experimental validation of the reliability based procedure presented in this report is necessary before the procedure can be put to practical use. This validation cannot be performed adequately at the present time. Although test data on failure strains are available, other necessary input data to the assessment procedure are frequently not available. For instance, it is necessary to have the full stress strain curves measured in longitudinal direction to determine appropriate values of strain hardening. These curves are generally not available. Future experimental plans will need to address those deficiencies.

7.0 Acknowledgement

The support of PRCI Pipeline Materials Technical is greatly appreciated. The authors are grateful to the guidance and support of Mr. David Horsley, the ad hoc chair of the project. The authors wish to thank Mr. Steve Foh, Program Manager at GRI, for his guidance.

8.0 References

---

1 API Standard 1104, "Welding of Pipelines and Related Facilities," 19th Edition, September 1999.

2 CSA Z662-2003, *Oil and Gas Pipeline Systems*, Canadian Standards Association, Etobicoke, Ontario, Canada, 2003.

3 Pisarski, H. G., “Comparison of Deterministic and Probabilistic CTOD Flaw Assessment Procedures,” Proceedings of 17th International Conference on Offshore Mechanics and Arctic Engineering, Materials Symposium, Lisbon, Protugal, ASME, 1998.

4 Wang, Y.-Y., and Horsley, D. J., “Tensile Strain Limits of Pipelines,” Proceedings of EPRG-PRCI-APIA 14th Joint Technical Meeting on Pipeline Research, Berlin, German, May 19-23, 2003.

5 DNV Offshore Standard OS-F101, *Submarine Pipeline System*, 2000.

6 BS 7910:1999, “Guide on Methods for Assessing the Acceptability of Flaws in Metallic Structures,” British Standards Institution, 1999.

7 “Fracture Control for Installation Methods Introducing Cyclic Plastic Strains, Development of Guidelines for Reeling of Pipelines,” a JIP performed jointed by DNV, SINTEF, and TWI.

8 Wilkowski, G. M., Barnes, C. R., Scott, P. M., and Ahmad, J., “Development of Analysis to Predict the Interaction of Fracture Toughness and Constraint Effects for Surface-Cracked Pipe,” final report to A.G.A. Welding Supervisory Committee, Project PR-3-407, April 25, 1985.

9 Ahmad, J., Papaspyropoulos, V, and Hopper, A. T., “Elastic-Plastic Analysis of Edge-Notched Panel Subjected to Fixed Grip Loading,” Engineering Fracture Mechanics, Vol. 38, No. 4/5, 1991, pp. 283-294.

10 Mohr. W. C., “Strain-Based Design of Pipelines,” MMS Project No. 434, EWI Project No. 45892GTH, October 8, 2003.

11 Denys, R., Lefevre, A., and Baets, P. D., "A Rational Approach to Weld and Pipe Material Requirements for a Strain Based Pipeline Design," Proceedings of Applications & Evaluation of High-Grade Linepipes in Hostile Environments, Pacifico Yokohama, Japan, November 7-8, 2002, pp. 121-157.

12 Denys, R. M., private communication with Yong-Yi Wang.

13 Wang, Y.-Y., Rudland, D., Denys, R., and Horsley, D., "A Preliminary Strain-Based Design Criterion for Pipeline Girth Welds," *Proceedings of the International Pipeline Conference 2002*, Calgary, Alberta, Canada, September 29-October 3, 2002.

14 Wang, Y.-Y. and Cheng, W., "Guidelines on Tensile Strain Limits," GRI-04/0030, GRI Contract No. 8656, April 2004.

15 Wang, Y.-Y., et. al., "Tensile Strain Limits of Girth Welds with Surface-Breaking Defects Part I an Analytical Framework," in Pipeline Technology, Proceedings of the 4th International Conference on Pipeline Technology, Edited by Rudi Denys, Ostend, Belgium, May 9-13, 2004.

16 Wang, Y.-Y., et al., "Tensile Strain Limits of Girth Welds with Surface-Breaking Defects Part II Experimental Correlation and Validation," in *Pipeline Technology, Proceedings of the 4th International Conference on Pipeline Technology,* Edited by Rudi Denys, Ostend, Belgium, May 9-13, 2004.

17 Wang, Y.-Y. and Cheng, W., "Extension of Strain Design Criteria to Buried HAZ Defects," final report, GRI Contract No. 8509, December 2004.

18 Wang, Y.-Y., Cheng, W., and Horsley, D., "Tensile Strain Limits of Buried Defects in Pipeline Girth Welds," Proceedings of the International Pipeline Conference 2004, Calgary, Alberta, Canada, October 4-8, 2004.

19 Burdekin, F. M. and Dawes, M. G., "Practical Use of Linear Elastic and Yielding Fracture Mechanics with Particular Reference to Pressure Vessels," *Proceedings of the Institute of Mechanical Engineers Conference*, London, May 1971, pp. 28-37.

20 BRITE EURAM Project: Structural Integrity Assessment Procedure for European Industry – SINTAP, Procedure Document, British Steel (now Corus Group) Swinden Technology Centre, Rotherham, UK, November 1999.

21 NEN 3650, *Requirements for Steel Pipeline Transportation Systems*, 1992.

22 API RP 1111, Design, *Construction, Operation, and Maintenance of Offshore Hydrocarbon Pipelines (Limit State Design),* third edition, American Petroleum Institute, July 1999.

23 Francis, A., Espiner, R. J., Edwards, A. M., and Senior, G., "The Use of Reliability-Based Limit State Methods in Unrating High Pressure Pipelines," Proceedings of the International Pipeline Conference, Calgary, Canada, June 1998.

24 Francis, A., Edwards, A. M., Espiner, R. J., and Senior, G., "An Assessment Procedure to Justify Operation of Gas Transmission Pipelines at Design Factors up to 0.8," Pipeline Technology Conference, Brugge, Belgium, May 2000.

25 Robert E. Belchers, Structural Reliability Analysis and Prediction, John Wiley & Sons, 2002

26 K. Broding, F. W. Diederich, and P.S. Parker, Structural optimization and design base on a reliability design criterion, J. Spacecraft, 1(1), 56-61, 1964.

27 "A Comprehensive Update in the Evaluation of Pipeline Weld Defects," a project funded by the U.S. Department of Transportation and PRCI, PI Yong-Yi Wang.

---

28 “Advanced Integration of Multi-Scale Mechanics and Welding Process Simulation in Weld Integrity Assessment,” a project funded by the U. S. Department of Energy, PRCI, and Emc^2, PI Yong-Yi Wang.

29 Wang, Y.-Y., and Horsley, D. J., “Application of Constraint-Sensitive Fracture Mechanics to the Assessment of Girth Weld Integrity,” IPC04-0525